UNIVERSITÉ DU LUXEMBOURG

PhD-FSTC-2019-20
The Faculty of Sciences, Technology and Communication

DISSERTATION

Presented on 15/03/2019 in Esch-sur-Alzette, Luxembourg
to obtain the degree of

DOCTEUR DE L'UNIVERSITÉ DU LUXEMBOURG EN PHYSIQUE

by

Hossam Elanzeery
Born on 9th of April 1987 in Cairo, (Egypt)

THE CAUSE OF INTERFACE RECOMBINATION IN CU-RICH CIS THIN FILM SOLAR CELLS

Dissertation defense committee

Dr. Susanne Siebentritt, dissertation supervisor
Professor, Université du Luxembourg
Dr. Thomas Schmidt, Chairman
Professor, Université du Luxembourg
Dr. Guy Brammertz
Principal Scientist, IMEC-IMOMEC
Dr. Alex Redinger, Vice Chairman
Professor, Université du Luxembourg
Dr. Marika Edoff
Professor, Uppsala University

Table of contents

List of Figures ……..……..I

List of Tables ……...……VI

Abstract ……...……VII

Chapter 1: Introduction ……..……....1

References Chapter 1……..5

Chapter 2: Thin Film Solar Cells …….....6

2.1 Thin film solar cells ……...…..7

2.2 CI(G)S thin film solar cells ……....8

2.3 Cu-rich & Cu-poor CI(G)S …….....10

2.4 Surface Post-deposition treatments (PDT) …….....12

2.4.1 Potassium Fluoride (KF) treatment ..…….....13

2.4.2 Indium-Selenium treatment …….....15

References Chapter 2 …….....16

Chapter 3: Synthesis of Thin Film CI(G)S Solar Cells …….....20

3.1 Standard baseline process ……....21

3.1.1 Synthesis of CI(G)S absorbers …….....22

3.1.2 Electron-beam Evaporation …….....26

3.2 Post-deposition treatments ……29

3.2.1 Ex-situ KF treatment …….....29

3.2.2 In-situ KF treatment …….....32

3.2.3 Selenium (Se) treatment ……..…….....35

References Chapter 3 …….....37

Chapter 4: Characterization methods for CI(G)S solar cells ……..…….....39

4.1 Solar cell performance …….....40

4.2 External Quantum Efficiency (EQE) & Bandgap calculations …….....47

4.3 Dominant recombination path …….....52

4.4 Doping Extraction ……..60

4.5 Capacitance steps and defects …….....67

References Chapter 4 …….....75

Chapter 5: Cu-rich versus Cu-poor CI(G)S thin film solar cells ……..…77

5.1 Physical characteristics of Cu-rich CI(G)S …….....78

5.2 V_{OC} deficit and collection efficiencies in CI(G)S solar cells …….....80

5.3 Dominant recombination path in CI(G)S solar cells ……..87

5.4 Apparent doping and defects in CI(G)S solar cells …….....91

5.5 Summary ……99

References Chapter 5 ……100

Chapter 6: Improving performance of CI(G)S thin film solar cells …….....104

6.1 Ex-situ KF post-deposition treatment for Cu-rich & Cu-poor CIS …….....106

6.2 In-situ KF post-deposition treatment for Cu-rich & Cu-poor CIS ……...122

6.3 Ga-Se post-deposition treatment for Cu-rich CIGS ……140

6.4 Se-only post-deposition treatment for Cu-rich CIS ……147

6.5 Low-bandgap Cu-poor CIS & CIGS for tandem applications ……162

References Chapter 6 ……175

Chapter 7: Root cause for interface recombination in Cu-rich CI(G)S cells ……....180

7.1 Characterization of the 200±20 meV defect in Cu-rich CI(G)S cells ……..182

7.2 Summary of the effects of PDTs on Cu-rich CI(G)S solar cells ……..192

7.2.1 Observations related to Cu-rich CI(G)S solar cells ……....193

7.2.2 Observations related to the effect of PDTs ……...194

7.2.3 *The root cause of interface recombination: Se-related defect* ……....196

7.3 The origin of the formation of the 200±20 meV defect ……..…….....200

7.3.1 The Stoichiometric CIS phase ……...202

7.3.2 The KCN etching process …….....210

7.4 Passivation of the 200±20 meV defect using modified buffer layers ……..217

7.5 Summary on interface recombination challenge in Cu-rich CIS cells …….....230

References Chapter 7 ……233

Chapter 8: Conclusion and Outlook ……...235

Acknowledgement …….....241

Annex A.1: Sample list for Chapter 5 ……...…….245

Annex A.2: Sample list for Chapter 6……247

Annex A.3: Sample list for Chapter 7 ……....249

Annex B: List of Publications ...……..251

Annex C: List of Conferences and workshops……...253

List of Figures

Figure 2.1: CI(G)S solar cell structure ……..8

Figure 3.1: A schematic for Physical Vapor Deposition (PVD) using a Molecular Beam Epitaxy (MBE) tool ……..22

Figure 3.2: Phase diagram of chalcopyrite CIS ……24

Figure 3.3: E-beam evaporation tool for depositing MgF_2 and grids ……..26

Figure 3.4: An example of a reflection spectrum for one of the solar cells ……27

Figure 3.5: Carbolite tube furnace for annealing in the presence of Se powder used for the ex-situ KF PDT ……..30

Figure 3.6: Annealing profile for CIS absorbers treated with the ex-situ KF PDT ……....31

Figure 3.7: A schematic for the PVD used during the in-situ KF PDT ……..33

Figure 3.8: Temperature profile for the in-situ KF PDT ……..34

Figure 3.9: Temperature profile for the Se-PDT ……36

Figure 4.1: IV curve of a solar cell ……....44

Figure 4.2: IV characterization tool setup ……....46

Figure 4.3: An example of the EQE spectrum for one of the solar cells ……..48

Figure 4.4: EQE tool setup ……..51

Figure 4.5: An illustration example for the IVT measurements ……....52

Figure 4.6: Band diagram of a CIS solar cell ……....54

Figure 4.7: IVT tool setup ……....59

Figure 4.8: An illustration example for deducing the doping in a solar cell ……...63

Figure 4.9: Band diagram of a CIS solar cell with a defect ……..65

Figure 4.10: CV tool setup ……..66

Figure 4.11: An illustration example for admittance measurements ……....71

Figure 4.12: An illustration example for extracting the activation energy of the main capacitance step from the admittance measurements ……..73

Figure 5.1: SEM top-view for Cu-rich and Cu-poor CIS absorbers ……...78

Figure 5.2: IV characteristics of Cu-rich and Cu-poor CI(G)S solar cells ...……..80

Figure 5.3: EQE response for Cu-rich and Cu-poor CI(G)S solar cells …….....83

Figure 5.4: Optical calculations for the carrier collection efficiency for both Cu-rich and Cu-poor CIS solar cells …….....85

Figure 5.5: Temperature dependence of the open circuit voltage for Cu-rich and Cu-poor CI(G)S solar cells ……89

Figure 5.6: The Arrhenius plot for the series resistance as function of temperature for Cu-rich and Cu-poor CI(G)S solar cells ……90

Figure 5.7: Arrhenius plot of the CV measurements for Cu-rich and Cu-poor CI(G)S cells..91

Figure 5.8: Admittance measurements for Cu-rich and Cu-poor CIS solar cells ……...95

Figure 5.9: Admittance measurements for Cu-rich CIGS solar cells …….....96

Figure 5.10: Admittance measurements for Cu-poor CIGS solar cells ……..97

Figure 5.11: Activation energies deduced from Admittance measurements as function of increasing the bandgap …….....98

Figure 6.1: EQE spectrum response for both Cu-rich and Cu-poor CIS cells with and without the ex- situ KF PDT ……...110

Figure 6.2: IV characteristics for both Cu-rich and Cu-poor CIS cells with and without the ex-situ KF PDT …….....111

Figure 6.3: Temperature dependence of voltage for Cu-rich and Cu-poor CIS cells with and without the ex-situ KF PDT …….....113

Figure 6.4: Arrhenius plot for the series resistance as function of temperature for Cu-rich and Cu-poor CIS cells with and without the ex-situ KF PDT …….....115

Figure 6.5: Arrhenius plot of the main capacitance step for Cu-rich and Cu-poor CIS cell after the ex-situ KF PDT …….....116

Figure 6.6: XRD measurements for a) Cu-rich and b) Cu-poor CIS absorbers before and after the ex- situ KF PDT …….....116

Figure 6.7: XPS measurements for Cu-rich and Cu-poor CIS absorbers after the ex-situ KF PDT ……120

Figure 6.8: SEM monographs for Cu-rich with and without the in-situ KF PDT 123

Figure 6.9: IV parameters for Cu-rich and Cu-poor CIS cells with and without the in-situ KF PDT ……124

Figure 6.10: EQE spectra for Cu-rich and Cu-poor CIS with and without the in-situ KF PDT ……126

Figure 6.11: Reflection measurements for Cu-rich CIS cells with and without the in-situ KF PDT …….....129

Figure 6.12: V_{OC} as function of temperature for Cu-rich and Cu-poor CIS with and without the in-situ KF PDT …….....129

Figure 6.13: Mott-Schottky plot for Cu-rich and Cu-poor CIS solar cells with and without the in-situ KF PDT …….....131

Figure 6.14: Low temperature PL measurements for Cu-rich CIS with and without the in-situ KF PDT ……..135

Figure 6.15: Admittance measurements for Cu-rich CIS cells with and without the in-situ KF PDT …….....137

Figure 6.16: The capacitance derivative plot for Cu-rich CIS cells with and without the in-situ KF PDT ……...138

Figure 6.17: IV characteristics for Cu-rich CIGS with and without Ga-Se PDT ……142

Figure 6.18: EQE spectra for Cu-rich CIGS cells with and without Ga-Se PDT 143

Figure 6.19: V_{OC} as a function of temperature for Cu-rich CIGS solar cells with and without the Ga-Se PDT …….....144

Figure 6.20: Schematic for Cu-rich CIS absorbers treated with Se-only PDT ……149

Figure 6.21: IV characteristics of Cu-rich CIS cell with & without Se-only PDT ……...150

Figure 6.22: EQE spectra for Cu-rich CIS cell with and without Se-only PDT ……...152

Figure 6.23: Temperature dependence of V_{OC} for Cu-rich CIS cell with and without Se-only PDT …….....153

Figure 6.24: Admittance spectra for Se-treated Cu-rich CIS absorber and cell …..156

Figure 6.25: Spectra of capacitance derivative peaks for Cu-poor CIS, Cu-rich CIS and Cu-rich CIS treated with Se-only PDT …….....158

Figure 6.26: Normalized PL spectra for Cu-rich CIS with and without Se-only PDT ….....159

Figure 6.27: Mott-Schottky for Cu-rich CIS absorber and solar cell with and without the Se-only PDT ……160

Figure 6.28: EQE spectra for CIS 0.95, CIGS 1.04 and CIGS 1.07 before and after adding an ARC layer ……..162

Figure 6.29: EQE spectra for CIS 0.95 measured in-house and CIGS 1.04 and CIGS 1.07 certified at Fraunhofer-ISE …….....163

Figure 6.30: IV characteristics for CIS 0.95 solar cell measured in-house as well as CIGS 1.04 and CIGS 1.07 solar cells certified ……....164

Figure 6.31: Deficiency in CIS 0.95, CIGS 1.04 and CIGS 1.07 with and without an optical filter of 780 nm …….....168

Figure 6.32: IV characteristics of CIS 0.95, CIGS 1.04 and CIGS 1.07 measured under a long-pass optical filter of 780 nm …….....169

Figure 6.33: V_{OC} (T) for CIS 0.95, CIGS 1.04 and CIGS 1.07 ……....170

Figure 6.34: Admittance spectra for CIS 0.95, CIGS 1.04 and CIGS 1.07 cells ……..172

Figure 7.1: Schematics for Cu-rich CIS etched absorbers processed in three different structures ……184

Figure 7.2: Admittance capacitance spectra for Cu-rich CIS absorbers grown under Low-Se flux ……..185

Figure 7.3: Admittance capacitance spectra for Cu-rich CIS absorbers grown under Med-Se flux ……..186

Figure 7.4: Admittance capacitance spectra for Cu-rich CIS absorbers grown under High-Se flux …….187

Figure 7.5: Activation energies extracted from the admittance measurements ……190

Figure 7.6: Activation energies for series resistance deduced from IVT measurements …..191

Figure 7.7: Admittance spectra for Cu-rich CIGS Schottky absorber and cell ….....199

Figure 7.8: SEM micrographs for Cu-rich, stoichiometric and Cu-poor CIS unetched absorbers ……203

Figure 7.9: X-Ray Diffraction measurements for Cu-rich, stoichiometric and Cu-poor CIS absorbers without etching ……..204

Figure 7.10: Arrhenius plot for stoichiometric CIS absorber …….....205

Figure 7.11: IV characteristics for Cu-rich, Cu-poor and stoichiometric CIS solar cells 206

Figure 7.12: EQE spectra for Cu-rich, Cu-poor and stoichiometric CIS cells …….....207

Figure 7.13: V_{OC} (T) curve for Cu-rich, Cu-poor and stoichiometric CIS cells ……...208

Figure 7.14: Admittance spectra for Cu-poor and stoichiometric CIS Schottky absorbers etched under strong KCN conditions …….211

Figure 7.15: PL yield intensities for Cu-rich and Cu-poor CIS absorbers: unetched, weak KCN etched and strong KCN etched …….....212

Figure 7.16: Arrhenius plots for Cu-rich CIS Schottky absorbers etched with strong KCN and strong NaCN …….....214

Figure 7.17: Admittance spectra for Cu-rich CIS devices with standard in-house CdS, CdS EMPA and Zn(O,S) deposited in-house ……220

Figure 7.18: Admittance spectra for Cu-rich CIS solar cells with Zn(O,S) deposited in-house with 6, 8 and 16 times TU concentrations ……..……...222

Figure 7.19: V_{OC} (T) curves for Cu-rich CIS solar cells with our in-house CdS, CdS deposited at EMPA and Zn(O,S) with 8 times TU concentrations …….....224

Figure 7.20: EQE spectra for Cu-rich CIS solar cells with CdS deposited in-house and CdS deposited at EMPA ……228

Figure 7.21: An overview of the capacitance steps observed by admittance measurements in this thesis …….....231

List of Tables

Table 5.1: EDX ratio for one of Cu-rich and Cu-poor CI(G)S absorbers before and after KCN etching ……..79

Table 5.2: IV parameters of Cu-rich and Cu-poor CI(G)S with different bandgap energies .80

Table 5.3: Carrier Collection Efficiency calculations for Cu-rich and Cu-poor CI(G)S cells ……...85

Table 5.4: Series resistance activation energy deduced from IVT measurements under dark conditions for Cu-rich and Cu-poor CIS & CIGS solar cells ……..90

Table 5.5: Activation energies deduced from IVT measurements compared to activation energies deduced from admittance measurements ……...……98

Table 6.1: IV parameters for Cu-rich CIS solar cells with and without different annealing conditions of the ex-situ KF PDT …….....107

Table 6.2: Calculations for the carrier collection efficiency of Cu-rich and Cu-poor CIS cells with and without the ex-situ KF PDT …….....110

Table 6.3: Electrical parameters for both Cu-rich and Cu-poor CIS cells with and without the ex-situ KF PDT ……..112

Table 6.4: Electrical parameters for both Cu-rich and Cu-poor CIS cells with and without the in-situ KF PDT …….....124

Table 6.5: Electrical parameters for Cu-rich CIGS cells with and without Ga-Se PDT …...142

Table 6.6: Electrical parameters for Cu-rich CIS cells with and without Se-only PDT ……150

Table 6.7: Electrical parameters for CIS 0.95, CIGS 1.04 and CIGS 1.07 cells ……...165

Table 6.8: Electrical parameters for CIS 0.95, CIGS 1.04 and CIGS 1.07 measured under a long-pass optical filter of 780 nm …….....169

Table 7.1: IV parameters for Cu-rich CIS solar cells with standard CdS, CdS deposited in EMPA and Zn(O,S) deposited in-house with 6, 8 and 16 times TU concentrations ……....226

Abstract

$Cu(In,Ga)Se_2$ (CIGS) thin film solar cells are considered one of the most promising thin film technologies reaching efficiencies beyond 22 %. The record efficiencies for CIGS thin film solar cells are based on CIGS absorbers grown under Cu-deficiency conditions. CIGS absorbers grown under Cu-excess (Cu-rich) show larger grains and better transport properties compared to CIGS absorbers grown under Cu-deficiency (Cu-poor) conditions. However, solar cells based on Cu-rich CIGS absorbers suffer from significantly lower efficiencies compared to Cu-poor CIGS solar cells.

The lower efficiency of Cu-rich CIGS solar cells compared to Cu-poor CIGS cells is attributed to lower open circuit voltage (V_{OC}) in Cu-rich CIGS cells compared to Cu-poor CIGS cells. The reason behind the lower V_{OC} values was investigated and was attributed to recombination losses at the absorber/buffer interface and higher doping of Cu-rich CIGS cells compared to Cu-poor CIGS cells but the complete picture behind the origin of these interface recombination losses and high doping in Cu-rich CIGS cells was not fully understood. The work of this thesis explains why Cu-rich CIGS cells suffer from interface recombination losses, higher doping and lower efficiencies. This explanation is divided into three parts:

The first part characterizes Cu-rich and Cu-poor solar cells of the ternary CIS and the quaternary CIGS. This part confirms that Cu-rich CI(G)S solar cells suffer from lower efficiencies, lower V_{OC}, interface recombination losses and higher doping compared to Cu-poor CI(G)S solar cells. Moreover, a 200 ± 20 meV defect was observed for Cu-rich CIS cells.

The second part introduces different post-deposition treatments (PDTs) to Cu-rich CI(G)S cells. An ex-situ KF, in-situ KF and a Se-only PDT were introduced to Cu-rich CIS cells. All the three treatments succeeded in improving the V_{OC}, improving the interface recombination losses, decreasing the doping and passivating the 200 ± 20 meV defect that has been identified as a Se-related defect in Cu-rich CIS solar cells. A Ga-Se PDT was introduced to Cu-rich CIGS solar cells and successfully improved the V_{OC}, improved the interface recombination losses and decreased the doping of Cu-rich CIGS solar cells.

The third part analyses the changes observed on Cu-rich CI(G)S cells before and after the PDTs. Based on these observations, it was concluded that the origin behind both the interface recombination losses and the high doping of Cu-rich CI(G)S cells is a Se-related acceptor defect (detected by admittance measurements for Cu-rich CIS and speculated for Cu-rich CIGS). The passivation of this defect reduces the recombination losses at the absorber/buffer interface, decreases the doping, improves the V_{OC} and consequently leads to an increase in the efficiency of Cu-rich CI(G)S solar cells. Moreover, this part shows that the Se-related defect is formed as a result of the strong etching step that is mandatory for Cu-rich CI(G)S absorbers to remove conductive copper selenide secondary phases. Applying the same strong etching conditions to Cu-poor CIS absorbers leads to the formation of the Se-related defect. After understanding that the Se-related defect is formed as a result of the strong etching conditions and that the Se-related defect can be passivated with PDTs that are rich in Se, an alternative mean of passivating this defect without PDTs was proposed. The Se-related defect was shown to be passivated using buffer layers of high enough thiourea (source of Sulphur) and without any PDTs leading to the reduction of interface recombination losses, decrease of the doping, increase of the V_{OC} and increase of the efficiency of Cu-rich CIS cells.

To conclude, the reason behind the interface recombination losses and high doping in Cu-rich CI(G)S solar cells is a Se-related acceptor defect originating after etching the absorbers with strong etching conditions. This defect can be passivated with high enough chalcogen either with PDTs (high enough Selenium) or buffer layers (high enough Sulphur).

Chapter 1: Introduction

Photovoltaics (PV) are currently one of the most promising renewable energy sources. There are two main challenges for photovoltaics nowadays: cost and efficiency. Thin film solar cells represent one potential mean of reducing the cost of solar cells while maintaining high efficiencies by using thin absorber layers. Thin film technologies based on $Cu(In,Ga)Se_2$ (CIGS) absorbers are considered one of the most promising thin film technologies as a result of the high efficiencies these CIGS solar cells can achieve. CIGS absorbers can be grown either under Cu-excess forming Cu-rich absorbers or under Cu-deficiency forming Cu-poor absorbers.

Cu-rich CIGS absorbers are characterized by larger grain sizes, higher mobility and better transport properties compared to Cu-poor CIGS absorbers. However, solar cells based on Cu-poor CIGS absorbers achieve higher efficiencies compared to solar cells based on Cu-rich CIGS absorbers. Current state-of-the-art high efficiency CIGS solar cells are based on Cu-poor CIGS absorbers. A fundamental question then rises up: Why do Cu-rich CIGS solar cells show lower efficiency compared to Cu-poor CIGS solar cells?

The main reason behind the lower electrical performance of Cu-rich CI(G)S solar cells compared to Cu-poor CI(G)S solar cells is the deficiency of V_{OC} values in Cu-rich CI(G)S solar cells compared to Cu-poor CI(G)S solar cells [1]. Several investigations were performed by my previous colleagues in order to understand the problem of Cu-rich CI(G)S solar cells. These investigations suggested that the main challenge in Cu-rich CI(G)S solar cells is the Cu-rich CI(G)S absorber/buffer interface [1]. Cu-rich CI(G)S solar cells suffer from recombination losses at the absorber/buffer interface. Another fundamental question then appears: What is the root cause of the interface recombination losses in Cu-rich CI(G)S solar cells? Different potential causes were proposed but the complete picture for the root cause of the interface recombination losses in Cu-rich CI(G)S solar cells was not yet clear. The answer to this question will be one of the challenges and the main goal of this thesis.

In order to find an explanation to the root cause of the interface recombination losses in Cu-rich CI(G)S solar cells, it was necessary to find different means of improving the absorber/buffer interface in Cu-rich CI(G)S solar cells. Observing the changes before and after improving the Cu-rich CI(G)S absorber/buffer interface would provide additional insights to understanding the challenge behind the interface recombination losses in Cu-rich CI(G)S solar cells.

Alkali post-deposition treatments have been known to play an important role in improving the efficiency of CIGS thin film solar cells by improving the absorber/buffer interface [2]. State-of-the-art record efficiencies for CIGS thin film solar cells are based on different alkali post-deposition treatments [3 – 6]. However, these alkali post-deposition treatments have been applied for Cu-poor CIGS solar cells and not for Cu-rich CIGS solar cells. It has been reported that these alkali post-deposition treatments have the following effects on Cu-poor CIGS absorbers and solar cells [7]:

- The post-deposition treatments form a Cu-depleted layer on the surface of Cu-poor CIGS absorbers
- The post-deposition treatments facilitate the diffusion of cadmium from the buffer layer to the absorber surface
- The post-deposition treatments improve the absorber/buffer interface of Cu-poor CIGS solar cells
- The post-deposition treatments increase the V_{OC} and the efficiency of Cu-poor CIGS solar cells.

Here comes a third fundamental question: Will the alkali post-deposition treatments be able to improve the absorber/buffer interface of Cu-rich CI(G)S solar cells and improve both the V_{OC} and the efficiency of Cu-rich CI(G)S solar cells? Taking in consideration that the complete picture of understanding the mechanism behind the effects of the alkali post-deposition treatments on Cu-poor CIGS solar cells is still not yet clear, the answer to this third question requires deep investigations to understand the differences between Cu-rich and Cu-poor CI(G)S absorbers and solar cells. Moreover, it is important to understand how the alkali post-deposition treatments interact with the surface of Cu-rich CI(G)S absorbers from different characterization perspectives. The answer to this third question will be an additional challenge for this thesis.

To achieve the goals of this thesis and understand the challenges at the Cu-rich front interface, the main focus of this thesis will be dedicated to Cu-rich CIS absorbers in comparison with Cu-rich CIGS absorbers. CIS is the ternary compound from the quaternary CIGS compound with a simpler lattice structure composed of copper, indium and selenium compared to the quaternary structure that contains copper, indium, gallium and selenium.

In addition to the main goals of this thesis on understanding the different challenges present in Cu-rich CI(G)S solar cells, one part of this thesis will be dedicated to improving Cu-poor CI(G)S solar cells with a low bandgap.

As mentioned earlier, state-of-the-art CIGS solar cells are based on Cu-poor CIGS absorbers. However, to achieve even higher efficiencies and exceed theoretical efficiency limits of single junction solar cells, new approaches are needed. The approach of tandem solar cells is considered one of the most effective means of exceeding the theoretical efficiency limits of single junction solar cells by stacking two or more solar cells together. To achieve this approach of tandem solar cells, a low bandgap and a high bandgap solar cells are needed to maximize the collection efficiency of the solar spectrum. While there is a lot of progress in achieving high performance high bandgap thin film solar cells, only few reports succeeded in achieving high performance low bandgap thin film solar cells [8]. These reported high performance low bandgap thin film solar cells were based on alkali post-deposition treatments. A new challenge then comes up: Can we develop in our laboratories high performance low bandgap thin film solar cells without any type of post-deposition treatments?

To conclude, the goal of this thesis is to answer the following three challenges:

1. What is the root cause of the interface recombination losses in Cu-rich CI(G)S solar cells? (main challenge)
2. Will the post-deposition treatments succeed in improving the absorber/buffer interface, increase the V_{OC} and improve the efficiency of Cu-rich CI(G)S solar cells?
3. Can we develop in our laboratories high performance CI(G)S solar cells with low bandgap and without any post-deposition treatments?

The work of this thesis is divided into eight chapters. This introduction represents the **first chapter** giving an overview of the work of the whole thesis.

Chapter 2 introduces the emerging thin film technologies in section 2.1 before focusing on CIGS thin film technology in section 2.2 and the classification of CIGS absorbers in terms of Cu-rich and Cu-poor in section 2.3. Section 2.4 provides a literature review on the post deposition treatments responsible for the recent progress in efficiencies of Cu-rich and Cu-poor CI(G)S solar cells.

Chapter 3 introduces the synthesis of both the absorber growth and the post deposition treatments. The synthesis process of the CI(G)S absorbers is explained in section 3.1. Section 3.2 is dedicated to the development of the post deposition treatments.

Chapter 4 introduces the theoretical background of the characterization techniques used to understand the performance of CI(G)S absorbers and solar cells. Section 4.1 focuses on the current-voltage characterization technique. Section 4.2 focuses on the quantum efficiency. Section 4.3 interprets the current-voltage measurements as a function of temperature. Section 4.4 focuses on the capacitance-voltage measurements and Section 4.5 discusses the admittance measurements.

Chapter 5 introduces the observed differences between Cu-rich and Cu-poor CI(G)S absorbers and solar cells. Section 5.1 highlights the structural characteristics of the absorbers. Section 5.2 focuses on the electrical performance of the solar cells in terms of electrical parameters and quantum efficiency. Section 5.3 discusses the absorber/buffer interface losses. Section 5.4 provides an overview of the doping and the defect signatures in Cu-rich and Cu-poor CI(G)S solar cells.

Chapter 6 presents the different approaches used to optimize and improve the electrical performance of Cu-rich and Cu-poor CI(G)S solar cells. Section 6.1 and Section 6.2 present the ex-situ and the in-situ potassium fluoride post deposition treatments respectively applied for Cu-rich and Cu-poor CIS solar cells. Section 6.3 introduces a Ga-Se treatment for Cu-rich CIGS solar cells. Section 6.4 introduces a Se-only post-deposition treatment for Cu-rich CIS solar cells. Section 6.5 introduces high performance low bandgap Cu-poor CI(G)S solar cells with the potential to be integrated for tandem applications.

Chapter 7 focuses on identifying the root cause of the interface recombination losses in Cu-rich CI(G)S solar cells. Section 7.1 identifies the defect signatures in Cu-rich CIS solar cells as a Se-related absorber defect. Section 7.2 identifies this Se-related defect as the root cause of the interface recombination losses in Cu-rich CI(G)S solar cells. Section 7.3 describes the origin behind the formation of this Se-related defect in terms of the strong etching step that is mandatory for Cu-rich CI(G)S absorbers. Finally, Section 7.4 provides alternative means of passivating this Se-related defect using modified buffer layers.

Chapter 8 provides a summary of the thesis with the final conclusions and outlooks.

References Chapter 1

[1] S. Siebentritt, L. Gütay, D. Regesch, Y. Aida, V. Deprédurand, "Why do we make Cu(In,Ga)Se_2 solar cells non-stoichiometric?", Solar Energy Materials and Solar Cells, 119: 18 – 25 (2013).

[2] F. Pianezzi, P. Reinhard, A. Chirila, B. Bissig, S. Nishiwaki, S. Buecheler, A. N. Tiwari, "Unveiling the effects of postdeposition treatment with different alkaline elements on the electronic properties of CIGS thin film solar cells", Physical chemistry chemical physics, 16:8843 – 8851 (2014).

[3] P. Jackson, R. Wuerz, D. Hariskos, E. Lotter, W. Witte, M. Powalla, "Effects of heavy alkali elements in Cu(In,Ga)Se_2 solar cells with efficiencies up to 22.6%", Physica status solidi: RRL, 10:583 – 586 (2016).

[4] P. Jackson, D. Hariskos, R. Wuerz, O. Kiowski, A. Bauer, T. M. Friedlmeier, M. Powalla, "Properties of Cu(In,Ga)Se_2 solar cells with new record efficiencies up to 21.7%", Physica status solidi: RRL, 9:28– 31 (2015).

[5] P. Jackson, D. Hariskos, R. Wuerz, W. Wischmann, M. Powalla, "Compositional investigation of potassium doped Cu(In,Ga)Se_2 solar cells with efficiencies up to 20.8%", Physica status solidi: RRL, 8:219– 222 (2014).

[6] R. Kamada, T. Yagioka, S. Adachi, A. Handa, K. F. Tai, T. Kato, H. Sugimoto, "New world record Cu(In,Ga)$(Se,S)_2$ thin film solar cell efficiency beyond 22%", Proceedings of IEEE 43rd Photovoltaic Specialists Conference (PVSC) in Denver, 1287 – 1291 (2016).

[7] S. Siebentritt, "Chalcopyrite compound semiconductors for thin film solar cells", Current Opinion in Green and Sustainable Chemistry, 4: pp. 1 - 7 (2017).

[8] H. Shen, T. Duong, Y. Wu, J. Peng, D. Jacobs, N. Wu, K. Weber, T. White and K. Catchpole, "Metal halide perovskite: a game-changer for photovoltaics and solar devices via a tandem design", Science and Technology of Advanced Materials, 19:1, pp. 53 - 75 (2018).

Chapter 2: Thin Film Solar Cells

Chapter 2 introduces an overview of the importance of thin film solar cells. The advantages of emerging thin film technologies of photovoltaics will be discussed in Section 2.1. The most promising thin film technology is based on $Cu(In,Ga)Se_2$ thin films. The characteristics of such films as a ternary compound $CuInSe_2$ and as a quaternary compound $Cu(In,Ga)Se_2$ are described in Section 2.2. These $Cu(In,Ga)Se_2$ thin film technologies can be grown either under Cu-excess or Cu-deficiency forming Cu-rich and Cu-poor absorbers respectively as will be explained in Section 2.3. Finally, Section 2.4 will be discussing means of improving such thin film absorbers using surface post-deposition treatments introduced in the literature. A post-deposition treatment based on potassium fluoride will be discussed in sub-section 2.4.1, while sub-section 2.4.2 will present post-deposition treatments based on Indium-Selenium.

2.1 Thin film solar cells

The main advantage of thin film solar cells is related to further minimizing the cost of PV cells by fabricating thin film absorbers with lower thicknesses compared to conventional Si. Thin film absorbers are characterized by their direct bandgap compared to the indirect bandgap of Si. In addition to their low material and energy consumption, thin film solar cells are characterized by their shorter energy payback time and the potential of these thin film absorbers to be tuned for different bandgaps making them suitable for wide range of potential applications and opportunities [1, 2]. The bandgap tunability of such solar cells based on thin film absorbers enables these solar cells to be integrated in tandem or multi-junction [3, 4] structures with the potential of achieving high efficiencies exceeding the Schockley-Queisser limit of 33 % [5].

There are different types of thin film PV technologies. The most popular thin film technologies are:

1. Amorphous silicon (a-Si)
2. Perovskite
3. Cadmium Telluride (Cd-Te)
4. Copper Indium Gallium di-selenide ($Cu(In,Ga)Se_2$ or CIGS)

CIGS is currently considered the most promising thin film technology due to the following reasons [6]:

1. CIGS solar cells achieved an efficiency of 23.35 % [7], which is currently higher than other thin film technologies (except for perovskite solar cells that have comparable efficiencies of 23.3 %).
2. CIGS solar cells are characterized by their stable performance with a minimum lifetime of 20 years unlike perovskite solar cells that are suffering from severe instability problems [8].

Based on these advantages of CIGS thin film technologies, CIGS absorbers and solar cells will be the main focus of this thesis. The ternary compound, CIS will be intensively used in the work of this thesis compared to the quaternary CIGS as the ternary compound is characterized by its simpler structure compared to the quaternary compound and thus provides a better mean of understanding the physical and chemical characteristics of such thin film solar cells.

2.2 CI(G)S thin film solar cells

$CuInSe_2$ is a ternary I-III-VI_2 compound with a chalcopyrite structure. Ga is introduced to the ternary $CuInSe_2$ compound forming the quaternary $Cu(In,Ga)Se_2$ compound. CI(G)S absorbers are characterized by their direct bandgap with a bandgap of around 1.0 eV for the pure $CuInSe_2$ absorbers and 1.7 eV for the pure $CuGaSe_2$ absorbers. The record efficiencies for CIGS and CIS thin film solar cells are 23.35 % [7] and 15.0 % [9] for the laboratory scale respectively. CI(G)S solar cells are based on a hetero-structure where the absorber and buffer are two different compounds as presented in Figure 2.1. Figure 2.1 represents the complete structure of CI(G)S thin film solar cells.

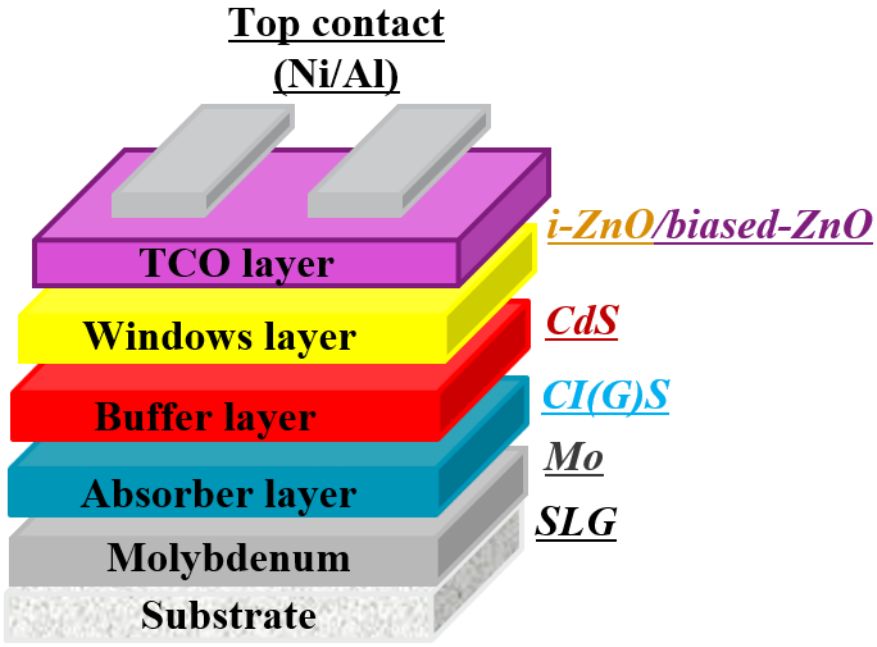

Figure 2.1: CI(G)S solar cell structure

A solar cell is basically a p-n junction where light excites the electrons from the valence band to the conduction band. Metal contacts are then used to collect electrons at the front side (front contact) and holes at the back side of the solar cell (back contact) [10]. This phenomena is reflected on the structure of the CI(G)S solar cell in Figure 2.1. The structure of the CI(G)S solar cell can be explained in the following points:

- The p-n junction is formed from the p-type CI(G)S absorber layer and the n-type CdS buffer and ZnO window layers. The ZnO layer is a double layer composed of an intrinsic Zinc Oxide (i-ZnO) and a transparent conductive oxide (TCO) window layer. The TCO layer used in this thesis is a biased ZnO layer [11, 12].

- CIS absorber layer is deposited on a Molybdenum (Mo) coated Soda Lime Glass (SLG) substrate. Mo is acting as the back contact.
- A front contact is deposited on top of the cell. The front contact layer is composed of Nickel (Ni) and Aluminium (Al).

2.3 Cu-rich & Cu-poor CI(G)S

CIS and CIGS absorbers are grown either with a Cu/III {Cu/(In + Ga)} ratio less than one, referred to as Cu-poor or with a Cu/III ratio of more than one, referred to as Cu-rich. III is either (In) only in case of the ternary CIS compound or (In + Ga) in case of the quaternary CIGS compound. According to the CIS [13] and the CGS [14] phase diagrams, there is no Cu-rich chalcopyrite phase. However, absorbers grown under Cu-excess form a stoichiometric chalcopyrite phase in addition to copper selenide conductive secondary phases.

State-of-the-art CI(G)S record cells are based on Cu-poor CI(G)S absorbers [7, 9, 15]. On the other side, Cu-rich CI(G)S absorbers are characterized by their larger grains, lower defect densities, higher mobility, less compensation, no electrostatic potential fluctuations and better transport properties [16 – 19] compared to Cu-poor ones. Furthermore, Cu-rich CIS solar cells will be shown to have higher collection efficiencies compared to Cu-poor CIS solar cells as will be discussed in Section 5.2. However, solar cells based on Cu-rich CI(G)S absorbers exhibit lower efficiencies compared to the Cu-poor ones due to a significant decrease in both the open circuit voltage (V_{OC}) and fill factor (FF).

The reason for this V_{OC} deficit gap between Cu-rich and Cu-poor CI(G)S solar cells is still not fully understood but has been observed to be related to an unfavourable absorber/buffer interface. This unfavourable front interface causes increased recombination losses at the absorber/buffer interface [20 – 22]. The origin of these interface recombination losses in Cu-rich CI(G)S solar cells is not fully understood but was speculated to be related to one of the following reasons:

- The high apparent doping of Cu-rich CI(G)S solar cells [17]
- The absence of an ordered defect compound (ODC) that is characterized by its relatively higher bandgap from the surface of such Cu-rich CI(G)S absorbers [20, 23].

During the work of this thesis, Finn Babbe who is responsible for the optical characterizations in this project, was able to confirm the interface problem of the Cu-rich CI(G)S solar cells as well as finding an additional problem for the Cu-rich CI(G)S solar cells in terms of the CI(G)S absorber bulk. Finn Babbe was responsible for measuring the quasi Fermi Level splitting (qFLs) for both Cu-rich and Cu-poor CI(G)S absorbers. The qFLs is the highest V_{OC} value an absorber can provide.

The qFLs for CIGS was found to show higher values for Cu-poor compared to Cu-rich ones on absorbers only, without any additional front interfaces [24] including CIS when taking the different Cu-rich and Cu-poor bandgaps into account. After adding a CdS buffer layer, the qFLs gap between Cu-rich and Cu-poor CI(G)S increased. This means that Cu-rich CI(G)S cells suffer from two main challenges:

1. A challenge at the absorber bulk confirmed by the fact that the qFLs of Cu-rich CI(G)S is lower than that of Cu-poor CI(G)S without additional interfaces.
2. A challenge at the absorber/buffer interface indicated by the increasing gap in qFLs between Cu-rich and Cu-poor CI(G)S after adding the CdS buffer layer.

In this thesis, I will explain the reason behind the interface problem of Cu-rich CI(G)S solar cells.

2.4 Surface Post-deposition treatments (PDT)

There are three main milestones that are responsible for the evolution of the CIGS thin film solar cell efficiencies:

1. The evolution of the 3-stage CIGS absorber growth process where the CIGS absorbers are grown moving between different phase transitions from a Cu-poor phase to a Cu-rich phase before a final Cu-poor phase. This 3-stage process provided the opportunity to benefit from different advantageous characteristics of Cu-rich and Cu-poor phases [25] as well as controlling the stress release between such phases [26 - 27].
2. The discovery and evolution of the importance of the alkali atoms on the CIGS absorber quality. It was discovered that the alkali atoms (especially sodium) from SLG substrates diffuse in the CIGS absorber and improve the quality of such absorbers [28, 29].
3. The evolution of the different alkali post-deposition treatments leading to current record efficiencies [7, 30] as explained in this section.

Based on the above three points, it can be concluded that in order to further optimize CIGS solar cells and achieve higher efficiencies, the improvement of both Cu-poor and Cu-rich absorber phases are important in addition to the improvement of the quality of their corresponding interface surfaces. The following sub-sections will introduce different post-deposition treatments (PDTs) that have showed significant potential towards achieving high efficiencies specifically in terms of decreasing the V_{OC} deficit values.

2.4.1 Potassium Fluoride (KF) treatment

Alkali fluoride PDTs have emerged in the last couple of years leading to significant increase in the V_{OC} values and consequently the efficiency [30].

Sodium (Na) was initially introduced in [31]. In [31], it was shown that alkalis other than Na did not show additional improvements compared to the improvements achieved by Na. However, later the potassium fluoride (KF) PDT was introduced and was proven to provide additional enhancements to the CIGS absorber/buffer interface leading to different record efficiencies [32 - 34]. These enhancements motivated the CIGS community to develop heavier alkali PDTs leading to further improvements in the CIGS record efficiencies [15].

The effect of such alkali PDTs is still not fully understood. All alkali PDTs have succeeded in increasing the V_{OC} values. This was attributed to a couple of different reasons [27]:

1. Cu is depleted at the surface as reported in [30, 35, 36] as a result of the diffusion of potassium into the CIGS absorber surface leading to the formation of a K-In-Ga-Se (KIGS) layer at the absorber surface [35, 37]. Thus, the absorber surface layer has potentially a higher bandgap and is thus responsible for increasing the V_{OC} values [36 - 38].
2. The diffusion of K in the CIGS absorber surface layer helps in reducing the recombination at the absorber surface leading to an enhanced absorber/buffer heterojunction quality [37] as well as accelerating the buffer layer deposition process with Cd in-diffusion allowing for a thinner buffer and consequently more photons to be absorbed [30, 33, 39, 40].
3. The passivation of the grain boundaries could be another explanation. Alkali atoms diffuse to the absorber surface and accumulate at grain boundaries [41 - 43].
4. The PDT affects the CIGS absorber doping with either an increase [44] or a decrease [37] in the apparent doping after the treatment.
5. The PDT has an effect on decreasing the non-radiative recombination with a reported increase in the carrier lifetime [44, 45] and an increase in the photoluminescence (PL) intensity [44, 46, 47].

The alkali PDT is performed either as an in-situ treatment where the PDT is performed directly after the absorber growth process in the same deposition chamber [15, 30, 35, 39, 48] or as an ex-situ treatment where the absorber growth and the PDT are performed in two different deposition chambers [34, 36, 49].

As one of the main challenges for the V_{OC} deficiency in Cu-rich CIS solar cells compared to Cu-poor CIS solar cells is related to the problematic Cu-rich CIS absorber/buffer interface and as the KF PDT has been reported to improve the absorber/buffer interface and increase the V_{OC} values for Cu-poor CIGS solar cells, it was thus interesting to apply the KF PDT on Cu-rich CIS solar cells to discover the answer for the following questions:

- Can the KF PDT improve the V_{OC} for Cu-rich CIS solar cells as it did for Cu-poor CIGS solar cells?
- Can the KF PDT enhance the absorber/buffer interface in Cu-rich CIS solar cells?
- Will the KF PDT introduce a Cu-depleted layer on the surface of Cu-rich CIS absorber?

The effect of the KF PDT on Cu-rich CIS absorbers and solar cells will be discussed within this thesis.

2.4.2 Indium-Selenium treatment

Several experiments were performed to improve the quality of Cu-rich CIS solar cells and decrease its V_{OC} deficit gap with Cu-poor CIS solar cells. An In-Se PDT was developed with the goal of increasing the V_{OC} of Cu-rich CIS solar cells. The In-Se PDT succeeded in improving the CIS absorber/buffer heterojunction interface by forming a Cu-poor surface layer on top of the CIS bulk absorber minimizing interface recombination and leading to an increase in the V_{OC} to values close to that of the Cu-poor CIS solar cells [21, 22, 50]. Cu-rich CIS solar cells treated with an In-Se PDT achieved an efficiency of 13.5 % (similar to Cu-poor CIS efficiency) compared to 8.3 % for the untreated Cu-rich CIS solar cells [50].

References Chapter 2

[1] http://cigs-pv.net/wortpresse/wp-content/uploads/2015/12/CIGS-WhitePaper.pdf

[2] D. Abou-Ras, S. Wagner, B. J. Stanbery, H.-W. Schock, R. Scheer, L. Stolt, S. Siebentritt, D. Lincot, C. Eberspacher, K. Kushiya, A. N. Tiwari, "Innovation highway: Breakthrough milestones and key developments in chalcopyrite photovoltaics from a retrospective viewpoint", Thin Solid Films, 633, 2–12 (2017).

[3] T. J. Coutts, K. A. Emery and J. S. Ward, "Modeled Performance of Polycrystalline Thin-Film Tandem Solar Cells", Prog. in photovoltaics: Research and applications, 10, 195–203 (2002).

[4] J. Coutts, J. S. Ward, D. L. Young, K. A. Emery, T. A. Gessert and R. Noufi, "Critical Issues in the Design of Polycrystalline, Thin-film Tandem Solar Cells", Prog. in photovoltaics: Research and applications, 11, 359–375 (2003).

[5] W. Shockley and H. J. Queisser, "Detailed Balance Limit of Efficiency of p-n Junction Solar Cells", Journal of Applied Physics, 32, pp. 510-519 (1961).

[6] T. D. Lee and A. U. Ebong, "A review of thin film solar cell technologies and challenges", Renewable and Sustainable Energy Reviews, 70, 1286-1297 (2017).

[7] http://www.solar-frontier.com/eng/news/2019/0117_press.html

[8] L. Meng, J. You and Y. Yang, "Addressing the stability issue of perovskite solar cells for commercial applications", Nature Communications, 9, 5265 (2018).

[9] J. AbuShama, R. Noufi, S. Johnston, S. Ward, X. Wu, "Improved performance in $CuInSe_2$ and surface modified $CuGaSe_2$ Solar Cells", IEEE Photovoltaics Specialists Conference and Exhibition, pp. 299-302 (2005).

[10] S. M. Sze, K. K. Ng, Physics of Semiconductor Devices, 3rd ed., Wiley India Pvt Limited, (2008).

[11] M. Hala, H. Kato, M. Algasinger, Y. Inoue, G. Rey, F. Werner, C. Schubbert, T. Dalibor and S. Siebentritt, "Improved environmental stability of highly conductive nominally undoped ZnO layers suitable for n-type windows in thin film solar cells", Solar Energy Materials & Solar Cells, 161, 232–239 (2017).

[12] M. Hala, S. Fujii, A. Redinger, Y. Inoue, G. Rey, M. Thevenin, V. Depredurand, T. P. Weiss, T. Bertram and S. Siebentritt, "Highly conductive ZnO films with high near infrared transparency", Progress in Photovoltaics Research Application, 23, 11, 1630 (2015).

[13] T. Gödecke, T. Haalboom, F. Ernst, "Phase equilibria of Cu-In-Se II. The $In\text{-}In_2Se_3\text{-}Cu_2Se\text{-}Cu$ subsystem", Z. Metallkd., 91: 635-650 (2000).

[14] J. C. Mikkelsen, "Ternary phase relations of the chalcopyrite compound $CuGaSe_2$", Journal of Electronic Materials, 10, 3, pp. 541–558 (1981).

[15] P. Jackson, R. Wuerz, D. Hariskos, E. Lotter, W. Witte, M. Powalla, "Effects of heavy alkali elements in $Cu(In,Ga)Se_2$ solar cells with efficiencies up to 22.6%", Physica status solidi: RRL, 10:583 – 586 (2016).

[16] S. Siebentritt, L. Gütay, D. Regesch, Y. Aida, V. Deprédurand, "Why do we make $Cu(In,Ga)Se_2$ solar cells non-stoichiometric?", Solar Energy Materials and Solar Cells, 119: 18–25 (2013).

[17] V. Depredurand, D. Tanaka, Y. Aida, M. Carlberg, N. Fevre, S. Siebentritt, "Current loss due to recombination in Cu-rich $CuInSe_2$ solar cells", Journal of Applied Physics, 115, 044503 (2014).

[18] F. Werner, D. Colombara, M. Melchiorre, N. Valle, B. El Adib, C. Spindler, S. Siebentritt, "Doping mechanism in pure $CuInSe_2$", Journal of Applied Physics, 119, 173103 (2016).

[19] S. Siebentritt, N. Rega, A. Zajogin, M. Ch. Lux-Steiner, "Do we really need another PL study of $CuInSe_2$?", Physica Status Solidi (c), 1, 9: 2304-2310 (2004).

[20] M. Turcu, O. Pakma and U. Rau "Interdependence of absorber composition and recombination mechanism in $Cu(In,Ga)(Se,S)_2$ heterojunction solar cells", Applied Physics Letter, 80, 2598 (2002).

[21] V. Depredurand, Y. Aida, J. Larsen, T. Eisenbarth, A. Majerus, S. Siebentritt, "Surface treatment of CIS solar cells grown under Cu-excess", 37th IEEE Photovoltaic Specialists Conference, Seattle, WA, pp. 000337-000342 (2011).

[22] Y. Aida, V. Depredurand, J. K. Larsen, H. Arai, D. Tanaka, M. Kurihara, S. Siebentritt, "Cu-rich $CuInSe_2$ solar cells with a Cu-poor surface", Prog. Photovolt: Res. Appl., 23: 754–764 (2015).

[23] D. Schmid, M. Ruckh, F. Grunwald, H. W. Schock, "Chalcopyrite/defect chalcopyrite heterojunctions on the basis of $CuInSe_2$", Journal of Applied Physics, 73: 2902–2909 (1993).

[24] F. Babbe, L. Choubrac, S. Siebentritt, "Quasi Fermi level splitting of Cu-rich and Cu-poor $Cu(In,Ga)Se_2$ absorber layers", Appl. Phys. Lett., 109: 082105 (2016).

[25] R. Mainz, E. Simsek Sanli, H. Stange, D. Azulay, S. Brunken, D. Greiner, S. Hajaj, M. D. Heinemann, C. A. Kaufmann, M. Klaus, Q. M. Ramasse, H. Rodriguez-Alvarez, A. Weber, I. Balberg, O. Millo, P. A. van Aken, D. Abou-Rasa, "Annihilation of structural defects in chalcogenide absorber films for high-efficiency solar cells", Energy Environ. Sci., 9: 1818–1827 (2016).

[26] R. Mainz, H. Rodriguez-Alvarez, M. Klaus, D. Thomas, J. Lauche, A. Weber, M. D. Heinemann, S. Brunken, D. Greiner, C. A. Kaufmann, T. Unold, H. W. Schock, C. Genzel, "Sudden stress relaxation in compound semiconductor thin films triggered by secondary phase segregation", Phys. Rev. B, 92:155310 (2015).

[27] S. Siebentritt, "Chalcopyrite compound semiconductors for thin film solar cells", Current Opinion in Green and Sustainable Chemistry, 4: 1-7 (2017).

[28] Wei S-H, Zhang SB and Zunger A, "Effects of Na on the electrical and structural properties of $CuInSe_2$", Journal of Applied Physics, 85:7214– 7218 (1999).

[29] A. Rockett, "The effect of Na in polycrystalline and epitaxial single-crystal $CuIn_{1-x}Ga_xSe_2$", Thin Sold Films, 480 481:2 (2005).

[30] A. Chirila, P. Reinhard, F. Pianezzi, P. Bloesch, A. R. Uhl, C. Fella, L. Kranz, D. Keller, C. Gretener, H. Hagendorfer, D. Jaeger, R. Erni, S. Nishiwaki, S. Buecheler, and A. N. Tiwari, "Potassium-induced surface modification of $Cu(In, Ga)Se_2$ thin films for high-efficiency solar cells", Nature Materials, 12, 1107 (2013).

[31] M. A. Contreras, B. Egaas, P. Dippo, J. Webb, J. Granata, K. Ramanathan, S. Asher, A. Swartzlander, R. Noufi, "On the role of Na and modifications to Cu(In,Ga)Se_2 absorber materials using thin-MF (M Na, K, Cs) precursor layers", Conference Record of the IEEE Photovoltaic Specialists Conference In Anaheim, 359– 362 (1997).

[32] P. Jackson, D. Hariskos, R. Wuerz, O. Kiowski, A. Bauer, T. M. Friedlmeier, M. Powalla, "Properties of Cu(In,Ga)Se_2 solar cells with new record efficiencies up to 21.7%", Physica status solidi: RRL, 9:28– 31 (2015).

[33] P. Jackson, D. Hariskos, R. Wuerz, W. Wischmann, M. Powalla, "Compositional investigation of potassium doped Cu(In,Ga)Se_2 solar cells with efficiencies up to 20.8%", Physica status solidi: RRL, 8:219– 222 (2014).

[34] R. Kamada, T. Yagioka, S. Adachi, A. Handa, K. F. Tai, T. Kato, H. Sugimoto, "New world record Cu(In,Ga)(Se,S)$_2$ thin film solar cell efficiency beyond 22%", Proceedings of IEEE 43rd Photovoltaic Specialists Conference (PVSC) in Denver, 1287– 1291 (2016).

[35] P. Reinhard, B. Bissig, F. Pianezzi, H. Hagendorfer, G. Sozzi, R. Menozzi, C. Gretener, S. Nishiwaki, S. Buecheler, A. N. Tiwari, "Alkali-Templated surface nanopatterning of chalcogenide thin films: a novel approach toward solar cells with enhanced efficiency", Nano letters, 15:3334– 3340 (2015).

[36] P. Pistor, D. Greiner, C. A. Kaufmann, S. Brunken, M. Gorgoi, A. Steigert, W. Calvet, I. Lauermann, R. Klenk, T. Unold, M. C. Lux-Steiner, "Experimental indication for band gap widening of chalcopyrite solar cell absorbers after potassium fluoride treatment", Applied Physics Letters, 105:063901 (2014).

[37] F. Pianezzi, P. Reinhard, A. Chirila, B. Bissig, S. Nishiwaki, S. Buecheler, A. N. Tiwari, "Unveiling the effects of postdeposition treatment with different alkaline elements on the electronic properties of CIGS thin film solar cells", Physical chemistry chemical physics, 16:8843– 8851 (2014).

[38] E. Handick, P. Reinhard, J. H. Alsmeier, L. Köhler, F. Pianezzi, S. Krause, M. Gorgoi, E. Ikenaga, N. Koch, R. G. Wilks, S. Buecheler, A. N. Tiwari, M. Bär, "Potassium postdeposition treatment induced band gap widening at Cu(In,Ga)Se_2 surfaces reason for performance leap?", ACS Applied Materials and Interfaces, 7:27414– 27420 (2015).

[39] O. Lundberg, E. Wallin, V. Gusak, S. Södergren, S. Chen, S. Lotfi, F. Chalvet, U. Malm, N. Kaihovirta, P. Mende, G. Jaschke, P. Kratzert, J. Joel, M. Skupinski, P. Lindberg, T. Jarmar, J. Lundberg, J. Mathiasson, L. Stolt, "Improved CIGS modules by KF post deposition treatment and reduced cell-to-module losses", IEEE 43rd Photovoltaic Specialists Conference (PVSC) in Denver, 1293– 1296 (2016).

[40] B. Umsur, W. Calvet, A. Steigert, I. Lauermann, M. Gorgoi, K. Prietzel, D. Greiner, C. A. Kaufmann, T. Unold, M. C. Lux-Steiner, "Investigation of the potassium fluoride post deposition treatment on the CIGSe/CdS interface using hard X-ray photoemission spectroscopy a comparative study", Physical chemistry chemical physics, 18:14129 – 14138 (2016).

[41] D. Abou-Ras, S. S. Schmidt, R. Caballero, T. Unold, H. W. Schock, C. T. Koch, B. Schaffer, M. Schaffer, P. P. Choi, O. Cojocaru-Miredin, "Confined and chemically flexible grain boundaries in polycrystalline compound semiconductors", Advanced Energy Materials, 2:992– 998 (2012).

[42] J. Keller, R. Schlesiger, I. Riedel, J. Parisi, G. Schmitz, A. Avellan, T. Dalibor, "Grain boundary investigations on sulfurized Cu(In,Ga)$(S,Se)_2$ solar cells using atom probe tomography", Solar Energy Materials and Solar cells, 117:592– 598 (2013).

[43] O. Cojocaru-Miredin, C. Pyuck-Pa, D. Abou-Ras, S. S. Schmidt, R. Caballero, D. Raabe, "Characterization of grain boundaries in Cu(In,Ga)Se_2 films using atom-probe tomography", IEEE journal of photovoltaics, 1, 2, 207– 212 (2011).

[44] I. Khatri, H. Fukai, H. Yama, M. Su giyam, T. Nak ada, "Effect of potassium fluoride post-deposition treatment on Cu(In,Ga)Se_2 thin films and solar cells fabricated onto sodalime glass substrates", Solar Energy Materials and Solar cells, 155:280 – 287 (2016).

[45] S. A. Jensen, S. Glynn, A. Kanevce, P. Dippo, J. V. Li, D. H. Levi, D. Kuciauskas, "Beneficial effect of post-deposition treatment in high-efficiency Cu(In,Ga)Se_2 solar cells through reduced potential fluctuations", Journal of Applied Physics, 120:063106 (2016).

[46] D. Shin, J. Kim, T. Gershon, R. Mankad, M. Hopstaken, S. Guha, B. T. Ahn, B. Shin, "Effects of the incorporation of alkali elements on Cu(In,Ga)Se_2 thin film solar cells", Solar Energy Materials and Solar cells, 157:695– 702 (2016).

[47] M. H. Wolter, B. Bissig, E. Avancini, R. Carron, S. Buecheler, P. Jackson and S. Siebentritt, "Influence of Sodium and Rubidium Postdeposition Treatment on the Quasi-Fermi Level Splitting of Cu(In,Ga)Se_2 Thin Films", IEEE Journal of photovoltaics, 8, 5 (2018).

[48] A. Laemmle, R. Wuerz, M. Powalla, "Efficiency enhancement of Cu(In,Ga)Se_2 thin-film solar cells by a post-deposition treatment with potassium fluoride", Physica Status Solidi: RRL, 7:631– 634 (2013).

[49] L. M. Mansfield, R. Noufi, C. P. Muzzillo, C. DeHart, K. Bowers, B. To, J. W. Pankow, R. C. Reedy, K. Ramanathan, "Enhanced performance in Cu(In,Ga)Se_2 solar cells fabricated by the two-step selenization process with a potassium fluoride postdeposition treatment", IEEE journal of photovoltaics, 4, 6, 1650– 1654 (2014).

[50] T. Bertram, V. Depredurand and S. Siebentritt, "In-Se surface treatment of "Cu-rich" grown CuInSe2", 40th IEEE Photovoltaic Specialist Conference (PVSC), Denver, CO, USA, pp. 3633-3636 (2014).

Chapter 3: Synthesis of Thin Film CI(G)S Solar Cells

Chapter 3 highlights the tools used for the fabrication of CI(G)S absorbers and the developed post-deposition treatments. Section 3.1 describes our standard baseline process. In our standard baseline process, I (in collaboration with Finn Babbe) were responsible for the fabrication of the CIS and CIGS absorbers. We fabricated the CIS and CIGS absorbers using a pre-developed process in a Physical Vapour Deposition (PVD) tool as described in sub-section 3.1.1. For the best solar cells (in terms of efficiency), I was responsible for the development and the deposition of the Anti-Reflection Coating (ARC) using an Electron beam evaporation tool as discussed in sub-section 3.1.2. In Section 3.2, I will discuss the details of the different post-deposition treatments that we (me and Finn Babbe) implemented in this thesis. Section 3.2 is divided as follows:

- Sub-section 3.2.1 focuses on the ex-situ potassium fluoride treatment. We published the experimental details of this treatment in [1].
- Sub-section 3.2.2 highlights the in-situ potassium fluoride treatment. We published the experimental details and optimizations of this treatment in [2].
- Sub-section 3.2.3 introduces the Selenium post-deposition treatment. We published the experimental details of this treatment in [3].

3.1 Standard baseline process

Our standard baseline process to fabricate CI(G)S solar cells can be summarized in the following order:

1. Sputtering Molybdenum (Mo) on Soda Lime Glass (SLG) substrates
2. Fabricating the CI(G)S absorber layers using physical vapour deposition
3. Etching the grown absorbers using potassium cyanide (KCN)
4. Adding a CdS buffer layer using Chemical Bath Deposition (CBD) [4]
5. Sputtering intrinsic ZnO (i-ZnO) and biased ZnO (b-ZnO) window layers [5 – 6]
6. Depositing Nickel/Aluminium (Ni/Al) contact grids using Electron beam evaporation
7. Depositing Magnesium Fluoride (MgF_2) Anti Reflection Coating (ARC) layer for the best solar cells in terms of efficiency using Electron beam evaporation.

From the above seven steps of our standard baseline process, I was responsible (in collaboration with Finn Babbe) for step 2; which is the fabrication of the CI(G)S absorber layers. We fabricated these CI(G)S absorbers using a pre-developed growth process [7]. This pre-developed process was performed using a Physical Vapour Deposition (PVD) tool as explained in sub-section 3.1.1. I was also responsible for the deposition of the ARC layer in step 7 presented in sub-section 3.1.2.

3.1.1 Synthesis of CI(G)S absorbers

CIS and CIGS absorbers have been fabricated on molybdenum-coated soda lime glass substrates using physical vapour deposition technique [8]. The fabrication process was performed in a Veeco molecular beam epitaxy system presented in Figure 3.1.

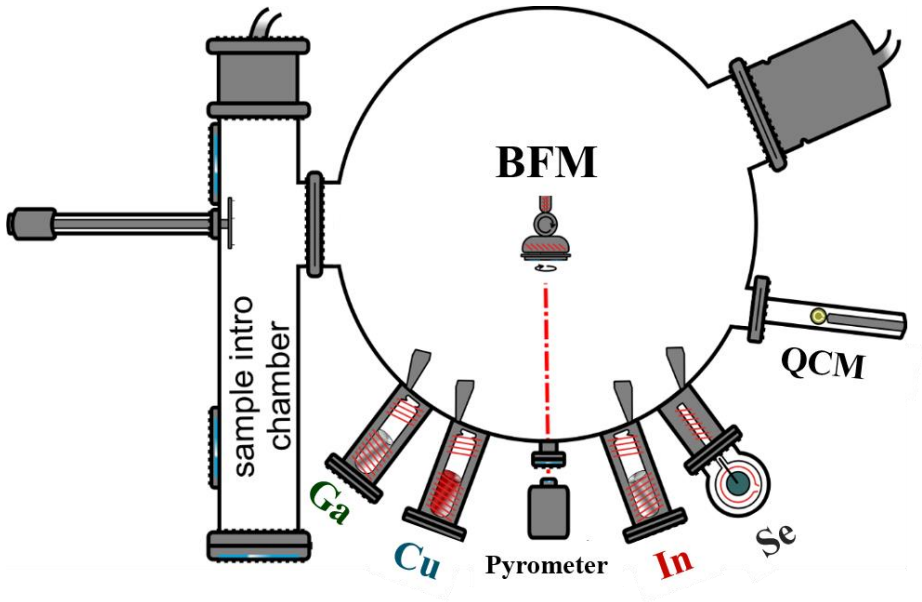

Figure 3.1: A schematic for Physical Vapor Deposition (PVD) using a Molecular Beam Epitaxy (MBE) tool

I (in collaboration with Finn Babbe) was responsible for the fabrication of CIS and CIGS absorbers using a pre-developed growth process as explained earlier. We did not optimize this growth process in terms of changing the process steps, sequence or temperatures. We were only controlling the fluxes for Cu, In, Ga and Se according to the required samples as follows:

- We control the ratio between Cu and In in CIS and Cu, In and Ga in CIGS to produce Cu-rich or Cu-poor absorbers:
  - Cu-rich absorbers are produced when the Cu/In ratio in CIS or the Cu/(Ga + In) in CIGS is more than one.
  - Cu-poor absorbers are produced when the Cu/In ratio in CIS or the Cu/(Ga + In) in CIGS is less than one.
- We also control the Se flux to produce high quality absorbers:
  - The Se flux used during the deposition of Cu-rich CIS and CIGS is slightly lower than that used for Cu-poor CIS and CIGS absorbers to produce high quality CI(G)S absorbers.

- For Cu-rich CI(G)S absorbers, the pressure for our standard Se flux is in the range of 4 - $5*10^{-6}$ mbar which is corresponding to the lowest possible Se flux that could be used to produce the CI(G)S phase. Low Se flux has been reported to be more beneficial for our Cu-rich absorbers [9]. Pressures of Se fluxes lower than 4 - $5*10^{-6}$ mbar are not sufficient to form the required CI(G)S absorber phase. We performed several experiments to produce CIS with lower Se-fluxes but we were only able to detect the secondary phases and not the ternary CIS phase.
- For Cu-poor CI(G)S absorbers, the pressure of the standard Se flux is in the range of 5 - $8*10^{-6}$ mbar.

It is important to note that according to the phase diagram [10, 11], a Cu-rich chalcopyrite phase does not exist as presented in the green region of Figure 3.2. Cu-rich CI(G)S (green region of Figure 3.2 with Cu atomic ratios above 25 %) is actually a stoichiometric phase (α) plus additional copper selenide (Cu_2Se) secondary phases that need to be etched before completing the baseline process [12 - 14].

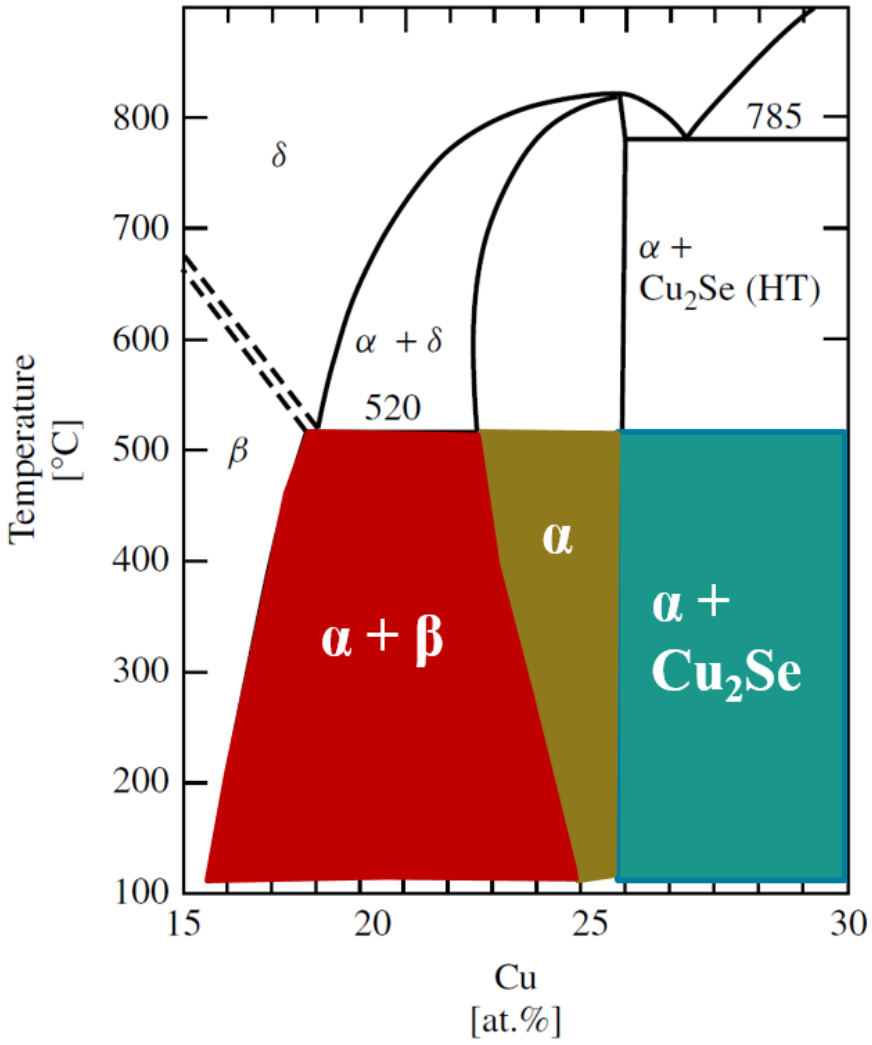

Figure 3.2: Phase diagram of chalcopyrite CIS. The x-axis represents the atomic ratio of Cu, while the y-axis represents the deposition temperature in Celsius. The Cu-rich chalcopyrite region is the green region with Cu atomic ratios of more than 25 %. This Cu-rich chalcopyrite region represents a stoichiometric chalcopyrite phase (α) plus additional copper selenide secondary phases. The yellow region represents the stoichiometric phase (α) region. The red region represents the Cu-poor chalcopyrite region. This figure is adapted from the phase diagram provided by [10].

The above parameters are the only parameters I (and Finn Babbe) was changing during the fabrication process of the CI(G)S absorbers. We were using a pre-developed process (developed by senior colleagues). This pre-developed growth process was different for CIS than for CIGS as follows:

For CIS absorbers: Cu, In and Se were evaporated inside the PVD chamber through a 1-stage process [15]. This 1-stage process is based on evaporating Cu, In and Se simultaneously first at a substrate temperature of 550 ^{0}C then at a substrate temperature of 590 ^{0}C corresponding to a real temperature of 530 ^{0}C. The real temperatures were measured using a pyrometer. The 1-stage process is simpler and faster compared to 2- or 3-stage processes. Cu and In ratios were varied to develop either Cu-rich absorbers (Cu/In ratio > 1) or Cu-poor absorbers (Cu/In ratio < 1).

For CIGS absorbers: CIGS absorbers were fabricated using a 3-stage process and not a 1-stage process like the CIS absorbers. Although a 1-stage process is much simpler and faster, but the 3-stage process is more favourable for CIGS absorbers. The 3-stage process helps in improving the V_{OC} and the efficiency of the produced solar cells by enhancing the quality of the CIGS absorbers. These enhancements to the CIGS absorber quality are achieved by developing a Ga gradient in the bulk of the CIGS absorbers. This Ga gradient can be achieved by the 3-stage process and not by the 1-stage process. The first stage of the 3-stage process is based on evaporating In, Ga and Se at a substrate temperature of 370 ^{0}C forming an In-rich, Ga-rich ternary compound. The second stage is performed at a substrate temperature of 540 ^{0}C in the presence of only Cu and Se to form the Cu-rich (In- and Ga-poor) quaternary compound, $Cu(In,Ga)Se_2$. After forming the quaternary CIGS compound, the third stage is then used to control the formation of Cu-rich or Cu-poor CIGS absorbers. The third stage is performed at a substrate temperature of 540 ^{0}C in the presence of In, Ga and Se. Shorter durations of the third stage produce Cu-rich CIGS absorbers while longer durations produce Cu-poor CIGS absorbers.

3.1.2 Electron-beam Evaporation

The best solar cell devices were further developed by evaporating an anti-reflection coating (ARC) layer. Magnesium Fluoride (MgF_2) was used as an ARC material with a refractive index of 1.38. The ARC layer was evaporated using an Oerlikon Leybold Univex 300 Electron beam evaporation tool presented in Figure 3.3.

To define the optimized thickness for depositing the ARC layer, reflection measurements were performed. The reflection spectrum of each of the best cells was measured to identify the wavelength of the highest reflection peaks and use Equation 3.1 to determine the required thickness [16].

$$d = \frac{\lambda}{4*n} \tag{3.1}$$

Where d is the targeted ARC thickness, λ is the wavelength of the high reflection peak and n is the refractive index of the ARC material used (1.38 for MgF_2 [17]).

Figure 3.3: E-beam evaporation tool for depositing MgF_2 and grids

An example on how to optimize the thickness of the ARC layer can be explained using Figure 3.4.

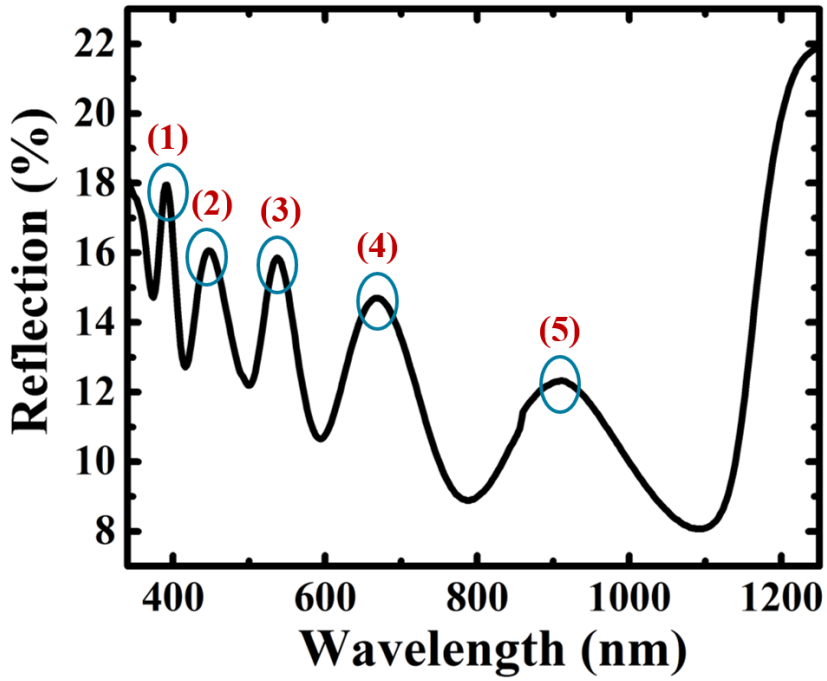

Figure 3.4: An example of a reflection spectrum for one of the solar cells. This reflection spectrum shows five reflection maxima peaks.

Figure 3.4 represents an example of a reflection spectrum for one of the solar cells. The reflection spectrum in Figure 3.4 shows 5 reflection maxima peaks at wavelengths of 392, 447, 538, 668 and 911 nm respectively. To optimize the thickness of the ARC layer that shall be deposited for this solar cell, the wavelength of one of the five reflection maxima peaks need to be targeted. The choice of the reflection maxima peak to target should consider the following parameters:

- After depositing the ARC layer, the most reflection improvements take place for the targeted wavelength and decrease gradually on both sides of the targeted wavelength. Therefore, the targeted reflection maxima peak should be relatively in the middle of the reflection spectrum. In the example of Figure 3.4, peaks number 3 and 4 are the best to target.
- The targeted wavelength of the reflection maxima peak should correspond to a wavelength of relatively high irradiance of the solar spectrum. According to the solar spectrum irradiance in [18], the highest solar irradiance can be observed in the range of 400 – 600 nm. Based on this range, the reflection maxima peak 3 (with a wavelength of 538 nm) is more favourable to target compared to the reflection maxima peak 4 (with a wavelength of 668 nm).

From the above two parameters, we can then choose the reflection maxima peak 3 with a wavelength of 538 nm as the target to optimize the thickness of the ARC layer.

Using Equation 3.1, with λ = 538 nm and n = 1.38 for MgF_2 ARC layer, the optimized thickness of the MgF_2 ARC layer is equal to 97.5 nm.

3.2 Post-deposition treatments

3.2.1 Ex-situ KF treatment

The ex-situ KF post-deposition treatment (PDT) was developed and optimized for CIS solar cells. Cu-rich and Cu-poor CIS cells were fabricated using the PVD tool as explained in sub-section 3.1.1 before applying the ex-situ KF PDT. This PDT is called an ex-situ due to two main reasons:

- The developed CIS absorbers need to be removed from the PVD tool to perform an etching step and remove the secondary phases. The etching step is different for Cu-rich CIS absorbers than for Cu-poor CIS absorbers as follows:
  - Cu-rich CIS absorbers were etched using a 10 % aqueous potassium cyanide (KCN) solution for 5 minutes removing additional copper selenide (Cu_2Se) secondary phases [14].
  - Cu-poor CIS absorbers were etched in a 5 % aqueous KCN solution for 30 seconds removing surface oxide layers [13].
- The post-deposition treatment was then performed directly after the etching step on two different steps:
  - KF was first evaporated using the same Electron beam evaporation tool presented in Figure 3.3 depositing KF thicknesses in the range of 5 – 30 nm. The optimized thickness was found to be in the range of 5 – 20 nm where excess KF deposition has proven to decrease both the V_{OC} and FF values. The deposition of KF thicknesses less than 5 nm was not practical as the control of the KF thickness is not possible due to the hygroscopic nature of KF. When KF is introduced to air, the KF immediately absorbs water from air. Water droplets can already be observed by eye after the exposure of KF to air. The proposed optimized thicknesses (5 – 20 nm) were only speculated after depositing a Lithium Fluoride (LiF) layer with a pre-defined thickness on top of the KF layer before exposing the KF layer to air. Then, the thickness of the double layer (LiF + KF) is measured using a profilometer and the thickness of the KF is deduced by subtracting the thickness of the pre-defined LiF layer.
  - After the KF deposition step, absorbers were removed from the e-beam tool and an annealing step in a Carbolite tube furnace takes place. The tube furnace used for this annealing step is presented in Figure 3.5.

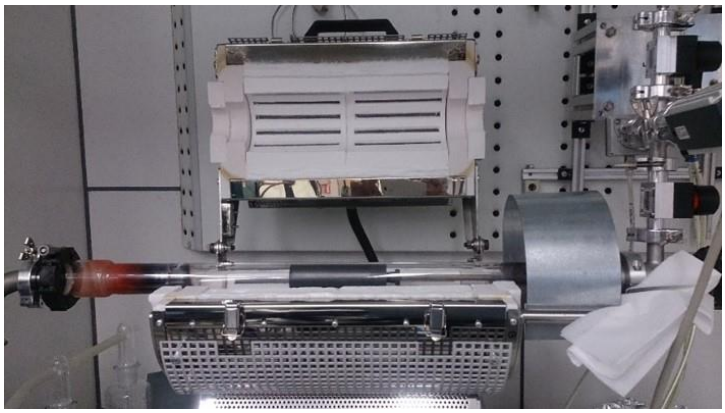

Figure 3.5: Carbolite tube furnace for annealing in the presence of Se powder used for the ex-situ KF PDT.

As a result of the mandatory etching step and the double KF treatment step (deposition + annealing), this PDT is referred to as an ex-situ KF PDT.

Different treatment parameters were varied to optimize the ex-situ KF PDT. The main objective of the optimization is to improve the V_{OC} of the Cu-rich treated solar cells. It is important to note that the optimization experiments were performed on Cu-rich CIS absorbers. The optimization conditions that succeeded in improving the V_{OC} values for the Cu-rich CIS treated cells were then applied to Cu-poor CIS absorbers without further optimization. The varied parameters can be summarized in the following points:

1. KF thickness as described above. The optimized KF thickness was set to be in the range of 5 – 20 nm.
2. Annealing temperature. Annealing temperatures were varied between 100 and 400 ^{0}C. Temperatures above 350 ^{0}C and below 300 ^{0}C were found to shunt the treated solar cells and affect negatively the electrical performance of the treated solar cells by significantly reducing the V_{OC} and FF values.
3. Annealing duration. Annealing durations were varied between 10 and 60 minutes. Annealing durations of more than 20 minutes were found to cause a strong shunting in the final device.
4. Annealing environmental gas condition. Two different environmental annealing conditions were experimented: Annealing in the presence of Nitrogen (N_2) gas and annealing in the presence of Se gas. The IV measurements showed that annealing in the presence of Se is mandatory to avoid the shunting of the treated device. Furthermore, the amount of Se was

varied and the results showed that the presence of Se of at least 40 mg is critical and strictly mandatory to maintain the absorber quality; otherwise, the treated absorber loses Se affecting negatively the electrical performance of the treated cells causing a significant decrease in the V_{OC} and FF values of the treated cells.

The experimental results of the optimization parameters are summarized in Section 6.1. The optimized annealing conditions for the ex-situ KF PDT were then set as follows:

- Annealing the CIS absorbers in a temperature range of 300 – 350 ^{0}C.
- Annealing durations of less than 20 minutes.
- Annealing in the presence of Se (in relatively high amount of at least 40 mg).

The annealing profile is presented in Figure 3.6. After annealing, the treated absorbers were rinsed in de-ionized water removing any remaining fluorides.

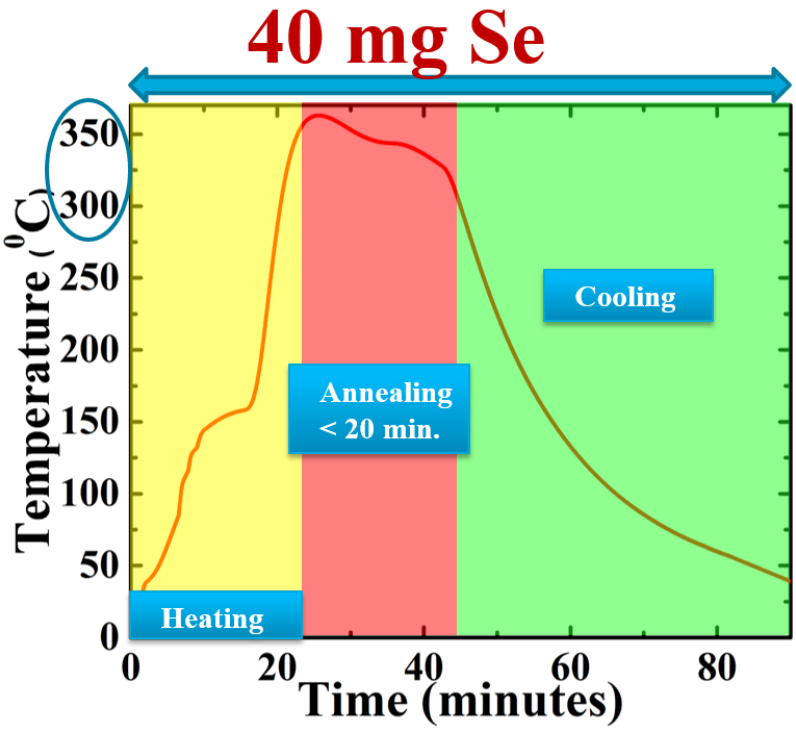

Figure 3.6: Annealing profile for CIS absorbers treated with the ex-situ KF PDT

3.2.2 In-situ KF treatment

Similar to the ex-situ KF PDT, the in-situ PDT was developed on CIS absorbers fabricated as mentioned in sub-section 3.1.1 and etched differently for Cu-rich and Cu-poor CIS absorbers as explained in sub-section 3.2.1. The main difference between the in-situ and the ex-situ treatments is the KF deposition and annealing steps as explained below:

- For the ex-situ KF PDT, the etched CIS absorbers were passed to the e-beam tool to deposit KF and then moved to the oven for an annealing step as explained in sub-section 3.2.1.
- However, for the in-situ KF PDT, the etched CIS absorbers are then returned back to the PVD tool (a schematic is presented in Figure 3.7), where the KF deposition and annealing steps take place simultaneously in the same chamber without getting the absorbers exposed to air between the KF deposition and annealing steps; that is why it is called an in-situ KF PDT.

By performing the deposition and annealing KF steps together in the same chamber without exposing the KF treated absorbers to air before the annealing step, we avoid the negative effect of the hygroscopic nature of KF that was problematic in the case of the ex-situ KF PDT as discussed in sub-section 3.2.1.

The deposited KF is then directly annealed inside the PVD chamber before getting the treated CIS absorbers out to be rinsed with de-ionized water to remove any remaining fluorides. After that, the CdS layer is deposited by chemical bath deposition where the duration of the deposition is defined by the turbidity change of the solution before completing the baseline process for finished solar cells.

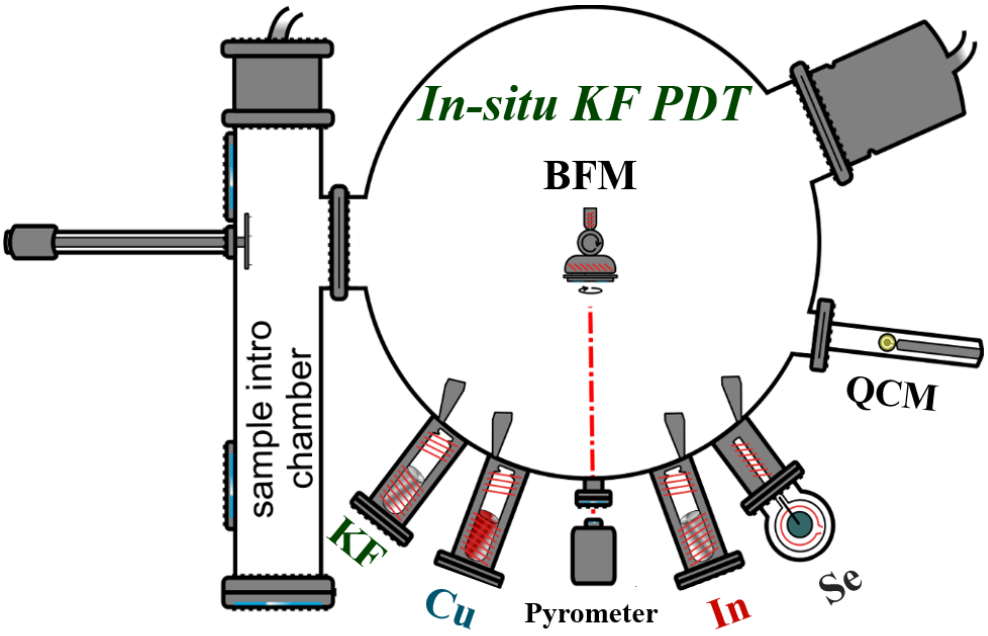

Figure 3.7: A schematic for the PVD used during the in-situ KF PDT

Several experiments were performed to optimize the in-situ KF DT. While the objective of the ex-situ KF PDT was to mainly improve the V_{OC} as explained in sub-section 3.2.1, the objectives of the optimization of the in-situ KF PDT can be summarized in the following two main objectives:

1. Improve the V_{OC} values of the treated cells.
2. Enhance the efficiency of the treated cells.

Similar to the ex-situ KF PDT (sub-section 3.2.1), the optimization process was performed to improve the Cu-rich CIS solar cells and then the optimized conditions were applied to Cu-poor CIS absorbers without further optimization. The optimization process was performed in terms of Se-flux, annealing temperature, annealing durations and KF thicknesses. The experimental details of the optimization process will be explained in Section 6.2.

The optimized conditions for the in-situ KF PDT can be summarized in the following steps:

- The first step is a double heating step to heat the etched CIS absorbers up to a substrate temperature of 350 ^{0}C under Se environment where the Se-flux is at least similar to the one used during CIS absorber fabrication. The double heating step is composed of an initial fast heating step (up to temperatures of 310 ^{0}C) followed by another slow heating step (up to temperatures of 350 ^{0}C).

- After reaching the desired substrate temperature, the second step takes place. The second step is the KF deposition and annealing steps. The KF deposition and annealing steps take place simultaneously at the same time. KF is deposited with a rate of approximately 1 nm/minute and for durations between 4 – 12 minutes.
- The last step is then the cooling down of the treated CIS absorbers to a substrate temperature of 200 ^{0}C.

It is important to note that Se is evaporated through all the steps of the in-situ KF PDT at a relatively high flux, similar to the flux used for CIS absorber growth.

The temperature profile for the in-situ KF PDT is illustrated in Figure 3.8.

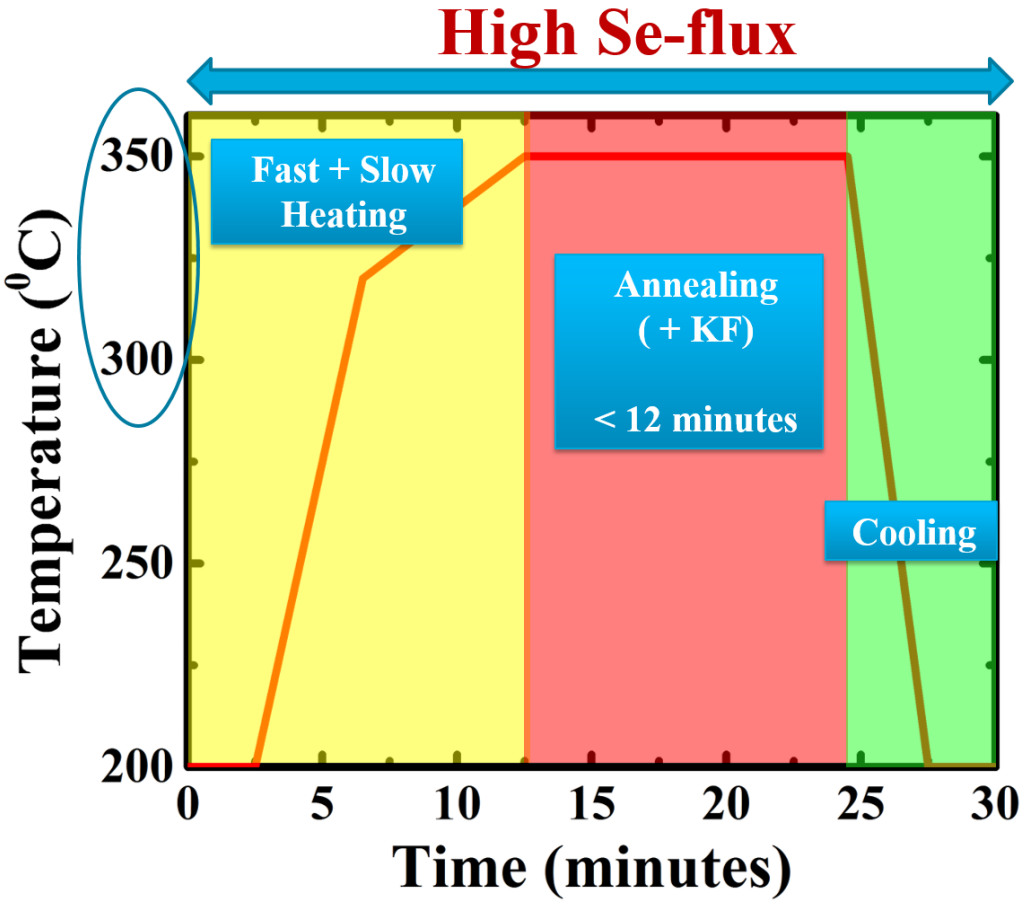

Figure 3.8: Temperature profile for the in-situ KF PDT

3.2.3 Selenium (Se) treatment

A Se-only PDT was developed for two main reasons:

1. Check the ability of the Se-only PDT to improve the absorber/buffer interface of Cu-rich CIS solar cells.
2. Discover if the Se-only PDT would be able to improve the V_{OC} and the efficiency of Cu-rich CIS solar cells or not.

The Se-only PDT is very similar to the in-situ KF PDT described in sub-section 3.2.2. The only difference between the Se-only PDT and the in-situ KF PDT is the absence of KF during the annealing step (step 2 of the in-situ KF PDT). The steps of the Se-only PDT can be explained in the following points:

1. The first step of the Se-only PDT is a double heating step:
    a. A fast-heating step up to a real temperature of 310 ^{0}C.
    b. A slow-heating step up to temperatures of approximately 350 ^{0}C.
2. The second step is an annealing step in the presence of Se for durations of less than 12 minutes.
3. The last step is a cooling step. The cooling step takes place down to temperatures of 200 ^{0}C.

It is important to note that Se is evaporated through all the steps of the Se-only PDT at a relatively high flux, similar to the flux used for CIS absorber growth. The Se-flux used for the Se-only PDT is similar to the Se-flux used for the in-situ KF PDT discussed in sub-section 3.2.2.

The temperature profile for the Se-only PDT is illustrated in Figure 3.9.

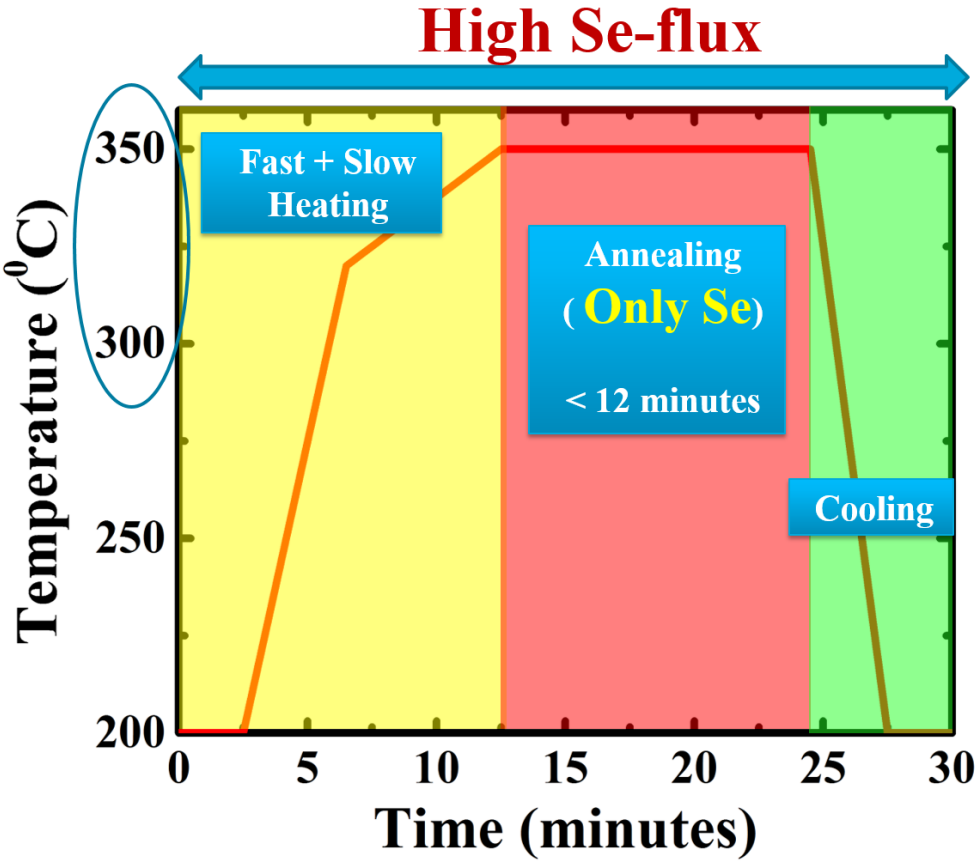

Figure 3.9: Temperature profile for the Se-PDT

References Chapter 3

[1] H. Elanzeery, F. Babbe, M. Melchiorre, A. Zelenina, S. Siebentritt, "Potassium Fluoride Ex-Situ Treatment on Both Cu-Rich and Cu-Poor $CuInSe_2$ Thin Film Solar Cells", IEEE Journal of Photovoltaics 7 684–689 (2017).

[2] F. Babbe, H. Elanzeery, M. Melchiorre, A. Zelenina, S. Siebentritt, "Potassium fluoride post deposition treatment with etching step on both Cu rich and Cu poor $CuInSe_2$ thin film solar cells", Physical Review Materials, 2, 10, 105405 (2018).

[3] H. Elanzeery, M. Melchiorre, M. Sood, F. Babbe, F. Werner, G. Brammertz and S. Siebentritt, "Challenge in Cu-rich Thin Film Solar Cells: Defect Caused by Etching", submitted (2018).

[4] M. A. Contreras, M. J. Romero, B. To, F. Hasoon, R. Noufi, S. Ward, K. Ramanathan, "Optimization of CBD CdS process in high-efficiency $Cu(In,Ga)Se_2$-based solar cells", Thin Solid Films, 403-404: 204–211 (2002).

[5] M. Hala, H. Kato, M. Algasinger, Y. Inoue, G. Rey, F. Werner, C. Schubbert, T. Dalibor, S. Siebentritt, "Improved environmental stability of highly conductive nominally undoped ZnO layers suitable for n-type windows in thin film solar cells", Solar Energy Materials & Solar Cells, 161, 232–239 (2017).

[6] M. Hala, S. Fujii, A. Redinger, Y. Inoue, G. Rey, M. Thevenin, V. Depredurand, T. P. Weiss, T. Bertram, S. Siebentritt, "Highly conductive ZnO films with high near infrared transparency", Progress in Photovoltaics Research Application, 23 (11), 1630 (2015).

[7] F. Babbe, PhD Thesis (2019).

[8] R. Prabu, S. Ramesh, M. Savith, M. Balachandar, "Review of physical vapour deposition (PVD) techniques", Proceedings of the International Conference on Sustainable Manufacturing, 10.13140/RG.2.1.5063.4964 (2013).

[9] V. Deprédurand, T. Bertram, S. Siebentritt, "Influence of the Se environment on Cu-rich CIS devices", Physica B, 439, pp. 101-104 (2014).

[10] T. Gödecke, T. Haalboom, F. Ernst, "Phase equilibria of Cu-In-Se I. The In_2Se_3-Se-Cu_2Se subsystem", Zeitschrift Für Met., 91, 622–634 (1948).

[11] J. C. Mikkelsen, "Ternary phase relations of the chalcopyrite compound $CuGaSe_2$", J. Electron. Mater., 10, 541 (1981).

[12] S. Niki, P. J. Fons, A. Yamada, Y. Lacroix, H. Shibata, H. Oyan-agi, M. Nishitani, T. Negami, T. Wada, "Effects of the surface $Cu_{2-x}Se$ phase on the growth and properties of $CuInSe_2$ films", Appl. Phys. Lett., 74, 1630 (1999).

[13] Y. Hashimoto, N. Kohara, T. Negami, M. Nishitani, T. Wada, "Surface characterization of chemically treated Cu(In,Ga)Se_2 thin films", Japanese Journal of Applied Physics Part 1-Regular Papers Short Notes & Review Papers, 35: 4760 – 4764 (1996).

[14] D. Regesch, L. Gütay, J. K. Larsen, V. Deprédurand, D. Tanaka, Y. Aida, S. Siebentritt, "Degradation and passivation of $CuInSe_2$", Applied Physics Letter, 101 (2012).

[15] T. Bertram, "Doping, Defects and solar cell performance of Cu-rich grown $CuInSe_2$", PhD. Thesis http://orbilu.uni.lu/handle/10993/28325 (2016).

[16] K. B. Messaoud, G. Brammertz, M. Buffière, S. Oueslati, H. Elanzeery, M. Meuris, M. Amlouk, J. Poortmans, "Modelling of $Cu_2ZnSnSe_4$-CdS-ZnO thin film solar cell", Materials Research Express, 4, 11 (2017).

[17] https://www.janis.com/Libraries/Window_Transmissions/MagnesiumFluoride_MgF2_TransmissionCurveDataSheet.sflb.ashx

Chapter 4: Characterization methods for CI(G)S solar cells

Chapter 4 discusses the theoretical background for the main characterization techniques used in this thesis. This thesis focuses on the electrical characterization of different CI(G)S absorbers and solar cells. Section 4.1 discusses the Current-Voltage (*IV*) characteristics of the solar cells. This section will identify the main *IV* parameters that define the performance of solar cells. These main parameters are the open circuit voltage (V_{OC}), the short circuit current density (J_{SC}), the Fill Factor (FF) and the efficiency, which is the figure of merit for any solar cell. The explanations, discussed in Section 4.1, are based on Chapter 2 in [1], Chapter 2 in [2] and Chapter 2 in [3]. Section 4.2 will introduce some aspects on the optoelectronic performance of the solar cells in terms of External Quantum Efficiency (*EQE*). Moreover, this section will also highlight how the bandgap of the solar cells in this thesis was extracted from such *EQE* measurements. The EQE discussions of Section 4.2 are based on Chapter 2 in [1]. Sections 4.3, 4.4 and 4.5 explain the methods used for the deep investigation of the characteristics of the CI(G)S absorbers and cells. Section 4.3 is dedicated to identifying the dominant recombination path by extracting the V_{OC} from the *IV* measurements as function of temperature (*IVT*). In addition to that, the *IVT* measurements are used to extract the activation energy of the series resistance. The interpretations of the IVT measurements in Section 4.3 are based on Chapter 2 in [1] and Chapter 6 in [2]. The doping is extracted from the Mott-Schottky plot of the Capacitance-Voltage (*CV*) measurements as explained in Section 4.4. The interpretations of the CV measurements in Section 4.4 are based on Chapter 4 in [1], Chapter 5 in [2], Chapter 2 in [3] and Chapter 5 in [4]. Finally, the main capacitance step is identified from the capacitance-frequency measurements as a function of temperature or admittance measurements (*ADM*). The main capacitance step should correspond to a barrier or a defect. The interpretations of the admittance measurements in Section 4.5 are based on Chapter 4 in [1], Chapter 5 in [2], Chapter 2 in [3], Chapter 5 in [4] and Chapter 2 in [5].

4.1 Solar cell performance

The solar cell is a p-n junction and its electrical performance (*JV* or *IV* characteristics) under dark conditions is explained in terms of a diode equation. The general diode equation relating current density (*J*) and voltage (*V*) for solar cells is described with a 1-diode model in Equation [4.1]:

$$J\,(V) = J_0\left[\exp\left(\frac{q\,(V - J\,R_S)}{A\,K\,T}\right) - 1\right] + \frac{V - J\,R_S}{R_{Sh}} \qquad [4.1]$$

Where *J (V)* is the current density function, J_0 is the saturation current density, q is the elementary charge, *V* is the voltage, R_S is the series resistance, R_{Sh} is the shunt resistance, *A* is the diode ideality factor, *K* is the Boltzmann constant and *T* is the absolute temperature.

Under illumination, the light shifts the *JV* curves to the fourth quadrant by the value of the photocurrent or the light generated current, J_{ph}. Equation [4.2] is then the extension of Equation [4.1] representing the IV characteristics of the solar cell under light conditions:

$$J\,(V) = J_0\left[\exp\left(\frac{q\,(V - J\,R_S)}{A\,K\,T}\right) - 1\right] + \frac{V - J\,R_S}{R_{Sh}} - J_{ph} \qquad [4.2]$$

For an ideal solar cell, $R_S = 0$ and $R_{Sh} = \infty$, then Equation [4.2] can be simplified to Equation [4.3]:

$$J\,(V) = J_0\left[\exp\left(\frac{q\,V}{A\,K\,T}\right) - 1\right] - J_{ph} \qquad [4.3]$$

The quality of any solar cell is determined by its power conversion efficiency (PCE). The power conversion efficiency (PCE or η) of any solar cell is expressed as the ratio between the output power a solar cell can generate compared to the incident power from the light source (potentially sun) or in another words the amount of the incident power that the solar cell can convert into electricity. The efficiency of the solar cell is expressed in Equation [4.4]:

$$\eta = \frac{P_{output}}{P_{incident}} = \frac{J_{SC}\,V_{OC}\,FF}{P_{incident}} \qquad [4.4]$$

The incident power ($P_{incident}$) is 1 kW/m^2 or 100 mW/cm^2 for 1 sun illumination.

Equation [4.4] reveals that the efficiency depends on three main parameters: the short circuit current density (J_{SC}), the open circuit voltage (V_{OC}) and the Fill Factor (FF). Each of these main efficiency parameters is explained as follows:

[1] The short circuit current density (J_{SC}) is the current passing through the solar cell at short circuit conditions (when the bias voltage is zero) as indicated in Figure 4.1. J_{SC} is the maximum current density that can be drawn from a solar cell. In an ideal solar cell, the J_{SC} shall be equal to the photocurrent (J_{ph}). The J_{SC} (the short circuit current density) is obtained by dividing the short circuit current (I_{SC}) by the area and the J_{SC} is then expressed in terms of mA/cm^2. The J_{SC} is dependent on the following parameters:

- The light intensity and the spectrum of the incident light source. AM1.5 spectrum is the standard used in this thesis [6].
- The optical properties of the absorber semiconductor material and the optical properties of the other layers forming the solar cell. This point will be understood better when discussing the EQE spectrum in Section 4.2. In this section, I will only discuss one of the optical properties of the absorber semiconductor material that affects the J_{SC} of the solar cell: the bandgap of the absorber semiconductor material. Each semiconductor is characterized by a specific bandgap energy (E_g). This bandgap energy determines the range of the light spectrum this semiconductor material can absorb. The semiconductor material absorbs the light spectrum of wavelengths less than the wavelength corresponding to the bandgap energy of the semiconductor material (λ_g). The relationship between the bandgap energy of a semiconductor material and the range of the light spectrum this semiconductor material can absorb is governed by Equation [4.5].

$$E_g = \frac{h\,c}{\lambda_g} \qquad [4.5]$$

Where h is the Planck's constant (6.626×10^{-34} Joule.sec) and c is the speed of light (3×10^8 m/sec). Converting hc to electron volt (eV) which is the standard unit compared to joule and represents the energy to raise an electron by 1 volt, we use the conversion factor: 1 eV = 1.602×10^{-19} Joules. Equation [4.5] can be re-written as:

$$E_g = \frac{6.626\ x\ 10^{-34}\ joule.\sec x\ 3\ x\ 10^8\ \frac{m}{\sec} \div (1.602\ x\ 10^{-19}\ \frac{joule}{eV})}{\lambda_g}$$

$$E_g \approx \frac{1240\ nm.eV}{\lambda_g} \qquad [4.5]$$

Based on Equation [4.5], it can be observed that depending on the bandgap of the semiconductor material, the range of the light spectrum this semiconductor material can absorber changes. The higher the bandgap of the absorber semiconductor material, the smaller the range of the light spectrum this semiconductor can absorb and consequently the lower the J_{SC} the solar cell (based on this semiconductor absorber) can produce.

[2] The open circuit voltage (V_{OC}) is the voltage of the solar cell at open circuit conditions (when the current is zero) as indicated in Figure 4.1. V_{OC} is the maximum voltage produced by a solar cell. V_{OC} depends on the bandgap of the absorber semiconductor material. The higher the bandgap, the higher the voltage that can be produced. Moreover, inserting $J\ (V) = 0$ in Equation [4.3] and rearranging for the V_{OC} gives us an expression for the V_{OC} as presented in Equation [4.6]:

$$V_{OC} = \frac{A\ K\ T}{q}\ Ln\left(\frac{J_{ph}}{J_0} + 1\right) \qquad [4.6]$$

From Equation [4.6], it can be observed that the V_{OC} depends mainly on J_{ph}, J_0 and A. J_0 depends heavily on the recombination mechanisms in the solar cell and can be described in general with an activation energy (E_a) as depicted from Equation [4.7]:

$$J_0 = J_{00} \exp\left(-\frac{E_a}{A\ K\ T}\right) \qquad [4.7]$$

Where J_{00} is the reference current density and varies with different recombination mechanisms. The temperature dependence of J_{00} can be neglected.

If we substitute Equation [4.7] into Equation [4.6] and neglect the (+1) term as the term $\frac{J_{ph}}{J_0}$ is much greater than one, then the V_{OC} can be expressed in terms of the activation energy (E_a) as presented in Equation [4.8]:

$$V_{OC} = \frac{E_a}{q} - \frac{A\ K\ T}{q}\ Ln\left(\frac{J_{00}}{J_{ph}}\right) \qquad [4.8]$$

Therefore, based on Equation [4.8], it can be concluded that the V_{OC} depends on E_a, A and J_{00} whose values depend on the recombination mechanisms present in the solar cell as well as the J_{ph} of the solar cell.

After identifying both the J_{SC} and the V_{OC} and their relationship with the bandgap energy, it can be observed that there is a trade-off between J_{SC} and V_{OC} as a function of the bandgap of the absorber semiconductor material. An absorber semiconductor material with higher bandgap allows for a higher V_{OC} but lowers the J_{SC}. An optimization between both (the J_{SC} and the V_{OC}) in terms of efficiency is required for the design of an efficient solar cell.

[3] The Fill Factor (FF) is a quality measure of the *JV* curve of the solar cell. Although the J_{SC} and the V_{OC} values are the maximum current and voltage produced from a solar cell respectively, but the power at each of these two values is zero. Therefore, the measurement of the FF is based on comparing the area of the rectangle at the point with the maximum output power, P_m (voltage at maximum output power, V_m multiplied by the current at maximum output power, J_m), to the area of the rectangle at the J_{SC} and the V_{OC} values as presented in Figure 4.1 and expressed in Equation [4.9]. The FF value is always less than one.

$$FF = \frac{V_m J_m}{V_{OC} J_{SC}} = \frac{Area\ 1\ (Figure\ 4.1)}{Area\ 2\ (Figure\ 4.1)} \qquad [4.9]$$

The FF depends on four main parameters:

a. Open circuit voltage, V_{OC}. Higher V_{OC} (if other parameters remain unchanged) provides an increase in the FF as the exponential increase in the *JV* curve consumes less area.
b. Series resistance, R_S. Series resistance dominates at higher voltages of the IV curve as presented in Figure 4.1. Higher values of series resistance lead to a decrease in the FF values.
c. Shunt Resistance, R_{Sh}. Shunt resistances dominate at lower voltages of the IV curve as presented in Figure 4.1. Parasitic resistance losses in terms of lower shunt resistances deteriorate the FF.
d. Ideality factor, A. The diode ideality factor is a quality measure of the p-n junction and describes the voltage dependence of the junction diode current in any solar cell. The diode ideality factor depends on the types of recombination taking place in the solar cell. An ideal solar cell under simple recombination mechanisms such as radiative-only recombination in the quasi-neutral region shall have an ideality factor of 1. More complex recombination mechanisms could increase the value of the ideality factor above 2. High values of ideality factor leads to a decrease in the FF and the V_{OC} as explained earlier where V_{OC} depends also on recombination effects.

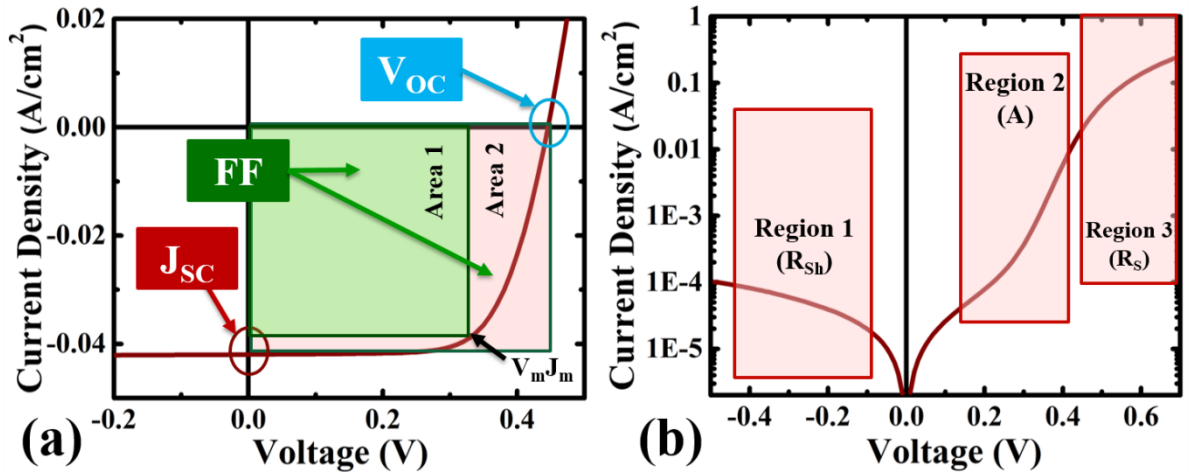

Figure 4.1: a) IV curve of a solar cell measured under illumination conditions on a linear scale to illustrate the extraction of V_{OC}, J_{SC} and FF. b) IV curve of the same solar cell measured under dark conditions on a logarithmic scale to illustrate the extraction of the shunt resistance (from Region 1), the ideality factor (from Region 2) and the series resistance (from Region 3).

Figure 4.1 presents an IV curve to illustrate the identification of the main electrical parameters of a solar cell. Figure 4.1a represents the IV behavior under illumination conditions on a linear scale. From this figure (Figure 4.1a), we can extract the following parameters:

1. V_{OC} as indicated on the x-axis when the current is equal to zero.
2. J_{SC} on the y-axis as indicated when the voltage is equal to zero.
3. FF as the ratio between the area at maximum power ($V_m J_m$) with the area at J_{SC} and V_{OC}.

$$FF = \frac{Area\ 1}{Area\ 2} = \frac{V_m\ J_m}{V_{OC}\ J_{SC}}$$

Figure 4.1b represents the IV behavior under dark conditions and on a logarithmic scale. In this thesis, the following parameters were extracted from fitting the IV curve under dark conditions to Equation [4.1] using the iv-fit software [7] as explained below:

1. Shunt resistance. The quality of the shunt resistance can be observed from Region 1 (reverse bias Region) in Figure 4.1b.
2. Ideality factor. The quality of the ideality factor can be observed from Region 2 in Figure 4.1b. The slope of the IV curve in Region 2 is equal to *1/AKT*.
3. Series resistance. The quality of the series resistance can be observed from Region 3 (far forward bias Region) in Figure 4.1b.

The tool used to characterize the solar cell performance is a Class AAA Standard Solar Simulator that is calibrated by a Si reference cell, with an *IV*-source-measure-unit as presented in Figure 4.2. The IV measurements are performed by applying a bias voltage to the solar cell and then measuring the current. The range of the bias voltage used in this thesis for the IV measurements is -0.6 – 0.6 V. Two IV measurements are performed for each solar cell. One measurement is performed under dark conditions and the other measurement is performed under illumination conditions with an intensity of 100 mW/cm^2. The two IV measurements (dark and illumination) are performed at room temperature. A cooling fan is installed beside the solar simulator to avoid excessive heat conditions as well as the IV measurements are performed in a closed box to avoid external temperature variations as illustrated in Figure 4.2. The main *JV* parameters (V_{OC}, J_{SC}, FF and Efficiency) are extracted from the measurements under illumination conditions. The series resistance, shunt resistance and ideality factor values are extracted from the IV measurements performed under dark conditions using iv-fit software [7]. The iv-fit software fits the measured IV curve under both dark and illumination conditions to Equation [4.1] and extract the required parameters using an orthogonal-distance regression that accounts for the strong variation in the slope of the IV curve.

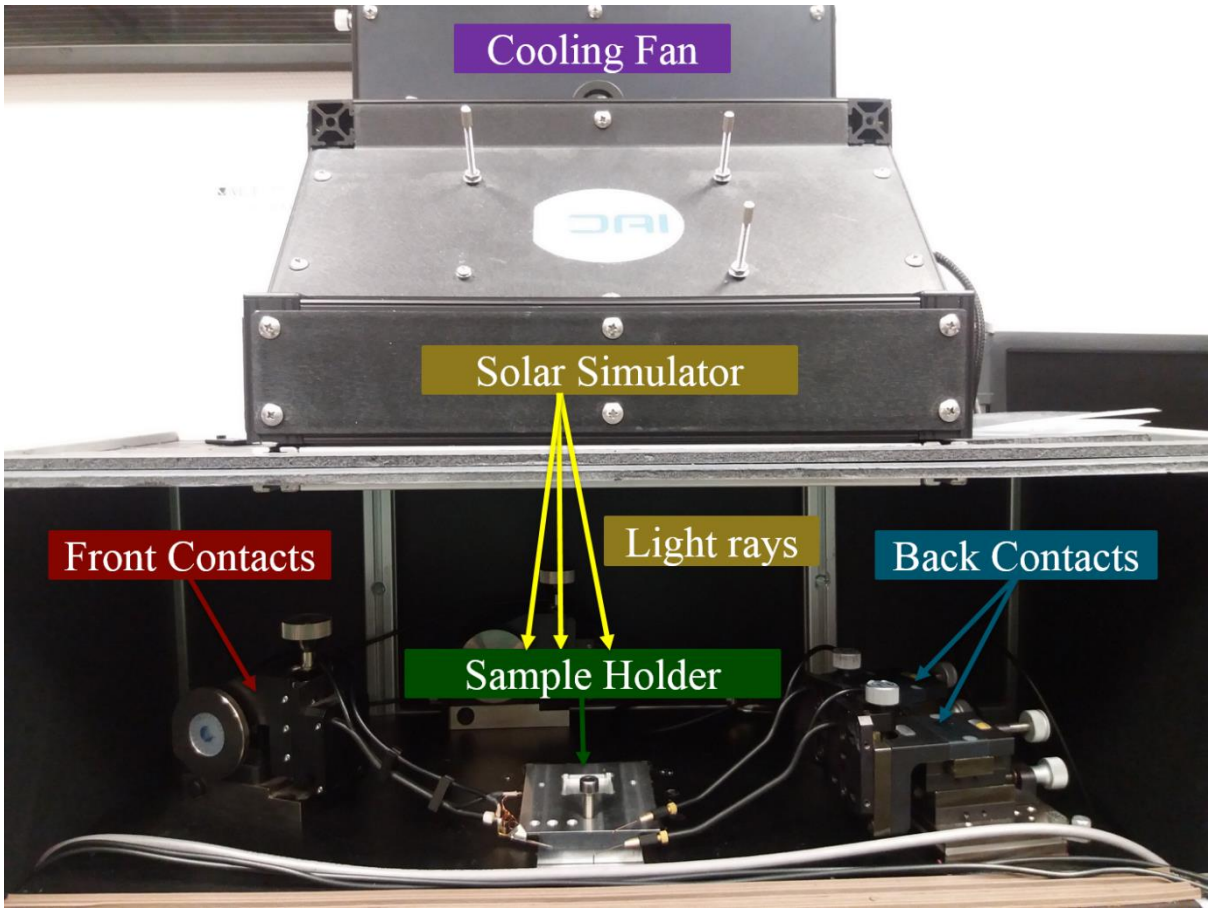

Figure 4.2: IV characterization setup indicating the solar simulator with a light intensity of 100 mW/cm^2 and a cooling fan for cooling the measurement system. The front and back contacts are connected to the sample that is placed on top of the sample holder.

4.2 External Quantum Efficiency (EQE) & Bandgap determination

Efficiency is simply the output power over the input power. The External Quantum Efficiency (EQE) is the number of electrons generated from a solar cell compared to the number of incident photons on a solar cell as a function of wavelength or energy of the incoming light as expressed in Equation [4.10]:

$$EQE = \frac{n_e}{n_{ph}} = \frac{\left(J_{EQE}/q\right)}{\left((P_L)\,\lambda/_{hc}\right)} \qquad [4.10]$$

where n_e is the number of generated electrons and n_{ph} is the number of incident photons. The number of electrons (n_e) can be expressed as the current density divided by the electron charge (q). The number of photons (n_{ph}) can be expressed as the power of the input light source (P_L) divided by the energy of the photons. The energy of the photons was previously presented in Equation [4.5] as hc/λ. Equation [4.10] can be re-arranged to be:

$$EQE = \frac{J_{EQE}}{P_L}\left(\frac{1}{\lambda}\right)\left(\frac{hc}{q}\right) \qquad [4.10]$$

With our EQE measurements, we measure the current of the solar cell as a function of wavelength, $J_{EQE}\left(\frac{1}{\lambda}\right)$ as well as the reference spectrum of the lamp as the light source (P_L).

When light is incident on a semiconductor material, the incident photons excite or raise the electrons from the valence band of the semiconductor to its conduction band provided that the energy of the incident photons is higher than the energy difference between the valence and conduction bands. This energy difference between the valence and conduction bands is called the bandgap energy (E_g) and is a specific property of each semiconductor material as explained earlier. Therefore, incident photons with energies higher than the bandgap of a semiconductor absorber material would be able to excite the carriers from the valence band to the conduction band and generate an electron-hole pair while incident photons with energies lower than the bandgap would be lost. The excited carriers are then collected according to the collection probability of the solar cell. As described above, the EQE is the number of collected electrons compared to the number of incident photons. Therefore, if all the photons with energies higher than a specific bandgap energy are absorbed and the generated carriers are collected, then the EQE at this bandgap energy is equal to unity (EQE = 1). On the other side, photons with energies below such bandgap energy will be lost, no electrons will be generated and the EQE is equal to zero.

Practically, the EQE spectrum is not a step function (zero below the bandgap energy and one (100 %) above the bandgap energy) as observed in Figure 4.3a. Figure 4.3a represents the EQE spectrum for one of the solar cells presented in this thesis. The lower EQE spectrum compared to a step function is attributed to different types of losses represented by the corresponding regions in Figure 4.3a [8].

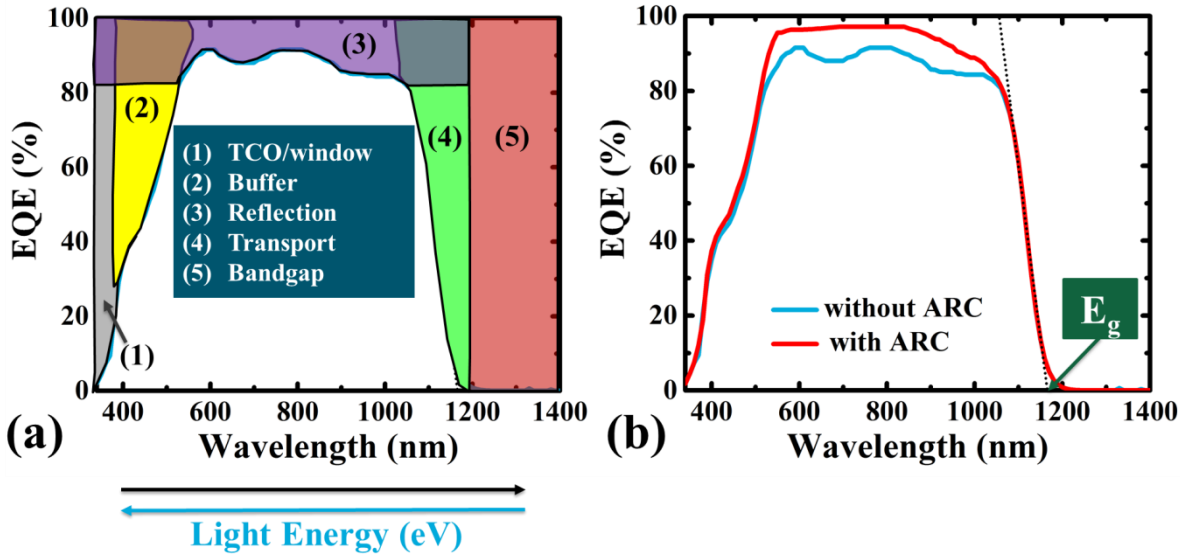

Figure 4.3: a) An example of the EQE spectrum for one of the solar cells with an illustration of the corresponding optical losses identified through five different regions. b) An illustration of the effect of using an Anti-Reflection Coating (ARC) layer in minimizing the optical losses in Region 3 of a). The short dotted line represents the linear fit from which the bandgap energy (E_g) is extracted.

Figure 4.3a represents the EQE spectrum for one of the solar cells. The EQE spectrum is expressed in terms of the wavelength (black arrow) or in terms of the energy of light (blue arrow).

The bandgap energy (E_g) of the absorber semiconductor material can be calculated using several methods [9]. The method used in this thesis is based on the linear fitting of the EQE spectrum at long wavelengths (at the decreasing slope of the EQE spectrum before the EQE values reach zero) as presented by the short dotted line in Figure 4.3a. Taking the curve presented in Figure 4.3a as an example, the bandgap energy of the absorber semiconductor material used in this example was calculated as follows:

- A linear fit of the EQE spectrum at long wavelengths was performed as explained (short dotted line in Figure 4.3a).
- The intercept value of the linear fit line (short dotted line) on the x-axis (wavelength axis) was found to be at a wavelength of 1164 nm.

- Using Equation [4.5], the bandgap energy of this absorber semiconductor material was calculated as follows:

$$E_g = \frac{1240\ nm.eV}{\lambda_g} = \frac{1240\ nm.eV}{1164\ nm} = 1.07\ eV$$

From Figure 4.3a, it can be observed that the EQE values below the bandgap (below 1.07 eV or above the wavelength of 1164 nm, represented approximately by the red Region or Region 5 in Figure 4.3a) show zero values as expected and explained earlier. It is important to note that an EQE response (not equal to zero) is still observed below the bandgap as can be observed in Figure 4.3b. This EQE response is related to the presence of band tails.

On the other side, the EQE spectrum above the bandgap does not show a unity step function (the EQE values are not 100 %). This deviation of the EQE spectrum from unity values is attributed to different types of losses illustrated by the different regions in Figure 4.3a and can be explained as follows:

[1] Region 1 (Grey region) represents the losses due to the absorption of the incident photons by the transparent conductive oxide (TCO) and window layers (the upper two layers of the solar cell structure presented in Section 2.3). The two layers used in this thesis are based on Zinc Oxide (ZnO) with a bandgap of 3.2 eV. These two layers are expected to absorb the incident photons above their bandgap energy (above 3.2 eV corresponding to a wavelength of 388 nm using Equation [4.5]). Therefore, these two layers are expected to absorber the incident photons in Region 1 in the wavelength range below 388 nm.

[2] Region 2 (Yellow region) represents the optical losses as a result of the absorption of the incident photons by the CdS buffer layer that is characterized by a bandgap of 2.4 eV. The CdS buffer layer is then expected to absorb the incident photons in Region 2 in the wavelength range between 388 nm (bandgap energy of the window layers) and 517 nm (the bandgap energy of CdS).

[3] Region 3 (Purple region) is the optical losses due to reflection. Reflection losses are active over the whole wavelength region. An Anti-Reflection Coating (ARC) layer is used to reduce these reflection losses. The ARC layer reduces the reflection losses over the whole wavelength spectrum (Region 3). Magnesium Fluoride (MgF_2) is the ARC layer used in this thesis and was deposited for the best solar cells in this thesis as presented in Section 3.1.2. The effect of using an ARC layer is illustrated in Figure 4.3b where the optical losses in Region 3 (Figure 4.3a) were minimized after using an ARC layer (red curve in Figure 4.3b).

[4] Region 4 (Green region) represents the optical losses due to incomplete generation of photons (incomplete absorption) or due to incomplete collection of carriers affected by low mobility.

[5] Region 5 (Red region) represents the optical losses of the incident photons whose energies are lower than the bandgap of the absorber semiconductor material as explained earlier.

As the EQE measurement is an optoelectronic characterization technique used to measure the generated electrons of a solar cell, an "optical" short circuit current density (J_{SC}) can then be extracted. This short circuit current density (J_{SC}) is an optical J_{SC} referred to in this thesis as "J_{SC_EQE}" and is related to the generation and collection of photo-generated carriers. Ideally, this "J_{SC_EQE}" shall be equal to the J_{SC} from IV measurements. However, practically, small differences are observed between both values due to losses by shading of the contact grids as well as the spectral mismatch between the solar simulator and the AM1.5 spectrum in the IV measurements. The J_{SC_EQE} is calculated by integrating the EQE spectrum as a function of wavelength and multiplying it with the AM1.5 spectrum as presented in Equation [4.11].

$$J_{SC\_EQE} = q * \int_{\lambda_1}^{\lambda_g} EQE\ (\lambda) * \varphi_{AM1.5}\, d\lambda \qquad [4.11]$$

Where λ_1 is the starting wavelength of the EQE measurement (in this thesis, the starting wavelength of the EQE measurement is 340 nm), $\phi_{AM1.5}$ is the spectral photon flux of the AM1.5 spectrum.

The EQE measurements are performed using a grating monochromator setup under a chopped illumination based on halogen and xenon lamps. The EQE measurements are performed at room temperatures. A Lock-in amplifier is used to measure the photocurrent of the solar cell. The EQE measurement setup is presented in Figure 4.4. Two detectors are used for these EQE measurements:

- Si-detector covering wavelengths from 300 – 1100 nm
- Indium-Gallium-Arsenide (InGaAs) detector covering wavelengths between 1100 – 1400 nm

The spectra of the above two detectors are measured as the reference spectra. These reference spectra account for the input power of the lamps (P_L) in Equation [4.10].

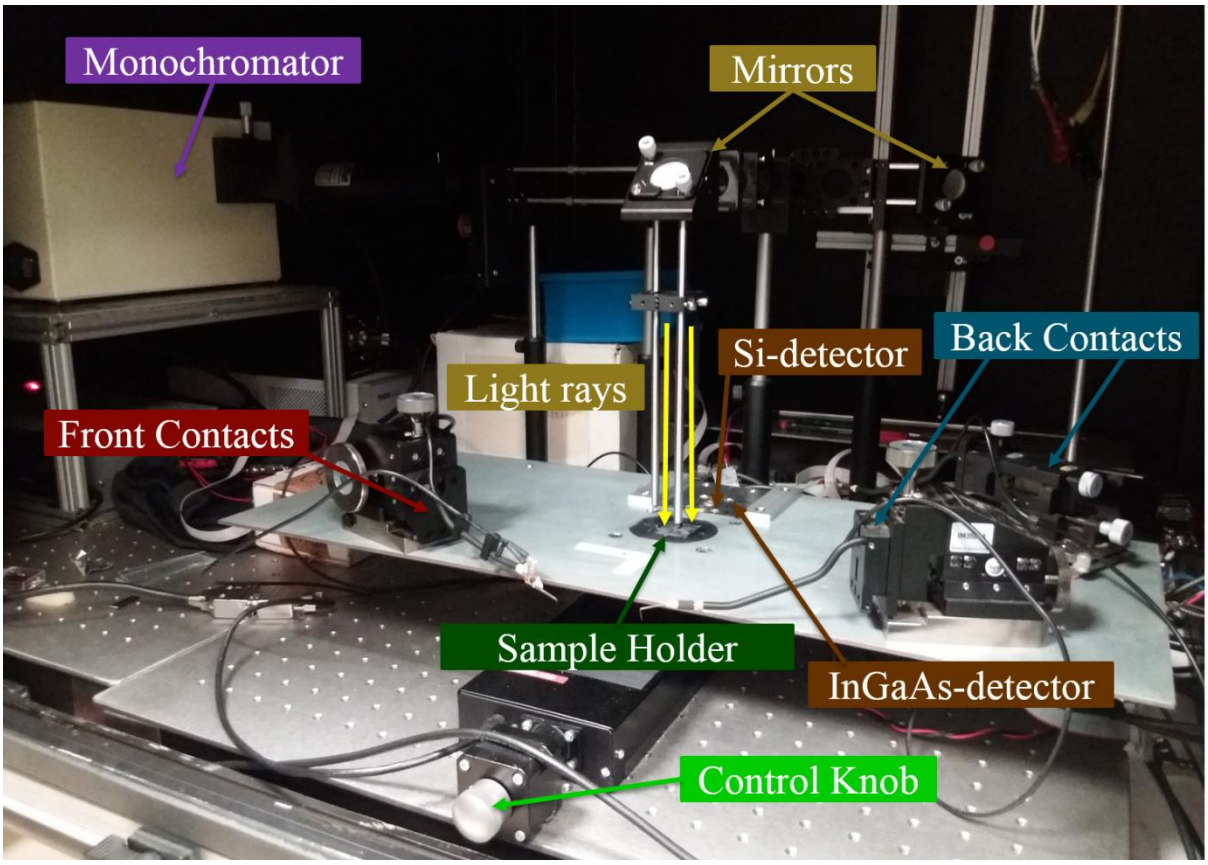

Figure 4.4: EQE setup. The monochromator passes a specific wavelength and the mirrors direct the light to the sample holder. Front and back contacts are connected to the sample on top of the sample holder. A control knob is used to control the X- and Y- axes to control the movement of the sample holder. Si and InGaAs detectors are used to perform the EQE measurements in the range of 300 – 1100 nm and 900 – 1400 nm respectively.

4.3 Dominant recombination path

One of the main fundamental challenges in thin film solar cells is the recombination activity of the absorber interface with the contact layers. The dominant recombination mechanism in any solar cell plays a vital role in identifying the electrical performance of the solar cell and affects the efficiency significantly. Thus, it is important to identify the dominant recombination path in the solar cell. IV measurements as a function of temperature (IVT) can be used to identify the dominant recombination path.

For the IVT measurements, the electrical parameters are extracted from the IV curves measured as a function of temperature under illumination conditions. In order to identify the dominant recombination path in the solar cell, the V_{OC} values are then plotted as a function of temperature, V_{OC} (T) as illustrated in Figure 4.5.

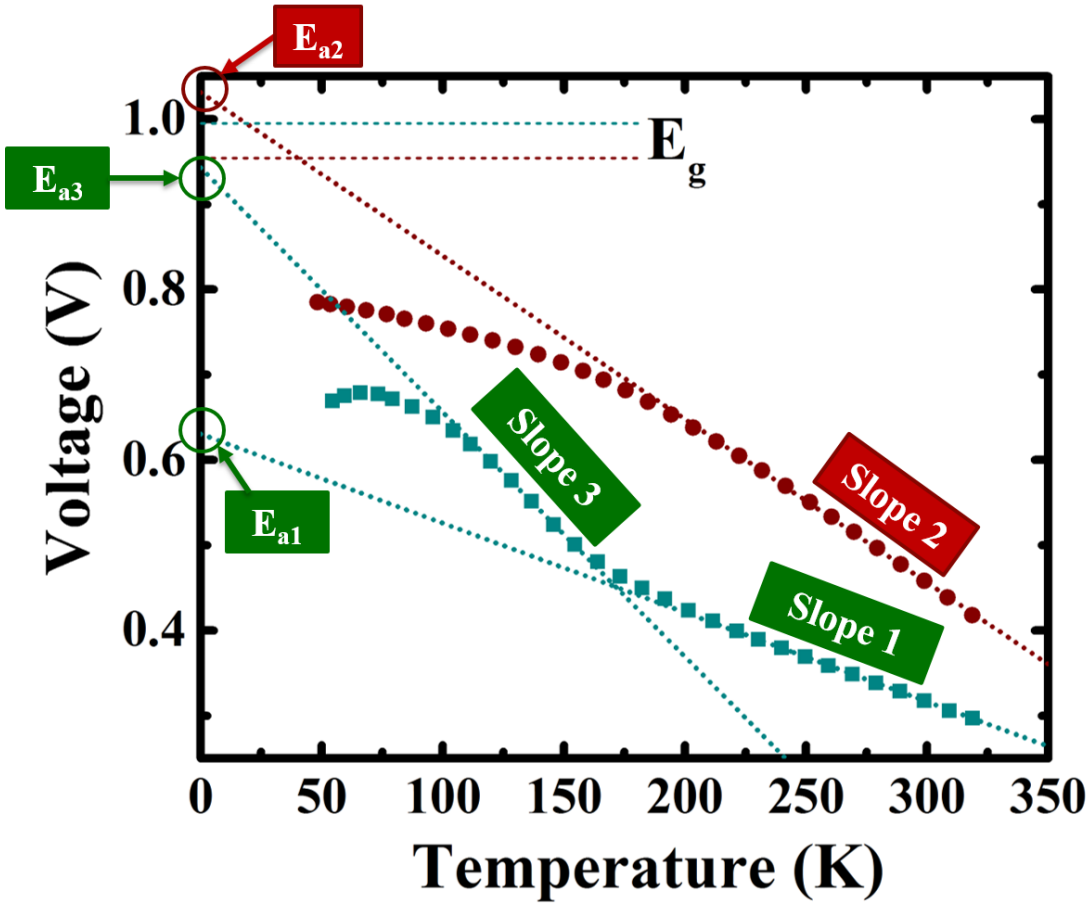

Figure 4.5: An illustration example for the IVT measurements of two different samples illustrating the plot of the V_{OC} as a function of temperature, V_{OC} (T). The fitting of the V_{OC} (T) curve to extrapolate the activation energy at zero Kelvin (E_a) is performed at high temperatures (short dotted lines) for Slope 1 and Slope 2. For Slope 3, the fitting of the V_{OC} (T) curve is performed at intermediate temperatures (100 – 160 K). The corresponding bandgap (E_g) of the two samples is represented by the short dashed lines.

Recalling Equation [4.8]:

$$V_{OC} = \frac{E_a}{q} - \frac{A\,K\,T}{q}\,Ln\left(\frac{J_{00}}{J_{ph}}\right) \qquad [4.8]$$

Applying Equation [4.8] on Figure 4.5, we can identify two main characteristics:

[1] The activation energy of the dominant recombination path (E_a). The activation energy of the dominant recombination path can be extrapolated using Equation [4.8] from the V_{OC} (T) curve in Figure 4.5 at zero Kelvin (Temperature, T = 0).

There are two possible recombination paths in any solar cell: Bulk recombination and Interface recombination.

If the dominant recombination path in the solar cell is due to bulk recombination, then the activation energy (E_a) should indicate values close to the bandgap of the solar cell. On the other side, if the dominant recombination path is in the absorber/buffer interface, then the activation energy (E_a) will suffer from additional losses showing values less than the bandgap energy as illustrated in Figure 4.6. These losses in the activation energy due to interface recombination can be attributed to conduction band misalignment, Fermi level pinning or interface defects [10].

Figure 4.6 illustrates a band diagram for a CIS solar cell showing that:

- In case that the bulk recombination is the dominant recombination path in the solar cell, the activation energy at the bulk (denoted by $E_{a,b}$) is equal to the bandgap energy.
- In case that the interface recombination is the dominant recombination path in the solar cell, the activation energy at the interface (denoted by $E_{a,i}$) is less than the bandgap energy. The activation energy at the interface ($E_{a,i}$) is equal to the energy between the conduction band and the interface trap/defect as indicated in Figure 4.6.

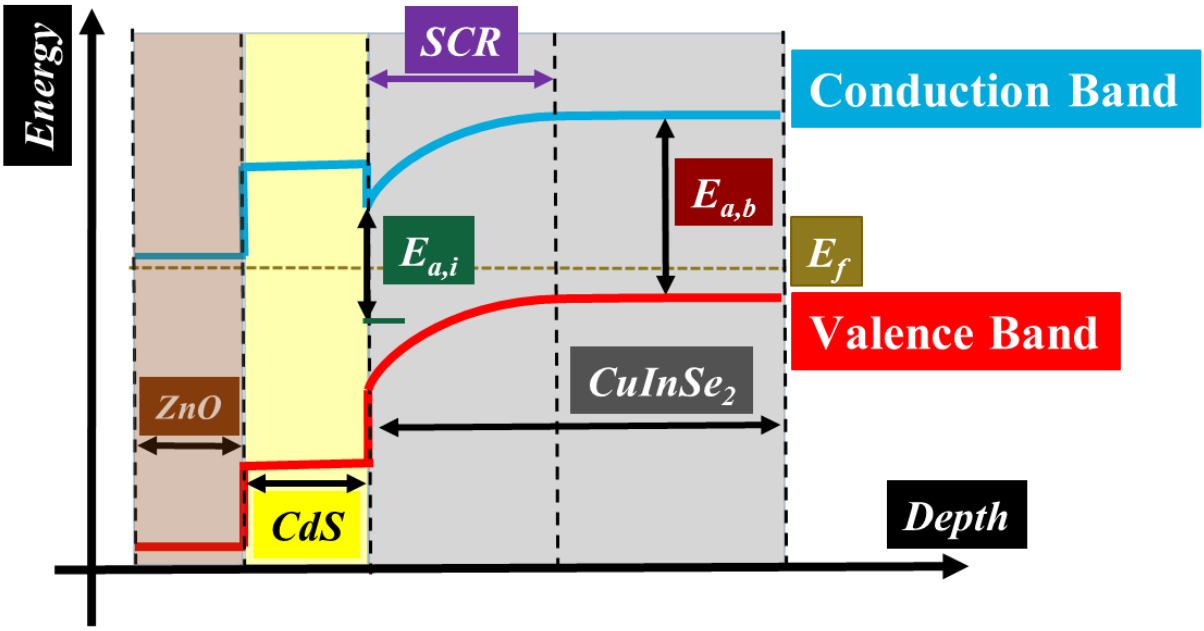

Figure 4.6: Band diagram of a CIS solar cell representing the Energy on the y-axis as a function of the solar cell depth on the x-axis. The brown region represents the window (ZnO) layer. The yellow region represents the buffer (CdS) layer. The grey region represents the absorber (CIS) layer. The purple arrow represents the SCR. The gold colour dashed line represents the fermi level (E_f). The conduction and the valence bands are represented by the blue and the red curves respectively. If the dominant recombination path in the solar cell is in the bulk, then the activation energy, $E_{a,b}$ is equal to the bandgap energy. If the dominant recombination path is in the absorber/buffer interface, then the activation energy, $E_{a,i}$ is less than the bandgap energy. The $E_{a,i}$ is then the energy between the conduction band and an interface defect (denoted by the green dash at the absorber/buffer interface).

The identification of these two types of recombination (bulk and interface) from the V_{OC} (T) curve is illustrated in Figure 4.5 for an example of two of the samples that will be discussed later in this thesis.

The bulk recombination as the dominant recombination path is identified for the red curve in Figure 4.5 whose extrapolated activation energy at zero Kelvin (E_{a2}) shows values close to the bandgap (The bandgap for the solar cell of the red curve is represented by the short dashed red line in Figure 4.5). The fitting of the V_{OC} (T) curve was performed at room temperature (where the solar cell operates) and below as indicated by Slope 2 (short dotted lines) in Figure 4.5 before the V_{OC} values saturate at temperatures below 200 K. It is important to note that the extrapolated activation energy (E_{a2}) at zero Kelvin of the V_{OC} (T) red curve in Figure 4.5 is showing values higher than the bandgap. Typically, the extrapolated activation energy of the V_{OC} (T) curve should show values equal to the bandgap (in case of bulk recombination) or values lower than the bandgap (in case of interface recombination).

The higher activation energy (E_{a2}) observed for the V_{OC} (T) red curve in Figure 4.5 compared to the bandgap could be attributed to two reasons:

1. The method of calculating the bandgap. In this thesis, the bandgap was calculated from the linear fitting of the EQE spectrum at long wavelengths as explained in Section 4.2. The bandgap extracted from the linear fitting of the EQE spectrum at long wavelengths could be an underestimated bandgap according to [9].
2. An expected 75 meV additional activation energy (corresponding to *3KT*) related to the effective density of states and temperature dependent thermal velocity [11].

On the other side, the extrapolated activation energy at zero Kelvin (E_{a1}) for the green curve in Figure 4.5 fitted at room temperature (represented by Slope 1) shows values much lower than the bandgap (The bandgap for the solar cell of the green curve is represented by the short dashed green line in Figure 4.5). This lower value of E_{a1} compared to the bandgap indicates that the dominant recombination path in the solar cell of the green curve (Figure 4.5) is in the absorber/buffer interface. It is important to note that this solar cell of the green curve shows an additional negative slope (Slope 3) at intermediate temperatures (100 – 160 K) before the V_{OC} values saturate at lower temperatures. The extrapolated activation energy (E_{a3}) at zero Kelvin of the V_{OC} (T) green curve fitted at intermediate temperatures (Slope 3) show values close to the bandgap as illustrated in Figure 4.5.

In this thesis, the dominant recombination path of the solar cell will be determined according to the fitting of the V_{OC} (T) curve near room temperature (where the solar cell operates).

The presence of two negative slopes in the solar cell of the green curve (Slope 1 and Slope 3) will be explained in terms of the photocurrent (J_{ph}) in the following discussion of the second characteristic point of Equation [4.8].

[2] The photocurrent (J_{ph}). The second characteristic that will be discussed in this thesis as an application of Equation [4.8] on Figure 4.5 is related to J_{ph}.

According to Equation [4.8], the slope of the V_{OC} (T) is: $\frac{A\,K}{q}\,Ln\left(\frac{J_{00}}{J_{ph}}\right)$. K as the Boltzmann's constant and q as the elementary charge are constants. The reference current density (J_{00}) is considered temperature independent and the ideality factor (A) is assumed to be only weakly temperature dependent. Therefore, the slope of the V_{OC} (T) curve could be determined by the photocurrent (J_{ph}).

To quantify and analyse the change in slope of the V_{OC} (T) curve in this thesis, J_{ph} will be extracted and plotted as a function of temperature.

Basically, the current of the solar cell measured under dark conditions represent the diode current, while the current of the solar cell measured under illumination conditions represent the diode current and the generation current. The generation current is the photocurrent (J_{ph}). In principle, the photocurrent could be extracted from the difference between the current of the solar cell under illumination (diode current + photocurrent) and under dark (diode current) conditions. The photocurrent in this thesis will be extracted from the IVT measurements as follows:

- At V_{OC}, the current under illumination conditions is equal to zero. This means that the total of the diode current and photocurrent is equal to zero.
- The photocurrent is then equal (and opposite) to the diode current (current under dark conditions).
- Therefore, the photocurrent is equal to the current under dark conditions at V_{OC}.
- The photocurrent as a function of temperature is then obtained from the current under dark conditions at the voltage corresponding to the V_{OC} at each temperature.

It is important to note that the photocurrent (J_{ph}) can depend on the voltage and the photocurrent at V_{OC}, J_{ph} (V_{OC}) is not equal to the short circuit current (J_{SC}).

The photocurrent at V_{OC}, J_{ph} (V_{OC}) as a function of temperature will be helpful in understanding the different slopes observed for the V_{OC} (T) curves as will be illustrated in Section 5.3.

One more parameter that is extracted from the IVT measurements and will be useful in the interpretation of defects and capacitance steps in Section 4.5 is the series resistance as a function of temperature [12]. The series resistance as a function of temperature, R_s (T) is deduced from the slope of the IV curve measured under dark conditions at far forward bias (1.2 V) as a function of temperature governed by Equation [4.12].

The behaviour of the IV curve at far enough forward bias (1.2 V) is affected mainly by the series resistance, where the current flowing in the solar cell is limited by one of the following:

- The transport of holes at the back interface barrier (absorber/back contact interface) into the absorber from the back contact layer.
- The transport of electrons at the front interface barrier (absorber/buffer interface) into the absorber from the buffer and window layers.

If none of the above two barriers are present, the series resistance as a function of temperature will not be activated meaning that the values of the series resistance will decrease as the temperature decreases.

However, if one of the above two barriers is present, the series resistance is then thermally activated as a function of temperature (the values of the series resistance increases as the temperature decreases). The activation energy or the height of this barrier (φ_b) is then extracted from the slope of the series resistance as a function of temperature plotted using Equation [4.12].

$$R_S = \frac{A^* q T}{K} \exp\left(\frac{q \varphi_b}{K T}\right) \qquad [4.12]$$

Where A^* is the effective Richardson constant and φ_b is the barrier height.

At very low temperatures, the series resistance is affected by the freeze-out of mobility and carriers, which is usually thermally activated, leading also to the thermal activation of the series resistance.

The tool used for the IVT measurements is based on a cold-mirror halogen lamp as the illumination source (supported by a cooling fan to dissipate heat energy) in a closed-cycle helium cryostat as illustrated in Figure 4.7. The power supply to the cooling fan is provided using a DC power supply. The full illumination intensity used for the IVT measurements is calibrated using the J_{SC} value measured with the standard IV setup under standard test conditions. A height adjuster is used to adjust the illumination intensity from the halogen lamp by adjusting the height of the halogen lamp according to that J_{SC} measured with the standard IV setup (Figure 4.2). A mechanical shutter and a filter with two different illumination intensities control dark and illumination conditions.

The shutter is open during measurement acquisition time to allow the filter-controlled illumination to reach the sample, while the shutter is closed between the different measurements to avoid heating effects. The filter then controls the illumination intensity. The first filter is used to provide dark conditions while the other filter provides full illumination conditions (100 % illumination).

The IVT measurements are performed at a temperature range of 320 – 50 K (with a step of 10 K) under vacuum conditions to avoid ice condensations at low temperatures. A calibrated Si diode temperature sensor mounted on a glass substrate (similar thickness to the glass substrate used for the solar cell fabrication) is used to deduce the temperature of the sample. The control of the temperature during the measurements is performed using a temperature controller as presented in Figure 4.7. A voltage sweep is used for the IVT measurements (using a Source-Meter) from a reverse bias voltage of -1.5 V to a forward bias voltage of 1.5 V with a step of 10 mV.

The same IVT setup is used for Capacitance measurements discussed in Section 4.4 and 4.5. The difference between the IVT and the Capacitance measurements is that for the IVT measurements, the solar cell is connected to a Source-Meter to record the IV data, while for the Capacitance measurements, the tool is connected to an LCR Precision meter.

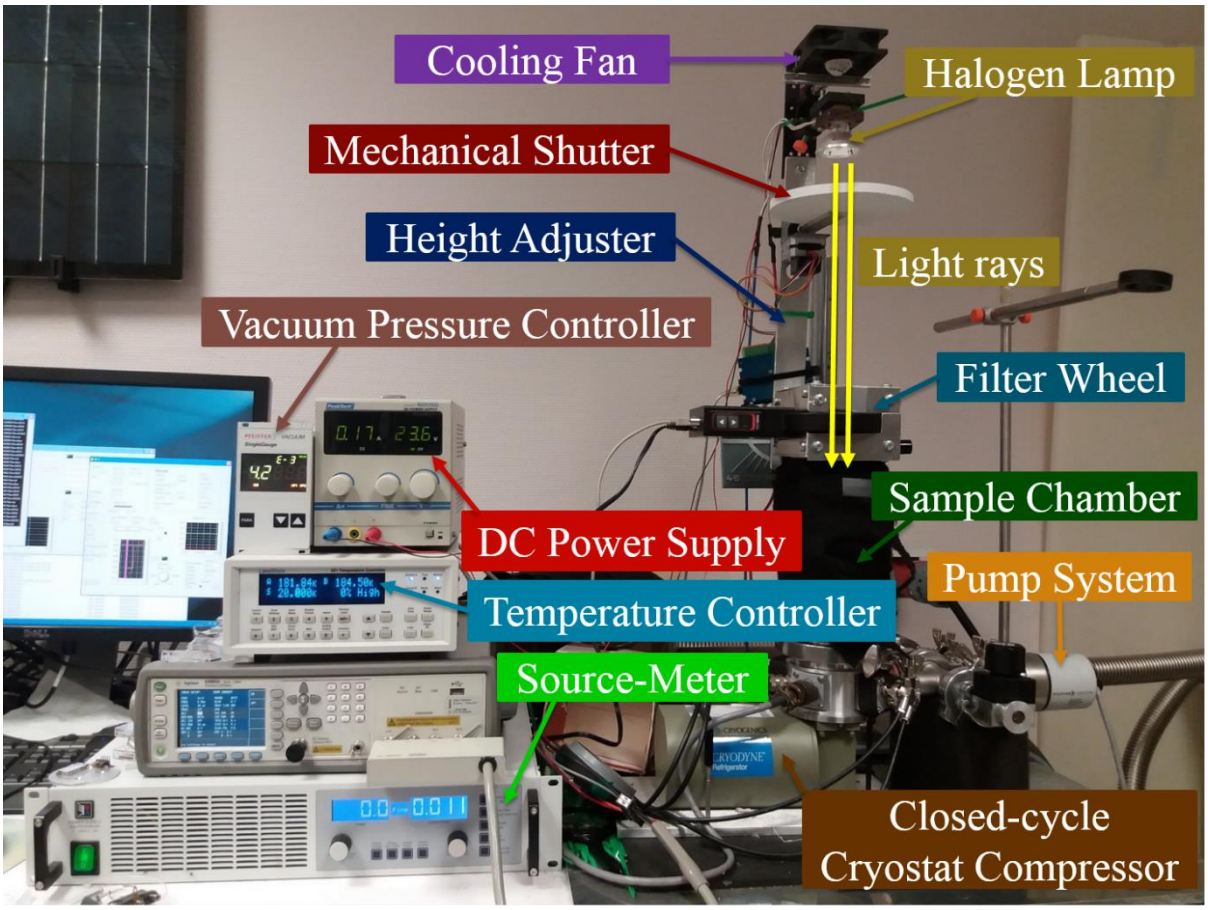

Figure 4.7: IVT setup. A halogen lamp is used for illumination with a cooling fan to avoid excessive heating conditions. A height adjuster is used to adjust the illumination intensity by adjusting the height of the lamp according to the J_{SC} measured by the standard IV setup. A mechanical shutter and a filter wheel are used to control illumination intensity from dark conditions to complete illumination intensity. A pump system is used to put the sample chamber under vacuum conditions with a vacuum pressure controller. A closed cycle cryostat generator is used to support the cooling process and the decrease of temperature down to 50 K. A temperature controller is used to control and monitor the temperature during measurements. A DC power supply is used to provide the voltage for the fan while a Source-Meter is used for supplying the modulation voltage of the measurements.

4.4 Doping Level Extraction

There are two types of capacitance measurements performed in this thesis. The first measurement is a capacitance measurement as a function of voltage and frequency at room temperature, referred to in this thesis as "CV measurements". The objective of this measurement is mainly to determine the doping as explained in this section. The other type of capacitance measurements is the measurement of capacitance as a function of temperature and frequency, referred to in this thesis as "Admittance or ADM measurements". At V = 0, admittance measurements are used to identify the main capacitance steps in the solar cell that could be related to either barriers or defects as explained in Section 4.5.

The capacitance (per unit area) can be defined as the ratio between the change in the charge density (ΔQ) to the change of the applied voltage (ΔV) as illustrated in Equation [4.13].

$$C = \frac{\Delta Q}{\Delta V} = \frac{dQ}{dV} \qquad [4.13]$$

As mentioned earlier in Section 4.1, most of the solar cells are based on a p-n junction. In this thesis, the p-side is the absorber layer and the n-side is the buffer and window layers. The interface region between these two semiconductors is the main region of interest playing a vital role in the quality and consequently the efficiency of the solar cell as discussed in Section 4.3. This interface region is called the space charge region (SCR). The width of this SCR (W_{SCR}) is defined in terms of the p-side (x_p) and the n-side (x_n) as expressed in Equation [4.14]:

$$W_{SCR} = x_p + x_n = \sqrt{\frac{2\varepsilon_0 \varepsilon_R V_{bi}}{q} \frac{N_A + N_D}{N_A N_D}} \qquad [4.14]$$

Where ε_0 is the permittivity in vacuum, ε_R is the dielectric constant of the semiconductor material, N_A is the doping density of acceptors, N_D is the doping density of donors and V_{bi} is the built-in voltage.

The built-in voltage (V_{bi}) is the potential difference between the Fermi level of the p-side and the Fermi level of the n-side in a solar cell and is related to the doping density of acceptors (N_A) and the doping density of donors (N_D) through Equation [4.15]:

$$V_{bi} = \frac{KT}{q} Ln\left(\frac{N_A N_D}{(N_i)^2}\right) \qquad [4.15]$$

Where N_i is the intrinsic carrier density.

For CI(G)S thin film solar cells, the doping of the n-side (donors from the n-type window layers) is much higher than the doping of the p-side (acceptors from the p-type absorber). Therefore, $N_D >> N_A$ and Equation [4.14] can be simplified as:

$$W_{SCR} \approx x_p \approx \sqrt{\frac{2\varepsilon_0 \varepsilon_{Rp} V_{bi}}{q\, N_A}}, \qquad x_n \approx 0 \qquad [4.16]$$

This means that the W_{SCR} extends much deeper to the lower doped side (the p-side) and the SCR capacitance (C_{SCR}) is dominated by the capacitance at the p-side of the SCR (C_{SCR}^{P}). It is important to note that here we are ignoring the buffer layer and we are assuming that the capacitance is dominated by one side (p-side).

Therefore, using Equations [4.13] and [4.16], the equation for the C_{SCR} is governed by the equation of the capacitance density for one-sided p-n junction under bias voltage and the C_{SCR} can be expressed as follows:

$$C_{SCR} \approx C_{SCR}^{P} = \frac{q\, N_A\, dx_p}{dV} = \sqrt{\frac{q\, \varepsilon_0 \varepsilon_{Rp}\, N_A}{2}} \left(V_{bi} - V_{app}\right)^{-1/2} \qquad [4.17]$$

Where $dQ = q\, N_A\, dx_p$, V_{bi} is the built-in voltage and V_{app} is the applied voltage. Equation [4.17] can be rearranged to be:

$$\frac{1}{C^2} = \frac{2}{q\, \varepsilon_0\, \varepsilon_{Rp}\, N_A} V = \frac{2}{q\, \varepsilon_0\, \varepsilon_{Rp}\, N_A} \left(V_{bi} - V_{app}\right) \qquad [4.18]$$

Equation [4.18] represents the well-known equation for the Mott-Schottky plot. The Mott-Schottky plot is then used to extract the built-in voltage and the doping. For the Mott-Schottky plot, the square inverse of the capacitance ($1/C^2$) is plotted on the Y-axis while the X-axis represents the applied bias voltage as illustrated in Figure 4.8. The built-in voltage is then the intersection of the plotted curve with the X-axis. The doping is extracted from the slope of the plotted curve (slope of Equation [4.18]) and the doping is expressed as:

$$N_A = \frac{-2}{q\ \varepsilon_0\ \varepsilon_{Rp} * Slope} \qquad [4.19]$$

It is important to note the following points:

- As I ignored the buffer layer from the equation of the C_{SCR} and assumed that the capacitance in the SCR is dominated by the capacitance at the p-side (absorber), I will use in this thesis the term "apparent doping" instead of "doping".
- The term "apparent doping" will be used throughout this thesis in order to remind myself that the extracted doping from the Mott-Schottky plot of the CV measurements could be influenced by the effect of the buffer layer as well as the effect of traps and defects.

The CV measurements are performed as a function of both voltage and frequency at room temperature. The apparent doping is then extracted from the slope of the Mott-Schottky plot, which represents the capacitance as a function of voltage at a specified frequency.

The choice of the frequency plays an important role in identifying the real doping. Generally, the frequency should be chosen high enough to avoid effects of traps or defects that would then be unable to follow the high frequency of the measurements. In this thesis, the frequency used for all the Mott-Schottky plots presented is the 100 KHz.

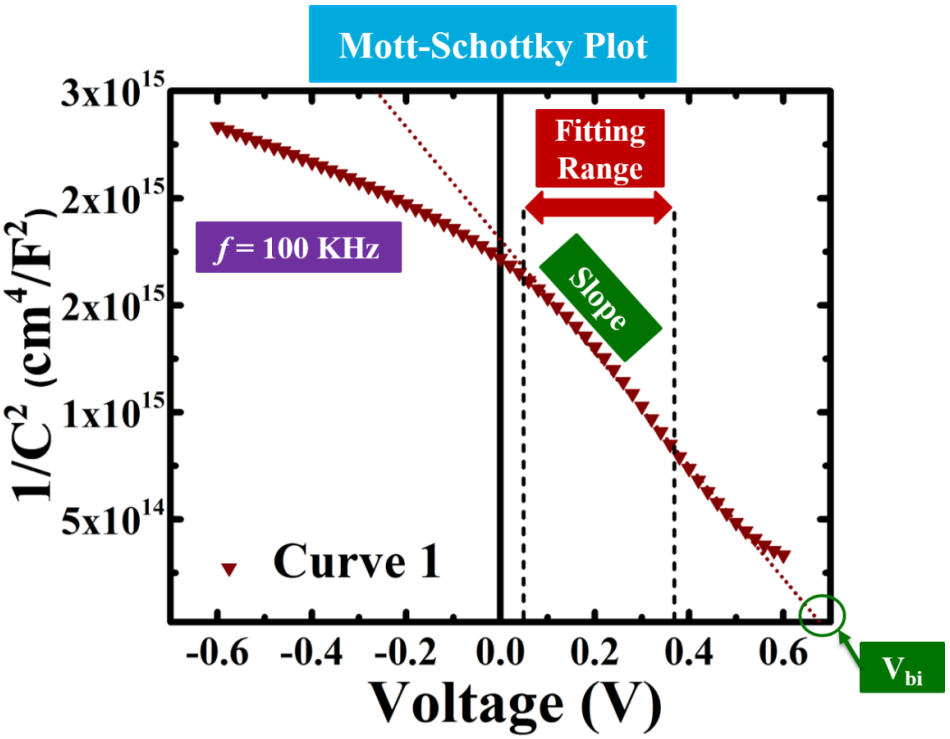

Figure 4.8: An illustration example for deducing the doping in a solar cell. The doping is extracted from the measurements of capacitance as a function of voltage and frequency through the Mott-Schottky plot. The Mott-Schottky plot represents the inverse square of the measured capacitance as a function of voltage (-0.6 V to 0.6 V) at a specified frequency. The frequency used for the Mott-Schottky plots in this thesis is 100 KHz. The fitting of the curve (red short dotted line) presented in the Mott-Schottky plots is performed at slight forward bias (0 V to 0.4 V) as indicated by the black short dashed lines. The intercept of the fitting with the X-axis indicates the built-in voltage. The doping is deduced from the slope of the curve using Equation [4.20].

Figure 4.8 illustrates the Mott-Schottky plot for one of the solar cells that will be presented in this thesis. The frequency used is 100 KHz as mentioned above. The voltage is swept from -0.6 to 0.6 V. There are two possible regions to fit a straight line to the curve of Figure 4.8: reverse-bias region or slight forward bias region (0 – 0.4 V).

In this thesis, the fitting of the Mott-Schottky plot curves is performed at slight forward bias region, as indicated by the short dashed lines in Figure 4.8, due to the following reasons:

- At reverse bias, the extracted doping is likely to represent the doping deeper in the absorber and could be influenced by diffusion from the buffer layer (Cd diffusion) making the doping level depth dependent [13]. At forward bias, the extracted doping should represent the doping in the SCR. We are interested in the doping of the SCR.

- At reverse or no bias, there is a strong band bending. If defects or trap states are present with this strong band bending, the defect level will cross the Fermi level within the SCR leading to a step in the capacitance response as illustrated in Figure 4.9a. The extracted doping at reverse bias will then be influenced by both the absorber doping (N_A) as well as the density of trap states (N_t). At forward bias, the bands become more flattened and the probability that the defect level crosses the Fermi level decreases as illustrated in Figure 4.9b.

Figure 4.9 represents the band diagram of a CIS solar cell when the conduction and valence bands are bent in Figure 4.9a (the case for reverse or no bias) and when the conduction and valence bands are more flattened in Figure 4.9b (the case for forward bias). It can be observed from Figure 4.9a that the conduction (blue) and valence (red) bands are strongly bent. The defect (gold colour) is then affected by this strong band bending and crosses the fermi level, E_{fp} (green) inside the SCR (purple). This crossing of the Fermi level (E_{fp}) causes a step in the capacitance response as explained later. On the other side, when the bands are more flattened as in the case of Figure 4.9b, the probability that the defect level crosses the fermi level (E_{fp}) decreases and the capacitance response becomes less affected by defect and trap states.

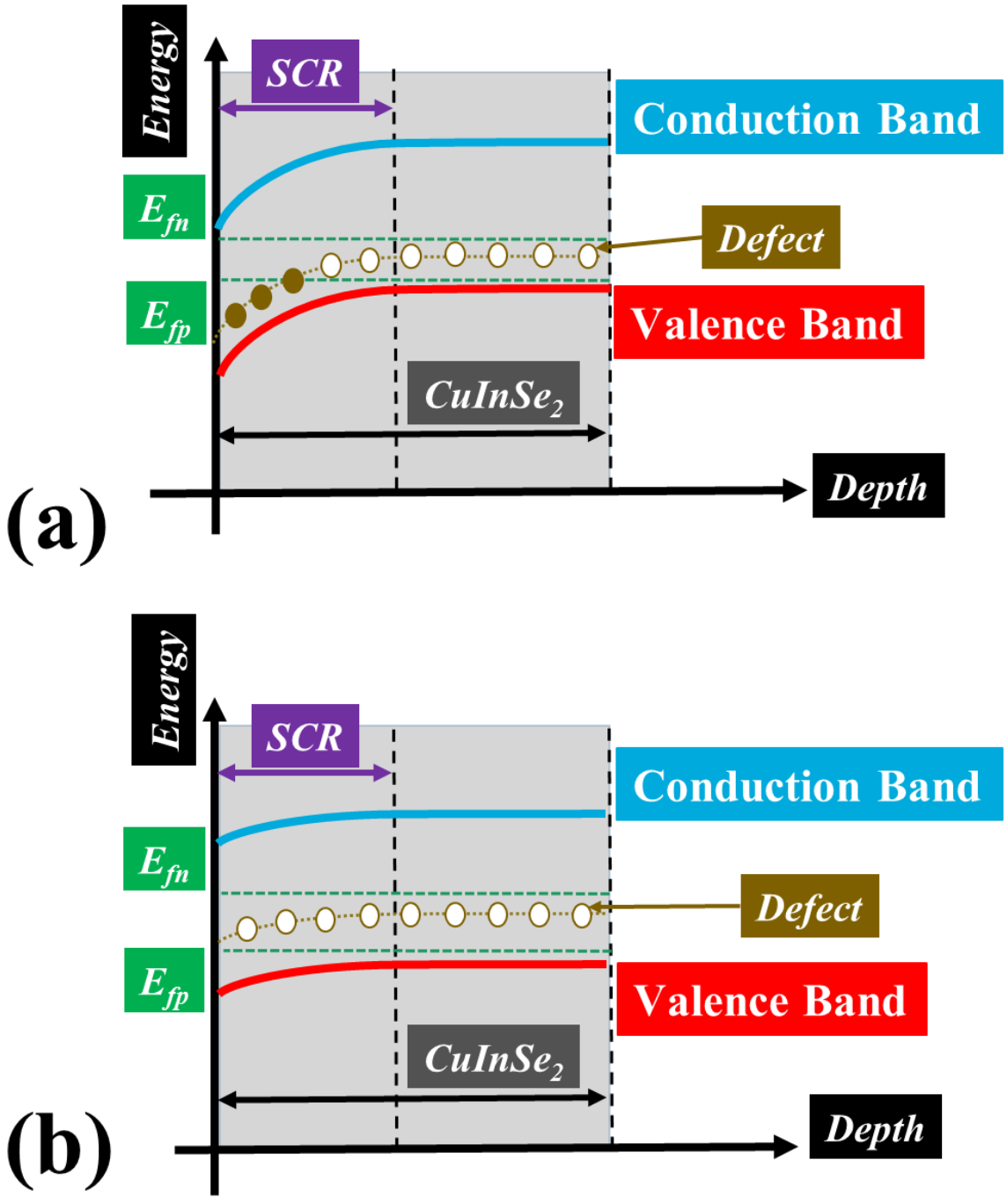

Figure 4.9: Band diagram of a CIS solar cell (adapted from Figure 4.6) representing the Energy on the y-axis as a function of the solar cell depth on the x-axis. The grey region represents the absorber (CIS) layer. The purple arrow represents the SCR. The gold colour circles represent a defect. The green dashed lines represent the fermi level on the p-side (E_{fp}) and the n-side (E_{fn}) respectively. The conduction (blue) and valence (red) bands are: a) strongly bent (in case of reverse or zero bias) where the defect level crosses the fermi level (E_{fp}) and b) more flattened (in case of forward bias) where the defect level does not cross the fermi level (E_{fp}).

The intercept of the fitting curve in the Mott-Schottky plot (short dotted line in Figure 4.8) with the X-axis represents the built-in voltage (V_{bi}) in the simplified case. The doping (N_A), will be named in this thesis as the apparent doping, is extracted from the slope of the fitting curve using Equation [4.19]. The values of $q, \varepsilon_0 \; and \; \varepsilon_R$ in Equation [4.19] are $1.602 \; x \; 10^{-19}$ coulombs, $8.854 \; x \; 10^{-12}$ F/m and 10 (ratio value) respectively.

The setup used for the CV measurements is similar to the setup used for the IVT measurements introduced in Figure 4.7 with replacing the Source-Meter with a Precision LCR Meter to record the capacitance data as presented in Figure 4.10. The sample is kept under dark conditions at room temperature (300 K) for at least 8 hours before any capacitance measurements (CV or admittance). The objective of keeping the sample under dark conditions for at least 8 hours is to avoid illumination or metastable effects and put the sample in equilibrium conditions. The CV measurements are performed with a voltage sweep ranging from -0.6 V on the reverse side to a voltage of 0.6 V at the forward bias (a step of 10 mV) under a small test voltage of 30 mV. The frequency is also varied between 100 – 1M Hz.

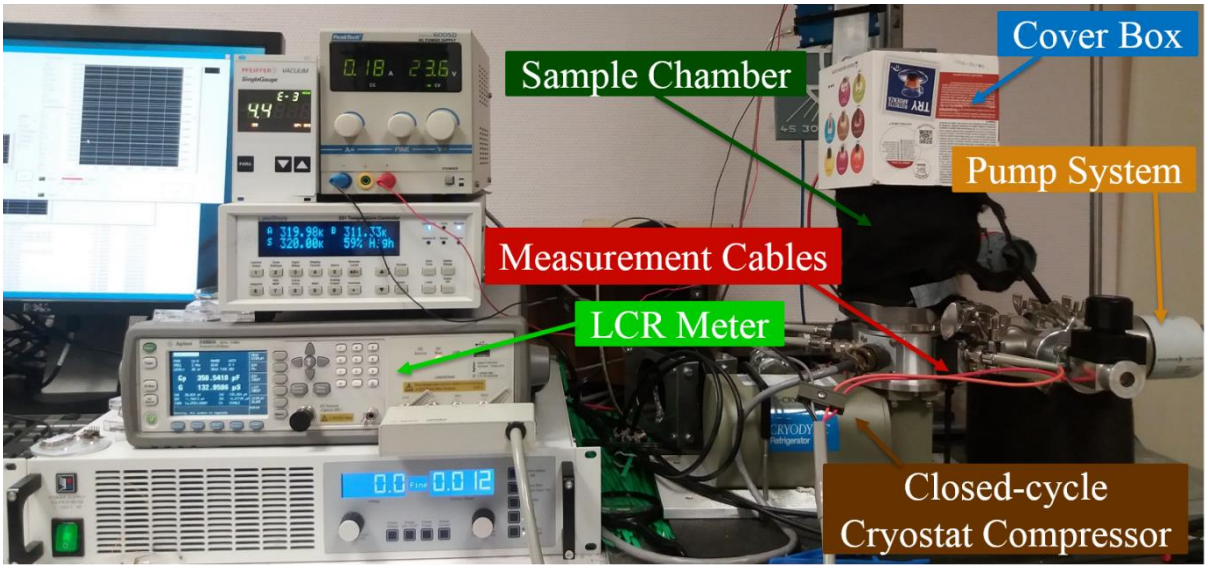

Figure 4.10: CV setup. This setup is the same like the one used for the IVT measurements in Figure 4.7. The only difference is replacing the Source-Meter (used to measure the IV data) with an LCR Precision Meter by changing the connecting cables as indicated by the red arrow. The sample is kept under dark for at least 8 hours before the CV measurements and is covered by an external box to provide maximum dark conditions.

4.5 Capacitance steps and defects

The second characterization technique used in this thesis based on the capacitance measurements is the admittance (ADM). The admittance measurements are helpful to identify the main capacitance steps in a solar cell that could be related to either barriers or defects. In principle, with the admittance measurements, we measure the response of the device under a small AC bias voltage as a function of changing the frequency and the temperature. With the admittance spectroscopy, we measure the admittance (Y), which is the complex conductance of a circuit. The admittance (Y) as a function of the angular frequency (ω), where ω = 2πf, is represented by Equation [4.20]:

$$Y\ (\omega) = G\ (\omega) + i\ S\ (\omega) = \ G\ (\omega) + i\ \omega\ C\ (\omega) \qquad [4.20]$$

The real part of Equation [4.20], G (ω), is the conductance (in-phase part of J/V) as a function of the angular frequency. The imaginary part of Equation [4.20], S (ω), is the susceptance as a function of the angular frequency. The capacitance is then extracted from the imaginary part of the admittance (C (ω) = S (ω) / ω) as presented in Equation [4.20]. From [5], the admittance, Y (ω), can be expressed as follows:

$$Y\ (\omega) = \left(1 - \frac{\tilde{x}_t}{x_{SCR}}\right)\frac{\omega^2 g_t}{f_0^2 + \ \omega^2} + i\ \omega\ \left[\frac{\varepsilon_0 \varepsilon_R}{x_{SCR}} + \left(1 - \frac{\tilde{x}_t}{x_{SCR}}\right)\frac{f_0 g_t}{f_0^2 + \ \omega^2}\right] \qquad [4.21]$$

Where $\tilde{x}_t$ is the intersect location between the deep defect and the Fermi level, x_{SCR} is the SCR width, g_t is the conductance due to deep defects and f_0 is the inflection frequency.

The capacitance is then the imaginary part of Equation [4.21] and can be expressed as:

$$C\ (\omega) = \left[\frac{\varepsilon_0 \varepsilon_R}{x_{SCR}} + \left(1 - \frac{\tilde{x}_t}{x_{SCR}}\right)\frac{f_0 g_t}{f_0^2 + \ \omega^2}\right] \qquad [4.22]$$

It can be observed from Equation [4.22] that at high frequencies, the capacitance drops to:

$$C\ (\omega) = \frac{\varepsilon_0 \varepsilon_R}{x_{SCR}} \qquad [4.23]$$

Based on the above discussion, it can be concluded that a capacitance step (capacitance drop) due to the presence of barriers, defects or trap states can be observed when measuring admittance from low to high frequencies.

The goal behind the admittance measurements is to identify the main capacitance steps where barriers or defects are likely to respond and study the electronic defect states in the semiconductor p-n junction [14, 15]. The admittance measurements will be combined with other characterization techniques to identify if those identified main capacitance steps correspond to barriers or defects as explained later in this section.

Before we discuss the capacitance steps in detail and how to identify these capacitance steps, it is important to provide some insights on the possible origins of such capacitance steps in any solar cell. The origin of the capacitance steps in admittance measurements can be attributed to:

1. Defects: Defects are considered one of the main causes to the drop in capacitance values as explained for Figure 4.9. The finite capture (emission) time constant of a defect level leads to the formation of distinct steps in the capacitance of the admittance spectrum. At a certain temperature, the defect response time defines the inflection frequency (f_0) of a certain capacitance step.
2. Barriers: Interface barriers (either at the back side with the back contact if the back contact is not ohmic or at the front side with the buffer and window layers) cause a thermal activation to the series resistance with decreasing temperature. The thermally activated series resistance acts as an additional element to the capacitance circuit with an additional R_S, leading to a decreasing step in the capacitance values [16, 17].
3. Carrier freeze-out: Carrier freeze-out means the freeze-out (decrease of free carrier concentrations) as the temperature decreases. In this case, as the temperature decreases, the electrons (holes) from the donor (acceptor) states will not be excited from the conduction (valence) band leading to a decrease in the number of free carriers. The absorber then acts as a dielectric and the solar cell behaves as a parallel plate capacitor. The capacitance value in this case can be calculated using Equation [4.24] and is referred to as the geometric capacitance ($C_{geometric}$).

$$C_{SCR} = C_{geometric} = \frac{\varepsilon_0 \varepsilon_R}{d} \qquad [4.24]$$

At $\varepsilon_0 = 8.854\,x\,10^{-12}$ F/m, $\varepsilon_R = 10$ and d = 2 – 3 μm, the geometric capacitance shall be about 3 – 5 nF/cm^2.

4. Mobility freeze-out: Mobility freeze-out means that the mobility decreases as the temperature decreases and the time constant for either the diffusion of carriers before the capture process or the drift of carriers after the emission process becomes higher than the time constant of the modulation voltage. The capacitance then eventually drops to the geometrical capacitance of the absorber (3 – 5 nF/cm^2).

An illustration example for the admittance spectrum is provided in Figure 4.11. Figure 4.11 represents the capacitance (per unit area) as a function of frequency and temperature. The temperature scale is presented on the right side of Figure 4.11 and is the same temperature scale for all the admittance spectra presented in this thesis. The temperature scale indicates the decrease of the temperature from red curves (320 K) to purple curves (50 K).

Two black dashed lines in Figure 4.11 identify three different capacitance regions:

- A high temperature region (Step 1) in the range of 320 – 200 K
- An intermediate temperature region (Step 2) in the range of 200 – 100 K
- A low temperature region (Step 3) in the range of 100 – 50 K

It can be observed from Figure 4.11 that the high temperature region (Step 1) represents a step that is likely to increase at lower frequencies and higher temperatures. This step shows a broad capacitance dispersion. This dispersion could be related to a broad deep defect, tail states or in-homogeneities recognized at lower frequencies and higher temperatures (outside our measurement range). However, capacitance steps at frequencies lower than 100 Hz indicate a weak recombination activity even at room temperature. In this thesis, this high temperature capacitance step (Step 1) could not be resolved within our measurement range.

For the low temperature region (Step 3), a capacitance step could be observed in Figure 4.11 at very low temperatures (50 – 80 K). This capacitance step reaches a value close to the geometric capacitance of the absorber (3 – 5 nF/cm^2) as indicated by the red dotted line and the red circle in Figure 4.11. This behaviour of capacitance values close to the geometric capacitance of the absorber for Step 3 applies to all the admittance spectra presented in this thesis. Therefore, this low temperature capacitance step (Step 3) will be attributed to freeze-out (carrier or mobility freeze-out). The identification of this step as a carrier or mobility freeze-out is not within the scope of this thesis.

The intermediate temperature region (Step 2) is the main capacitance step for the solar cells presented in this thesis. This capacitance step is not attributed to carrier or mobility freeze-out as the capacitance values are much higher than the geometric capacitance (3 – 5 nF/cm^2). The activation energy of this capacitance step can be resolved from the Arrhenius plot explained below. Therefore, this capacitance step (Step 2) could be attributed to either an interface barrier or a defect. To identify this capacitance step (Step 2) as a barrier or a defect, a comparison between the activation energy extracted from the Arrhenius plot of the capacitance step (explained below) and the activation energy deduced from the series resistance as a function of temperature (Equation [4.12] in Section 4.3) is performed as follows:

- If the activation energy from the series resistance as a function of temperature is close to the activation energy from admittance measurements, then the corresponding capacitance step is attributed to a barrier [18, 19].
- If the activation energy of the series resistance as a function of temperature is lower than the activation energy extracted from admittance measurements, then the corresponding capacitance step is attributed to a defect [19, 20]. This defect could then be an interface or a bulk defect. The identification between an interface and a bulk defect will be discussed in Section 7.1.

Therefore to sum up, the high temperature region (Step 1) is generally not resolved and the low temperature region (Step 3) is attributed to a freeze-out. The intermediate temperature region (Step 2) is the main focus of this thesis and is attributed to either a barrier or a defect.

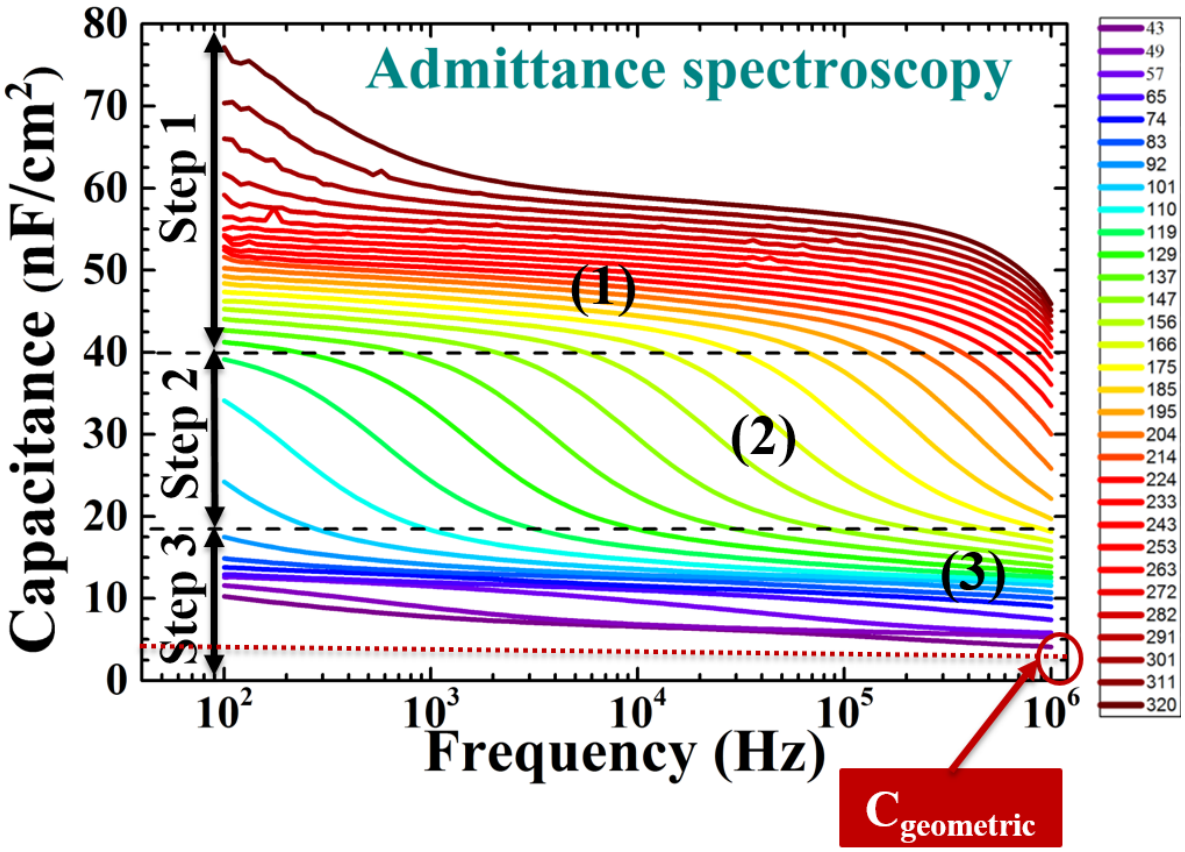

Figure 4.11: An illustration example for admittance measurements. This figure represents the capacitance as a function of frequency and temperature. The frequency measurement range is 100 Hz – 1 MHz. The temperature measurement range is 320 K – 50 K as indicated by the temperature scale on the right side of the figure. The admittance measurements were performed from high to low temperatures. The black dashed lines identify three different capacitance steps regions: a high temperature (Step 1), an intermediate temperature (Step 2) and a low temperature (Step 3) capacitance step regions. The geometric capacitance of the absorber has a value in the range of 3 – 5 nF/cm^2 as indicated by the red dotted line. The capacitance values for the low temperature capacitance step (Step 3) approaches the values of the absorber geometric capacitance.

The activation energy of the main capacitance step (Step 2 in this thesis) can be calculated based on the following steps:

- The capacitance values are divided by the area of the device and calculated as in Equation [4.25] and as presented in Figure 4.11:

$$C\ (\frac{nF}{cm^2}) = \frac{C_{measured}}{A} \qquad [4.25]$$

- The derivative of the capacitance (per unit area) from Equation [4.25] is multiplied with the angular frequency (ω) and plotted versus the angular frequency (ω) as presented in Figure 4.12a for the corresponding temperatures of the main capacitance step (Step 2).
- The frequencies of the inflection points (maximum peak of the derivative) are extracted from the derivative plot as illustrated as an example in Figure 4.12a (green arrows).

These extracted inflection frequency points represent the inflection frequencies of the main capacitance drop (main capacitance step) that could be attributed to either defects or barriers. The activation energy of this capacitance step (E_a) can be calculated from the inflection frequency (f_0) using Equation [4.26]:

$$f_o = v_0 \exp\left(-\frac{E_a}{K\,T}\right) \qquad [4.26]$$

where v_0 is the attempt-to-escape frequency. This attempt-to-escape frequency (v_0) represents the product of the capture cross section of the defect, the effective density of states and the thermal voltage. The effective density of states and the thermal voltage are temperature dependent. Therefore, the attempt-to-escape frequency (v_0) could be written as a function of temperature as presented in Equation [4.27]:

$$v_o = 2\xi_0 * T^2 \qquad [4.27]$$

where ξ_0 is a pre-factor that includes the effective density of states, the thermal voltage and the capture cross section of defects.

Substituting Equation [4.27] into Equation [4.26] and re-arranging Equation [4.26], the inflection frequency can be expressed as follows:

$$Ln\left(\frac{f_0}{T^2}\right) = Ln\,(\,2\,\xi_0\,) - \frac{E_a}{K} * \frac{1}{T} \qquad [4.28]$$

where K is the Boltzmann's constant with a value of $8.617 \cdot 10^{-5}$ eV/K.

- The inflection frequency points that were extracted from Figure 4.12a are inserted in Equation [4.28] and a corresponding Arrhenius plot is then produced. This Arrhenius plot presents the frequency of the inflection points on the Y-axis $Ln\left(\frac{f_0}{T^2}\right)$ versus the inverse of the temperature (temperatures corresponding to the inflection frequency peaks) on the X-axis $\left(\frac{1}{T}\right)$ as illustrated in Figure 4.12b.
- The activation energy of the main capacitance step (E_a) is then deduced from the slope of the Arrhenius plot (Figure 4.12b) using Equation [4.28] by multiplying the slope with (- K).
- The pre-factor (ξ_0) can be extracted from the intercept of the curve in Figure 4.12b with the X-axis (at X = 0) using Equation [4.29].

$$\xi_0 = \frac{\exp(Intercept\ with\ X-axis)}{2} \qquad [4.29]$$

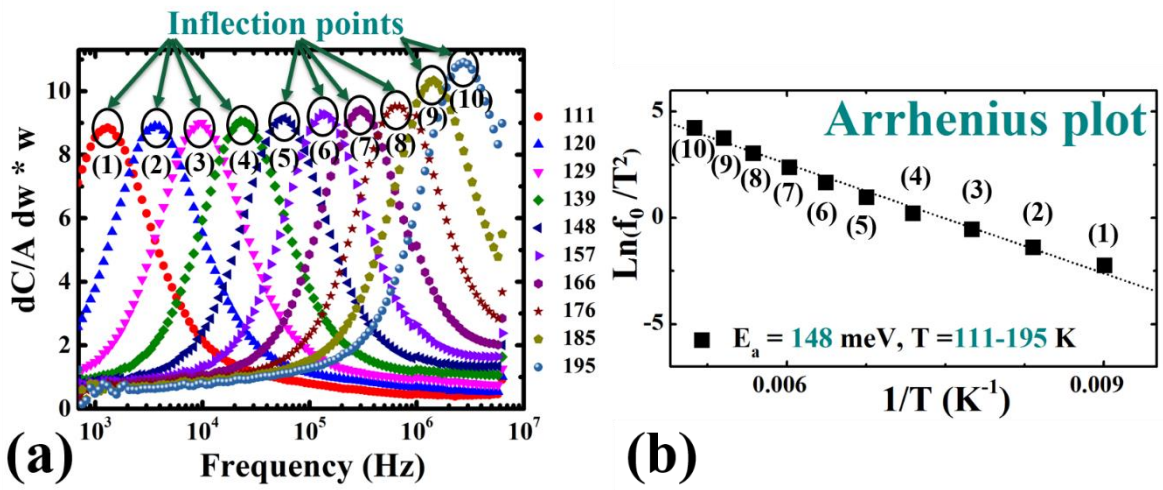

Figure 4.12: An illustration example for extracting the activation energy of the main capacitance step (Step 2) from the admittance measurements. a) The inflection frequency peak points are deduced from the derivative of the capacitance spectrum presented in Figure 4.11 as a function of frequency. The temperatures where these curves were measured are indicated on the right side of a). b) The Arrhenius plot with the points of the inflection frequencies deduced from a) as a function of temperature. Each number in b) represents the corresponding inflection frequency peak point in a). The activation energy of the capacitance step is then deduced from the slope of the Arrhenius plot using Equation [4.29].

The setup used for the admittance measurements is the same like the setup used for the CV measurements presented in Figure 4.10. Admittance measurements are performed as a function of frequency from 100 Hz – 1 MHz and as a function of temperature from 320 – 50 K at zero bias voltage and at a modulation voltage of 30 mV. Similar to the CV measurements, the device is kept under dark conditions for at least 8 hours to eliminate metastablities and put the device under an equilibrium state.

References Chapter 4

[1] D. Abou-Ras, T. Kirchartz, and U. Rau, "Advanced Characterization Techniques for Thin Film Solar Cells", WILEY-VCH Verlag GmbH & Co. KGaA, (2011).

[2] T. Weiss, "Doping, Electrical characterization of Kesterite thin film absorbers and solar cells", PhD Thesis (2015). Available at https://orbilu.uni.lu/bitstream/10993/23357/1/thomas_weiss_dissertation.pdf

[3] R. Scheer and H. W. Schock, "Chalcogenide Photovoltaics", Wiley-VCH (2011).

[4] P. Blood and J. W. Orton, "The Electrical Characterization of Semiconductor: Majority Carriers and Electron States", Academic Press (1992).

[5] T. Bertram, "Doping, Defects and Solar Cell Performance of Cu-rich Grown $CuInSe_2$", PhD Thesis (2016). Available at http://orbilu.uni.lu/handle/10993/28325

[6] American Society for Testing and Materials (ASTM) G-173-03, International standard ISO 9845-1 (1992).

[7] A. R. Burgers, J. A. Eikelboom, A. Schonecker and W. C. Sinke, "Improved treatment of the strongly varying slope in fitting solar cell i-v curves", Proceedings of the 25th IEEE photovoltaic specialists conference, pp. 569 – 572 (1996).

[8] W. Shafarman and L. Stolt, "$Cu(In,Ga)Se_2$ solar cells," in Handbook of photovoltaic science and engineering, John Wiley and Sons (2003).

[9] R. Carron, C. Andres, E. Avancini, T. Feurer, S. Nishiwaki, S. Pisoni, F. Fu, M. Lingg, Y. E. Romanyuk, S. Buecheler, A. N. Tiwari, "Bandgap of thin film solar cell absorbers: A comparison of various determination methods", Thin Solid Films, 669, 1, pp. 482-486 (2019).

[10] R. Scheer, "Activation energy of heterojunction diode current in the limit of interface recombination", Journal of Applied Physics, 105:104505 (2009).

[11] T. Hölscher, S. Förster, T. Schneider, M. Maiberg, W. Widdra, R. Scheer, "Light induced degradation of $Cu(In,Ga)Se_2$ thin film surfaces", Applied Physics Letters, 111, 011604 (2017).

[12] T. P. Weiss, A. Redinger, J. Luckas, M. Mousel and S. Siebentritt, "Admittance spectroscopy in kesterite solar cells: defect signal or circuit response", Applied Physics Letters, 102(20):202105 (2013).

[13] F. Werner, T. Bertram, J. Mengozzi, S. Siebentritt, "What is the dopant concentration in polycrystalline thin-film $Cu(In,Ga)Se_2$?", Thin Solid Films, 633: 222 (2017).

[14] D. L. Losee, "Admittance spectroscopy of impurity levels in Schottky barriers", Journal of Applied Phy, 46:2204 – 2214 (1975).

[15] F. Werner and S. Siebentritt, "Buffer Layers, Defects, and the Capacitance Step in the Admittance Spectrum of a Thin-Film Solar Cell", Phys. Rev. Applied American Physical Society, 9: 054047 (2018).

[16] J. H. Scofield, "Effects of series resistance and inductance on solar cell admittance measurements", Solar Energy Materials and Solar Cells, 37:217 – 233 (1995).

[17] T. Eisenbarth, T. Unold, R. Caballero, C. A. Kaufmann and H. W. Schock, "Interpretation of admittance, capacitance-voltage, and current-voltage signatures in Cu(In,Ga)Se_2 thin film solar cells", Journal of Applied Physics, 107:034509 (2010).

[18] T. P. Weiss, A. Redinger, J. Luckas, M. Mousel and Susanne Siebentritt, "Admittance spectroscopy in kesterite solar cells: defect signal or circuit response", Applied Physics Letters, 102(20):202105 (2013).

[19] F. Werner, M. H. Wolter, S. Siebentritt, G. Sozzi, S. D. Napoli, R. Menozzi, P. Jackson, W. Witte, R. Carron, E. Avancini, T. Weiss and S. Buecheler, "Alkali treatments of Cu(In,Ga)Se_2 thin-film absorbers and their impact on transport barriers", Prog Photovolt Res Appl., 1 – 13 (2018).

[20] C. Schubbert, P. Eraerds, M. Richter, J. Parisi, I. Riedel, T. Dalibor, J. Palm, "A simulation study on the impact of band gap profile variations and secondary barriers on the temperature behavior, performance ratio, and energy yield of Cu(In,Ga)$(Se,S)_2$ solar cells", physica status solidi (a), 212: 336-347 (2015).

Chapter 5: Cu-rich versus Cu-poor CI(G)S thin film solar cells

Chapter 5 introduces the characteristics of Cu-rich CIS and CIGS absorbers and cells and compares them to their corresponding Cu-poor ones. Section 5.1 provides a short introduction on the physical properties of Cu-rich absorbers in terms of grain size and elemental composition before focusing on the electrical characteristics in the remaining sections of this chapter. Section 5.2 highlights the electrical characteristics of Cu-rich and Cu-poor CI(G)S solar cells in terms of IV as well as the opto-electronic characteristics in terms of EQE. This section presents the lower conversion efficiency of Cu-rich cells compared to their corresponding Cu-poor solar cells as a result of their high deficits in terms of both open circuit voltage (V_{OC}) and Fill Factor (FF). Section 5.3 identifies the dominant recombination path in Cu-rich and Cu-poor cells. In Cu-rich CI(G)S solar cells, the dominant recombination path is at the absorber/buffer front interface while in Cu-poor CI(G)S solar cells, the dominant recombination path is in the absorber bulk. Section 5.4 discusses the differences in apparent doping and defects deduced from admittance measurements with their corresponding activation energies between Cu-rich and Cu-poor CI(G)S solar cells. Cu-rich CI(G)S cells are characterized by their higher apparent doping compared to Cu-poor CI(G)S cells. Moreover, Cu-rich CIS cells are characterized by a defect with an activation energy of 200 ± 20 meV. The nature of this defect will be revealed in Chapter 7. Passivating this 200 ± 20 meV defect in Cu-rich CIS cells using post-deposition treatments (PDTs) presented in Chapter 6 indicated the presence of another defect with an activation energy of 130 ± 15 meV that is present before and after the PDT. This defect can be attributed to the A3 acceptor normally related to Indium vacancy. Cu-poor CIS cells are characterized by a defect with an activation energy of 130 ± 15 meV that can be also attributed to the A3 acceptor defect. For Cu-rich CIGS solar cells, the same defect with an activation energy of 130 ± 15 meV is observed up to bandgaps of 1.2 eV before the activation energy of the main capacitance step from admittance measurements decreases. For Cu-poor CIGS solar cells, the activation energy of the main admittance capacitance step decreases with increasing the bandgap.

5.1 Physical characteristics of Cu-rich CI(G)S

Cu-rich CIS absorber is by definition, a stoichiometric bulk phase plus additional copper selenide secondary phases [1] as explained in Section 2.4. Section 2.4 discussed the advantages of Cu-rich absorbers over Cu-poor [2 – 7]. One of these advantages of Cu-rich absorbers is explained in terms of grain sizes that are larger for Cu-rich compared to Cu-poor as presented with CIS as an example in Figure 5.1 for top-view [Figure 5(a, b)] as well as cross-section [Figure 5(c, d)].

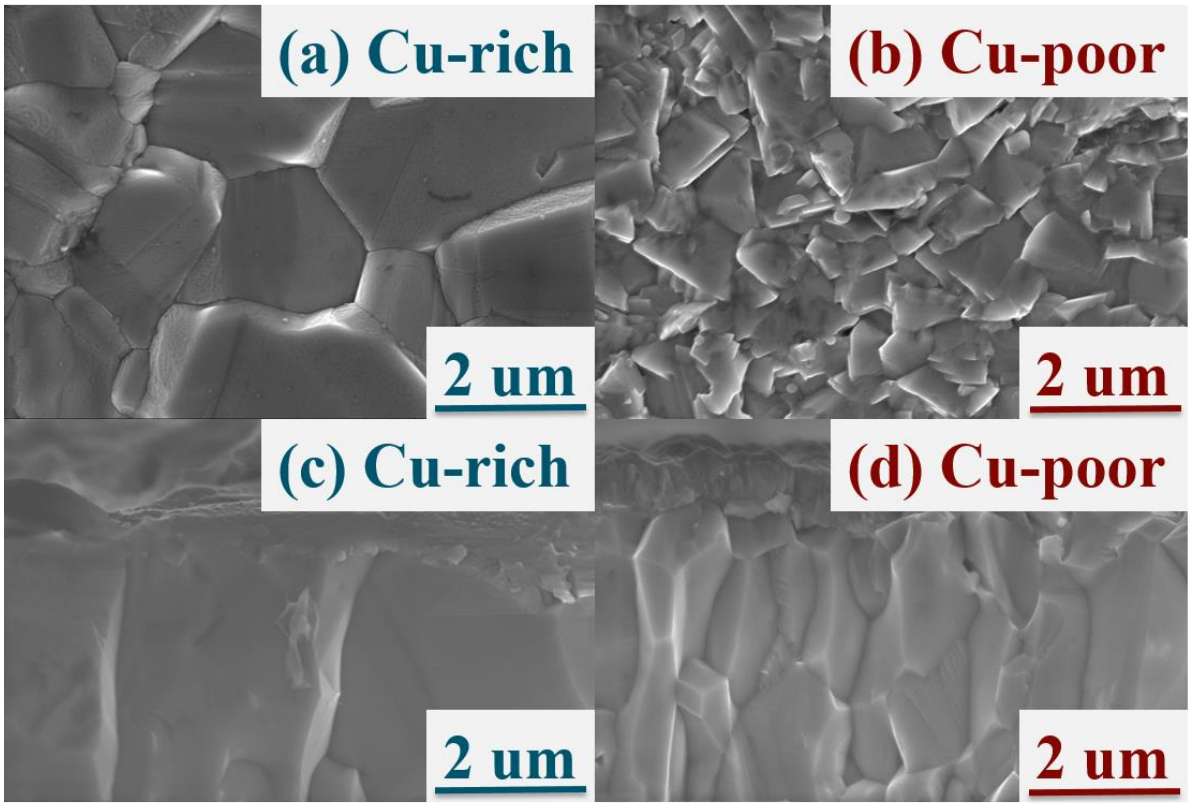

Figure 5.1: SEM top-view for a) Cu-rich and b) Cu-poor and cross-section for c) Cu-rich and d) Cu-poor CIS absorbers

However, to develop solar cells based on these absorbers, an etching step is mandatory for Cu-rich absorbers to remove the conductive secondary phases as discussed in sub-sections 3.1.1 and 3.2.1 [8 - 9]. The etching step is performed using potassium cyanide (KCN) either with a weak KCN etching of 5 % aqueous KCN solution for 30 seconds or with a strong KCN etching of 10 % aqueous KCN solution for 5 minutes.

It is important to note that for Cu-poor solar cells, a diode behaviour can still be achieved without an etching step but using a KCN weak etching step helps in further improving the electrical performance of such cells by removing additional remaining oxides. On the other side, processing Cu-rich absorbers with no etching or with a weak KCN etching is not sufficient to remove the copper selenide secondary phases and achieve a diode behaviour. A strong KCN is then mandatory removing copper selenide secondary phases and obtaining a diode behaviour. Therefore, in this thesis, a weak KCN etching step was used for Cu-poor absorbers while a strong KCN etching step was used for Cu-rich ones.

Several CI(G)S absorbers were grown within the work of this thesis. Cu-poor CI(G)S absorbers were fabricated under Cu-deficiency with a Cu/(III) ratio in the range of 0.7 – 1.0, while Cu-rich CI(G)S absorbers were grown under Cu-excess with a Cu/(III) ratio in the range of 1.0 – 3.0. It is important to note that the KCN strong etching was successful in removing copper selenide secondary phases from Cu-rich absorbers with all different Cu/(III) ratios leading to a Cu/(III) ratio of 1.0 ± 7 % after etching. Table 5.1 indicates the effect of KCN etching on both Cu-rich (KCN strong) and Cu-poor (KCN weak) absorbers on one of the Cu-rich and Cu-poor CI(G)S absorbers. While the Cu/III ratio for Cu-poor CI(G)S absorbers is nearly the same before and after etching, Cu/III ratio for Cu-rich CI(G)S absorbers decreased to stoichiometric values (1.0 ± 7 %) indicating the removal of the copper selenide secondary phases.

Table 5.1 EDX ratio for one of Cu-rich and Cu-poor CI(G)S absorbers before and after KCN etching

Sample	Cu-ratio (at. %)	III-ratio (at. %)	Se-ratio (at. %)	Cu/III ratio
Cu-poor before etching	22.8	25.5	51.7	0.89
Cu-poor after etching	23.4	25.8	50.7	0.91
Cu-rich before etching	29.5	22.1	48.4	1.30
Cu-rich after etching	25.8	24.5	49.7	1.0 ± 7 %

5.2 V_{OC} deficit and collection efficiencies in CI(G)S solar cells

As explained above, several CI(G)S absorber runs were performed. About 100 CIS and 50 CIGS absorber runs were completed and characterized by IV within this thesis. As explained in Section 4.1, the main electrical parameters are extracted from IV characteristics. An example for CIS IV characteristics is presented in Figure 5.2a, while Figure 5.2b presents an example for IV characteristics of CIGS solar cells. The electrical parameters extracted from IV measurements are summarized in Table 5.2. The values for series and shunt resistances in Table 5.2 were extracted by fitting the dark curve of the IV characteristics with a single diode model using an ECN fitting program as described in [10].

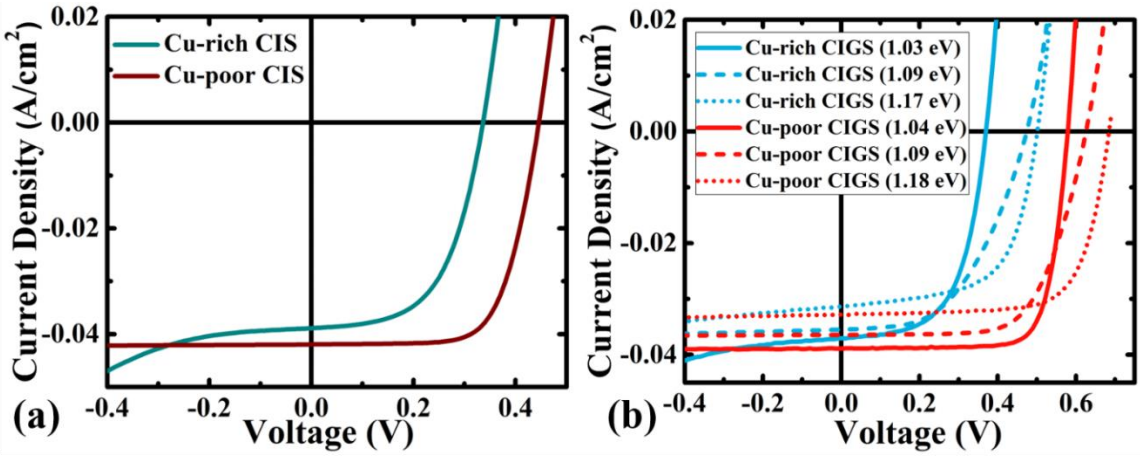

Figure 5.2: IV characteristics of a) Cu-rich and Cu-poor CIS and b) Cu-rich and Cu-poor CIGS solar cells with different bandgaps measured under light conditions.

Table 5.2 IV parameters of Cu-rich and Cu-poor CI(G)S with different bandgap energies.

Sample	Efficiency (%)	FF (%)	V_{OC} (mV)	J_{SC} (mA/cm^2)	R_S (Ω.cm^2)	R_{Sh} (Ω.cm^2)
Cu-rich CIS	7.5 ± 1.5	45.0 ± 5.0	340 ± 20	40.0 ± 2.0	0.4 ± 0.1	100 ± 50
Cu-poor CIS	12.5 ± 1.5	70.0 ± 5.0	440 ± 20	42.0 ± 2.0	0.4 ± 0.1	2000 ± 1000
Cu-rich CIGS (1.03 eV)	8.14	59.4	370	37.0	0.24	206
Cu-poor CIGS (1.04 eV)	17.3	77.0	578	38.9	0.2	13182
Cu-rich CIGS (1.09 eV)	8.5	50.3	474	35.5	0.2	250
Cu-poor CIGS (1.09 eV)	15.1	66.1	626	36.4	0.2	3129
Cu-rich CIGS (1.17 eV)	9.7	62.0	501	31.5	0.4	269
Cu-poor CIGS (1.18 eV)	16.2	72.0	685	33.0	0.2	1345

Based on Figure 5.2a, it can be observed that Cu-rich CIS cells suffer from strong V_{OC} and FF deficit compared to Cu-poor cells as also reported [2, 9]. This is reflected on the electrical parameters of CIS extracted in Table 5.2 representing the statistics of all the CIS cells measured in this thesis. From Table 5.2, it can be realized that the average efficiency of Cu-rich CIS cells is in the range of 7.5 ± 1.5 % much less than that of Cu-poor CIS that is in the range of 12.5 ± 1.5 %. This strong decrease in efficiency is attributed mainly to a significant decrease in the V_{OC} and the FF. Average values for V_{OC} in Cu-rich CIS cells is in the range of 340 ± 20 mV about 100 mV less than that of Cu-poor cells that are in the range of 440 ± 20 mV. Moreover, a deficit of around 15 % in FF is observed between Cu-rich (45.0 ± 5.0 %) and Cu-poor (70.0 ± 5.0 %) CIS solar cells. This deficit in FF can be explained in terms of shunt resistances that are significantly lower for Cu-rich CIS cells compared to Cu-poor cells as presented in Table 5.2 while the series resistance is fairly constant in both Cu-rich and Cu-poor CIS cells. These lower values of shunt resistances in Cu-rich CIS had been analysed and were explained in terms of space charge limited current [11] that leads to non-linear shunt behaviour. The origin of this non-linear shunt behaviour was found to be located at the front interface (absorber/buffer) [11]. Moreover, this non-linear shunt is also responsible for the breakdown behaviour observed in reverse-bias voltage for Cu-rich CIS solar cells (green curve in Figure 5.2a) and not observed for Cu-poor CIS solar cells (red curve in Figure 5.2a) [11].

On the other side, the introduction of Ga to the ternary CIS forming the quaternary CIGS plays a significant role on the electrical performance of CIGS solar cells. As the amount of introduced Ga increases, the bandgap of the formed absorber phase increases leading to a corresponding increase in the V_{OC} and decrease in the short circuit current density (J_{SC}). Figure 5.2b illustrates examples of Cu-rich (blue curves) and Cu-poor (red curves) CIGS cells with different bandgaps. The bandgap was extrapolated from the linear extrapolation of the EQE measurements as explained below. The cells presented in Figure 5.2b were chosen in order to illustrate two points. The first point is to show the trend of increasing bandgaps and its effect on the electrical performance of both Cu-rich and Cu-poor CIGS solar cells. The other point is to compare the IV characteristics between Cu-rich and Cu-poor CIGS cells of similar bandgaps. The electrical parameters of those cells are extracted and presented in Table 5.2.

Figure 5.2b illustrates that Cu-rich CIGS solar cells suffer from V_{OC} and FF deficits compared to Cu-poor cells [12] similar to the behaviour of CIS cells. Indeed, the more we add Ga, the more the bandgap increases with a corresponding increase in the V_{OC} for Cu-rich (370 to 474 to 501 mV) and for Cu-poor (578 to 626 to 685 mV) CIGS solar cells. However, the V_{OC} deficit between Cu-rich and Cu-poor CIGS cells is in the range of 150 – 200 mV. This V_{OC} deficit was previously observed and was explained in terms of interface recombination at the absorber/buffer surface [13], relatively high absorber doping [14] or due to the absence of an ordered defect compound at the Cu-rich absorber surface [15 - 16].

A strong FF deficit is also observed between Cu-rich and Cu-poor CIGS cells in the range of 10 – 20 % as presented in Table 5.2. This FF deficit between Cu-rich and Cu-poor CIGS cells decreases with the addition of Ga improving from 18 to 16 to 10 % for bandgaps of 1.04, 1.09 and 1.18 eV respectively. Similar to CIS, the FF deficit can be attributed to the shunt resistances in Cu-rich CIGS cells that deteriorate the FF of such cells, while the series resistance is fairly constant as presented in Table 5.2. It is interesting to note that the breakdown behaviour normally observed for Cu-rich CIS at reverse bias voltages and attributed to space charge limited current [11] is still observed for Cu-rich CIGS cells (CIGS with bandgap of 1.03 eV in Figure 5.2b) but improves with the addition of Ga. The V_{OC} and FF deficits in Cu-rich CIGS cells are the main responsible for the reduced efficiency of such cells (presented in Table 5.2) compared to Cu-poor CIGS solar cells.

The J_{SC} values decrease with the addition of Ga and the increase of the bandgap. The J_{SC} values for Cu-rich cells decreased from 40.0±2.0 mA/cm^2 for the pure CIS with a bandgap of 0.995 eV to 37.0, 35.5 and 31.5 mA/cm^2 with the addition of Ga for bandgaps of 1.03, 1.09 and 1.17 eV respectively. A similar trend is observed for Cu-poor CI(G)S cells where the J_{SC} decreased from 42.0 ± 2.0 to 38.9, 36.4 and 33.0 mA/cm^2 for bandgaps of 0.95, 1.04, 1.09 and 1.18 eV respectively as presented in Table 5.2. From these values, it can be observed that the J_{SC} of Cu-rich CI(G)S cells is less than that of Cu-poor CI(G)S cells by around 1 – 2 mA/cm^2. It was then expected that the collection efficiencies of Cu-poor CI(G)S cells is better than that of Cu-rich CI(G)S cells. However, the EQE measurements below proved the opposite for CIS showing that Cu-rich CIS cells have better collection efficiencies compared to their Cu-poor CIS solar cells.

EQE measurements reflect important characteristics on the optoelectronic performance of both Cu-rich and Cu-poor cells as will be depicted from Figure 5.3. Figure 5.3a presents the EQE spectra for Cu-rich and Cu-poor CIS (same cells presented in Figure 5.2a) while Figure 5.3b presents the EQE response of Cu-rich and Cu-poor CIGS (same cells presented in Figure 5.2b). An overview of the effect of adding Ga on the EQE response of Cu-rich and Cu-poor solar cells is illustrated in Figure 5.3c and 5.3d respectively.

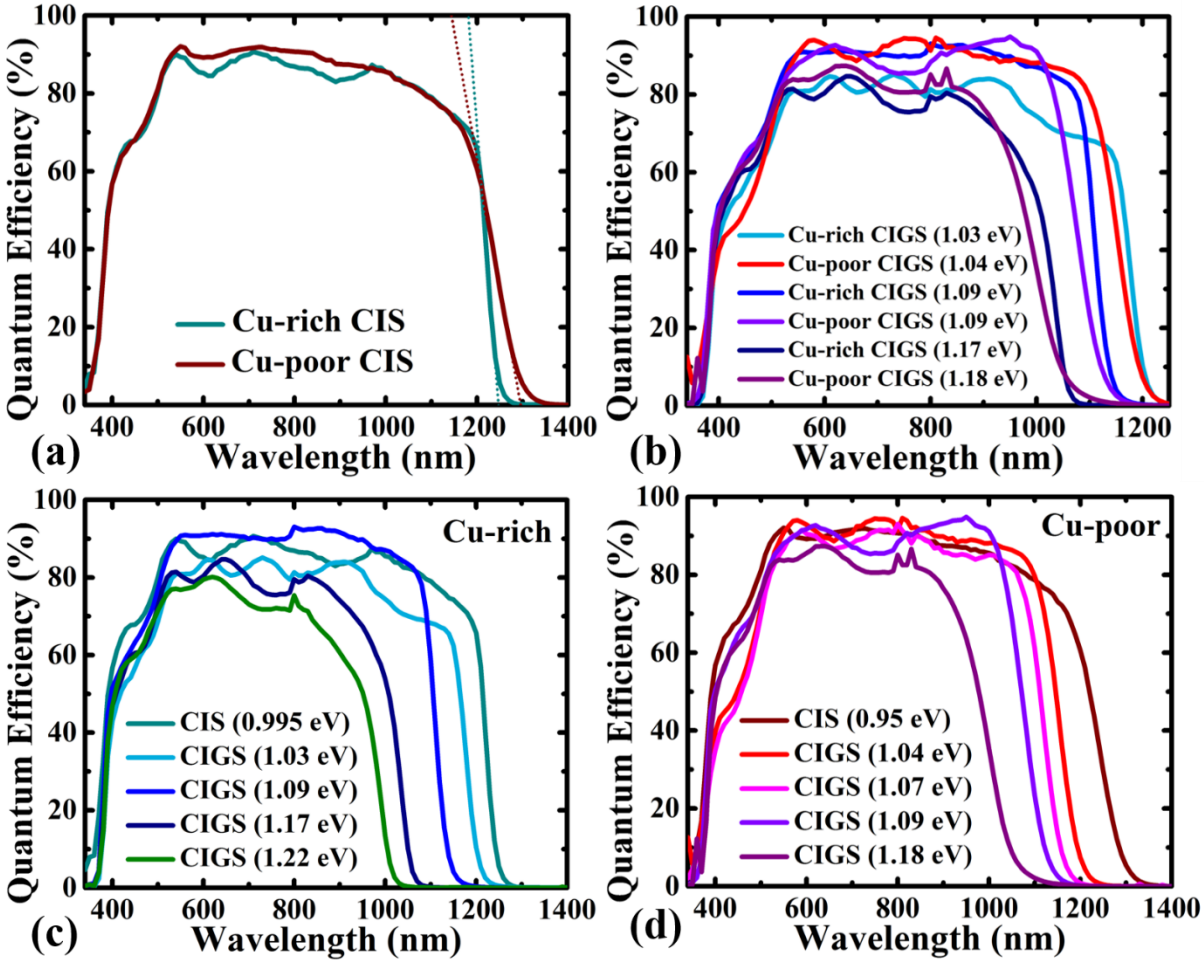

Figure 5.3: EQE response for a) Cu-rich and Cu-poor CIS, b) Cu-rich and Cu-poor CIGS solar cells, c) Cu-rich cells as function of adding Ga and d) Cu-poor cells as function of adding Ga. The short dotted lines in Figure 5.3a represent the fitting from which the bandgap is extrapolated.

One common feature that can be revealed from the EQE responses of Cu-rich and Cu-poor CIS (Figure 5.3a) and CIGS cells (Figure 5.3b) is that Cu-rich cells show steeper responses at longer wavelengths (near absorption edge region) compared to Cu-poor cells. This steep behaviour of Cu-rich CIS and CIGS cells could reveal improved absorption properties with steeper absorption edge and less tails in Cu-rich cells compared to Cu-poor cells.

The optical bandgap was deduced from the linear extrapolation around the minimum point fitted in the longer wavelengths of the EQE response as illustrated by the short dotted lines in Figure 5.3a. The optical bandgap for Cu-rich CIS cells shows higher values (0.995 eV) in comparison to that of Cu-poor CIS cells (0.956 eV). This lower bandgap for Cu-poor CIS cells compared to Cu-rich CIS cells could be explained in terms of anion displacement that is weakly dependent on the concentration of copper vacancies [17] or sharper bandgap onsets [18 – 19]. The optical bandgaps of CIGS cells in Figure 5.3b were deduced in a similar manner to the CIS bandgap in Figure 5.3a.

If we focus on CIS cells in Figure 5.3a, Cu-rich (green curve) cells show slightly improved behaviour at longer wavelengths (1100 – 1200 nm) compared to Cu-poor cells (red curve) while Cu-poor cells shows higher values for wavelengths between 600 – 1000 nm. To analyse and compare the collection efficiency for Cu-rich and Cu-poor CIS cells, the optical J_{SC} was deduced. The optical J_{SC} was deduced through integrating the EQE spectrum multiplied with the AM1.5 spectrum [20] and referred to as "J_{SC_EQE}" as explained in Section 4.2. The J_{SC_EQE} for Cu-rich CIS cells indicated a value of 37.9 mA.cm^{-2}, while Cu-poor CIS cells showed values of 38.8 mA.cm^{-2}. It is important to note that these J_{SC_EQE} values are lower than those extracted from IV measurements and reported in [2] (38.9 mA/cm^2 for Cu-rich and 42.0 mA/cm^2 for Cu-poor CIS solar cells). The higher J_{SC} values from IV compared to EQE values are attributed to spectral mismatch in our IV setup between the solar simulator and the AM1.5 spectrum. After obtaining the J_{SC_EQE}, the maximum J_{SC}, referred to as "J_{SC_MAX}", was calculated as the maximum J_{SC} that could be achieved at a specific bandgap by integrating the AM1.5 spectrum until that specific bandgap. J_{SC_MAX} was calculated to be 48.2 mA.cm^{-2} for Cu-rich CIS cells with the bandgap of 0.995 eV and 50.3 mA.cm^{-2} for Cu-poor CIS cells with the bandgap of 0.956 eV. After that, the carrier collection efficiency was determined based on Equation 5.1 as in [21].

$$\text{Carrier Collection Efficiency} = \frac{J_{SC\_EQE}}{J_{SC\_MAX}} \times 100 \quad \% \qquad (5.1)$$

Based on the above calculations, Cu-rich CIS cells proved to have superior performance in terms of carrier collection efficiency with 78.6 % compared to 77.1 % for Cu-poor CIS cells [2]. It is important to note that these calculations are valid for all our CIS cells. The results of these calculations are summarized in Table 5.3 and illustrated in Figure 5.4 [2].

Table 5.3 Carrier Collection Efficiency calculations for Cu-rich and Cu-poor CI(G)S solar cells. Calculations are based on EQE measurements.

Sample	Optical band gap (eV)	J_{SC_EQE} ($mA.cm^{-2}$)	J_{SC_MAX} ($mA.cm^{-2}$)	Carrier Collection Efficiency (%)
Cu-rich CIS	0.995	37.9	48.2	78.6
Cu-poor CIS	0.957	38.8	50.3	77.1
Cu-rich CIGS (1.09 eV)	1.09	36.8	44.1	83.4
Cu-poor CIGS (1.09 eV)	1.09	35.5	44.1	80.5
Cu-rich CIGS (1.17 eV)	1.17	28.9	41.2	70.1
Cu-poor CIGS (1.18 eV)	1.18	29.4	40.7	72.2

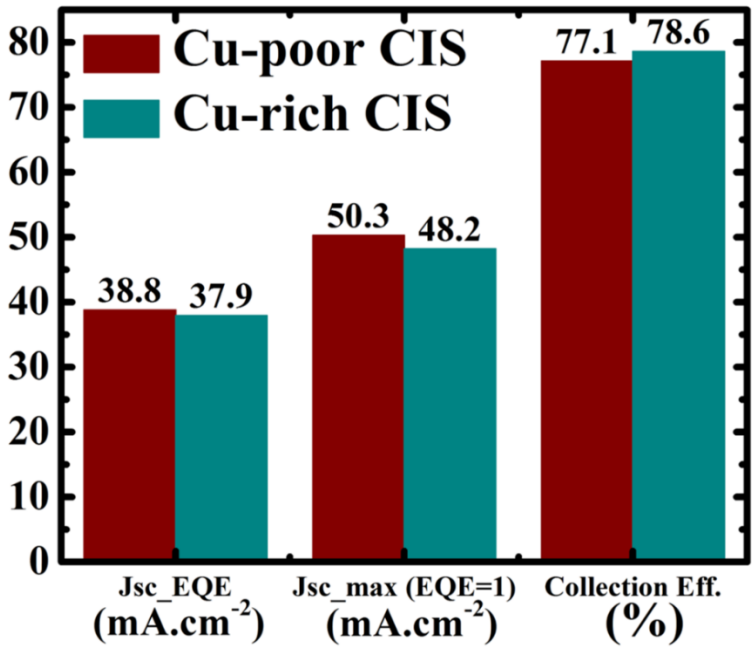

Figure 5.4: Optical calculations for the carrier collection efficiency for both Cu-rich and Cu-poor CIS solar cells

For CIGS cells, the EQE response changes with the addition of Ga and increasing the bandgap. Increasing the bandgap shifts the EQE response at longer wavelengths (near absorption edge) to lower values as observed for Cu-rich CIGS cells in Figure 5.3c and for Cu-poor CIGS cells in Figure 5.3d. It is important to note that the EQE response at shorter wavelengths (400 – 550 nm) for Cu-poor CIGS cells with bandgaps of 1.04 and 1.07 eV showed lower values compared to other Cu-poor CIGS cells as observed in Figure 5.3 (b, d). This decrease in EQE response for these two cells is due to the CdS buffer layer that was intentionally deposited for longer durations forming a thicker CdS buffer layer increasing parasitic absorptions and decreasing the EQE response at shorter wavelengths.

Comparing the collection efficiency between Cu-rich and Cu-poor CIGS cells is quite difficult. This is due to the 3-stage process used to grow CIGS absorbers that affects the quality of the absorbers as well as the amount of Ga that affects the bandgap of the formed absorber phase.

To illustrate that, the collection efficiency was deduced for Cu-rich and Cu-poor CIGS cells with the same bandgap of 1.09 eV in the same way used for CIS cells using Equation 5.1. The J_{SC_EQE} values for Cu-rich and Cu-poor CIGS cells were calculated to be 36.8 and 35.5 mA/cm^2 respectively with a collection efficiency of 83.4 % for Cu-rich compared to 80.5 % for Cu-poor CIGS solar cells. This means for the same bandgap for two CIGS runs grown on the same day, Cu-rich CIGS cells showed better collection efficiency compared to Cu-poor CIGS cells.

However, taking another two CIGS cells with a bandgap of 1.17 eV for Cu-rich and 1.18 eV for Cu-poor CIGS cells, the J_{SC_EQE} values showed 28.9 and 29.4 mA/cm^2 respectively. These J_{SC_EQE} values of CIGS cells are again lower than the J_{SC} values extracted from IV measurements (similar to CIS cells) and attributed to the spectral mismatch in our IV setup. The calculated collection efficiency of Cu-rich CIGS cell showed a value of 70.1 % lower than that for Cu-poor CIGS that has a collection efficiency of 72.2 %.

5.3 Dominant recombination path in CI(G)S solar cells

To understand more about the V_{OC} deficit in Cu-rich cells, IVT measurements were performed to extract the V_{OC} as function of temperature V_{OC} (T), determine the dominant recombination path in Cu-rich solar cells and compare it to Cu-poor cells. The dominant recombination path is determined from the activation energy extrapolated from the V_{OC} (T) curve at zero Kelvin. If the activation energy is close to the bandgap, then the dominant recombination path is in the bulk, otherwise if the activation energy is lower than the bandgap, then the dominant recombination path is in the interface as explained earlier in Section 4.3 [22, 23].

Two main observations were deduced for the V_{OC} (T) curve in Cu-rich CI(G)S cells compared to Cu-poor CI(G)S cells as depicted from Figure 5.5a:

1. The first observation is related to the activation energy at zero Kelvin extrapolated from the linear fit that was fitted at room temperatures (where the cell operates) as indicated by the short dotted lines in Figure 5.5a and can be summarized in the following points:
    - The extrapolated activation energy at zero Kelvin for Cu-rich CIS cells in Figure 5.5a shows values around 0.6 V, much lower than the bandgap of Cu-rich CIS cells (0.995 eV).
    - On the other side, the extrapolated activation energy at zero Kelvin for Cu-poor CIS cells indicated values close to the bandgap (0.956 eV). The short dashed lines in Figure 5.5a represent the bandgaps of the corresponding cells extracted from EQE measurements as explained above. It is important to note that the extrapolated activation energies at zero Kelvin typically indicate higher values compared to the EQE bandgap. These higher values are in accordance to an expected 75 meV extra activation energy related to the effective density of states and temperature dependent thermal velocity [24].
    - CIGS solar cells behave similar to CIS solar cells where the activation energy at zero Kelvin for Cu-rich CIGS samples shows values of 0.7 eV lower than the corresponding bandgap of 1.1 eV while the activation energy at zero Kelvin for Cu-poor CIGS cells shows values close to the bandgap (1.07 eV) as presented in Figure 5.5a.
    - This means that the dominant recombination path in Cu-rich CIS and CIGS cells is at or near the interface of the absorber, while the dominant recombination path of Cu-poor CIS and CIGS cells is in the bulk of the absorber [2, 25].

2. The second observation was related to the number of negative slopes for the V_{OC} (T) curve and can be summarized in the following observations:
    - There is one negative slope for the V_{OC} (T) curve of Cu-poor CIS and Cu-poor CIGS solar cells before the V_{OC} values saturate (or decrease) at lower temperatures as illustrated in Figure 5.5a.
    - There are two negative slopes for Cu-rich CIGS and Cu-rich CIS solar cells before the V_{OC} values saturate (or decrease) at lower temperatures as illustrated in Figure 5.5a. This second slope in Cu-rich CIS could be explained in terms of the photocurrent at V_{OC} that coincides with a strong temperature dependence as presented in Figure 5.5b making the model for the activation energy invalid [25].

The photocurrent at V_{OC} is extracted from the IVT measurements as explained in Section 4.3. In Figure 5.5b, the photocurrent at V_{OC} for Cu-poor CIS cells decreases with decreasing temperature in one step (Step 1) corresponding to a one slope observed for its corresponding V_{OC} (T) (red curves in Figure 5.5b). However, for Cu-rich CIS cells, it can be observed that there is a strong temperature dependence where the photocurrent at V_{OC} increases with decreasing temperature at relatively high temperatures (Step 2) before it decreases in a similar manner to Cu-poor CIS cells at relatively lower temperatures (Step 1). Interestingly, the temperature range corresponding to the two steps of the photocurrent at V_{OC} in Cu-rich CIS cells are in the same temperature range of the two slopes in the V_{OC} (T) curve as presented by the green curves and indicated by the black dashed lines in Figure 5.5b. The behaviour of Step 2 of the photocurrent at V_{OC} is corresponding to the slope, whose extrapolated activation energy (short dotted lines) showed values lower than the bandgap in a temperature range of 190 – 320 K. On the other side, the behaviour of Step 1 lies in temperature range of 110 – 190 K (indicated by the black dashed lines) similar to that of the second slope whose extrapolated activation energy (short dashed lines) showed values close to the bandgap. This strong temperature dependence of the photocurrent at V_{OC} in Cu-rich CIS cells makes the model of the activation energy invalid and raises the question if Cu-rich CIS cells are actually suffering from interface recombination or not. Chapter 7 will identify a defect that could be passivated by post-deposition treatments introduced in Chapter 6 leading to the removal of Step 2 [25].

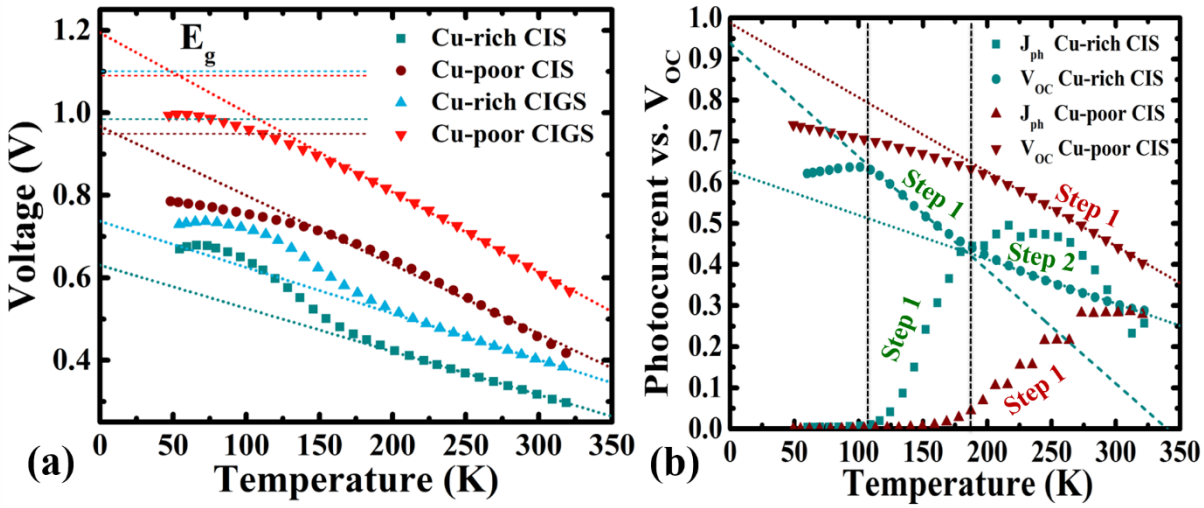

Figure 5.5: a) Temperature dependence of the open circuit voltage for Cu-rich and Cu-poor CIS and CIGS solar cells. A linear fit at high temperatures (short dotted line) is used to extract the activation energy at zero Kelvin. The bandgap (E_G) of all CIS and CIGS solar cells is represented by a short dashed line. b) Temperature dependence of both the photocurrent at V_{OC} and the V_{OC} for both Cu-rich (green) and Cu-poor (red) CIS solar cells. Short dotted lines represent the linear fit at high temperatures similar to a), short dashed green line represents the linear fit for Cu-rich CIS at lower temperatures and black dashed lines represent the temperature regions separating Step 1 and Step 2.

Moreover, the series resistance as function of temperature was extracted from the IVT measurements under dark conditions at far forward bias (1.2 V) as explained in Section 4.3 and presented in Figure 5.6. At high temperatures, the series resistance decreases with decreasing temperature. However, at lower temperatures, the series resistance is thermally activated and increases with decreasing temperature. The potential reason behind the thermal activation of the series resistance is attributed to a transport barrier through either the transport of holes over the back interface barrier at the absorber/back contact interface or the transport of electrons at the front interface barrier at the absorber/buffer interface [25]. The activation energy of the thermally activated series resistance was deduced from the slope of the Arrhenius plot in Figure 5.6 for both Cu-rich and Cu-poor CIS and CIGS solar cells as explained in Section 4.3. While in Cu-poor cells, a small activation energy (20±10 meV) was deduced at low temperatures (below 50 K) for both CIS and CIGS, Cu-rich cells indicated considerably higher activation energy (100±10 meV) for both CIS and CIGS and interestingly at the same temperature range (120 – 200 K). The exact deduced activation energies with their corresponding temperature ranges are provided in Table 5.4. This indicates that Cu-rich CIS and CIGS cells suffer additionally from a barrier with an activation energy around 100±10 meV.

Table 5.4 Series resistance activation energy deduced from IVT measurements under dark conditions for Cu-rich and Cu-poor CIS & CIGS solar cells.

Sample	Series Resistance activation energy (meV)	Temperature Range (K)
Cu-rich CIS	92	127 - 184
Cu-poor CIS	18	38 - 65
Cu-rich CIGS	90	127 - 204
Cu-poor CIGS	26	44 - 74

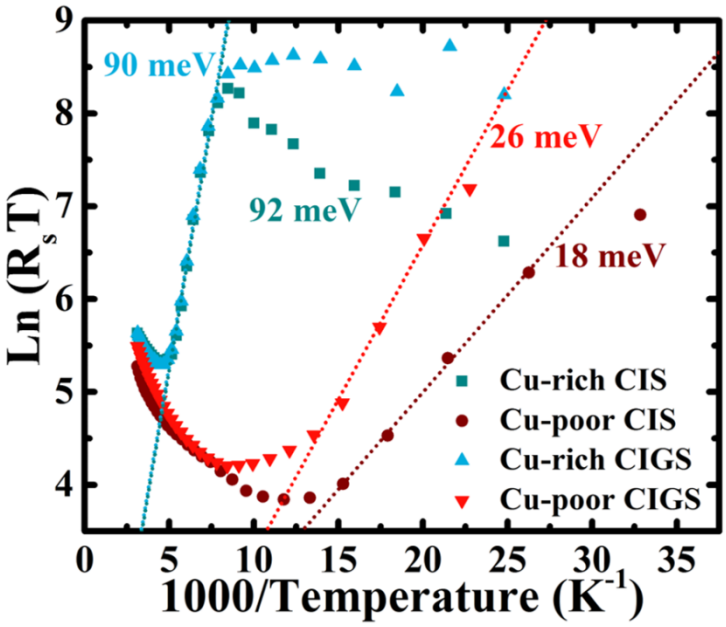

Figure 5.6: The Arrhenius plot for the series resistance as function of temperature for Cu-rich and Cu-poor CIS & CIGS solar cells. The energy of the thermally activated series resistance is deduced from the slope of the corresponding curves fitted at low temperatures as indicated by the short dotted lines.

5.4 Apparent doping and defects in CI(G)S solar cells

Capacitance measurements as a function of frequency, voltage and temperature were performed on Cu-rich and Cu-poor CIS and CIGS solar cells. Capacitance measurements as a function of voltage (CV) was used to deduce the apparent doping from the slope of the corresponding Mott-Schottky plot as explained in Section 4.4 and as indicated in Figure 5.7. The apparent doping was extracted from the slope of the frequency curve measured at 100 KHz fitted at small forward bias (explained in Section 4.4) as illustrated by the short dotted line in Figure 5.7.

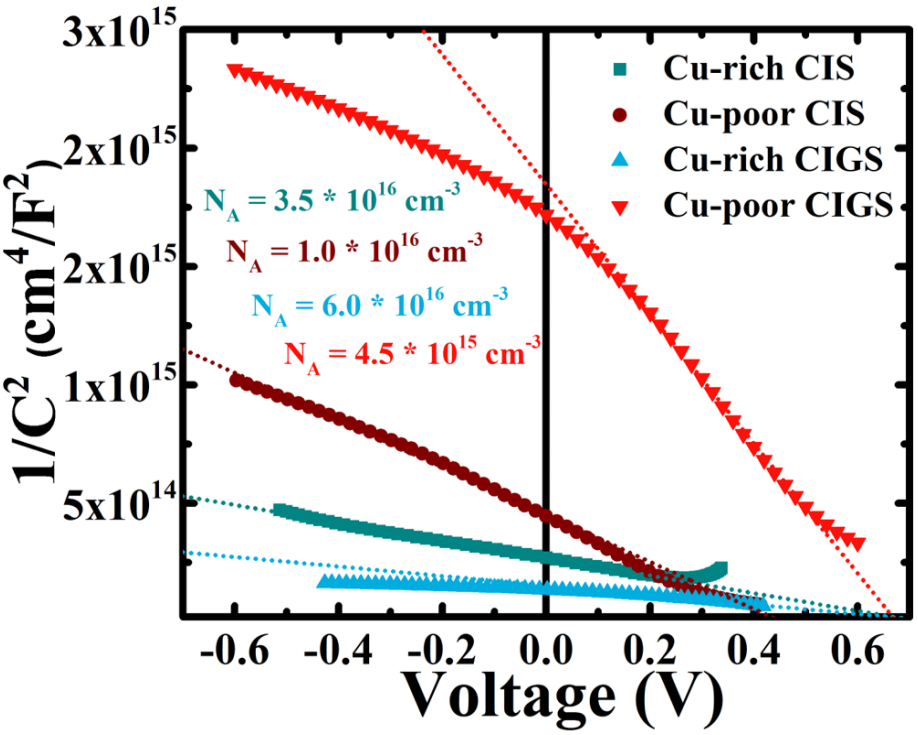

Figure 5.7: Arrhenius plot of the CV measurements for Cu-rich and Cu-poor CIS & CIGS. The apparent doping is extracted from the slope of the corresponding curves fitted at small forward bias measured at a frequency of 100 KHz.

Figure 5.7 illustrates the differences of apparent doping between Cu-rich and Cu-poor cells. Cu-rich cells exhibit higher apparent doping of $3.5*10^{16}$ and $6*10^{16}$ cm^{-3} for CIS and CIGS cells respectively compared to Cu-poor cells that show values of $1.0*10^{16}$ and $4.5*10^{15}$ cm^{-3} for CIS and CIGS cells respectively. The higher apparent doping observed for Cu-rich cells will be attributed to an acceptor defect that is present in Cu-rich cells only and not Cu-poor cells as explained in Chapter 7. The passivation of this defect using PDTs presented in Chapter 6 leads to the decrease in the apparent doping of Cu-rich cells.

On the other side, capacitance measurements as a function of frequency and temperature (ADM) were performed on Cu-rich and Cu-poor CIS and CIGS solar cells to provide information on the activation energies of the main capacitance steps for each cell [26] as explained in Section 4.5. The admittance spectra of each of the Cu-rich and Cu-poor CIS and CIGS solar cells with their corresponding Arrhenius plots are illustrated in Figures 5.8, 5.9 and 5.10. The admittance spectra show the capacitance behaviour of the cells as a function of frequency (100 – 1M Hz) and as a function of temperature (320 – 50 K) as presented in Figure 5.8a for Cu-rich CIS cells, Figure 5.8c for Cu-poor CIS cells, Figure 5.9 (a, c, e, g) for Cu-rich CIGS cells and Figure 5.10 (a, c, e, g) for Cu-poor CIGS cells. The short dashed lines in the admittance spectra of Figures 5.8, 5.9 and 5.10 represent the regions of the main capacitance steps (where barriers or defects are likely to respond). The inflection point of these capacitance steps are deduced from the maxima in the derivative with respect to the log of the frequency. The values of the inflection points are then plotted in an Arrhenius plot and the activation energies of these capacitance steps are calculated from the slope of the linear fit of the corresponding Arrhenius plots as explained in Section 4.5 [27, 28]. These Arrhenius plots with the corresponding deduced activation energies are presented in Figure 5.8b for Cu-rich CIS cells, Figure 5.8d for Cu-poor CIS cells, Figure 5.9 (b, d, f, g) for Cu-rich CIGS cells and Figure 5.10 (b, d, f, g) for Cu-poor CIGS cells. The temperature ranges, from which the activation energies of the main capacitance steps were deduced, are also indicated in the corresponding Arrhenius plots.

The admittance spectra for Cu-rich and Cu-poor CIS and CIGS solar cells in Figures 5.8, 5.9 and 5.10 revealed three main capacitance steps as indicated by the short dashed lines:

1. The first step (Step 1) at higher temperatures is characterized by a broad capacitance dispersion that might be related to either tail states or in-homogeneities [29, 30]. Moreover, this dispersion might also be attributed to the presence of a broad defect-related capacitance step located at frequencies that are below our measurement range (below 100 Hz). Frequencies below 100 Hz (long characteristic lifetime) shall suggest a relatively weak recombination activity even at room temperature.
2. The second step (Step 2) at intermediate temperatures shall correspond to the step where significant recombination-active deep defects or barriers related to the absorber would appear.

3. The third step (Step 3) at lower temperatures can be attributed to mobility or carrier freeze-out as the capacitance values drop to the absorber geometrical capacitance (approximately 5 nF/cm^2).

Therefore, the main capacitance step in all Cu-rich and Cu-poor CIS and CIGS solar cells where a defect or a barrier shall respond is the second step (Step 2) at intermediate temperatures.

The deduced activation energies of the main capacitance steps (Step 2) in Figures 5.8, 5.9 and 5.10 could be attributed to either a defect or a barrier [25] as explained in Sections 4.3 and 4.5. If this step was a barrier, it should reflect on the activation energies of the series resistance measured as function of temperature [31, 32] and represented above in Figure 5.6 showing values similar to the activation energies deduced from admittance measurements. Otherwise, if the activation energy from series resistance is less than that of admittance, then the main capacitance step in admittance is likely to be a defect. The activation energies (E_a) extracted from both the series resistance and the admittance measurements for Cu-rich and Cu-poor cells with their corresponding temperature ranges are compared in Table 5.5. From Table 5.5, it can be observed that the activation energies extracted from series resistance are much less than that extracted from admittance measurements. Therefore, it can be concluded that the activation energies from admittance measurements for all Cu-rich and Cu-poor CIS and CIGS solar cells are related to defects and not barriers.

After identifying the main capacitance steps (Step 2) from admittance measurements as defects, I will analyse the activation energy of the main capacitance step (Step 2) for each of Cu-rich and Cu-poor cells and relate these activation energies to their possible corresponding defects.

For Cu-rich CIS cells, the activation energy of the main capacitance step (Step 2) indicated an activation energy around 200$\pm$20 meV as presented in Figure 5.8b. This step has been observed in all our Cu-rich CIS cells in the same temperature range (120 – 180 K) regardless changing Cu/In or Se-flux ratios during deposition [2, 25, 33]. The nature of this defect will be revealed in Chapter 7. Passivating this 200$\pm$20 meV defect using PDTs indicated the presence of another defect with an activation energy of 130$\pm$15 meV. This 130$\pm$15 meV defect is present in Cu-rich CIS cells before and after PDTs as presented in Sections 6.1 and 6.2 as well as Chapter 7. This 130$\pm$15 meV can be attributed to the A3 acceptor defect observed by Photoluminescence measurements as reported in [34].

For Cu-poor CIS solar cells, the main capacitance step (Step 2) is a double-step with activation energies of 130±15 meV in a temperature range of 160 – 220 K and 50±10 meV in a temperature range of 90 – 160 K [29] as presented in Figure 5.8d. These activation energies are in good agreement with the activation energies of shallow acceptor defects observed by Photoluminescence with values of 130±15 meV for the A3 acceptor and 50±10 meV for the A1 acceptor [4, 34, 35, 36].

On the other side, for Cu-rich and Cu-poor CIGS cells, the activation energy of the main capacitance step (Step 2) varies with the bandgap.

For Cu-rich CIGS cells, the activation energy of the main capacitance step (Step 2) showed values of 140, 144, 124 and 94 meV for bandgaps of 1.03, 1.11, 1.17 and 1.22 eV respectively as presented in Figure 5.9 (b, d, f, g) and summarized in Figure 5.11. It can be observed from Figure 5.11 that the activation energy of the main capacitance step in Cu-rich CIGS lies in the range of 130±15 meV with increasing the bandgap up to a bandgap of 1.17 eV before the activation energy starts to decrease with further increase of the bandgap. This activation energy of 130±15 meV is similar to that of Cu-rich CIS cells after passivating the 200±20 meV as explained above and can be also attributed to the A3 acceptor observed by Photoluminescence measurements. This A3 acceptor is normally attributed to Indium vacancy [34]. Therefore, we can conclude that this A3 acceptor (Indium vacancy) is present in Cu-rich CIS cells and remains there with adding Ga and increasing the bandgap up to bandgaps of around 1.2 eV. Further increasing of the bandgap (adding more Ga) for Cu-rich CIGS cells would then passivate the Indium vacancy and introduce defects of lower activation energies reflected in a decrease of the activation energy of the main capacitance step (Step 2) for Cu-rich CIGS cells with bandgaps higher than 1.2 eV as observed in Figure 5.11.

For Cu-poor CIGS cells, the activation energy of the main capacitance step (Step 2) decreases with increasing the bandgap (addition of more Ga) showing values of 115, 98, 90 and 64 meV for bandgaps of 1.04, 1.07, 1.11 and 1.17 eV respectively. It is important to note that the activation energy of the main capacitance step (Step 2) for Cu-poor CIS cells showed values of 130±15 meV as presented above. Plotting these activation energies together for Cu-poor cells as a function of adding Ga (from pure CIS to CIGS cells with bandgaps of 1.17 eV) indicates the decrease of the activation energy of the main capacitance step (Step 2) with the addition of Ga as presented in Figure 5.11. The addition of Ga is then changing the activation energy of the main capacitance step similar to what was observed for Cu-rich CIGS cells with

bandgaps higher than 1.2 eV. This could be attributed to different defect possibilities including Ga vacancy and In-Ga related anti-sites.

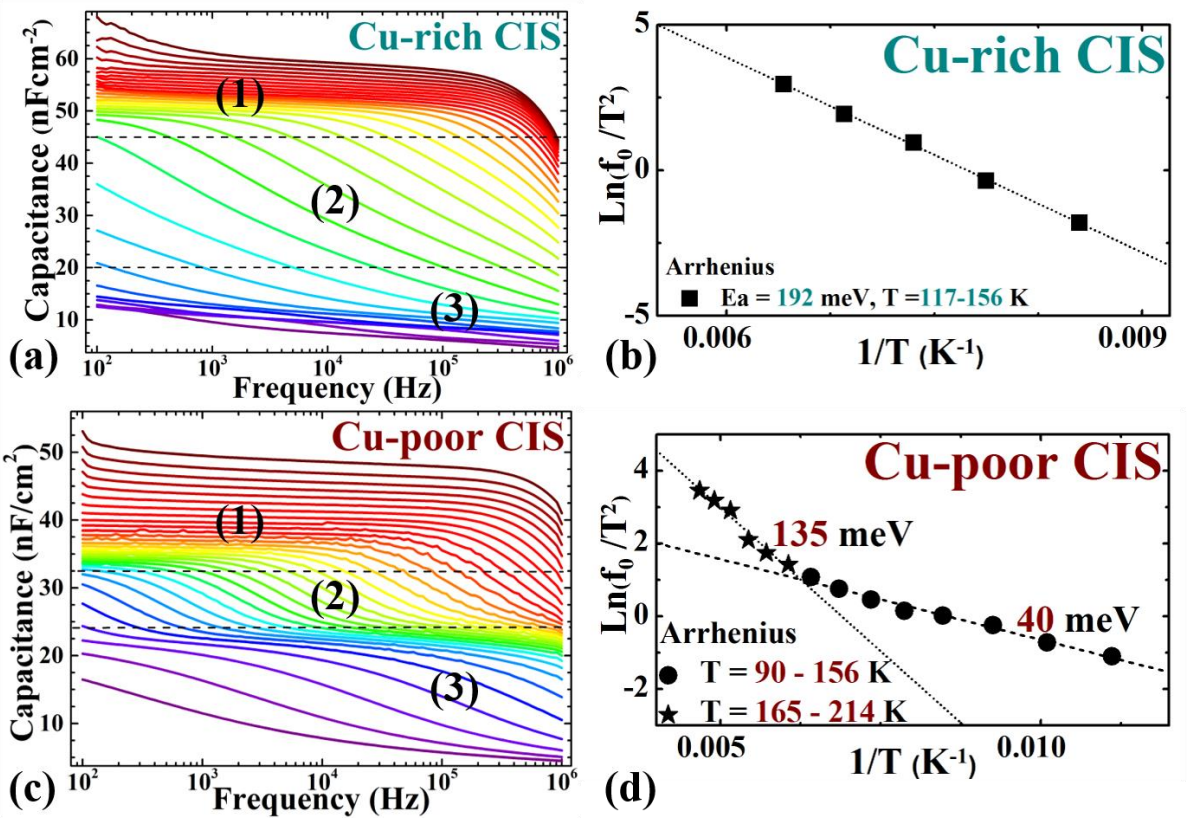

Figure 5.8: Admittance measurements for a) Cu-rich CIS and c) Cu-poor CIS solar cells for temperatures between 320 K and 50 K. The black dashed lines identify the three regions of main capacitance steps named Step 1, Step 2 and Step 3 respectively. The Arrhenius plot indicates the activation energy of the main capacitance step (Step 2) for b) Cu-rich CIS and d) Cu-poor CIS solar cells. The activation energies of the main capacitance step (Step 2) and their corresponding temperature ranges are also indicated.

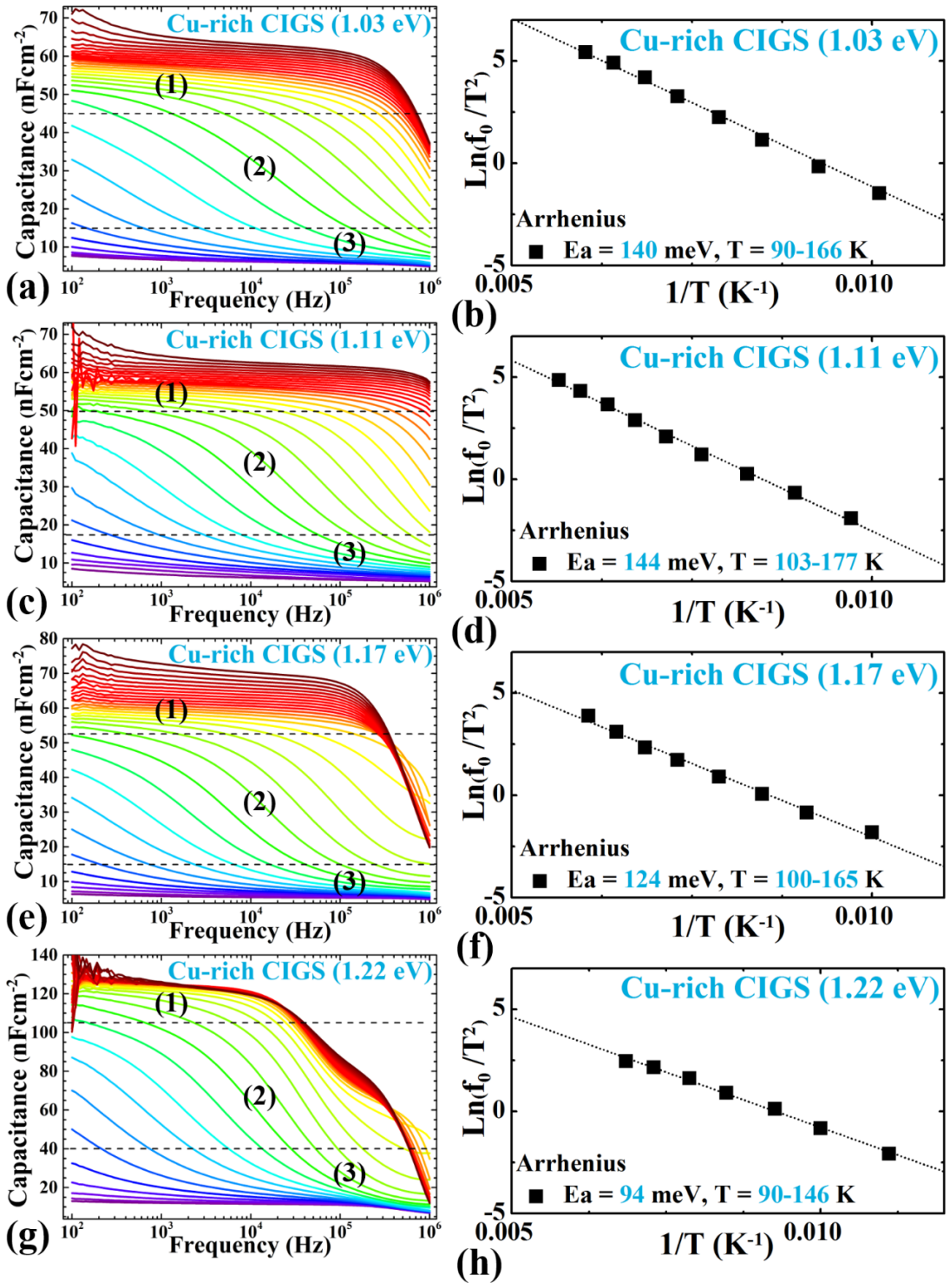

Figure 5.9: Admittance measurements for Cu-rich CIGS solar cells with bandgaps of a) 1.03 eV, c) 1.11 eV, e) 1.17 eV and g) 1.22 eV for temperatures between 320 K and 50 K. The black dashed lines identify the three regions of main capacitance steps named Step 1, Step 2 and Step 3 respectively. The Arrhenius plot indicates the activation energy of the main capacitance step (Step 2) for Cu-rich CIGS solar cells with bandgaps of b) 1.03 eV, d) 1.11 eV, f) 1.17 eV and h) 1.22 eV. The activation energies of the main capacitance step (Step 2) and their corresponding temperature ranges are also indicated.

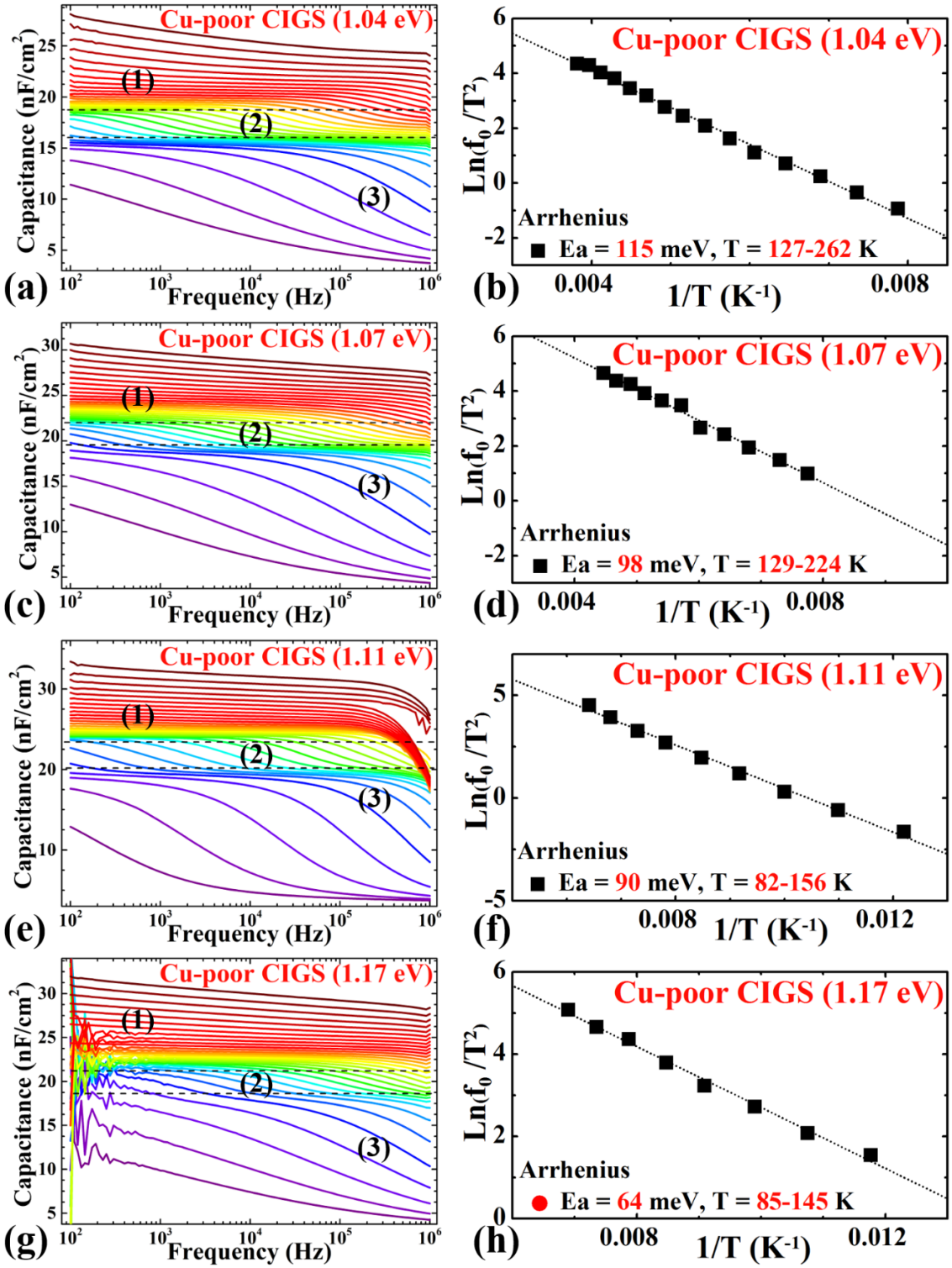

Figure 5.10: Admittance measurements for Cu-poor CIGS solar cells with bandgaps of a) 1.04 eV, c) 1.07 eV, e) 1.11 eV and g) 1.17 eV for temperatures between 320 K and 50 K. The black dashed lines identify the three regions of main capacitance steps named Step 1, Step 2 and Step 3 respectively. The Arrhenius plot indicates the activation energy of the main capacitance step (Step 2) for Cu-poor CIGS solar cells with bandgaps of b) 1.04 eV, d) 1.07 eV, f) 1.11 eV and h) 1.17 eV. The activation energies of the main capacitance step (Step 2) and their corresponding temperature ranges are also indicated.

Table 5.5 Activation energies deduced from IVT measurements (Ea series resistance) compared to activation energies deduced from admittance measurements (Ea ADM) with the respective temperature range from where the activation energies were deduced for both Cu-rich and Cu-poor CIS & CIGS solar cells.

Sample	E_a Series Resistance (meV)	Temperature Range (K)	E_a ADM (meV)	Temperature Range (K)
Cu-rich CIS	92	127 - 184	200	120 - 180
Cu-poor CIS	18	38 - 65	40 – 60, 130 - 140	90 – 160, 160 - 220
Cu-rich CIGS	90	127 - 204	130 - 140	90 – 170
Cu-poor CIGS	26	44 - 74	100 - 140	120 - 260

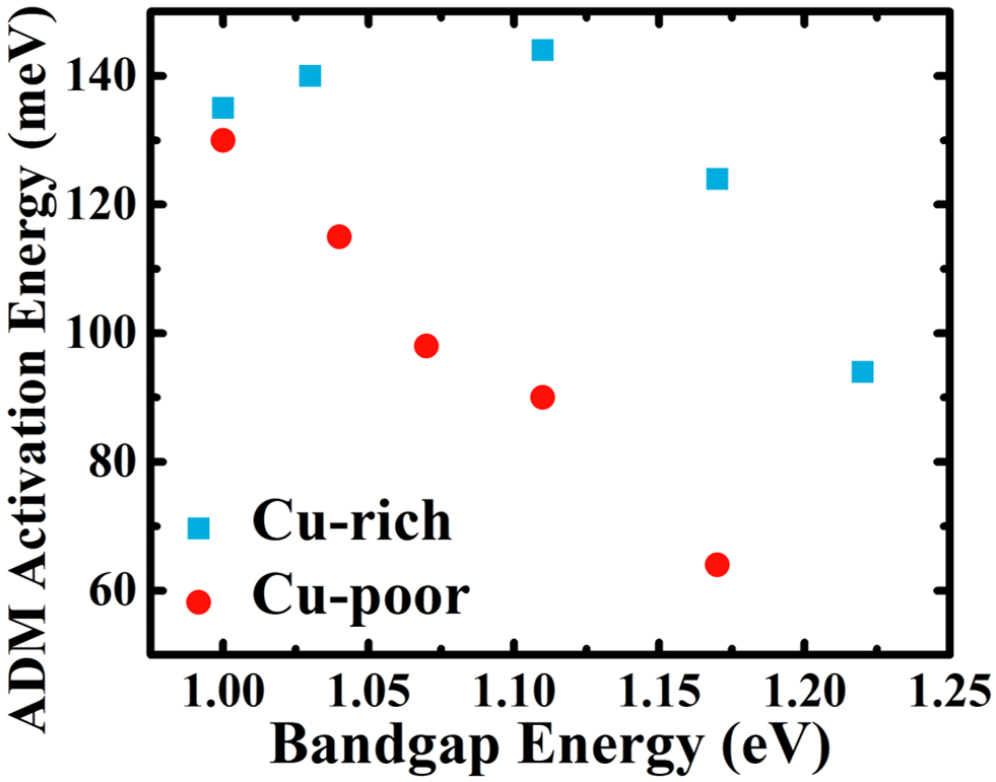

Figure 5.11: Activation energies deduced from Admittance measurements as function of increasing the bandgap (adding more Ga) for Cu-rich (blue) and Cu-poor (red) solar cells starting from pure CIS cells.

5.5 Summary

Chapter 5 introduced the characteristics of Cu-rich CIS and CIGS absorbers and solar cells comparing them to their corresponding Cu-poor absorbers and solar cells.

Although Cu-rich CIS absorbers are characterized by their larger grain sizes and better collection efficiencies compared to Cu-poor CIS absorbers as illustrated in Section 5.1 and 5.2, the electrical performance of Cu-rich CIS cells show lower efficiency compared to Cu-poor CIS cells. The lower efficiency of Cu-rich CIS cells is attributed to lower V_{OC} and FF values compared to Cu-poor CIS cells. The reason behind the V_{OC} deficit will be identified in terms of a detrimental defect that will be introduced in Chapter 7. The FF deficit is related to lower shunt resistance values explained in terms of space-charge limited current. The dominant recombination path in Cu-rich CIS cells is at the absorber/buffer interface while the dominant recombination path in Cu-poor CIS cells is at the absorber bulk. Moreover, Cu-rich CIS cells show higher apparent doping compared to Cu-poor CIS cells as observed in Section 5.3. This high apparent doping in Cu-rich CIS cells will be attributed in Chapter 7 to a 200 ± 20 meV acceptor defect that was revealed from admittance measurements as presented in Section 5.4. This 200 ± 20 meV defect is only present in Cu-rich CIS cells and not in Cu-poor CIS cells that showed a defect with an activation energy of 130 ± 15 meV attributed to an A3 acceptor defect.

Cu-rich CIGS cells show similar behaviour to Cu-rich CIS cells. Cu-rich CIGS cells suffer from significant V_{OC} and FF losses compared to Cu-poor CIGS cells with higher apparent doping. The dominant recombination path of Cu-rich CIGS cells is also at the absorber/buffer interface while the dominant recombination path for Cu-poor CIGS cells is at the absorber bulk. The activation energy of defects in Cu-rich CIGS cells changes with the addition of Ga and increasing the bandgap, showing values of 130 ± 15 meV up to bandgaps of 1.17 eV before the activation energy decreases with further increase of the bandgap.

References Chapter 5

[1] T. Godecke, T. Haalboom, F. Ernst, "Phase equilibria of Cu-In-Se. Stable states and non-equilibrium states of the In_2Se_3-Cu_2Se subsystem", Zeitschrift für Metallkunde, 91(8): 622–634 (2000).

[2] H. Elanzeery, F. Babbe, M. Melchiorre, A. Zelenina, S. Siebentritt, "Potassium Fluoride Ex-Situ Treatment on Both Cu-Rich and Cu-Poor $CuInSe_2$ Thin Film Solar Cells", IEEE Journal of Photovoltaics, 7, 684 – 689 (2017).

[3] M. T. Wagner, I. Dirnstorfer, D. M. Hofmann, M. D. Lampert, F. Karg, B. K. Meyer, "Characterization of $CuIn(Ga)Se_2$ thin films Cu-Rich Layers", Physica Status Solidi A-Applied Research, 167: 131–142 (1998).

[4] S. Siebentritt, N. Rega, A. Zajogin, M. C. Lux-Steiner, "Do we really need another PL study of $CuInSe_2$?", Proceedings of Conference on Photo-Responsive Materials (Phys. Stat. Sol. C 1(9)), Kariega, South Africa; 2304–2310 (2004).

[5] S. Siebentritt and S. Schuler, "Defects and transport in the wide gap chalcopyrite $CuGaSe_2$", Journal of Physics and Chemistry of Solids; 64: 1621–1626 (2003).

[6] J. K. Larsen, L. Gütay, S. Siebentritt, "Influence of secondary phase Cu_xSe on the optoelectronic quality of chalcopyrite thin films", Applied Physics Letters, 98: 201910-1–201910-3 (2011).

[7] S. Siebentritt, L. Gütay, D. Regesch, Y. Aida, V. Deprédurand, "Why do we make $Cu(In,Ga)Se_2$ solar cells non-stoichiometric?", Solar Energy Materials and Solar Cells, 119: 18 – 25 (2013).

[8] Y. Hashimoto, N. Kohara, T. Negami, M. Nishitani, T. Wada, "Surface Characterization of Chemically Treated $Cu(In,Ga)Se_2$ Thin Films", Japan Journal of Applied Physics, 35, 4760 – 4764 (1996).

[9] V. Deprédurand, D. Tanaka, Y. Aida, M. Carlberg, N. Fèvre, S. Siebentritt, "Current loss due to recombination in Cu-rich $CuInSe_2$ solar cells", J. Appl. Phys. 115, 44503 (2014).

[10] A. R. Burgers, J. A. Eikelboom, A. Schonecker, W. C. Sinke, "Improved Treatment of the Strongly Varying Slope in Fitting Solar Cell I-V Curve", Proceedings of the 25th IEEE Photovoltaic Specialist Conference, pp. 569 – 572 (1996).

[11] A. Zelenina, F. Werner, H. Elanzeery, M. Melchiorre, S. Siebentritt, "Space-charge-limited currents in CIS-based solar cells", Appl. Phys. Lett. 111, 213903 (2017).

[12] L. Choubrac, T. Bertram, H. Elanzeery, S. Siebentritt, "Cu(In,Ga)Se_2 solar cells with improved current based on surface treated stoichiometric absorbers", Physica Status Solidi A, 214, 1, 1600482 (2017).

[13] V. Depredurand, Y. Aida, J. Larsen, T. Eisenbarth, A. Majerus, S. Siebentritt, "Surface treatment of CIS solar cells grown under Cu-excess", 37th IEEE Photovoltaic Specialists Conference, Seattle, WA, pp. 000337-000342 (2011).

[14] V. Deprédurand, T. Bertram, S. Siebentritt, "Influence of the Se environment on Cu-rich CIS devices", Physica B, 439, 101 – 104 (2014).

[15] M. Turcu, O. Pakma, U. Rau, "Interdependence of absorber composition and recombination mechanism in Cu(In,Ga)$(Se,S)_2$ heterojunction solar cells", Applied Physics Letters, 80, pp. 2598–2600 (2002).

[16] D. Schmid, M. Ruckh, F. Grunwald, HW. Schock, "Chalcopyrite/defect chalcopyrite heterojunctions on the basis of $CuInSe_2$", Journal of Applied Physics, 73, pp. 2902–2909 (1993).

[17] L. Gutay *et al.*, "Feedback mechanism for the stability of the band gap of $CuInSe_2$", Phys. Rev. B, 86, 045216 (2012).

[18] U. Rau, B. Blank, T. C. M. Müller and T. Kirchartz, "Efficiency Potential of Photovoltaic Materials and Devices Unveiled by Detailed-Balance Analysis", Physical Review Applied, 7, 044016 (2017).

[19] E. Avancini, R. Carron, B. Bissig, P. Reinhard, R. Menozzi, G. Sozzi, S. Di Napoli, T. Feurer, S. Nishiwaki, S. Buecheler and A. N. Tiwari, "Impact of compositional grading and overall Cu deficiency on the near-infrared response in Cu(In,Ga)Se_2 solar cells", Prog. Photovolt: Res. Appl., 25:233 – 241 (2017).

[20] American Society for Testing and Materials (ASTM) G-173-03, International Standard ISO 9845-1, (1992).

[21] C. J. Hages, N. J. Carter, R. Agrawal, "Generalized quantum efficiency analysis for non-ideal solar cells: Case of $Cu_2ZnSnSe_4$", J. Appl. Phys., 119, 014505 (2016).

[22] U. Rau, A. Jasenek, H. W. Schock, F. Engelhardt, T. H. Meyer, "Electronic loss mechanisms in chalcopyrite based heterojunction solar cells", Thin Solid Films, 361: 298 – 302 (2000).

[23] R. Scheer, H. W. Schock, "Chalcogenide Photovoltaics: Physics, Technologies, and Thin Film Devices", Weinheim, Germany: Wiley-VCH, 112 – 116 (2011).

[24] T. Hölscher, S. Förster, T. Schneider, M. Maiberg, W. Widdra, R. Scheer, "Light induced degradation of Cu(In,Ga)Se_2 thin film surfaces", Applied Physics Letters, 111, 011604 (2017).

[25] H. Elanzeery, M. Melchiorre, M. Sood, F. Babbe, F. Werner, G. Brammertz and S. Siebentritt, "Challenge in Cu-rich $CuInSe_2$ Thin Film Solar Cells: Defect Caused by Etching", submitted (2018).

[26] F. Werner, F. Babbe, H. Elanzeery, S. Siebentritt, "Defects, buffer layer, or artefact – what do we see in capacitance measurements of thin film solar cells?", Prog. Photovolt. Res. Appl. (2018).

[27] F. Werner and S. Siebentritt, "Buffer Layers, Defects, and the Capacitance Step in the Admittance Spectrum of a Thin-Film Solar Cell", Phys. Rev. Applied, 9, 054047 (2018).

[28] P. Blood, J. W. Orton, "The Electrical Characterization of Semiconductor: Majority Carriers and Electron States", Academic Press, (1992).

[29] H. Elanzeery, F. Babbe, M. Melchiorre, F. Werner, S. Siebentritt, "High-performance low bandgap thin film solar cells for tandem applications", Prog. Photovolt. Res. Appl., 26, pp. 437 – 442 (2018).

[30] B. Hirschorn, M. E. Orazem, B. Tribollet, V. Vivier, I. Frateur and M. Musiani, "Determination of effective capacitance and film thickness from constant-phase-element parameters", Electrochim. Acta, 55, 6218 (2010).

[31] O. Gunawan, T. K. Todorov, D. B. Mitzi, "Loss mechanisms in hydrazine processed $Cu_2ZnSn(Se,S)_4$ solar cells", Applied Physics Letters, 97:233506, 62, 94, 100, 105 (2010).

[32] T. Ericson, J. J. Scragg, A. Hultqvist, J. T. Watjen, P. Szaniawski, T. Torndahl, C. Platzer-Bjorkman, "Zn(O,S) Buffer Layers and Thickness Variations of CdS Buffer for Cu_2ZnSnS_4 Solar Cells", IEEE Journal of Photovoltaics, 4:465 – 469, 62, 103, 105 (2014).

[33] T. Bertram, V. Depredurand, S. Siebentritt, "Electrical Characterization of Defects in Cu-Rich Grown $CuInSe_2$ Solar Cells", IEEE Journal of Photovoltaics, 6: 546 – 551 (2016).

[34] F. Babbe, H. Elanzeery, M. H. Wolter, K. Santhosh, S. Siebentritt, "The hunt for the third acceptor in $CuInSe_2$ and Cu(In,Ga)Se_2 absorber layers", submitted (2018).

[35] A. Bauknecht, S. Siebentritt, J. Albert and M. Ch. Lux-Steiner, "Radiative recombination via intrinsic defects in $Cu_xGa_ySe_2$", J. Appl. Phys., 89, 8, 4391 – 4400 (2001).

[36] S. Siebentritt and U. Rau, "Wide-Gap Chalcopyrites", Springer, Berlin, Heidelberg, 113 – 156 (2006).

Chapter 6: Improving performance of CI(G)S thin film solar cells

Chapter 5 introduced some of the characteristic aspects for Cu-rich and Cu-poor CIS and CIGS thin film solar cells. Although Cu-rich films showed some promising physical characteristics compared to Cu-poor films in terms of large grains, but solar cells based on Cu-rich films showed worse electrical performance compared to Cu-poor cells. Chapter 5 has identified the main problems affecting negatively the electrical performance of Cu-rich cells: open circuit voltage and fill factor. The significant decrease in the open circuit and fill factor values for Cu-rich cells compared to Cu-poor cells was attributed to a problematic interface between the Cu-rich absorber films and the buffer layer.

The question that rises from the characteristics discussed in Chapter 5 is: "How can we improve the open circuit voltage and the fill factor in order to obtain higher efficiencies?" The answer to this question is related to improving the interface between the Cu-rich absorber films and the buffer layer. One of the common means that was applied on Cu-poor films to improve the absorber/buffer interface is to use a surface post-deposition treatment. The challenge is then if the post-deposition treatments will work on Cu-rich films in the same way like Cu-poor or not? What are the optimizations that can be performed on the post-deposition treatments to increase the open circuit voltage and fill factor of the Cu-rich cells? Will the post-deposition treatments succeed in improving the interface and eventually improve the efficiency? These are the main questions that this chapter will answer.

The main quality factor for a solar cell is the efficiency, so the goal of the optimizations and improvements performed in this chapter is to eventually improve the efficiency. However, the main criteria this chapter will focus on it in the beginning is the open circuit voltage and the interface challenges as they represent the main challenges in Cu-rich cells compared to Cu-poor cells.

The first post-deposition treatment discussed in this Chapter is an ex-situ potassium fluoride (KF) treatment. This treatment is discussed in Section 6.1 and is performed on Cu-rich and Cu-poor CIS absorbers. I developed this post-deposition treatment (in collaboration with Finn Babbe). I was responsible for all the electrical characterizations (Chapter 4) presented in this section as well as the XRD characterizations (with the help of Erika Robert). XPS characterizations were performed externally by Luxembourg Institute of Science and Technology (LIST). We published the results of this ex-situ KF PDT in [1].

The second post-deposition treatment is an in-situ KF treatment. This treatment was developed on Cu-rich and Cu-poor CIS absorbers and the details of the characterizations of the treated absorbers are presented in Section 6.2. This in-situ KF post-deposition treatment was developed by me (in collaboration with Finn Babbe). I performed the electrical characterizations presented in this section while Finn Babbe performed the optical characterizations. Michele Melchiorre was responsible for characterizations using SEM and EDX. We published the results of this in-situ KF post-deposition treatment in [2].

The third post-deposition treatment introduced in this Chapter is a Gallium-Selenium (Ga-Se) treatment performed on Cu-rich CIGS absorbers. The details of the improvements achieved by this treatment are presented in Section 6.3. I was not responsible for developing this treatment. This treatment was developed by Leo Choubrac who also performed most of the electrical characterizations. I was only responsible for part of the electrical characterizations. Moreover, I was responsible for depositing the anti-reflection coating (ARC) layer and optimizing the ARC thickness layer in terms of lower optical losses. I performed IV, EQE measurements before and after adding the ARC layer as well as IVT, CV and ADM measurements for some of the cells. We published the results of this Ga-Se treatment in [3].

The fourth post-deposition treatment developed in this Chapter is a Se-only post-deposition treatment. This Se-only post-deposition treatment was performed on Cu-rich CIS absorbers. The characteristics of the treated absorbers and cells are presented in Section 6.4. I was responsible for developing this Se-only post-deposition treatment (in collaboration with Finn Babbe). Moreover, I was responsible for the electrical characterizations performed in this section while Finn Babbe was responsible for the optical characterizations. We published the results of this Se-only post-deposition treatment in [4].

The fifth optimization was performed on Cu-poor CIS and CIGS absorbers as presented in Section 6.5. The optimizations were performed by improving the absorber layer without using any post-deposition treatments. The optimizations were based on improving the efficiency and producing high performance low bandgap solar cells with the potential to be integrated for tandem applications. I was responsible for the fabrication of these absorbers (in collaboration with Finn Babbe). I performed the electrical characterizations presented in this section while Finn Babbe was responsible for measuring the quasi-Fermi Level splitting (qFLs). We published the results of these high performance low bandgap cells in [5].

6.1 Ex-situ KF post-deposition treatment for Cu-rich & Cu-poor CIS

The first post-deposition treatment introduced in this Chapter is an ex-situ KF post-deposition treatment (PDT). This treatment was mainly optimized for Cu-rich CIS absorbers with the objective of increasing the open circuit voltage. Then, the same conditions were applied on Cu-poor CIS absorbers to compare the effect of the treatment on both Cu-rich and Cu-poor CIS absorbers and solar cells. An ex-situ KF treatment means that the absorbers (developed in the PVD as presented in Section 3.1) were removed from the PVD, etched with KCN and then a 2-step post-deposition treatment was applied before completing the baseline process. The first step is depositing the KF using E-beam evaporation and then the second step is to place the absorbers (with KF on top) in a tube furnace to anneal the sample under certain conditions as explained in Section 3.2.1. Several conditions were tested to optimize the ex-situ KF treatment for Cu-rich solar cells. The objective of the optimization is to mainly improve the open circuit voltage and the absorber/buffer interface of Cu-rich cells.

As mentioned earlier, the ex-situ KF treatment used here is a 2-step process:

1. The first step is depositing the KF using E-beam evaporation. The possible optimization in this process is related to the KF thickness. The control of the KF thickness using the E-beam evaporation was quite challenging. The challenge is related to the nature of the KF being hygroscopic meaning that the KF absorbs water from air immediately after removing the treated absorber from the E-beam tool forming small water bubbles on the surface that can be observed by eye. Therefore, we decided to use the minimum possible amount of KF without performing further optimization for the thickness. We don't have an exact calculation for the thickness of the KF deposited but we speculate the KF thickness to be around 5 - 30 nm. This speculation is based on one experiment where we used two reference glass samples and deposited on one of them Lithium and for the other sample, we deposited a double layer of KF and Lithium (Lithium thickness is the same like the first sample). Lithium is more stable and when covering KF with Lithium, it becomes more realistic to measure the thickness. By comparing both thicknesses (Lithium only and KF plus Lithium), the KF thickness was found to be in the range of 5 – 30 nm.

2. The second step in the ex-situ KF PDT process is the annealing step. The process starts by heating the sample, annealing at a certain temperature and certain durations and then cooling down as presented in sub-section 3.2.1. Se was used throughout the whole process. The optimization for this process was based on changing the temperature of annealing, the duration and the amount of Se used. We found that using low amounts of Se always deteriorate the cell electrical performance showing a shunted behaviour. High enough Se did not show a real difference in terms of efficiency.

Therefore, the minimum amount of Se we decided to use is 40 mg. Two more critical parameters were tested: Annealing temperature and duration. It is important to note that our main criteria factor for optimization is the open circuit voltage (V_{OC}). A better V_{OC} means a better optimized performance. The annealing temperature was varied from 400 ^{0}C down to 300 ^{0}C in a step of 50 ^{0}C with the annealing duration fixed at 20 minutes. The annealing was then performed at temperatures of 400, 350 and 300 ^{0}C and the samples were then rinsed with de-ionized water to remove remaining fluorides and/or oxides. To study the effect of de-ionized water, the sample that was annealed at 350 ^{0}C was cut into half: one half was followed by de-ionized water after the annealing and the other half was etched with KCN etching after the annealing. The electrical performance of those cells was compared as presented in Table 6.1.

Table 6.1: IV parameters for Cu-rich CIS solar cells with and without different annealing conditions of the ex-situ KF PDT. The annealing temperature was varied from 400 ^{0}C down to 300 ^{0}C with a fixed annealing durations of 20 minutes. The sample annealed at 350 ^{0}C was cut into half where one half was followed by de-ionized water after annealing while the other half was followed by KCN etching after annealing. All other samples were followed by de-ionized water after annealing. The values presented in Table 6.1 represent the average of 6 solar cells while the values in bracket represent the maximum of these 6 solar cells.

Sample	Efficiency (%)	FF (%)	V_{OC} (mV)	J_{SC} (mA.cm^{-2})
Cu-rich CIS reference	**7.5 (7.8)**	**56.2 (57.9)**	**371 (375)**	**36.1 (39.8)**
Annealing @ 400 ^{0}C (de-ionized water)	0.0 (0.0)	5.8 (20.7)	10 (14)	10.5 (12.5)
Annealing @ 350 ^{0}C (de-ionized water)	1.5 (2.2)	33.1 (38.3)	145 (197)	29.6 (30.1)
Annealing @ 350 ^{0}C (KCN etching)	0.6 (0.9)	27.1 (28.4)	77 (102)	26.4 (29.7)
Annealing @ 300 ^{0}C (de-ionized water)	4.9 (5.3)	53.7 (56.0)	302 (313)	30.5 (31.9)

Based on Table 6.1, it can be observed that the efficiency improves with decreasing the annealing temperature. At 400 ^{0}C, the treated cell did not show a diode behaviour and the cell was shunted. Decreasing the temperature to 350 ^{0}C improved the efficiency to an average value of 1.5 % with a corresponding increase in the other electrical parameters. The FF, V_{OC} and J_{SC} increased to average values of 33.1 %, 145.4 mV and 29.6 mA/cm^2. Further decreasing the temperature to 300 ^{0}C leads to a further improvement in the electrical performance of the treated cells where the efficiency, FF, V_{OC} and J_{SC} improved to average values of 4.9 %, 53.7 %, 301.7 mV and 30.5 mA/cm^2. It is important to note that although the electrical performance of the treated samples improved as a function of decreasing temperature but the electrical performance is still lower compared to the reference Cu-rich CIS cell.

Further decrease of the temperature below 300 ^{0}C was found to produce shunted solar cells. Therefore, the optimization condition for the annealing temperature was chosen to be in the range of 300 – 350 ^{0}C. Table 6.1 also shows that a KCN etching step following the annealing step instead of a de-ionized water step is not beneficial for the electrical performance of the treated cell. At 350 ^{0}C, the electrical performance of the treated cell showed higher values for all the electrical parameters of the device with de-ionized water compared to the device with KCN etching step. Based on that, the de-ionized water was chosen to be more favourable following the annealing step.

The last optimization parameter was related to the annealing durations. The annealing duration used for the last experiment was 20 minutes. Using annealing durations of less than 20 minutes was found to further improve the electrical performance of the solar cell as shown below in Figure 6.2. The optimized conditions were then set to a KF thickness of 5 – 30 nm, annealing in the presence of at least 40 mg of Se, annealing temperatures in the range of 300 – 350 ^{0}C and annealing durations of less than 20 minutes. These optimized conditions succeeded in improving the V_{OC} values compared to the reference Cu-rich CIS untreated cell which is our main criteria for optimization, but failed to improve the FF and J_{SC} leading to a lower efficiency compared to the reference untreated Cu-rich CIS cell as presented below in Figure 6.2. A set of untreated Cu-rich and Cu-poor CIS absorbers were treated with these optimized conditions for the ex-situ KF PDT and compared to untreated CIS absorbers of the same deposition run. The characteristics of the treated cells compared to the untreated cells are presented below. Before introducing the IV characteristics, the EQE characteristics are presented to give an overview of the opto-electronic performance of the treated solar cells to be able to analyse better the IV performance.

EQE measurements were performed to the treated CIS absorbers and compared to untreated CIS absorbers as illustrated in Figure 6.1. A decrease in the short wavelength region (350 – 550 nm) of the EQE spectrum was observed for both treated Cu-rich and Cu-poor CIS cells. It is important to note that the turbidity of the CdS solution took longer time to change its colour from white to yellow for the treated CIS absorbers compared to untreated CIS absorbers. For the untreated absorbers (Cu-rich and Cu-poor CIS), the turbidity changes to a yellow colour after about 9 minutes while for the treated CIS absorbers the turbidity colour changed to yellow after about 10.5 minutes. The change of the turbidity colour in the chemical bath deposition process from white to yellow is the indication for the formation of the CdS buffer layer. The longer duration of the treated CIS absorbers (10.5 minutes) in the chemical bath compared to untreated CIS absorbers (9 minutes) shall indicate a thicker CdS buffer layer and could explain the decrease in the short wavelength region for the treated CIS absorbers. The decrease in the short wavelength region of the treated CIS absorbers can then be explained in terms of parasitic absorption by the CdS buffer layer. It is important to note that the same behaviour was observed for the CIS cells treated with the in-situ KF PDT compared to untreated CIS solar cells as presented in Section 6.2. The absorbers treated with in-situ KF PDT were also exposed to longer durations during the chemical bath deposition where the turbidity took longer time to change the colour from white to yellow.

In Section 6.2, we were able to measure the thickness of the CdS buffer layer for untreated and treated CIS cells and the CdS buffer layer was proven to be thicker for the treated CIS cells (Cu-rich and Cu-poor). Moreover, the same behaviour of the decrease in the short wavelength region of the EQE spectrum was observed for the CIS cells treated with the in-situ KF PDT compared to untreated CIS solar cells. Furthermore, this behaviour of thicker CdS buffer layer and decrease in the short wavelength region for the EQE spectrum of the treated CIS cells has been also reported for Cu-poor CIGS solar cells [6]. Therefore, it can be concluded that this decrease in short wavelength region observed in Figure 6.1 for the CIS cells treated with an ex-situ KF PDT compared to untreated CIS cells can be attributed to an increased CdS absorption through the formation of a thicker CdS buffer layer.

At higher wavelengths close to the bandgap (1100 – 1200 nm), Cu-rich CIS treated cells show slightly higher EQE response compared to untreated Cu-rich CIS cells (green curves). On the other side, the treated Cu-poor CIS cells showed lower EQE values compared to untreated Cu-poor CIS cells (red curves) as indicated in Figure 6.1.

Moreover, the integrated J_{SC} (J_{SC_EQE}) for the whole spectrum did not suffer the same loss for Cu-rich (ΔJ_{SC_EQE} = -0.5 mA/cm^2) as for Cu-poor (ΔJ_{SC_EQE} = -2.5 mA/cm^2) CIS solar cells. The carrier collection efficiency calculated based on equation 5.1 after the ex-situ KF treatment showed values of 77.4 % for Cu-rich CIS, less than the untreated Cu-rich CIS, but still higher than the untreated Cu-poor CIS cells (77.1 %) as presented in Table 6.2.

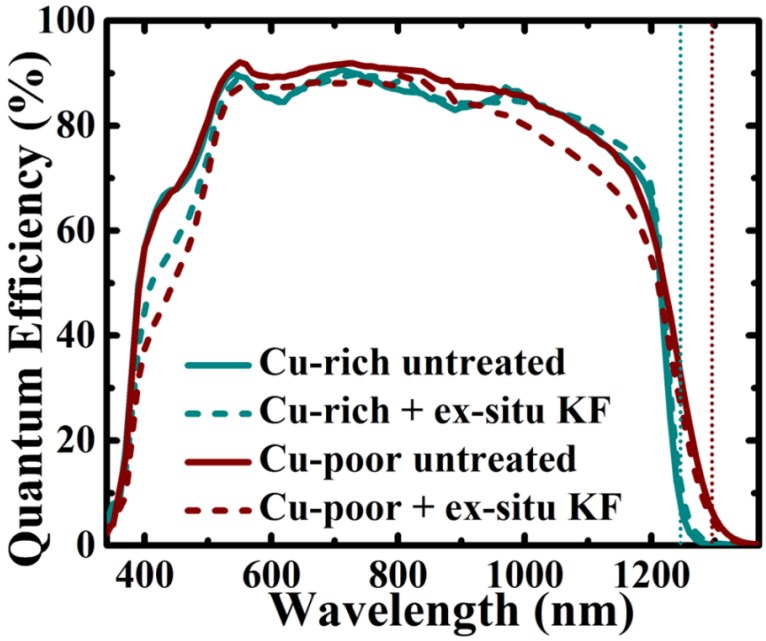

Figure 6.1: EQE spectrum response for both Cu-rich and Cu-poor CIS cells with and without the ex-situ KF PDT. The bandgaps are extrapolated from the linear interception of the EQE curve with the wavelength axis (X-axis) as explained in Section 4.2. The extrapolated bandgaps for each of the Cu-rich and Cu-poor are represented by the short dotted lines

Table 6.2: Calculations for the carrier collection efficiency of Cu-rich and Cu-poor CIS cells with and without the ex-situ KF PDT. Calculations are based on the EQE measurements.

Sample	J_{SC_EQE} (mA.cm^{-2})	J_{SC_MAX} (mA.cm^{-2})	Carrier Collection Efficiency (%)
Cu-rich	37.9	48.2	78.6
Cu-rich treated	37.4	48.3	77.4
Cu-poor	38.8	50.3	77.1
Cu-poor treated	36.3	50.2	72.3

The drop in the J_{SC_EQE} is reflected on the J_{SC} from IV measurements. The J_{SC} for both Cu-rich and Cu-poor CIS cells decreased after the ex-situ KF treatment as presented in Table 6.2. The decrease in the J_{SC} of the treated Cu-rich CIS cell (J_{SC_EQE} = 37.4 mA/cm^2 and J_{SC} from IV = 37.8 mA/cm^2) compared to the untreated Cu-rich CIS cell (J_{SC_EQE} = 37.9 mA/cm^2 and J_{SC} from IV = 38.9 mA/cm^2) is mainly attributed to the optical losses in the short wavelength region presented in Figure 6.1.

However, for the Cu-poor CIS cells, the decrease in the J_{SC} values is more severe due to the optical losses in the short wavelength region presented in the EQE spectrum of Figure 6.1 (similar to Cu-rich CIS cells) plus additional losses observed at long wavelength regions of the EQE spectrum and not observed for Cu-rich CIS cells. The origin of these additional losses in Cu-poor CIS treated cells is not fully clear. These additional losses were responsible for further decreasing the J_{SC} values of the Cu-poor CIS treated cells (J_{SC_EQE} = 36.3 mA/cm^2 and J_{SC} from IV = 40.3 mA/cm^2) compared to Cu-poor CIS untreated cells (J_{SC_EQE} = 38.8 mA/cm^2 and J_{SC} from IV = 42.0 mA/cm^2).

On the other side, the main success of the ex-situ KF PDT is in the improvement of the V_{OC}. The V_{OC} increased for Cu-rich CIS cells (ΔV_{OC} = + 36.6 mV) and Cu-poor CIS cells (ΔV_{OC} = + 12.9 mV) as observed in Figure 6.2. These V_{OC} improvements for both Cu-rich and Cu-poor CIS cells are close to the values reported in literature which showed an improvement of 30 – 60 mV after an ex-situ KF PDT [7, 8]. The improvement in the V_{OC} for Cu-rich CIS cells can be attributed to a passivation of a defect that will be discussed in chapter 7. The passivation of this defect lead to an increase of the V_{OC} for Cu-rich CIS treated cells as well as a corresponding improvement to the interface as explained later in Figure 6.3. Moreover, it can be observed from Figure 6.2 that the ex-situ KF PDT succeeded in minimizing the breakdown behaviour observed for Cu-rich CIS devices at reverse bias [9]. This breakdown behaviour of untreated Cu-rich CIS cells is not observed for the treated Cu-rich CIS cells within the measurement range.

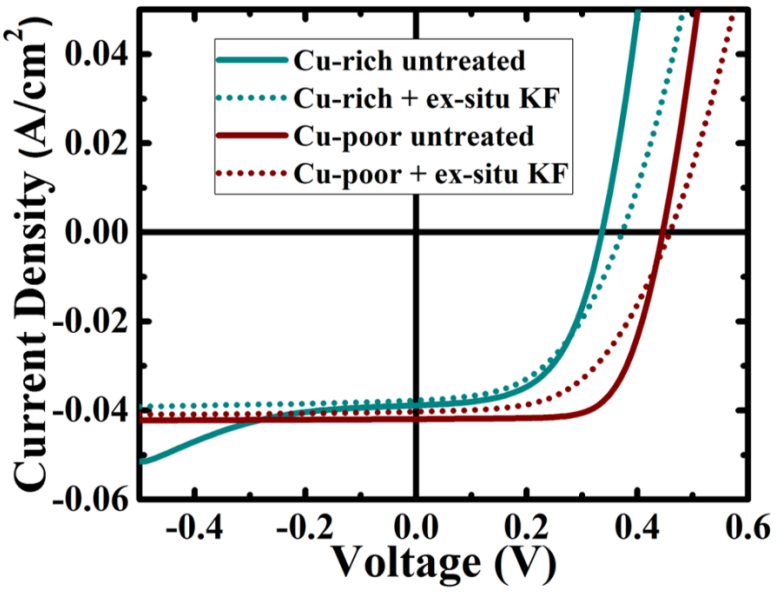

Figure 6.2: IV characteristics for both Cu-rich and Cu-poor CIS cells with and without the ex-situ KF PDT. The presented IV curves are for the same cells presented in Figure 6.1. The same trend in EQE and IV characteristics of Cu-rich and Cu-poor with and without the ex-situ KF PDT was observed for another five solar cells.

However, the improvement in the V_{OC} was not enough to increase the efficiency of the treated CIS absorbers due to a drop in the FF observed in the treated CIS cells and presented in Figure 6.2. The FF depends mainly on the series resistance, shunt resistance and ideality factor as explained in Section 4.1. As the shunt resistances improved after the ex-situ KF PDT for both Cu-rich and Cu-poor CIS cells, the drop in FF can be attributed to the increase in the series resistance as well as an increase in the ideality factor for both Cu-rich and Cu-poor CIS treated cells as presented in Table 6.3. The increase in the series resistance after the ex-situ KF treatment can be attributed to the formation of a new layer at the surface of the absorbers as explained below. Moreover, an additional potential reason for the increase in the series resistance and the corresponding decrease in FF is the introduction of a transport barrier after the ex-situ KF treatment as can be deduced from the series resistance measurements as function of temperature presented in Figure 6.4.

Table 6.3: Electrical parameters for both Cu-rich and Cu-poor CIS cells with and without the ex-situ KF PDT. The values of R_S and A were obtained by fitting the IV curve measured under dark conditions with the single diode model of the ECN IV curve fitting program ivfit [10].

Sample	Efficiency (%)	FF (%)	V_{OC} (mV)	J_{SC} ($mA.cm^{-2}$)	R_S ($Ohm.cm^2$)	A
Cu-rich CIS	7.4	57	336	38.9	0.5	1.4
Cu-rich treated	7.0	49	372	37.8	0.9	1.8
Cu-poor CIS	12.8	68	446	42.0	0.6	1.3
Cu-poor treated	9.9	54	458	40.3	1.2	2.0

IVT measurements were performed for Cu-rich and Cu-poor CIS solar cells after the ex-situ KF treatment to understand the mechanism behind the improvement of the V_{OC} and the impact of the treatment on the absorber/buffer interface [11, 12]. The interpretation of the IVT measurements and the extrapolation of the activation energy at zero Kelvin from the V_{OC} (T) were explained in Section 4.3. The V_{OC} (T) curves are presented in Figure 6.3.

It can be observed from Figure 6.3 that for Cu-poor CIS cells, the extrapolated activation energies with and without the ex-situ KF treatment are almost the same with no negative impact of the ex-situ KF treatment. However, for Cu-rich CIS cells, a significant improvement is achieved after the ex-situ KF PDT. The extrapolated activation energy at zero Kelvin for the treated Cu-rich CIS cell is close to the bandgap.

This improvement in the extrapolated activation energy at zero Kelvin for Cu-rich CIS devices after the ex-situ KF PDT means that the ex-situ KF treatment succeeded in moving the dominant recombination path in Cu-rich CIS cells from the interface to the bulk. Not only that, but it is interesting to note that the ex-situ KF treatment succeeded also in removing one of the two slopes typically observed for untreated Cu-rich CIS solar cells in the V_{OC} (T) curve as presented in Section 5.3. In Section 5.3, it has been highlighted that Cu-rich CIS cells show two different negative slopes in the V_{OC} (T) curve before the V_{OC} values saturate or decrease at lower temperatures. The ex-situ KF PDT succeeded in removing one of these two negative slopes (removing the slope whose activation energy at zero Kelvin extrapolates to values much lower than the bandgap) leading to only one slope for the treated Cu-rich CIS cell (whose activation energy at zero Kelvin extrapolates to values close to the bandgap) before the V_{OC} values decrease at lower temperatures. The reason behind the decrease in the V_{OC} values at lower temperatures is not fully understood. The removal of one of the two slopes in the V_{OC} (T) curve and the increase in the V_{OC} values are two of the characteristics of the passivation of one defect present in Cu-rich CIS cells and explained in detail in chapter 7.

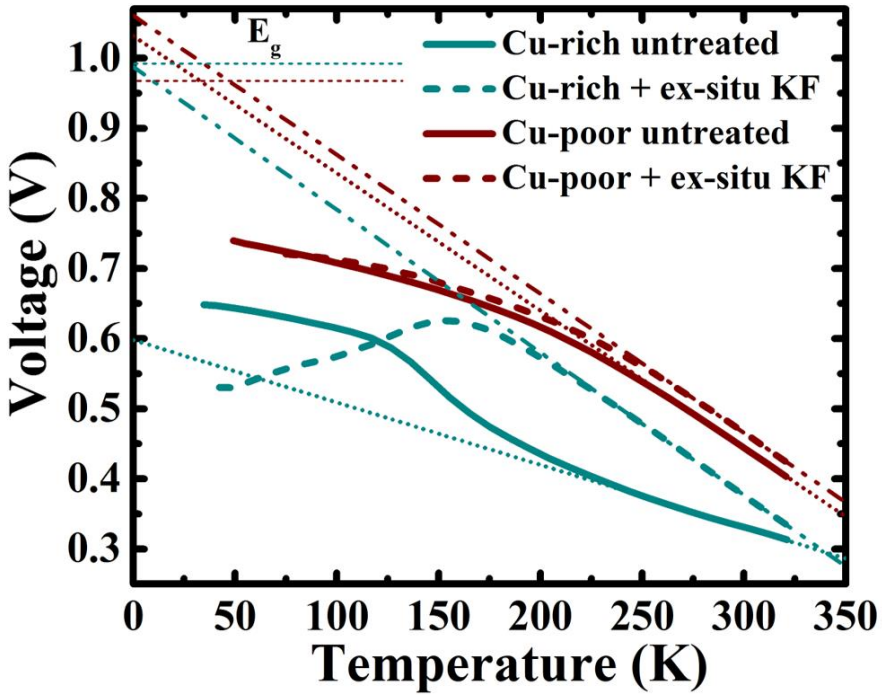

Figure 6.3: Temperature dependence of voltage for Cu-rich and Cu-poor CIS cells with and without the ex-situ KF PDT. Dashed double dotted lines represent the extrapolated activation energy to zero Kelvin. The bandgap (deduced from EQE measurements) is represented by the short dashed lines.

From the IVT measurements, the series resistance as function of temperature was extracted at far forward bias (1.2 V) for each of the treated Cu-rich and Cu-poor CIS cells and the corresponding Arrhenius plot is presented in Figure 6.4. The series resistance is extracted from the slope of the IV curve at the voltage of 1.2 V at each temperature (from 320 K down to 50 K) as explained in Section 4.3. The activation energy of the thermally activated series resistance was then deduced from the Arrhenius plot explained in Section 4.3 and presented in Figure 6.4. From Figure 6.4, it can be observed that there is a significant increase in the activation energy of the series resistance for Cu-rich CIS cells after the ex-situ KF PDT while a slight increase is observed for the activation energy of the series resistance for Cu-poor CIS cells after the ex-situ KF PDT. The activation energy of the thermally activated series resistance for the Cu-rich CIS cell increased from 65 to 220 meV while the values for Cu-poor CIS cells slightly increased from 80 to 90 meV. It is important to note that the increase in the activation energy of the series resistance for Cu-poor CIS solar cells after the ex-situ KF PDT starts from higher temperatures compared to untreated Cu-poor CIS cell where the series resistance was only activated at very low temperatures. At intermediate temperatures, the series resistance values were decreasing for untreated Cu-poor CIS cells but were then thermally activated and increased after the ex-situ KF PDT with the decrease of the temperature. This means that the ex-situ KF treatment introduced a transport barrier for both Cu-rich (indicated by the significant increase of the series resistance activation energy) and Cu-poor (indicated by the presence of a thermally activated series resistance for the treated Cu-poor CIS cell at temperatures where the series resistance was not activated for the untreated Cu-poor CIS cell) CIS solar cells. This transport barrier can then be responsible for the increase in the series resistance and consequently the decrease in the FF as mentioned earlier.

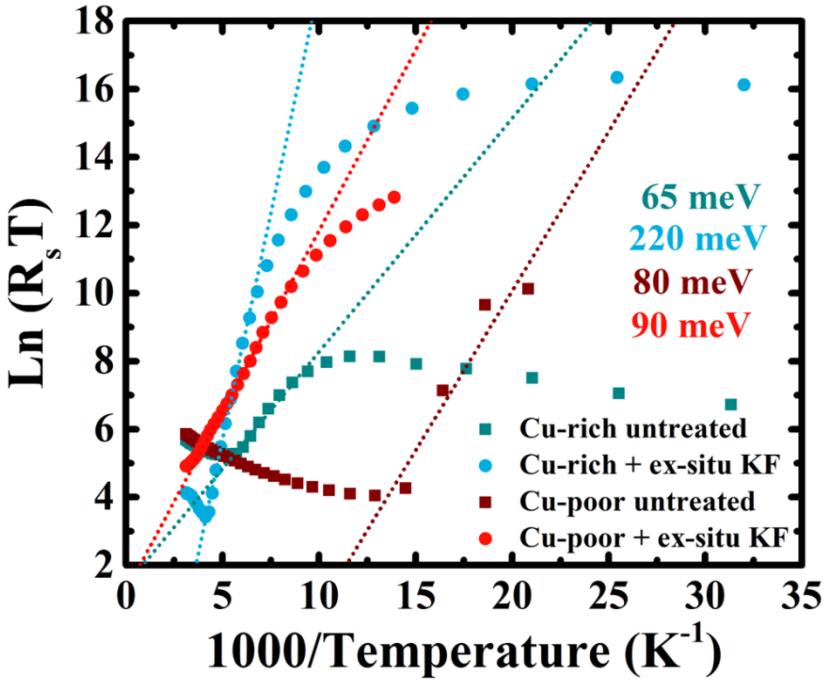

Figure 6.4: Arrhenius plot for the series resistance as function of temperature deduced from IVT measurements at 1.2 V for both Cu-rich and Cu-poor CIS cells with and without the ex-situ KF PDT. The activation energies of the series resistance increased significantly for Cu-rich CIS cells from 65 to 220 meV and slightly increased for Cu-poor CIS cells from 80 to 90 meV after the ex-situ KF PDT.

Admittance measurements were also performed for both Cu-rich and Cu-poor CIS cells after the ex-situ KF treatment. The Arrhenius plots of the main capacitance step for the treated Cu-rich and Cu-poor CIS cells are presented in Figure 6.5. Cu-rich CIS treated cells show an admittance step with an activation energy of 260 meV. This value is in close proximity with the activation energy of the series resistance extracted from the IVT measurements in Figure 6.4 (220 meV). Combining these results could mean that this 260 meV capacitance step is due to a barrier and not the typical defect for the untreated Cu-rich CIS devices. On the other side, Cu-poor CIS cells still showed the 130±15 meV capacitance step typically observed for our Cu-poor CIS cells as presented in Section 5.4 and Figure 5.8. We have attributed this 130±15 meV to a third acceptor defect as explained in Section 6.4 and we published these results in [13].

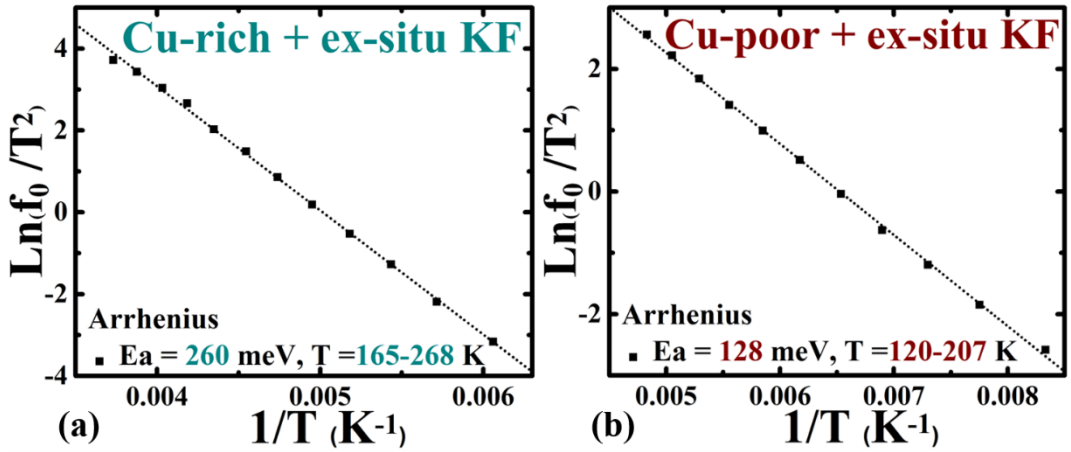

Figure 6.5: Arrhenius plot of the main capacitance step deduced from admittance measurements for a) Cu-rich CIS cell and b) Cu-poor CIS cell after the ex-situ KF PDT.

The origin of the transport barrier observed by the IVT measurements and responsible for the increase in the series resistance could be explained in terms of the introduction of a new layer formed at the surface of the CIS absorbers after the ex-situ KF treatment [7, 8, 14]. This layer has been proven to be present in both the treated Cu-rich and Cu-poor CIS absorbers after performing XRD and XPS measurements explained below.

XRD measurements were performed to check if new peaks could appear after the ex-situ KF treatment indicating the formation of new compounds or not. Figure 6.6a shows the XRD measurements for Cu-rich CIS absorber with and without the ex-situ KF treatment, while Fig. 6.6b presents that for Cu-poor CIS absorber with and without the ex-situ KF treatment.

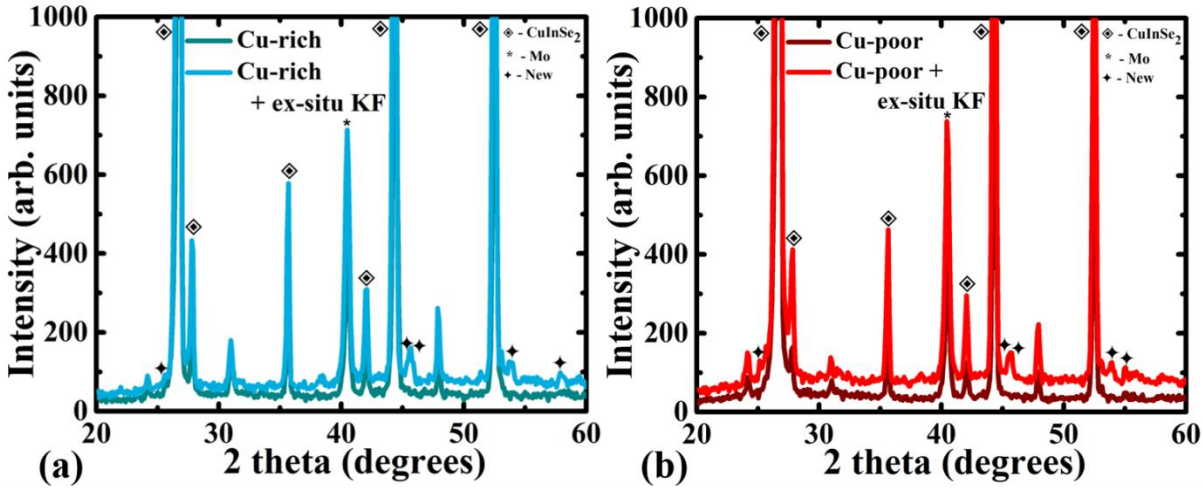

Figure 6.6: XRD measurements for a) Cu-rich and b) Cu-poor CIS absorbers before and after the ex-situ KF PDT

Interestingly, five new peaks appeared for both Cu-rich and Cu-poor CIS absorbers after the ex-situ KF treatment. Four of these five peaks are identical for Cu-rich and Cu-poor CIS absorbers after the ex-situ KF PDT while the fifth peak is different between Cu-rich and Cu-poor CIS treated absorbers. The identification of the new peaks formed after the ex-situ KF treatment was not clear but these new peaks are themselves an indication for the formation of a new layer. We also suggest that the new peaks may not be attributed to a single compound.

On the other side, XPS measurements were performed to highlight the chemical changes taking place at the surface of the absorbers after the ex-situ KF treatment. XPS measurements were performed for both Cu-rich and Cu-poor CIS absorbers after the ex-situ KF treatment at the surface with 0 second of sputtering, then deeper after three sputtering steps of 120, 240 and 720 seconds. The sputtering step at 720 seconds should correlate to an approximate depth of 50 nm deep and is expected to reflect the CIS bulk properties. The results of these measurements are presented in Figure 6.7. The binding energies were normalized to the In peak binding energy.

It can be observed from Figure 6.7 that the XPS spectra as a function of depth are quite similar between Cu-rich and Cu-poor CIS treated absorbers. Moreover, the XPS spectra between 120, 240 and 720 seconds of sputtering are identical but different from the surface spectra (0 second of sputtering). This means that the unsputtered surface spectrum is the one showing the characteristics of the surface layer while the other deeper sputtered spectra indicate the bulk of the absorbers. It is important to note that the spectra of Cu, In and Se peaks at the surface (unsputtered) have lower intensity compared to the bulk (deeper spectra) putting in consideration the multiplication factors indicated in Figure 6.7. As the absorbers were transferred in ambient air to the XPS, it is expected that they became contaminated and the intensity at the surface became lower. The oxygen from the ambient air reacts with the absorber surface (indicated by EDX and XPS measurements and explained in more detail in Chapter 7). This oxygen contamination then dominates on the surface leading to a decrease in the intensity of Cu, In and Se on the absorber surface compared to the absorber bulk.

What is indeed interesting in these measurements is three observations:

1. The first one is that the Cu peak is observed (but in lower amounts) at the surface of both treated CIS absorbers which is contradictory to several reports [7, 8, 15] where the KF PDT leads to a completely Cu-depleted surface.

2. The second observation is related to the Cu/In ratio where the Cu/In ratio is reduced in Cu-rich CIS treated absorber by a factor of 2 compared to the bulk while it was reduced by a factor of 8 in the case of the Cu-poor CIS surface compared to its bulk. This could mean that either the KF PDT formed a non-continuous layer at the surface as reported in [14] or this means that the ex-situ KF PDT formed a different layer at the surface that still contains Cu.
3. The last interesting observation is related to the energy of the Cu-peak at the surface. The Cu-peak at the surface was observed to be shifted by 0.4 eV to lower energies compared to the bulk peak. This 0.4 eV shift is towards the lower binding energies and cannot be explained in terms of Cu surface oxidation as Cu oxides should have moved the Cu-peak towards higher binding energies and not lower ones [16]. Moreover, this shift is not due to Cu_xSe compounds since it can be observed at both Cu-rich and Cu-poor CIS surfaces and not only in Cu-rich CIS surface. In addition to that, both Cu-rich and Cu-poor CIS surfaces were KCN etched before performing the measurements which means no Cu_xSe compounds are expected to be present on the surface of the etched CIS absorbers. Based on that, it can be concluded that the surface layer of both Cu-rich and Cu-poor CIS treated absorbers does contain Cu but present in a different chemical structure or different chemical environment compared to their bulks.

The In peaks (In 3d peak) did not show any change on the surface compared to the bulk for both Cu-rich and Cu-poor CIS treated absorbers. This means that the In concentrations measured at the surface and the bulk of the treated CIS absorbers are more or less stable with no signature for the change of the In chemical structure between the surface and the bulk of the treated CIS absorbers. The Se peaks (Se 3d peak) show a peak doublet for the Se spectra at the absorber surface and bulk of the treated CIS absorbers. For the Cu-poor treated CIS absorber, the same Se peak doublet at the same binding energies was observed at the surface and the bulk. However, for the Cu-rich CIS treated absorber, the Se-peak doublet showed a relatively small shift (0.15 eV) to higher binding energies at the surface compared to the bulk. This shift of Se peak at the surface of the Cu-rich CIS treated absorber could indicate the presence of Se in a different chemical structure at the surface. An additional Se peak is observed at a binding energy of approximately 59 eV for both Cu-rich and Cu-poor CIS treated absorbers but only at the surface and not in the bulk of the treated absorbers. This additional Se peak could be attributed to Se oxides whose binding energies lie in the same energy range of 58 – 59 eV [17]. This additional Se peak is marked as a SeO_2 in Figure 6.7 (c, d).

The interpretation of the results from both the XRD and XPS measurements together can be summarized in the following points:

- The XRD measurements showed four new peaks that are similar for Cu-rich and Cu-poor CIS treated absorbers and one additional new peak that is different from Cu-rich and Cu-poor CIS treated absorbers.
- The XPS measurements showed that In peaks (In 3d peak) did not change between the bulk and the surface of both Cu-rich and Cu-poor CIS treated absorbers.
- However, the XPS revealed that the Cu-peak (Cu 2p peak) was shifted to lower binding energies at the surface compared to the bulk of the Cu-rich and Cu-poor CIS treated absorbers. This means that Cu is present in a different chemical structure at the surface of both Cu-rich and Cu-poor CIS treated absorbers.
- Assuming that the bulk represents the CIS phase and the surface represents the changes occurred as a result of the ex-situ KF PDT, the shift in the Cu-peak at the surface of the treated absorbers could be in an excellent agreement with the four new peaks observed by XRD.
- We can then speculate that at least some of these four new peaks are related to a different compound that contains Cu and was formed at the surface of the treated CIS absorbers.
- We can also speculate that some of these four new peaks (observed by XRD) could be attributed to Se-oxides that were observed by XPS at the surface of both treated absorbers.
- XPS also revealed the shift of Se-peaks (Se 3d peak) to higher binding energies at the surface of the Cu-rich CIS treated absorber only and not at the surface of the Cu-poor CIS treated absorber.
- We can then speculate that Se is present in a different chemical compound on the surface of Cu-rich CIS treated absorber and then the fifth new peak observed by XRD for Cu-rich CIS treated absorber and not for Cu-poor CIS treated absorber could be attributed to this different chemical compound containing Se.

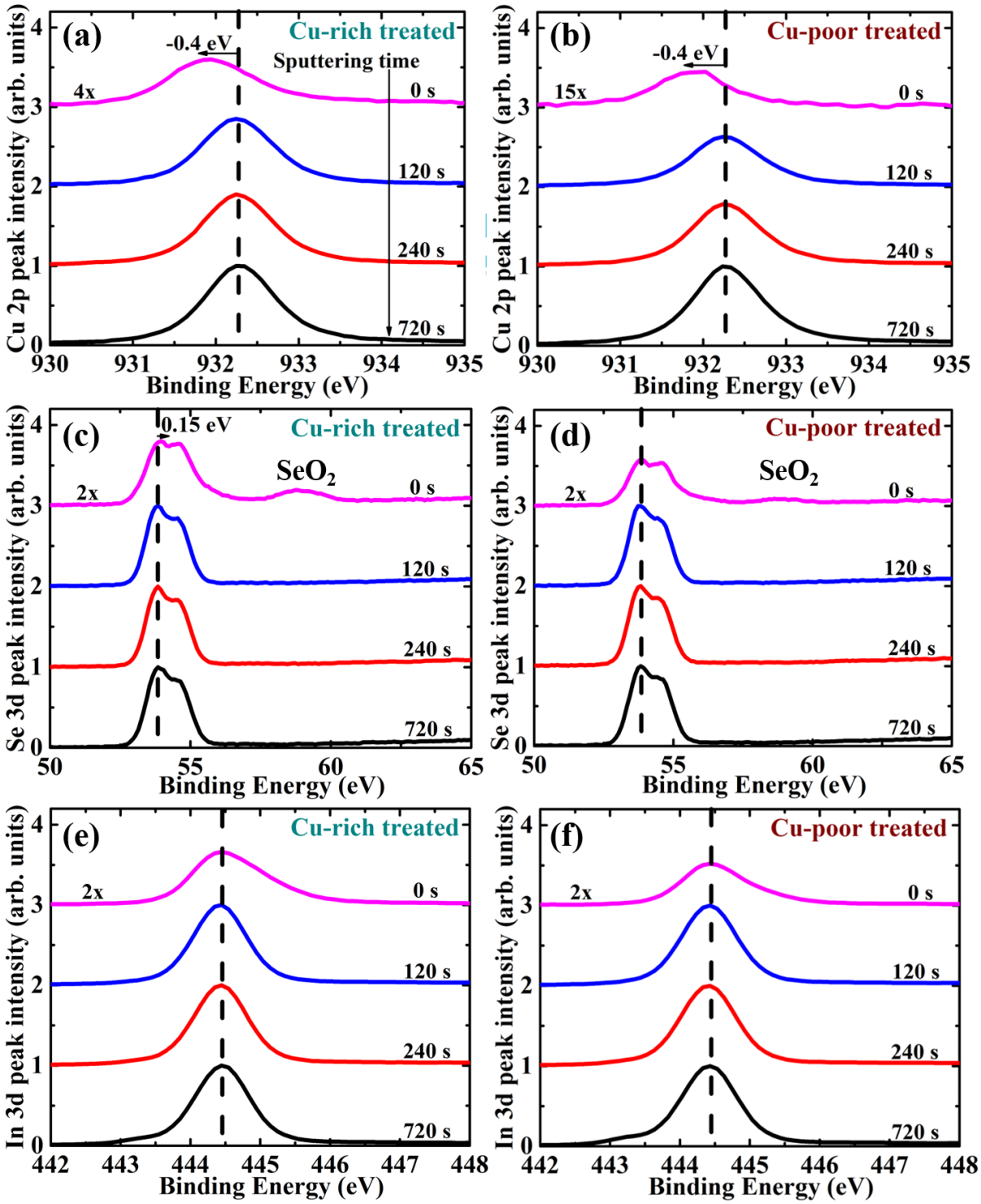

Figure 6.7: XPS measurements for a) Cu 2p-peak for Cu-rich, b) Cu 2p-peak for Cu-poor, c) Se 3d-peak for Cu-rich, d) Se 3d-peak for Cu-poor, e) In 3d-peak for Cu-rich, f) In 3d-peak for Cu-poor CIS absorbers after the ex-situ KF PDT

To conclude, the ex-situ KF PDT indeed succeeded in increasing the V_{OC} and improving the interface of the Cu-rich CIS cells but it is still not the ideal surface treatment due to the strong hygroscopic nature of KF that hindered the control of the KF layer thickness as explained earlier from one side and introduced oxygen and hydrogen atoms to the CIS absorber surface from another side. This has impacted negatively the electrical performance of CIS solar cells especially in terms of FF through introducing a transport barrier for both Cu-rich and Cu-poor CIS treated absorbers. To overcome these issues and avoid the hygroscopic KF behaviour, an in-situ KF PDT was developed in the next section.

6.2 In-situ KF post-deposition treatment for Cu-rich & Cu-poor CIS

To overcome the strong drop in FF that happened with the ex-situ KF treatment and improve the quality of the PDT used, an in-situ KF treatment was developed as explained in section 3.2.2. The in-situ KF treatment was performed such that the KF deposition and annealing are performed in one step without exposing the KF to air to avoid the negative effects of the hygroscopic nature of KF explained in Section 6.1. In this section, I will introduce the most optimized in-situ KF treatment on Cu-rich and Cu-poor CIS absorbers as described in Section 3.2.2. As the ex-situ KF PDT succeeded in improving the V_{OC} but not the efficiency, the goal of the optimization of the in-situ KF PDT was set to improve both the V_{OC} and the efficiency of the treated solar cells. The optimization was performed in terms of both annealing temperature and annealing duration. The optimization of the annealing temperature revealed the same trend observed by the ex-situ KF PDT and discussed in Section 6.1. Annealing at temperatures above 350 ^{0}C produce shunted solar cells and annealing at temperatures below 300 ^{0}C affects the V_{OC} and FF negatively. Therefore, for the annealing temperature, the optimized conditions were set in the range of 300 – 350 ^{0}C. The optimization of the annealing duration is discussed in this section as presented below. The optimization of the annealing duration was performed on Cu-rich CIS absorbers with the goal of improving the V_{OC} and efficiency values and the optimized conditions were then applied to Cu-poor CIS absorbers to compare the different characteristics between Cu-rich and Cu-poor CIS treated absorbers and solar cells. It is then important to highlight that the optimization was not performed for Cu-poor CIS absorbers, only the optimized conditions for Cu-rich CIS solar cells were applied on Cu-poor CIS absorbers.

As mentioned earlier, in this section I will introduce the different characterizations performed to optimize the in-situ KF PDT for Cu-rich CIS absorbers in terms of annealing duration. A series of Cu-rich CIS absorbers (from the same growth deposition run) treated with an in-situ KF PDT with exactly the same treatment conditions except for the treatment annealing duration that was varied between 4, 8 and 12 minutes is introduced in this section to understand the different characteristics of KF PDT as function of annealing time and consequently KF thickness. For comparison, a Cu-poor CIS absorber was treated with an in-situ KF PDT for an annealing duration of 6 minutes. The annealing duration for Cu-poor CIS absorber was chosen to be 6 minutes as a mean value between 4 and 8 minutes which proved to be the most optimized conditions for Cu-rich CIS solar cells.

Some characteristics of the in-situ KF PDT can be already observed on the CIS absorbers themselves through the SEM monographs shown in Figure 6.8.

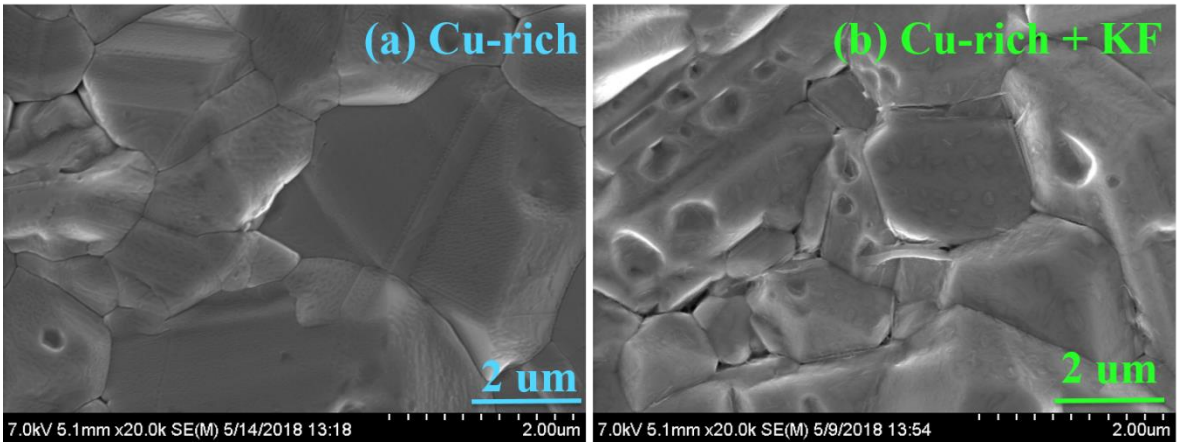

Figure 6.8: SEM monographs for a) Cu-rich and b) Cu-rich CIS treated with in-situ KF for 8 minutes

The top view SEM monograph in Figure 6.8 indicates clearly the formation of a surface patterning on the treated Cu-rich CIS absorber (Figure 6.8b) compared to the untreated Cu-rich CIS absorber (Figure 6.8a). The Cu-rich CIS absorber in Figure 6.8 was treated for 8 minutes. This basically proves that the in-situ KF treatment is already changing the surface morphology of the absorbers in a similar manner to Cu-poor absorbers as reported for CIGS [14, 18].

Finished solar cells were characterized to analyse the effect of the in-situ KF treatment from an electrical and optical point of views. Cu-rich CIS absorbers treated for more than 12 minutes suffered from reduced V_{OC} and FF. In this section, we will focus on Cu-rich CIS absorbers treated for 12 minutes or less (a series of 4, 8 and 12 minutes) and compare them to Cu-poor CIS absorbers treated for 6 minutes. The electrical parameters of these treated CIS solar cells are presented in Table 6.4 and their corresponding IV curves are illustrated in Figure 6.9.

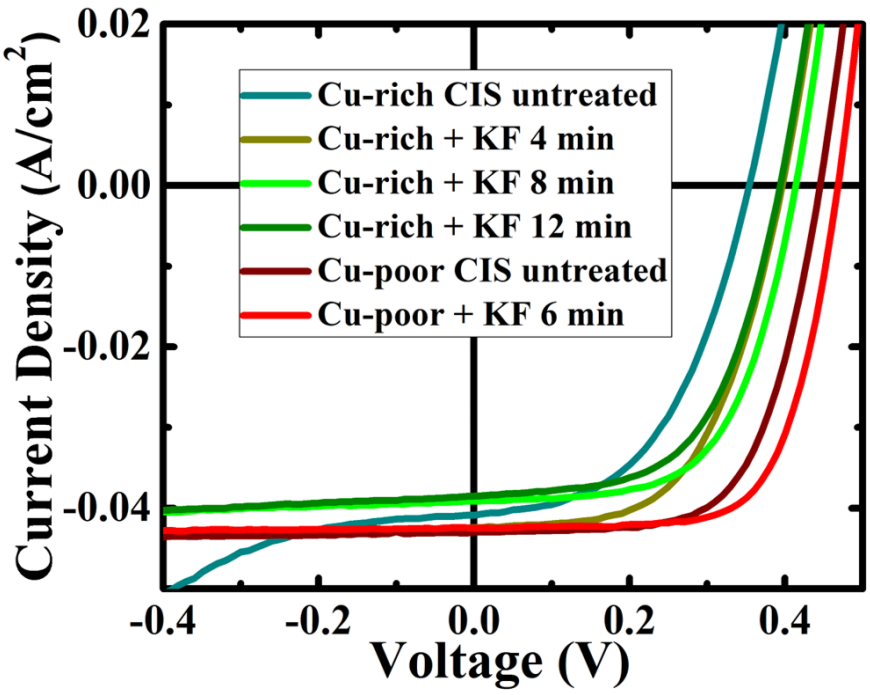

Figure 6.9: IV parameters for Cu-rich and Cu-poor CIS cells with and without the in-situ KF PDT

Table 6.4: Electrical parameters for both Cu-rich and Cu-poor CIS cells with and without the in-situ KF PDT. The values of R_S, R_{Sh} and A were obtained by fitting the IV curve measured under dark conditions with the single diode model of the ECN IV curve fitting program ivfit [10].

Sample	Efficiency (%)	FF (%)	V_{OC} (mV)	J_{SC} (mA.cm^{-2})	R_S (Ohm.cm^2)	R_{Sh} (Ω.cm^2)	A (-)
Cu-rich CIS untreated	7.0 (7.2)	50.6 (52.8)	347 (355)	39.5 (41.5)	0.4 (0.3)	120 (370)	1.87 (1.81)
Cu-rich CIS + KF 4 min	9.5 (10.0)	58.0 (61.2)	398 (405)	41.1 (42.4)	0.6 (0.4)	1400 (1860)	1.63 (1.54)
Cu-rich CIS + KF 8 min	9.4 (9.9)	60.8 (64.3)	410 (416)	37.7 (39.1)	0.4 (0.3)	1110 (1340)	1.63 (1.50)
Cu-rich CIS + KF 12 min	8.8 (9.3)	59.9 (61.7)	395 (403)	37.0 (38.7)	0.5 (0.3)	900 (1230)	1.64 (1.60)
Cu-poor CIS untreated	11.8 (12.3)	64.0 (66.0)	445 (447)	41.3 (43.0)	0.4 (0.2)	853 (1285)	2.05 (1.95)
Cu-poor CIS + KF 6 min	13.0 (13.6)	68.3 (69.4)	467 (471)	40.8 (42.5)	0.3 (0.2)	3884 (5025)	1.57 (1.51)

The in-situ KF treatment succeeded in improving the Cu-rich and Cu-poor CIS solar cells in terms of both V_{OC} and FF as illustrated in Figure 6.9. In terms of V_{OC}, Cu-rich CIS cells improved by 50 – 60 mV for the three treatment durations of 4, 8 and 12 minutes where the best improvement in terms of V_{OC} occurred for the 8-minute treatment. For Cu-poor CIS cells, a less pronounced improvement was observed for the V_{OC} (20 – 30 mV). These improvements in the V_{OC} after the in-situ KF PDT (50 – 60 mV) are higher compared to the V_{OC} improvements after the ex-situ KF PDT (35 mV). However, these V_{OC} improvements after the in-situ KF PDT (50 – 60 mV) are less than the V_{OC} improvements reported in literature after an in-situ KF PDT [19] which show an increase in the V_{OC} values in the range of 100 – 120 mV. It is important to note that the KF PDT in [19] was performed on Cu-poor CIGS absorbers while our in-situ KF PDT was optimized mainly for Cu-rich CIS absorbers.

In terms of FF, the in-situ KF treatment succeeded in avoiding the drop that occurred with the ex-situ KF PDT (as presented in Section 6.1) improving the FF by around 10 % for Cu-rich CIS cells with the best improvement taking place for the 8-minute treatment. This makes the 8-minute treatment the best one in terms of both V_{OC} and FF. Similar to Cu-rich CIS cells; the in-situ KF treatment increased the FF by 4 – 5 % for Cu-poor CIS cells. The improvement in V_{OC} for Cu-rich CIS cells will be explained in chapter 7 as a result of passivating a 200 ± 20 meV defect. For the FF, the improvement for both Cu-rich and Cu-poor CIS cells after the in-situ KF PDT compared to the ex-situ treatment can be explained in terms of avoiding the transport barrier that appeared in the activation energy of the series resistance as a function of temperature after the ex-situ KF PDT (as explained in section 6.1) and did not appear after the in-situ KF PDT as explained below when discussing the IVT measurements. Moreover, the in-situ KF PDT succeeded in improving significantly the shunt paths in both Cu-rich and Cu-poor CIS cells as depicted by the increase of the shunt resistances values after the in-situ KF PDT as well as lowering the diode ideality factor (reduced in Cu-rich CIS from 1.9 to 1.6 and in Cu-poor CIS from 2.0 to 1.6) as presented in Table 6.4. These improvements in shunt resistances and ideality factor played an additional role in the improvement observed for the FF. Furthermore, the in-situ KF treatment succeeded in improving the breakdown behaviour observed for Cu-rich CIS untreated solar cells at reverse bias [9], where this breakdown is not observed for any of the treated solar cells within the measurement range as illustrated in Figure 6.9.

These successful improvements lead to a corresponding increase in the efficiency from an average of 7 % for the untreated Cu-rich CIS cells to around 10 % for the treated Cu-rich CIS cells while for Cu-poor CIS cells, the efficiency increased from around 12 to 13.5 % after the in-situ KF PDT. These significant improvements in the efficiency are mainly due to the corresponding improvements in the V_{OC} and the FF, while the J_{SC} dropped for all treated Cu-rich and Cu-poor CIS cells. The only exception for that was the 4-minute treated Cu-rich CIS cell where the J_{SC} improved after the treatment making the 4-minute treatment the best treatment optically (in terms of J_{SC}) for Cu-rich CIS cells. This improvement in J_{SC} for the 4-minute treated cell compensated the slightly less V_{OC} and FF compared to the 8-minute one making both the 4- and the 8-minute treatments the best treatments for Cu-rich CIS absorbers. The behaviour of the J_{SC} can be explained by analysing the EQE spectra for both Cu-rich and Cu-poor CIS cells in Figure 6.10.

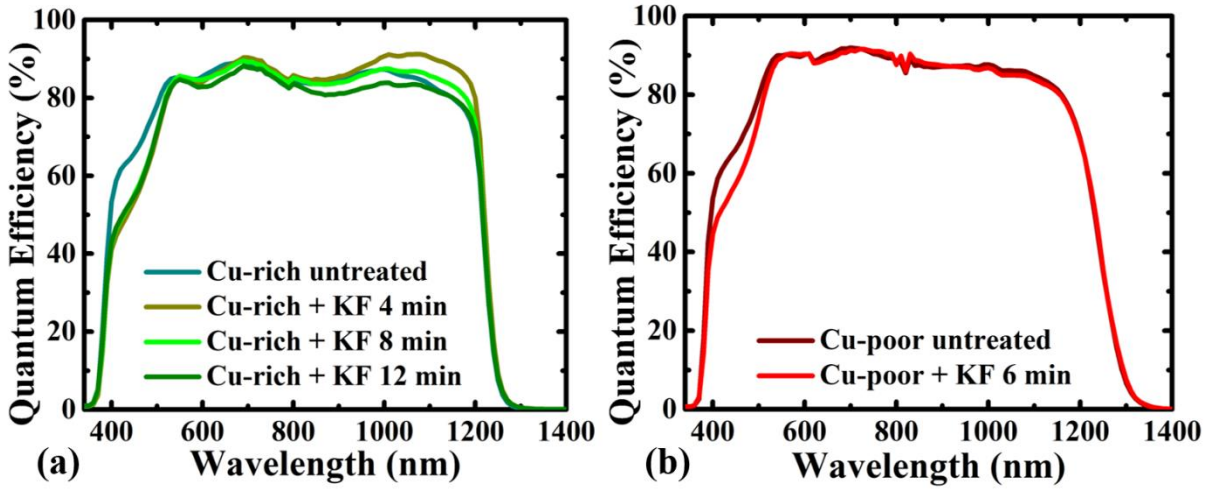

Figure 6.10: EQE spectra for a) Cu-rich untreated and Cu-rich treated with in-situ KF PDT for 4, 8 and 12 minutes and b) Cu-poor untreated and Cu-poor treated with in-situ KF PDT for 6 minutes.

For Cu-rich CIS cells in Figure 6.10a, two main observations could be highlighted. The first observation is related to the short wavelength region (400 – 600 nm). In this region, all treated CIS absorbers suffer from reduced EQE response with approximately the same drop regardless of the treatment duration. This means that this EQE reduced response is due to an increased absorption in this wavelength region. This increased absorption happened due to a thicker CdS buffer layer. In the presence of KF, the chemical bath deposition process becomes longer where the turbidity takes longer time (10.5 minutes) to change from white to yellow which is the indication for the formation of the CdS buffer layer compared to the standard recipe (9 minutes). This behaviour is similar to the behaviour observed with the ex-situ KF PDT where the turbidity took the same longer time (10.5 minutes) to change from

white to yellow producing a thicker CdS layer and a corresponding decrease in the EQE short wavelength response as discussed in Section 6.1. Cu-poor CIS cells in Figure 6.10b showed similar EQE response to Cu-rich CIS cells at the shorter wavelength region.

Based on the above interpretations of the EQE response at the short wavelength region, it can be observed that the KF in both the ex-situ and the in-situ KF PDTs makes the chemical bath deposition process slower for both Cu-rich and Cu-poor CIS absorbers forming a thicker CdS buffer layer on top of both CIS absorbers. This thicker CdS buffer layer causes parasitic absorption decreasing the EQE response in the short wavelength region for both Cu-rich and Cu-poor CIS treated cells.

To further support this observation, the thickness of the CdS buffer layer was deduced from cross-section SEM micrographs. The thickness of the CdS buffer layer for both the untreated Cu-rich and Cu-poor CIS absorbers was in the range of 35 nm, while the thickness of the CdS buffer layer for the treated Cu-rich and Cu-poor CIS absorbers was in the range of 48 nm confirming the above observation. This observation can be considered a motivation to decrease the duration of the chemical bath deposition process and produce solar cells with thinner CdS buffer layers with a potential to increase the J_{SC} and eventually increase the efficiency. However, this type of optimization was not my main concern. My main concern as explained earlier is to optimize the efficiency through optimizing the V_{OC} and the FF, but this motivation of improving the J_{SC} will be considered as a future look and will be highlighted in Chapter 8.

While the EQE response for Cu-poor CIS cells at long wavelength region (1100 – 1200 nm) remained unchanged with and without the in-situ KF PDT, the response for Cu-rich CIS cells was different. For Cu-rich CIS cells, the long wavelength EQE response changed as a function of treatment duration. A strong improvement was achieved for the 4-minute treatment and then the improvement gradually decreased as the treatment duration increases. The significant improvement in the 4-minute treatment was higher than the corresponding drop at short wavelength region resulting in a total increase in the J_{SC} explaining the improvement for the J_{SC} measured by IV compared to the untreated Cu-rich CIS cell. As the treatment duration increased, the improvement at the long wavelength region decreased and could no longer compensate the drop at the short wavelength region leading to a decrease in the overall J_{SC} as measured by IV and presented in Table 6.4.

This improvement for Cu-rich CIS treated absorbers at longer wavelength region can be attributed to enhanced optical and carrier recombination losses [20]. The in-situ KF PDT succeeded in the passivation of a 200±20 meV defect as illustrated by the admittance measurements below. Passivating this 200±20 meV defect reduces the recombination losses at the hetero-interface as indicated by the IVT measurements below, enhancing the optical absorption in the bulk of the absorber and thus leading to this specific improvement at longer wavelength region for all Cu-rich CIS treated cells compared to Cu-poor CIS treated cells that remained unchanged with and without the in-situ KF treatment.

Moreover, the EQE response for the Cu-rich CIS treated samples at longer wavelengths can be more understood through the reflection measurements presented in Figure 6.11. In Figure 6.11, it can be observed that the 4-minute treatment clearly shows an additional improvement compared to the other treated samples and over a wide wavelength range. This means that from an optical point of view, a 4-minute treatment was enough to reduce the reflection losses and consequently increase the absorption of the Cu-rich CIS absorbers before the reflection losses gradually increase with the addition of more KF and with longer annealing duration.

A possible explanation for the behaviour of the reflection measurements as a function of annealing duration can be discussed in the following points:

- A 4-minute in-situ KF treatment is enough to passivate a defect that was responsible for some reflection losses. The passivation of this defect then restored those reflection losses.
- With an 8-minute treatment, more KF was deposited on the surface of Cu-rich CIS absorbers. This additional KF reacted with the surface of the Cu-rich CIS absorbers forming a new layer at the surface of the treated CIS absorbers [6, 7, 14]. This new surface layer is revealed by the SEM micrographs and is illustrated by the PL measurements below.
- With a 12-minute treatment, the thickness of the new surface layer increases with longer treatment durations. The increase in the thickness of the new surface layer causes an additional increase in the reflection losses with a corresponding decrease in the optical absorption by the Cu-rich CIS absorber layer. This decrease in the optical absorption is then reflected in a decrease of the EQE response at longer wavelength regions.

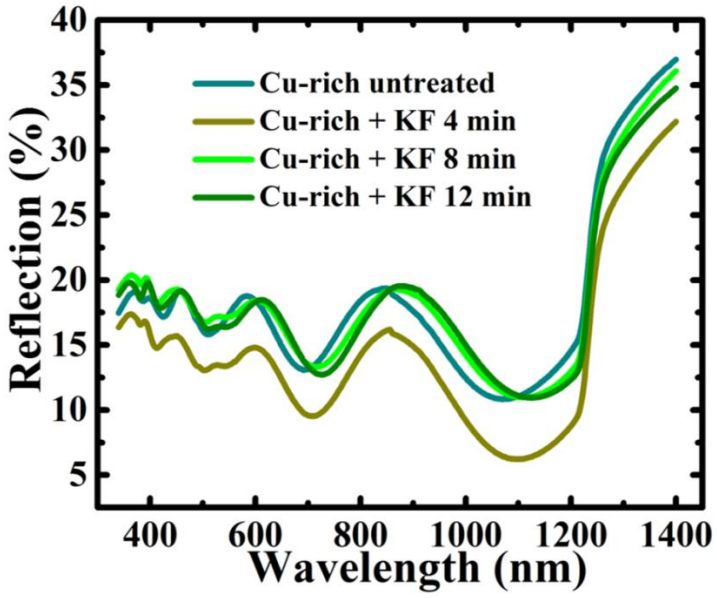

Figure 6.11: Reflection measurements for Cu-rich CIS cells with and without the in-situ KF PDT for 4, 8 and 12 minutes.

IVT measurements were performed to understand the V_{OC} improvement for both Cu-rich and Cu-poor CIS solar cells after the in-situ KF treatment. Moreover, the activation energy at zero Kelvin was extrapolated to determine the dominant recombination path (as explained in Section 4.3) for all the treated cells as illustrated in Figure 6.12.

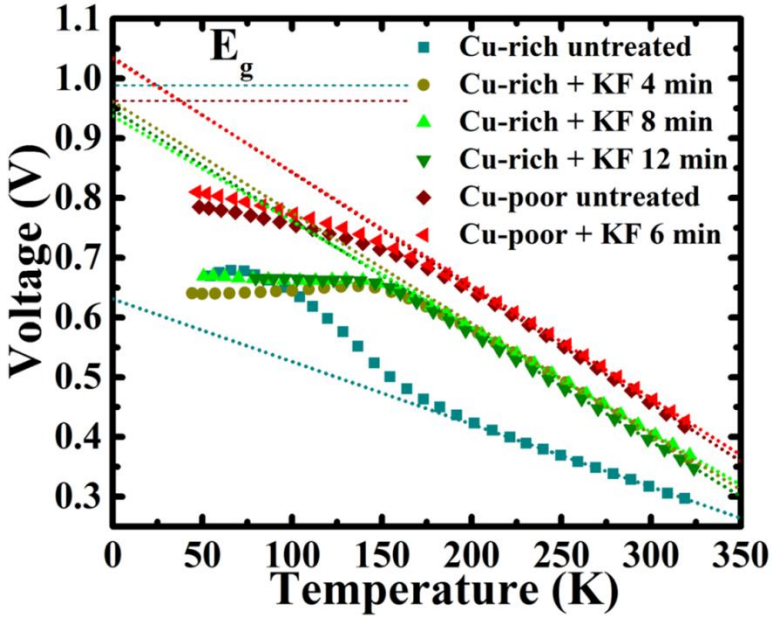

Figure 6.12: V_{OC} as function of temperature for Cu-rich and Cu-poor CIS with and without the in-situ KF PDT. The short dotted lines represent the fitting performed at high temperatures to extrapolate the activation energy at zero Kelvin. The short dashed lines represent the bandgap for Cu-rich (green) and Cu-poor (red) CIS solar cells.

From Figure 6.12, it can be observed that the extrapolated activation energy at zero Kelvin for the untreated Cu-rich CIS cell (by fitting the presented curves at room temperature; where the cells operate) is showing the typical values around 0.6 eV (presented in Section 5.3), which is much less than the bandgap (0.995 eV). As explained in Section 4.3, if the extrapolated activation energy at zero Kelvin is lower than the bandgap, then the dominant recombination path is in the interface but if the extrapolated activation energy at zero Kelvin is close to the bandgap, then the dominant recombination path is in the absorber bulk.

For the case of the untreated Cu-rich CIS cells, the extrapolated activation energy at zero Kelvin is lower than the bandgap. This means that the dominant recombination path for these cells is at the absorber/buffer interface [21]. Moreover, untreated Cu-rich CIS cells show also the typical two negative slopes discussed in Section 5.3 and related to a loss in the photocurrent near V_{OC}.

Interestingly, after the in-situ KF treatment, all treated Cu-rich CIS cells show a significant improvement of the extrapolated activation energy with values of more than 0.9 eV. Furthermore, all treated Cu-rich CIS cells show only one negative slope for their V_{OC} (T) curves before the V_{OC} values saturate at lower temperatures. This means that the in-situ KF PDT succeeded in improving two main aspects:

- The first aspect is the ability of the in-situ KF PDT to reduce recombination losses at the absorber/buffer interface indicated by the significant improvement in the extrapolated activation energy (from 0.6 eV to values above 0.9 eV). We should not ignore the fact that these values of the extrapolated activation energy are still lower than the bandgap (0.995 eV) meaning that there are still rooms for further improving the recombination losses at the absorber/buffer interface.
- The other advantage is the success of the in-situ KF PDT to remove one of the two slopes and this can be attributed to the passivation of a 200 ± 20 meV defect that will be revealed from the admittance measurements below.

On the other side, the extrapolated activation energy at zero Kelvin for Cu-poor CIS solar cells with and without the in-situ KF PDT remained unchanged. This similarity in the extrapolated activation energy values at zero Kelvin for the Cu-poor CIS cells with and without the in-situ KF PDT with the increase in the V_{OC} values observed earlier after the in-situ KF PDT indicate a further reduction in the recombination losses of the Cu-poor CIS cells with the in-situ KF PDT.

In order to further characterize the electrical performance of the treated CIS cells, CV and ADM measurements were performed. Figure 6.13 illustrates the Mott-Schottky plot derived from the CV measurements performed at a frequency of 100 KHz for both Cu-rich and Cu-poor CIS cells with and without the in-situ KF PDT. Based on the Mott-Schottky plots, the apparent doping was extracted from the inverse slope of the presented curves [22] in Figure 6.13 by fitting the curves at small forward bias (0 – 0.2 V). This fitting range (0 – 0.2 V) was chosen to avoid a possible overestimated or underestimated values of the apparent doping at reverse bias as explained in Section 4.4. The doping at reverse bias could be affected by one of the following:

- Deep defects that could increase the apparent doping [23]
- The depth dependent of the doping level that could decrease the apparent doping as a result of Cd diffusion [24].

A detailed explanation of the CV measurements and the extraction of the apparent doping from the Mott-Schottky plot is provided in Section 4.4.

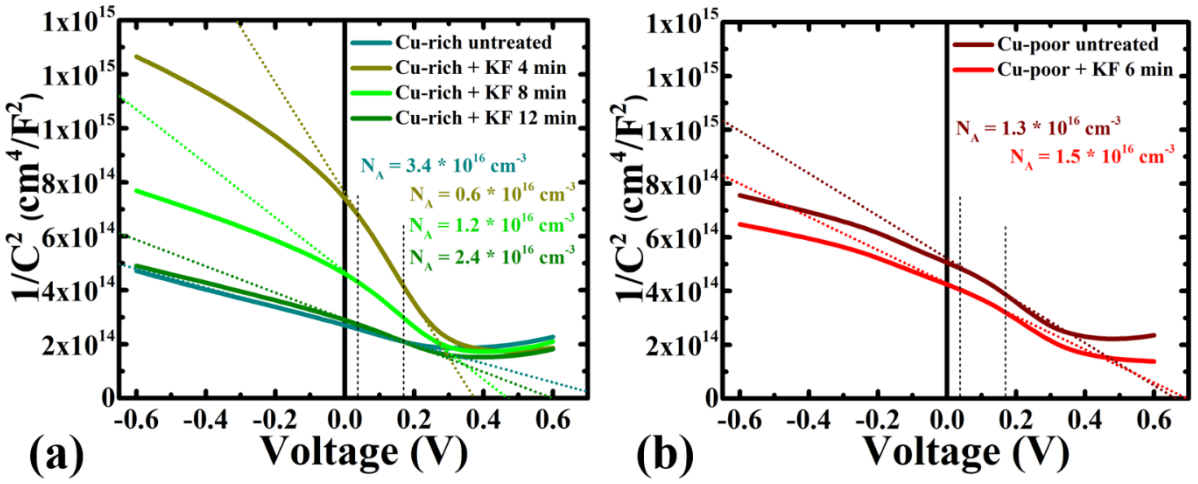

Figure 6.13: Mott-Schottky plots to extract the apparent doping for a) Cu-rich and b) Cu-poor CIS solar cells with and without the in-situ KF PDT. Short dotted lines represent the fitting from which the inverse slope was deduced. The fitting range is represented by the short dashed lines.

From Figure 6.13a, it can be deduced that for Cu-rich CIS cells, the apparent doping was reduced for all treated cells and a 4-minute treatment was enough to decrease the apparent doping from 3.4 * 10^{16} to 0.6 * 10^{16} cm^{-3} before the apparent doping increases to 1.2 * 10^{16} and 2.4 * 10^{16} cm^{-3} for the 8- and 12-minutes of the in-situ KF treatment respectively. The apparent doping of all Cu-rich CIS treated cells is still lower than that of the untreated one similar to what has been reported in [19].

This decrease in the apparent doping for all treated Cu-rich CIS cells can be attributed to the passivation of the 200±20 meV defect as depicted from the admittance measurements below. This defect has been observed as an acceptor defect (as discussed in Section 7.2) and passivating this defect leads to the reduction of the apparent doping as observed in Figure 6.13a.

On the other side, the increase of the apparent doping for the Cu-rich CIS treated cells as a function of increasing treatment duration can be attributed to the formation of a new Cu-poor surface layer after the in-situ KF treatment as deduced from the PL measurements below. This new formed layer provides an additional capacitance that is responsible in increasing the apparent doping in a similar manner to our Cu-poor CIS cells as shown in Figure 6.13b.

For Cu-poor CIS cells (Figure 6.13b), the apparent doping slightly increased from 1.3 * 10^{16} to 1.5 * 10^{16} cm^{-3} after the in-situ KF treatment similar to what has been reported in [18, 25]. This increase in the apparent doping after the in-situ KF PDT could be attributed to the formation of a new layer on the surface of the Cu-poor CIS treated absorber. This new surface layer then adds an additional capacitance that plays a role in the increase of the apparent doping observed in Figure 6.13b.

The interpretation of the CV measurements can be summarized in the following points:

- The doping extracted from the Mott-Schottky plots is not the real absorber doping as explained in Section 4.4. The doping extracted from the Mott-Schottky plots in this thesis is the apparent doping that is affected by the doping of the layers at the SCR.
- For Cu-rich CIS cells, the apparent doping decreased for all the cells treated with an in-situ KF PDT.
- The 4-minute in-situ KF treatment showed the lowest apparent doping, while increasing the treatment duration to 8 and 12 minutes increases the apparent doping.
- For Cu-poor CIS cells, the apparent doping increases after the in-situ KF PDT.
- Based on these results, two effects could be deduced:
    - ❖ The in-situ KF PDT passivates a 200±20 meV acceptor defect from Cu-rich CIS cells decreasing the apparent doping for all Cu-rich CIS treated cells.
    - ❖ The in-situ KF PDT introduces a new layer on the surface. This layer adds an additional capacitance to the capacitance of the SCR and plays a role in increasing the apparent doping. This effect is observed on Cu-poor CIS cells and observed also on Cu-rich CIS cells when increasing the in-situ KF treatment duration and after the passivation of the 200±20 meV acceptor defect.

To further support that the in-situ KF treatment introduced a Cu-poor layer on the surface of the Cu-rich CIS absorbers, PL measurements were performed. Low temperature PL measurement provides a mean to differentiate between Cu-rich and Cu-poor CIS absorbers [26]. Cu-rich CIS bare-absorbers were measured by PL at 10 K under different illumination intensities with and without the in-situ KF treatment. A comparison between the untreated and the 8-minute treated Cu-rich CIS absorber is presented in Figure 6.14. It is worth to note that the PL measurements for the 4 and the 12 minutes treated Cu-rich CIS absorbers showed similar results to the 8-minute treated Cu-rich CIS absorber.

With low temperature PL, it is easy to distinguish between Cu-rich and Cu-poor CIS as Cu-rich CIS materials show narrow peaks accompanied by an excitonic luminescence [26] while Cu-poor CIS materials show only one broad peak [27, 28, 29]. Therefore, from Figure 6.14a, it is easy to recognize the typical response for untreated Cu-rich CIS absorber with its well-known peaks [26]. The Cu-rich CIS peaks can be identified as a donor-acceptor pair transitions known as DA2 at 0.97 eV with its corresponding two phonon replica (+LO) peaks at 0.91 and 0.94 eV and an excitonic transition at 1.03 eV.

For the treated Cu-rich CIS sample, two PL measurements were performed. One measurement was performed at low excitation presented in Figure 6.14c and another measurement performed at high excitation presented in Figure 6.14b. The PL response at low excitation for the treated Cu-rich CIS absorber (Figure 6.14c) indicates the typical spectrum for Cu-poor CIS [27, 28] with an additional shoulder at high energies. The origin of this shoulder can be revealed by the PL response at higher intensities (Figure 6.14b).

At high intensities (Figure 6.14b), an excitonic luminescence starts to appear and the shoulder observed in Figure 6.14c becomes the main peak with a corresponding phonon replica. It is important to note that the broad luminescence is still present but blue shifted compared to the peak in Figure 6.14c. This response means that the luminescence spectrum is a combination of Cu-rich and Cu-poor CIS responses. This is further corroborated by the observation that as we increase the excitation, the right peaks shift by values around 5 meV/decade (similar to the response of DA transitions) while the left peaks are shifted by 14 meV/decade (similar to the response of Cu-poor CIS). This means that the two peaks are originating from two different transitions where all spectra for Cu-rich CIS treated absorber were fitted with a DA2 transition peak (transition for Cu-rich CIS) in addition to an asymmetric Gaussian peak (transition for Cu-poor CIS). Based on that, it can be concluded that both Cu-poor and Cu-rich CIS phases are present in the treated Cu-rich CIS sample.

The interesting conclusion that can be revealed from the above PL measurements is related to the mechanism of the KF effect at the surface. It has been reported that a KF PDT leads to the formation of a Cu-depleted layer on the surface of Cu-poor absorbers as a result of the diffusion of Cu from the surface to the bulk [6, 7, 15]. On the other side, the phase diagram for CIS [30] reveals that Cu-rich does not mean the formation of a Cu-rich chalcopyrite phase but it means a stoichiometric chalcopyrite phase saturated with Cu in addition to secondary phases. According to that, a Cu-diffusion to the bulk from the surface is not relevant for Cu-rich or stoichiometric chalcopyrite conditions.

The only explanation for the presence of both Cu-rich and Cu-poor CIS phases in the treated Cu-rich CIS sample can be summarized in the following points:

- The in-situ KF PDT introduced K, F and Se to the surface of Cu-rich CIS absorbers.
- K and Se reacted with Cu and In (Cu and In are diffusing out of the CIS absorber) forming a new layer on the surface of the Cu-rich CIS absorber.
- This hypothesis is supported by the fact that both DA1 and DA2 transitions can be detected by the low temperature PL measurements on the treated Cu-rich CIS absorbers even for the long treatment durations (8 and 12 minutes of in-situ KF PDT). DA1 and DA2 are two donor-acceptor pair transitions sharing the same donor but different acceptors. A1 is normally attributed to Cu vacancies while A2 is normally attributed to Cu_{In} antisite.

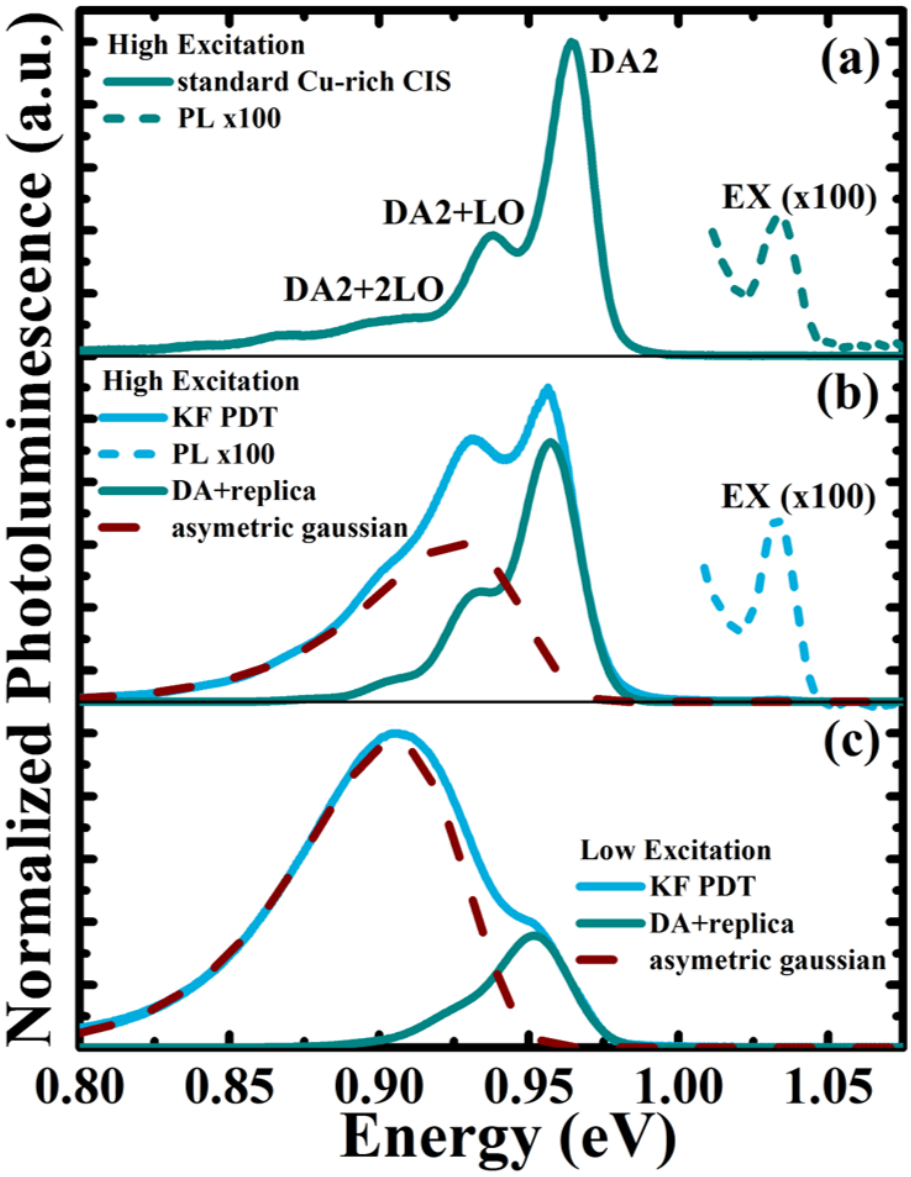

Figure 6.14: Low temperature PL measurements performed at 10 K for a) Cu-rich CIS bare absorber, b) Cu-rich CIS treated with an in-situ KF PDT for 8 minutes and measured at high excitation, and c) the same Cu-rich CIS treated absorber measured at low excitation. The dashed dark red lines represent asymmetric Gaussian profile for a Cu-poor CIS phase and solid green lines represent a DA transition plus phonon replica for a Cu-rich CIS phase.

ADM measurements were performed for Cu-rich CIS cells with and without the in-situ KF treatment to understand the changes in the electronic structure after the in-situ KF PDT [23]. The admittance spectra and their corresponding Arrhenius plots, from which the activation energies were deduced, are presented in Figure 6.15 showing an additional improvement to the electronic structure of Cu-rich CIS cells after the in-situ KF PDT. The interpretation of the admittance spectra and the extraction of the activation energy of the main capacitance step from the Arrhenius plots are explained in Section 4.5.

The admittance measurements in Figure 6.15 revealed the following observations:

- Untreated Cu-rich CIS cells in Figure 6.15(a, b) showed the typical 200±20 meV capacitance step observed for all our Cu-rich CIS cells [31] and discussed in Section 5.4.
- With a 4-minute in-situ KF PDT, the activation energy of the main capacitance step (indicated by the two dashed lines in Figure 6.15c) showed a value of 122 meV as presented in Figure 6.15d.
- In Figure 6.15 (e, f), the activation energy of the main capacitance step for Cu-rich CIS cells with an 8-minute KF PDT showed a value of 145 meV.
- After a 12-minute in-situ KF PDT, the activation energy of the main capacitance step showed an activation energy of 176 meV as presented in Figure 6.15 (g, h).

The derivative of the capacitance data in Figure 6.15 (a, c, e, g) from which the inflection frequency peaks were deduced and plotted in the corresponding Arrhenius plots in Figure 6.15 (b, d, f, g) (as explained in Section 4.5) are presented in Figure 6.16.

Figure 6.16a illustrates that the derivative of the capacitance for the untreated Cu-rich CIS cells show broad peaks while Figures 6.16 (b, c, d) show narrow peaks in the same temperature range for the capacitance derivative of the Cu-rich CIS cells treated with 4, 8 and 12 minutes respectively. It is important to note that the capacitance derivative for all untreated Cu-rich CIS cells showed the same behaviour of broad peaks.

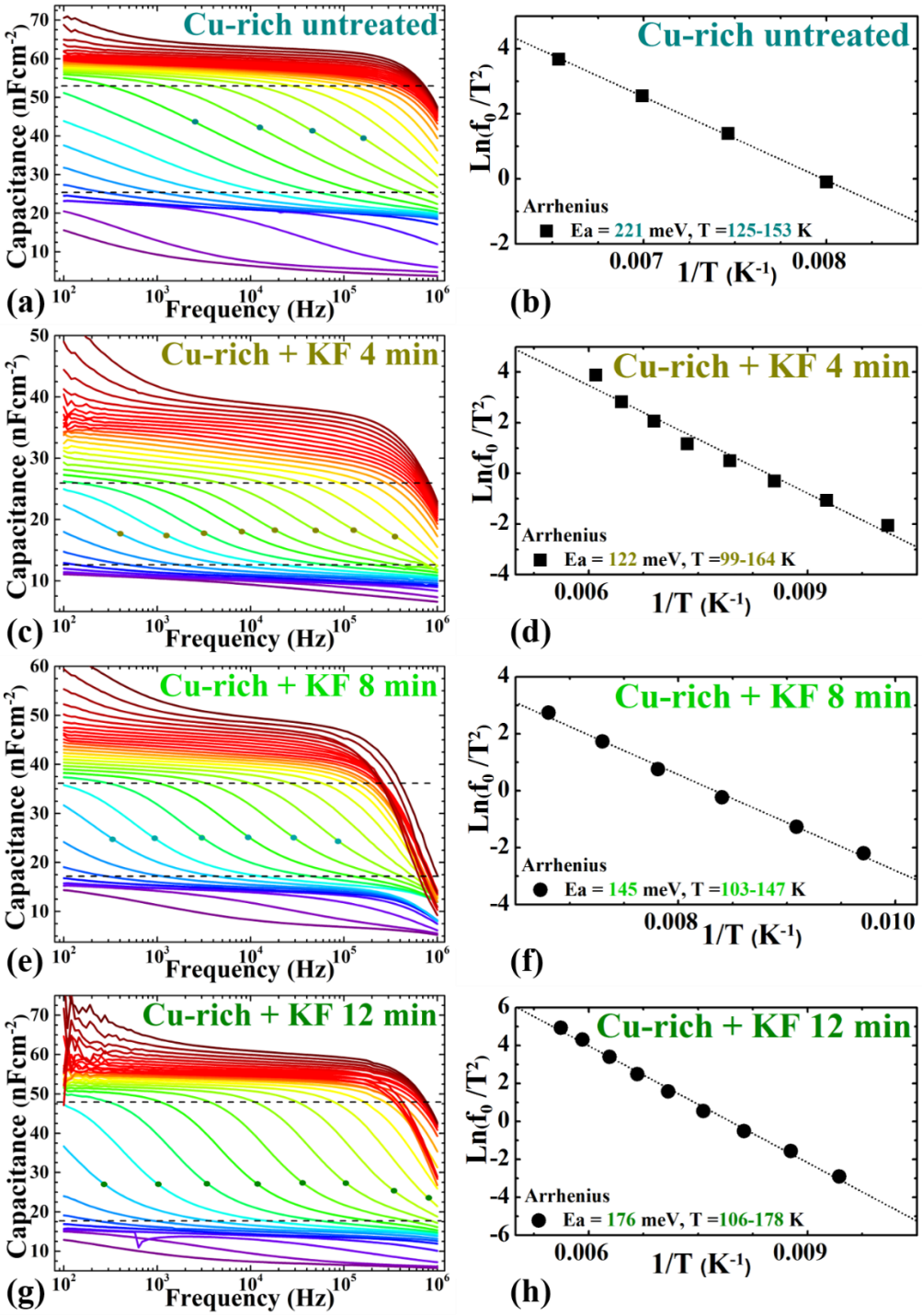

Figure 6.15: Admittance measurements for Cu-rich CIS cells a) without KF PDT, c) with a 4-minute KF PDT, e) with an 8-minute KF PDT and g) with a 12-minute KF PDT performed at temperatures between 50 K and 320 K. The two dashed lines identify the main capacitance step. The dots represent the inflection frequencies (peak frequencies in the capacitance derivative plot of Figure 6.16). These inflection frequencies are plotted as a function of temperature in Arrhenius plots (b, d, f, h). The Arrhenius plots indicate the activation energy and the corresponding temperature range of the main capacitance step for Cu-rich CIS cells b) without KF PDT, d) with a 4-minute, f) with an 8-minute and h) with a 12-minute KF PDT.

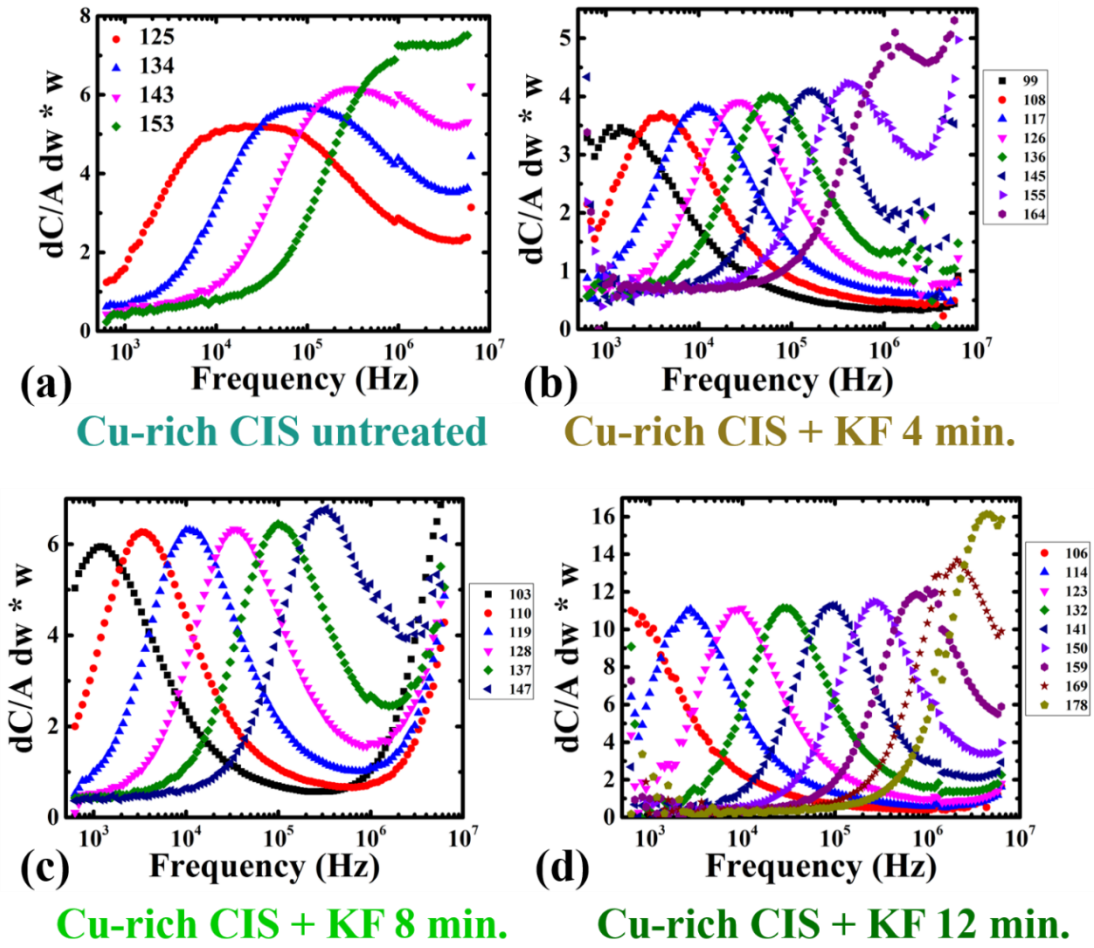

Figure 6.16: The capacitance derivative plot of the admittance spectra in Figure 6.15 for Cu-rich CIS cells a) without KF PDT, b) with a 4-minute, c) with an 8-minute and d) with a 12-minute KF PDT. The temperatures corresponding to each plot represents the temperature of the capacitance curves of the main capacitance step deduced from Figure 6.15.

Based on the above results, the interpretation of the admittance spectra, Arrhenius plots (Figure 6.15) and capacitance derivatives (Figure 6.16) can be summarized in the following points:

- Untreated Cu-rich CIS cells showed the typical 200±20 meV capacitance step. This capacitance step will be attributed to a defect as explained in more detail in Section 7.1.
- The broad peak behaviour of the capacitance derivative for the untreated Cu-rich CIS cells suggests the contribution of two capacitance steps to this broad peak; one capacitance step with an activation energy of 200±20 meV and a second capacitance step with a lower activation energy hidden below the first capacitance step (200±20 meV step) but broadens the capacitance derivative peak and should be observed in the same temperature range.
- The in-situ KF PDT then passivates the 200±20 meV defect facilitating the identification of the second capacitance step that was hidden below the 200±20 meV defect.

- This second capacitance step is then revealed from the main capacitance step of the treated Cu-rich CIS cells. The activation energy of this second capacitance step varies according to the annealing duration of the in-situ KF PDT showing values of 122, 145 and 176 meV for the 4, 8 and 12 minutes of in-situ KF PDT respectively.
- The activation energy of 122 and 145 meV for the 4 and 8 minutes of in-situ KF PDT could be likely attributed to a third acceptor defect (A3 defect) that has an activation energy of 130±15 meV. More details on the identification of this defect will be provided in Section 6.4. We published the results of the identification of this third acceptor defect in [13].
- The activation energy of 176 meV observed after a 12-minute of in-situ KF PDT is likely to be attributed to a defect as the activation energy deduced from the series resistance as a function of temperature showed lower values than 176 meV. If the activation energy deduced from the series resistance as a function of temperature was close to 176 meV, this capacitance step (176 meV step) would have been identified as a transport barrier. The identification of this 176 meV defect was not possible within the work of this thesis.
- This second capacitance step (122, 145 and 176 meV for the 4, 8 and 12 minutes of in-situ KF PDT) that appeared after the in-situ KF PDT represents the contribution from a single defect (not a double contribution as for the untreated Cu-rich CIS cells) in the same temperature range observed for the first defect (200±20 meV defect) in the untreated Cu-rich CIS cell explaining the narrow behaviour of the capacitance derivative peaks for the Cu-rich CIS cells treated with an in-situ KF PDT.
- In summary:
    - ❖ The untreated Cu-rich CIS cells are characterized by two defects; a 200±20 meV defect and another defect that appeared after the in-situ KF PDT. These two defects are in the same temperature range and are then contributing together to the broad peak behaviour observed for the capacitance derivative of the untreated Cu-rich CIS cells.
    - ❖ The in-situ KF PDT passivates the first defect (200±20 meV defect) and the treated Cu-rich CIS cells show the second defect with narrow capacitance derivative peaks.

6.3 Ga-Se post-deposition treatment for Cu-rich CIGS

In order to improve the performance of our Cu-rich CI(G)S cells, a PDT is required. An increase in the V_{OC} of Cu-rich CIS cells was obtained by using an In-Se PDT [32], an ex-situ KF PDT discussed in Section 6.1 and an in-situ KF PDT as explained in Section 6.2. It is interesting to note that the three treatments share two important characteristics. All treatments include Se all along the treatments' duration and they all turn the surface of the Cu-rich CIS absorbers into Cu-poor. In order to improve the performance of Cu-rich CIGS cells, the same concepts were targeted; to obtain a Cu-poor surface at the Cu-rich CIGS/buffer interface and use Se during the whole treatment. A Ga-Se treatment was then proposed. The Ga-Se PDT was not developed by me as mentioned in the introduction of this chapter. The Ga-Se PDT was developed by Leo Choubrac who also performed most of the electrical characterizations related to this treatment. I only participated in the optimization of the ARC layer and the electrical characterizations of some of the optimized solar cells. I performed all the electrical characterizations presented in this section except for the IV measurements of the champion cell presented in Table 6.5 that was performed by Leo Choubrac. We published the results of this Ga-Se PDT on Cu-rich CIGS solar cells in [3].

When Leo Choubrac was optimizing the Ga-Se PDT, he deduced three observations. I will mention these three observations here because I will use them in the interpretation of the 200±20 meV defect in Cu-rich CIS and CIGS in Section 7.2. The three observations are:

1. The first observation is that small amounts of Ga deposition on the surface of Cu-rich CIGS absorbers are sufficient to turn the Cu-rich CIGS surface to Cu-poor and increase the V_{OC}.
2. The second observation was related to Se where a Low-Se treatment (about ten times lower flux compared to the Se-flux used during the absorber growth) was found to be mandatory to restore some of the lost J_{SC}. This can be attributed to the effect of the Low-Se reactivity passivating the grain boundaries and improving the collection length.
3. The third observation is also related to the Se-flux where a High-Se flux annealing step (Se-flux similar to the one used during the absorber growth) was able to provide an additional improvement to the V_{OC}. This additional increase in the V_{OC} with High-Se treatment can be explained by an improved absorber/buffer interface as a result of either the formation of a thin Cu-poor layer on the absorber surface or to the passivation of some defects or both effects. In Section 7.2, I will speculate this improvement in the V_{OC} with the High-Se flux annealing to the passivation of a defect.

Based on these three observations, Leo Choubrac developed a Ga-Se PDT. The details of this Ga-Se PDT can be summarized in the following steps:

- The Cu-rich CIGS absorbers were grown and etched using KCN etching
- The etched Cu-rich CIGS absorbers were returned to the PVD for the Ga-Se PDT.
- The optimized treatment consists of two steps:
    1. The first step is the deposition of Ga for 60 seconds under Low-Se flux to passivate the grain boundaries and improve the collection length (improve J_{SC}).
    2. The second step is the depositing of Ga for another 60 seconds under High-Se flux to enhance the absorber/buffer interface (improve V_{OC}).

The two steps of the Ga-Se PDT were performed at substrate temperature set points of 200 - 220 ^{0}C corresponding to real temperatures of 300 – 350 ^{0}C.

The optimized Ga-Se PDT succeeded in improving the V_{OC} significantly as well as both the FF, J_{SC} and correspondingly, the efficiency as observed in Figure 6.17 for one of the treated Cu-rich CIGS cells (without using an ARC layer). The presented Cu-rich CIGS solar cell in Figure 6.17 has a bandgap of 1.15 eV and for comparison, a Cu-poor CIGS solar cell with quiet similar bandgap (1.1 eV) is presented in Figure 6.17 showing that the Ga-Se PDT indeed improved the V_{OC} of the Cu-rich CIGS solar cells but there are still some rooms for further improvement. The electrical parameters of the champion cell (without an ARC layer) are presented in Table 6.5.

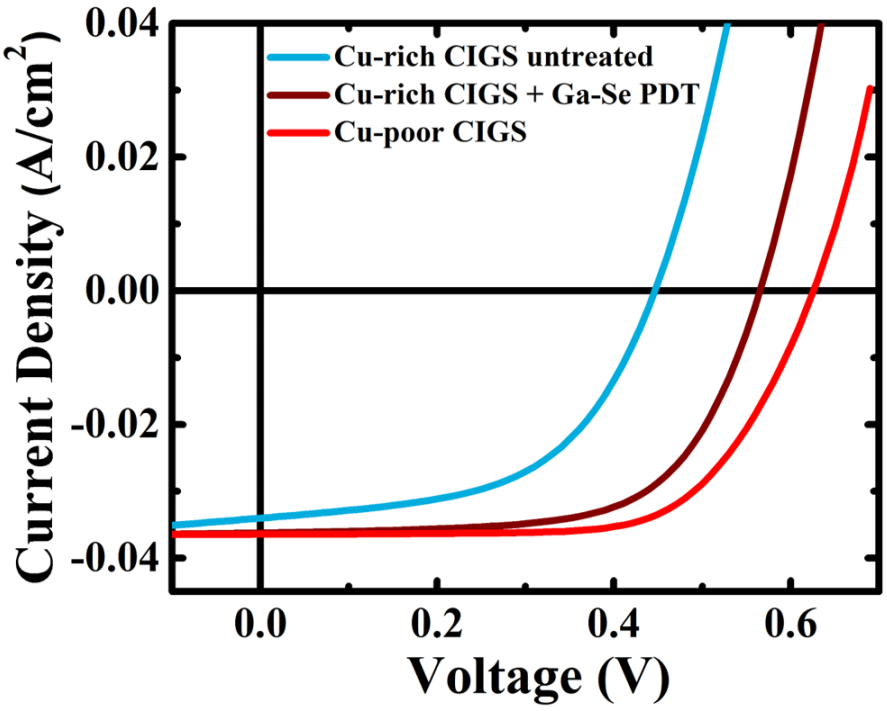

Figure 6.17: IV characteristics for Cu-rich CIGS (bandgap of 1.15 eV) with and without the Ga-Se PDT and a Cu-poor CIGS solar cell with a bandgap of 1.1 eV.

Table 6.5: Electrical parameters for Cu-rich CIGS cells with and without the Ga-Se PDT. No ARC layer was added to these solar cells. The presented values correspond to the average values of six solar cells while the values in brackets are for the champion ones.

Sample	Efficiency (%)	FF (%)	V_{OC} (mV)	J_{SC} (mA.cm^{-2})	R_S (Ohm.cm^2)	R_{Sh} (Ω.cm^2)
Cu-rich CIGS untreated	7.5	55.0	438	30.8	0.4	167
Cu-rich CIGS + Ga-Se PDT	14.4 (15.4)	68.0 (69.0)	587 (589)	35.9 (37.8)	0.5 (0.5)	378 (330)

Based on the values in Table 6.5, it can be observed that the Ga-Se PDT succeeded in improving the V_{OC} of the Cu-rich CIGS solar cells by about 150 mV, the FF by 13 % and the J_{SC} by about 5 mA/cm^{-2} leading to an increase in the efficiency from an average of 7.5 % to 15.4 % for the best solar cell.

Moreover, the improvement of the J_{SC} can be observed by the EQE measurements presented in Figure 6.18. The EQE measurements in Figure 6.18 are for the same solar cells presented in Figure 6.17 after adding an ARC layer.

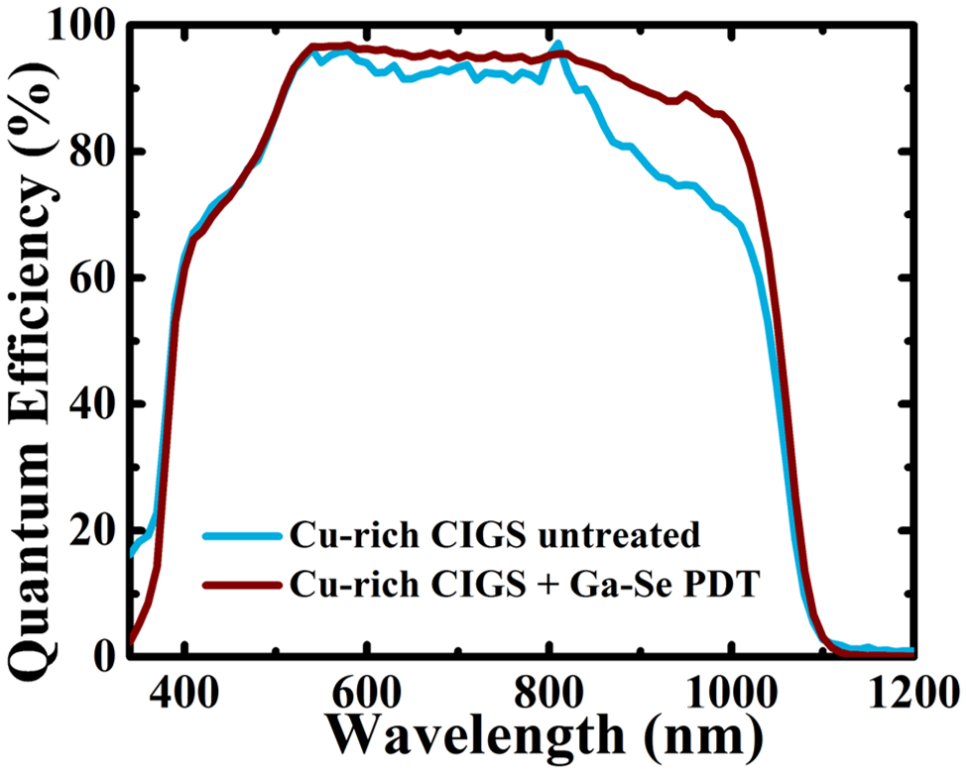

Figure 6.18: EQE spectra for Cu-rich CIGS solar cells with and without the Ga-Se PDT. An ARC layer was added to both solar cells.

From Figure 6.18, it can be observed that the main improvement taking place after the Ga-Se PDT is the improvement at longer wavelengths (800 – 110 nm). This confirms the superior transport properties for the Cu-rich CIGS treated cell as a result of passivating the grain boundaries, improving the absorber/buffer interface after the Ga-Se treatment and likely passivating some defects as will be discussed in Section 7.2. This improvement in the EQE response at longer wavelengths after the Ga-Se PDT is similar to the improvements observed by the EQE measurements at longer wavelengths after both the ex-situ KF PDT (discussed in Section 6.1) and the in-situ KF PDT (discussed in Section 6.2).

It is important to note that the bandgap of the treated Cu-rich CIGS solar cell did not change compared to the untreated Cu-rich CIGS cell (1.15 eV as deduced from the linear extrapolation of the EQE measurements in Figure 6.17). The extrapolation of the bandgap from the EQE measurements is explained in Section 4.2. The unchanged behaviour of the bandgap of the Cu-rich CIGS cell with and without the Ga-Se PDT confirms that the effect of Ga addition took place only at the absorber surface without affecting the bulk of the absorber.

To further characterize the Cu-rich CIGS solar cells treated with the Ga-Se PDT and study the changes to the CIGS absorber/buffer interface, IVT measurements were performed for a Cu-rich CIGS solar cell with and without the Ga-Se PDT. The V_{OC} as a function of temperature is plotted in Figure 6.19. The V_{OC} (T) curve is used to extract the activation energy at zero Kelvin. If the extrapolated activation energy at zero Kelvin is close to the bandgap, then the dominant recombination path is in the absorber bulk. Otherwise, if the extrapolated activation energy at zero Kelvin is lower than the bandgap, then the dominant recombination path is in the absorber/buffer interface. For Cu-rich CIGS solar cells, the extrapolated activation energy is typically lower than the bandgap as presented in Section 5.3 and therefore the Cu-rich CIGS solar cells suffer from recombination losses at the absorber/buffer interface.

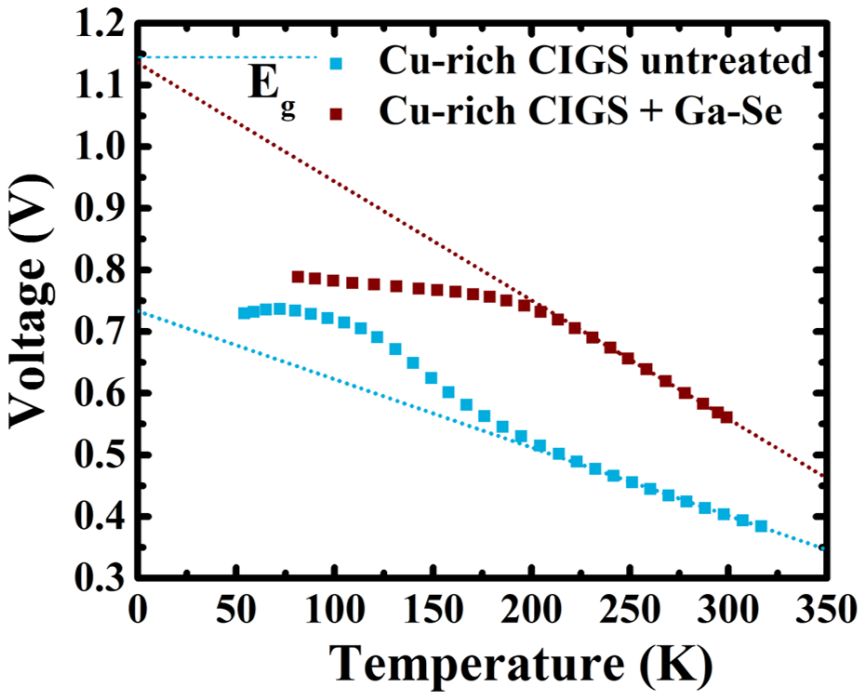

Figure 6.19: V_{OC} as a function of temperature for Cu-rich CIGS solar cells with and without the Ga-Se PDT. The dotted lines represent the extrapolation of the activation energy to zero Kelvin. The fitting of the curve was performed at room temperatures. The dashed line at 1.15 eV represents the bandgap of the Cu-rich CIGS solar cell.

The interpretation of the V_{OC} (T) curves in Figure 6.19 for the Cu-rich CIGS solar cells with and without the Ga-Se PDT revealed two main observations:

1. The first observation is related to the extrapolated activation energy and can be summarized in the following points:
    - The extrapolated activation energy at zero Kelvin for the untreated Cu-rich CIGS solar cells showed a value around 0.75 eV.
    - This means that the dominant recombination path in the untreated Cu-rich CIGS solar cells is in the CIGS absorber/buffer interface.
    - The extrapolated activation energy at zero Kelvin for the Cu-rich CIGS solar cell treated with the Ga-Se PDT increased from 0.75 eV reaching values close to the bandgap (1.15 eV).
    - This means that the Ga-Se PDT succeeded in reducing the recombination losses at the CIGS absorber/buffer interface and moving the dominant recombination path from the interface to the bulk of the CIGS absorber.

2. The second observation is related to the number of slopes of the V_{OC} (T) curve and can be summarized in the following points:
    - The V_{OC} (T) curve of the untreated Cu-rich CIGS solar cells show two negative slopes before the V_{OC} values saturate at low temperatures. This behaviour of two negative slopes for the V_{OC} (T) curve of the Cu-rich CIGS solar cells was previously discussed in Section 5.3.
    - With a Ga-Se PDT, one of the two negative slopes disappear and the V_{OC} (T) curve for the Cu-rich CIGS solar cell treated with Ga-Se PDT show one negative slope before the V_{OC} values saturate at low temperatures.

Interestingly, the above two observations taking place as a consequence of the Ga-Se PDT were also observed after the ex-situ KF PDT discussed in Section 6.1 and after the in-situ KF PDT presented in Section 6.2. The improvement of the absorber/buffer interface in terms of reducing interface recombination losses as well as the disappearance of a second slope in the V_{OC} (T) curve will be attributed to the passivation of a defect that will be discussed in Section 7.2.

Admittance measurements performed for the Cu-rich CIGS solar cells with and without the Ga-Se PDT did not show any significant changes. The typical 130±15 meV defect observed for Cu-rich CIGS solar cells at such bandgaps (1.0 – 1.15 eV) as discussed in Section 5.4 was observed for Cu-rich CIGS solar cells with and without the Ga-Se PDT.

The apparent doping extracted from the CV measurements showed the decrease of the apparent doping for Cu-rich CIGS solar cells after the Ga-Se PDT. The CV measurements were performed by Leo Choubrac. This decrease in the apparent doping for Cu-rich CIGS solar cells after the Ga-Se PDT will support the hypothesis that the Ga-Se PDT passivates an acceptor defect. This hypothesis will be discussed in Section 7.2.

To conclude, the Ga-Se PDT succeeded in improving the electrical parameters of Cu-rich CIGS solar cells in terms of V_{OC}, J_{SC}, FF and consequently the efficiency. The improvement is mainly due to passivating the grain boundaries as well as improving the CIGS absorber/buffer interface by the passivation of some defects.

6.4 Se-only post-deposition treatment for Cu-rich CIS

In Section 6.1 and Section 6.2, an ex-situ and an in-situ KF PDTs were introduced for Cu-rich CIS cells respectively. In Section 6.3, a Ga-Se PDT was introduced to Cu-rich CIGS solar cells. I observed that all the three treatments succeeded in improving the V_{OC} and the absorber/buffer interface for the corresponding treated cells with relatively similar improvement characteristics although the ex-situ and the in-situ KF PDT were applied on Cu-rich CIS cells while the Ga-Se PDT was performed on Cu-rich CIGS solar cells. A summary for the improvement characteristics of the three treatments as well as the Se-only PDT presented in this section will be provided in Section 7.2. I was wondering if the improvements achieved by the three treatments (ex-situ KF, in-situ KF and Ga-Se) in terms of improving the absorber/buffer interface and increasing the V_{OC} are coming from one common player in the three treatments or not. I studied carefully the development methods and conditions of the three treatments searching for a common player. I found that Se was mandatory and a key player in all the three treatments. So, I thought of developing a Se-only PDT. The objectives of this Se-only PDT are to:

1. The first objective (main objective) is to check if the Se-only PDT would be able to improve the absorber/buffer interface and increase the V_{OC} or not. If the Se-only PDT succeeded in improving the absorber/buffer interface and increase the V_{OC}, then I can speculate that Se plays at least an important role in the improvements observed by the three treatments (ex-situ KF, in-situ KF and Ga-Se). If the Se-only PDT did not succeed in improving the absorber/buffer interface or improving the V_{OC}, then I would speculate that the improvements achieved by the three treatments (ex-situ KF, in-situ KF and Ga-Se) are likely attributed to the KF and Ga part.
2. The second objective is to discover if the Se-only PDT would be able to passivate the 200 ± 20 meV defect typically observed for Cu-rich CIS cells discussed in Section 5.4. The identification of the 200 ± 20 meV defect is explained in Section 7.1 and the passivation of this defect was observed by the in-situ KF PDT discussed in Section 6.2.

In order to exclude the effect of any other parameters, I (in collaboration with Finn Babbe) developed the Se-only PDT using exactly the same parameters used for the development process of the in-situ KF PDT with changing only one variable. The only variable that was changed in the in-situ KF PDT process parameters to perform a Se-only PDT is using Se-only flux instead of using both KF and Se.

The details of the Se-only PDT are described in sub-section 3.2.3. The Se-only PDT was developed based on the in-situ KF and not the ex-situ KF or the Ga-Se PDT because of the following reasons:

- The in-situ KF PDT was better and simpler than the ex-situ KF PDT as the ex-situ KF PDT failed to improve the efficiency as well as the in-situ KF PDT is developed in one-step while the ex-situ KF PDT is a two-step process.
- The in-situ KF PDT was developed for Cu-rich CIS cells while the Ga-Se PDT was developed for Cu-rich CIGS cells. CIS has simpler structure than CIGS. Therefore, to minimize the variables, developing a Se-only PDT on Cu-rich CIS was preferred compared to Cu-rich CIGS. Moreover, the 200$\pm$20 meV defect was observed for Cu-rich CIS devices and not for Cu-rich CIGS devices.

To provide a detailed study on the effect of the Se-only PDT, the following experiment was performed. One Cu-rich CIS absorber run with four samples was developed. The four Cu-rich CIS absorbers were etched using the standard KCN etching procedure to remove the copper selenide secondary phases as explained in Section 3.1.

One of these four absorbers was used as a reference, was completed with the standard baseline process and was then characterized. The main characteristics of Cu-rich CIS cells discussed in Chapter 5 were observed for this reference Cu-rich CIS cell. These characteristics can be summarized mainly in the significant V_{OC} losses observed by the IV measurements, the increased recombination losses at the absorber/buffer interface observed by the IVT measurements and the 200$\pm$20 meV capacitance step (defect) observed by the admittance measurements.

Two of the remaining three absorbers were treated with the Se-only PDT and were then processed in two different structures as presented in Figure 6.20 and referred to in the text as: “Se-treated bare” and “Se-treated cell”. These two structures are similar to two of the three structures presented in Figure 7.1 and used for the identification of the 200$\pm$20 meV defect. The explanation of the two structures can be summarized in the following points:

- The “Se-treated bare” is the Se-treated Cu-rich CIS etched absorber with only Al Schottky contacts on top (Figure 6.20a).
- The “Se-treated cell” is the same Se-treated Cu-rich CIS etched absorber processed with the standard baseline process of buffer, window and grid layers (Figure 6.20b).

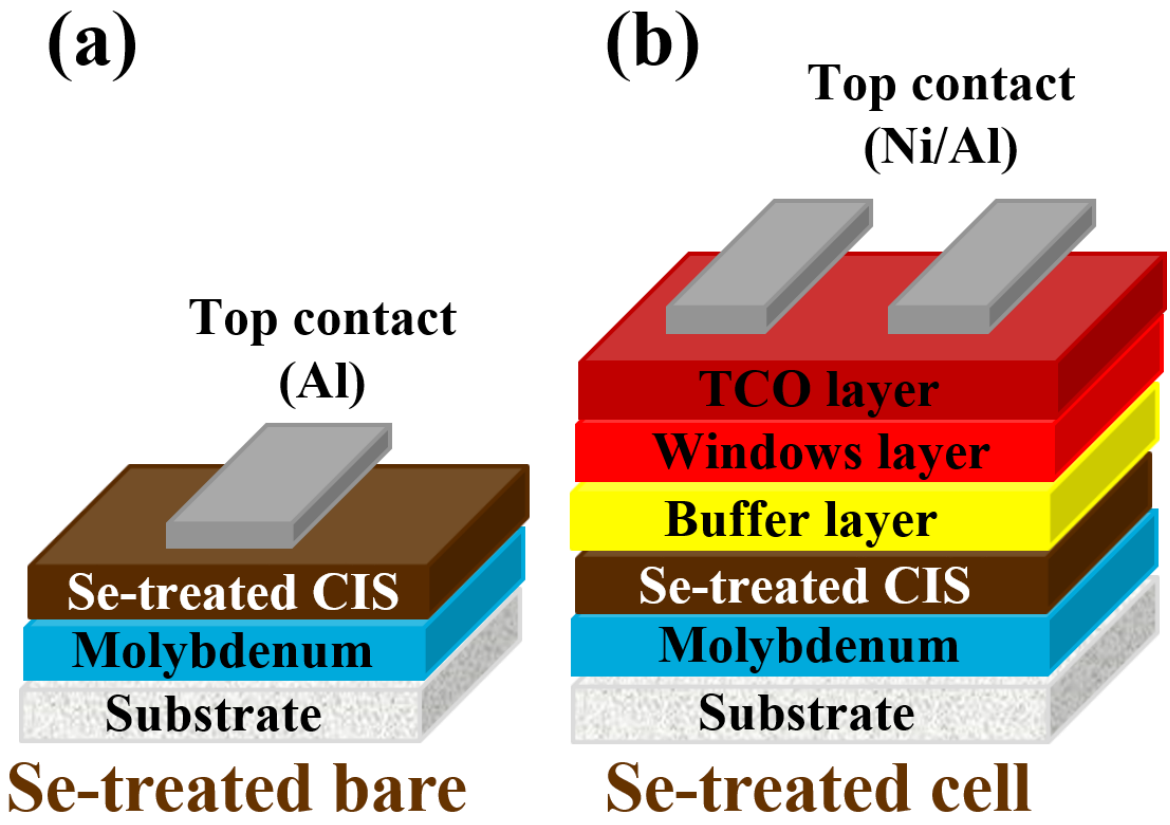

Figure 6.20: Schematic for Cu-rich CIS absorbers etched with strong KCN etching, treated with a Se-only PDT and processed in two different structures: a) Se-treated absorber with only Al Schottky contacts referred to as “Se-treated bare”, b) Se-treated absorber processed with our standard baseline process referred to as “Se-treated cell”.

IV measurements were performed on the reference Cu-rich CIS cell and the Se-treated Cu-rich CIS cell (Figure 6.20b) and their IV characteristics are illustrated in Figure 6.21. The electrical parameters for the untreated Cu-rich CIS cell and the Se-treated Cu-rich CIS cell are presented in Table 6.6.

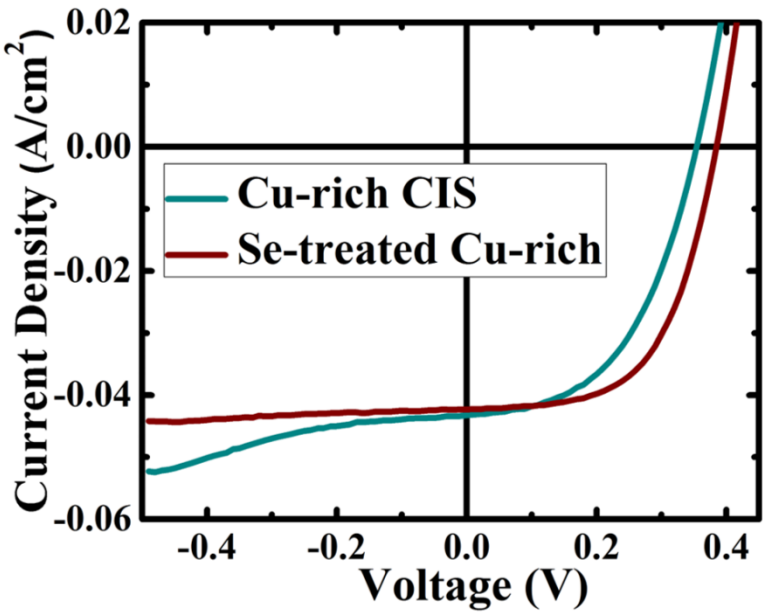

Figure 6.21: IV characteristics of the same Cu-rich CIS cell with (red) and without (green) a Se-only PDT.

Table 6.6: Electrical parameters for the average of six solar cells of Cu-rich CIS cells with and without the Se-only PDT. Values in brackets represent the best solar cells.

Sample	Efficiency (%)	*FF* (%)	V_{OC} (mV)	J_{SC} (mA/cm^2)	R_S (Ω/cm^2)	R_{Sh} (Ω/cm^2)
Cu-rich CIS cell	7.0 (7.7)	46.8 (50.3)	355 (357)	42.1 (44.3)	0.5 (0.4)	124 (198)
Cu-rich CIS cell treated with Se-only PDT	9.2 (9.4)	59.2 (60.6)	382 (385)	40.7 (42.3)	0.4 (0.3)	794 (1153)

The IV characteristics of the Se-treated Cu-rich CIS cell in Figure 6.21 and Table 6.6 revealed that the Se-only PDT succeeded in improving the V_{OC} (ΔV_{OC} = 30 mV), the FF (ΔFF = 10 %) and consequently the efficiency of Cu-rich CIS cells that increased from an average of 7.0 to 9.2 %. The increase in the V_{OC} and the FF achieved by the Se-only PDT is close to (slightly less) the improvements achieved to the V_{OC} and the FF by the in-situ KF PDT. The increase in the FF after the Se-only PDT is attributed to an improvement in the shunt resistances (R_{Sh}) as illustrated in Table 6.6. In addition to that, the breakdown behaviour generally observed for Cu-rich CIS cells at reverse bias voltages as explained in Section 5.2 and presented in Figure 6.21 (green curve), was significantly improved by the Se-only PDT and not observed within the measurement range as presented in Figure 6.21 (red curve).

It is important to note that the other post-deposition treatments that succeeded in improving the V_{OC} for Cu-rich CIS cells also succeeded in removing the breakdown behaviour like the ex-situ KF (Section 6.1), in-situ KF (Section 6.2) and In-Se (31) PDTs.

The decrease in the J_{SC} values observed after the Se-only PDT in Table 6.6 and Figure 6.21 where the average J_{SC} values decreased from 42.1 to 40.7 mA/cm^2 can be explained by looking at the EQE spectra in Figure 6.22. Figure 6.22 illustrates the EQE spectra for the same Cu-rich CIS solar cell with and without the Se-only PDT. The effect of the Se-only PDT can be observed in the short wavelength region (400 – 550 nm) of Figure 6.22 where an increased parasitic absorption by the CdS buffer layer is observed for the treated cell compared to the untreated one. This increased parasitic absorption by the CdS buffer layer can be explained in terms of an increased CdS layer thickness. The thickness of the CdS buffer layer differs for the Se-treated Cu-rich CIS cell compared to the untreated Cu-rich CIS cell. This difference in the CdS layer thickness is observed by the slower chemical bath deposition process for the Se-treated Cu-rich CIS cell where the turbidity took longer time (10.5 minutes) to change its colour to yellow (the indication for the formation of the CdS buffer layer) compared to the standard CdS deposition process for the untreated Cu-rich CIS cell (9 minutes). These observations of slower chemical bath deposition process, thicker CdS buffer layer formed and reduced EQE response in the short wavelength region were also observed after the ex-situ KF PDT (Section 6.1) and the in-situ KF PDT (Section 6.2). Moreover, the Se-only PDT causes an additional slight decrease of the EQE behaviour over the intermediate wavelengths (600 – 1000 nm) compared to the untreated Cu-rich CIS cell as observed in Figure 6.22. The reason behind this decrease in EQE response in intermediate wavelengths is not clear but I speculate that this decrease may be attributed to parasitic absorptions at the grain boundaries or at the treated absorber surface as a result of the reaction of the Se with the Cu-rich CIS surface.

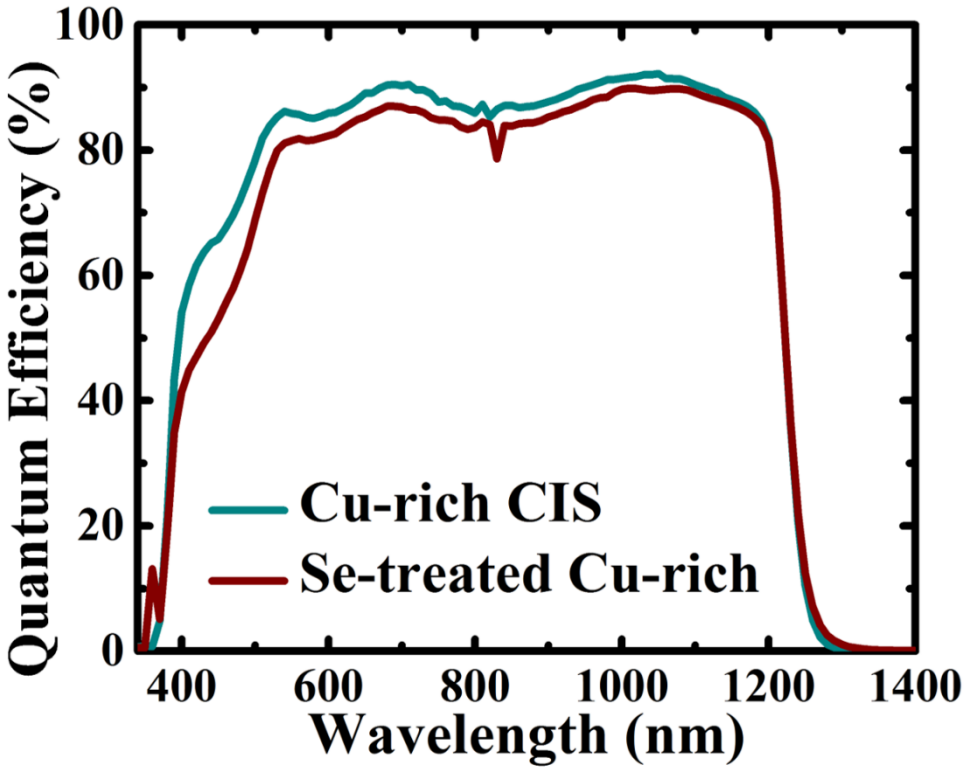

Figure 6.22: EQE spectra for the same Cu-rich CIS solar cell with (red) and without (green) a Se-only PDT.

Based on the above IV characteristics of the Cu-rich CIS solar cell treated with the Se-only PDT, it can be observed that the first half of the first objective of performing the Se-only PDT has been achieved. The Se-only PDT succeeded in improving the V_{OC}. The other half of the first objective is to check if the Se-only PDT is able to improve the absorber/buffer interface of the Cu-rich CIS cells or not. IVT measurements were then performed for both the reference untreated Cu-rich CIS cell and the Cu-rich CIS cell treated with the Se-only PDT (Figure 6.20b) to study the changes at the absorber/buffer interface after the Se-only PDT. Figure 6.23 illustrates the V_{OC} (T) curve for both the reference untreated Cu-rich CIS cell (green curve) and for the Cu-rich CIS cell treated with the Se-only PDT (red curve).

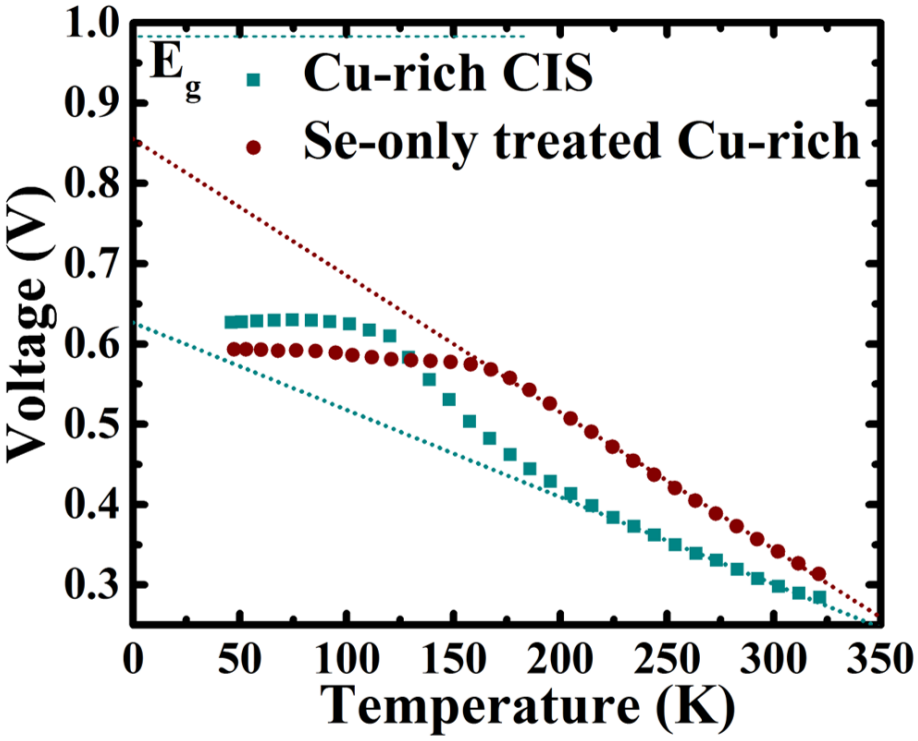

Figure 6.23: Temperature dependence of V_{OC} for Cu-rich CIS cell with and without a Se-only PDT. The short dotted lines represent the fitting (performed at high temperatures) to extract the activation energies at zero Kelvin. Short dashed line at 0.995 eV represent the bandgap for Cu-rich CIS (deduced from EQE measurements).

The interpretation of the results in Figure 6.23 can be summarized in the following points:

- For the untreated Cu-rich CIS cell (green curve):
  - The extrapolation of the activation energy of the V_{OC} (T) curve at zero Kelvin (extrapolation of the fit at room temperature) showed values in the range of 0.6 V much less than the bandgap energy (0.995 eV). This energy gap between the extrapolated activation energy at zero Kelvin and the Cu-rich CIS bandgap is typical for Cu-rich CIS cells as explained in Section 5.3. This energy gap indicates that the dominant recombination path for Cu-rich CIS cells is at or near the absorber/buffer interface as explained in Section 4.3.
  - The V_{OC} (T) curve of the untreated Cu-rich CIS cell shows two negative slopes before the V_{OC} values saturate at lower temperatures: one slope at higher temperatures extrapolating to values around 0.6 eV as discussed above and a second slope at intermediate temperatures extrapolating to values closer to the bandgap of Cu-rich CIS cells. These two negative slopes are typically observed for Cu-rich CIS cells as discussed in Section 5.3.

- For the Se-treated Cu-rich CIS cell (red curve):
  - ❖ The extrapolation of the activation energy of the V_{OC} (T) curve at zero Kelvin showed values around 0.85 eV. This value (0.85 eV) is still lower than the bandgap energy (0.995 eV) but is significantly higher compared to the activation energy of the untreated Cu-rich CIS cell (0.6 eV). This means that there are still recombination losses at the absorber/buffer interface but these interface recombination losses are much reduced compared to the untreated Cu-rich CIS cell. This indicates that the Se-only PDT succeeded in improving the absorber/buffer interface.
  - ❖ The V_{OC} (T) curve for the Se-treated Cu-rich CIS cell shows the disappearance of one of the two negative slopes observed for the untreated Cu-rich CIS cells leaving only one negative slope (extrapolating to values around 0.85 eV) before the V_{OC} values saturate at lower temperatures.

Comparing the results observed by the IVT measurements for the Se-only PDT to the results of the IVT measurements observed after the ex-situ and the in-situ KF PDT, the following points could be deduced:

- The Se-only PDT is similar to the ex-situ and the in-situ KF PDTs where the Se-only PDT succeeded in removing one of the two negative slopes of the V_{OC} (T) curve typically observed for the untreated Cu-rich CIS solar cells.
- The Se-only PDT is also similar to the ex-situ and the in-situ KF PDTs in reducing the recombination losses at the absorber/buffer interface and improving the interface of the Cu-rich CIS solar cells.
- However, the effect of reducing the interface recombination losses and improving the interface is less pronounced for the Se-only PDT compared to the ex-situ and the in-situ KF PDTs. The extrapolated activation energy for the V_{OC} (T) curve of the Se-treated Cu-rich CIS cell showed values around 0.85 eV compared to values above 0.9 eV for Cu-rich CIS cells treated with the ex-situ and the in-situ KF PDTs.

Based on the above results, it can be concluded that the Se-only PDT succeeded in fulfilling the first objective of improving the V_{OC} and the absorber/buffer interface of Cu-rich CIS solar cells. The second objective of the Se-only PDT is related to the 200 ± 20 meV defect typically observed for Cu-rich CIS solar cells as presented in Section 5.4. The second objective is to discover if the Se-only PDT would be able to passivate the 200 ± 20 meV defect or not.

To answer the above question and discover if the Se-only PDT would passivate the 200±20 meV defect or not, admittance measurements were performed.

Admittance measurements were performed on the two structures presented in Figure 6.20 and the corresponding admittance spectra and Arrhenius plots are presented in Figure 6.24. Figure 6.24 (a, c) presents the admittance spectra for the Se-treated bare (Figure 6.24a) and the Se-treated cell (Figure 6.24c) and Figure 6.24 (b, d) represents the corresponding Arrhenius plots for the Se-treated bare (Figure 6.24b) and the Se-treated cell (Figure 6.24d).

As can be observed in Figure 6.24 (a, c), there are three capacitance regions (separated by the dashed lines). The high temperature capacitance step (Region 1) could not be resolved within our setup measurement range. The inflection frequency points in both spectra could not be deduced. The low temperature capacitance step (Region 3) is related to freeze-out as explained earlier in Section 5.4 with activation energies in the range of 50±10 meV. The main capacitance step is then the intermediate temperature one (Region 2). The activation energy of the main capacitance step (Region 2) was extracted from the corresponding Arrhenius plots for the "Se-treated bare" (Figure 6.24b) and for the "Se-treated cell" (Figure 6.24d). From the activation energies presented in Figure 6.24 (b, d), it can be observed that the 200±20 meV defect was passivated with the Se-only PDT. The disappearance of the 200±20 meV defect was not only observed for the "Se-treated cell" (Figure 6.24d) but was not observed also for the "Se-treated bare" (Figure 6.24b). This means that this 200±20 meV defect was passivated not only in the complete cell but also for the treated bare-absorber. The 200±20 meV defect is observed for Cu-rich CIS cells (discussed in Section 5.4) and also observed for Cu-rich CIS absorbers with only Schottky contacts and no front interface layers (will be discussed in Section 7.1). The disappearance of the 200±20 meV defect from the Cu-rich CIS absorbers and solar cells after the Se-only PDT indicates that the passivation of this 200±20 meV defect is a pure direct property of the Se-only PDT and supports the observation that the 200±20 meV defect is a Se-related defect as will be discussed in Section 7.1. The activation energy of the main capacitance step after performing the Se-only PDT is in the range of 135±15 meV for both Se-treated Cu-rich CIS absorbers and Se-treated Cu-rich CIS solar cells as illustrated in Figure 6.24 (b, d).

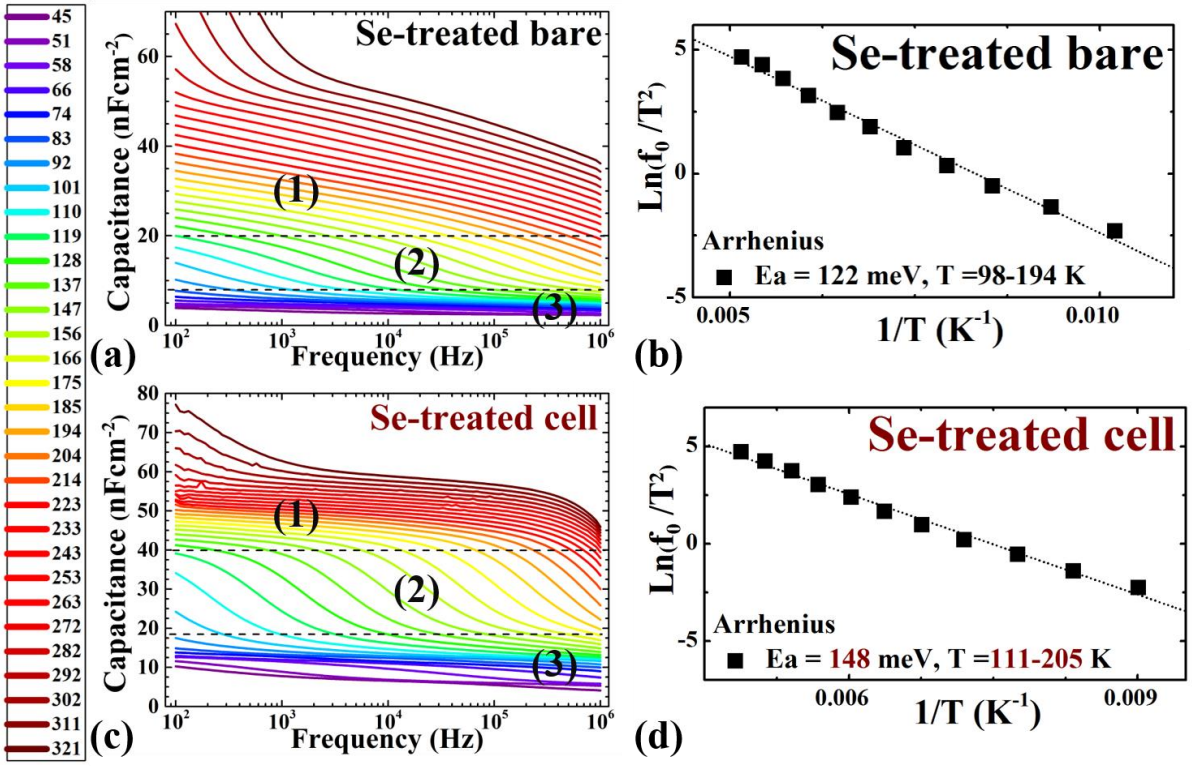

Figure 6.24: Admittance spectra at temperatures between 320 – 50 K as indicated by the temperature scale on the left for: a) Se-treated bare, c) Se-treated cell of Cu-rich CIS absorbers treated with Se-only PDT. The corresponding Arrhenius plots indicate the activation energy of the main capacitance step for b) Se-treated bare and d) Se-treated cell.

While analysing the admittance measurements, I observed an additional difference between the untreated Cu-rich CIS absorbers and solar cells from one side and the Se-treated Cu-rich CIS absorbers and solar cells from the other side. This difference is related to the capacitance derivative plot. The capacitance derivative plot is the plot of the derivative of the capacitance values of the main capacitance step of the admittance spectra (Figure 6.24 (a, c) for example) as a function of frequency and temperature. The inflection frequency peaks are then deduced from the capacitance derivative plot and are plotted in an Arrhenius plot as a function of temperature (Figure 6.24 (b, d) for example). The activation energy of the main capacitance step is deduced from the Arrhenius plot. A detailed explanation of the capacitance derivative plot is provided in Section 4.5.

While analysing the capacitance derivative plots for the untreated and the Se-treated Cu-rich CIS absorbers and solar cells, I observed the following:

- For the untreated Cu-rich CIS absorbers and solar cells, the inflection frequency peaks of the main capacitance step in the capacitance derivative plot are broad peaks as illustrated in Figure 6.25b.
- For comparison, the inflection frequency peaks of the main capacitance step in Cu-poor CIS cells are presented in the capacitance derivative plot of Figure 6.25a showing narrow peaks.
- After analysing the capacitance derivative plot of all Cu-rich CIS absorbers and solar cells, I found that this behaviour of broad inflection frequency peaks for untreated Cu-rich CIS absorbers and solar cells in the capacitance derivative plot of the main capacitance step is observed in all Cu-rich CIS absorbers and solar cells. As the main capacitance step for all Cu-rich CIS absorbers and solar cells has an activation energy of 200±20 meV, I then speculated that the broad behaviour of the inflection frequency peaks for all Cu-rich CIS absorbers and solar cells is related to the 200±20 meV defect.
- For the Se-treated Cu-rich CIS absorbers and solar cells, the inflection frequency peaks of the main capacitance step showed narrow peaks in the capacitance derivative plot as illustrated in Figure 6.25c.

Based on the above observations and putting in consideration that the narrow inflection frequency peaks of the Se-treated Cu-rich CIS absorbers and solar cells are in the same temperature range of the broad inflection frequency peaks of the untreated Cu-rich CIS absorbers and solar cells, I speculated that I can explain the above behaviour in the following points:

- In Cu-rich CIS absorbers and solar cells, there are two main defects overlapping each other and dominating in the same temperature range leading to the formation of those broad peaks (Figure 6.25b).
- These two defects are the 200±20 meV defect observed for Cu-rich CIS as presented in Section 5.4 and the 130±15 meV defect that appeared in Cu-rich CIS after the passivation of the 200±20 meV defect by the Se-PDT.
- The signatures of the second defect are hidden behind the defect of the higher activation energy (200±20 meV), but broadens the peak in the admittance derivative curves.

- In the Se-treated Cu-rich CIS absorbers and solar cells, only the 130±15 meV defect is present and therefore, their inflection frequency peaks of the capacitance derivative plot are narrow.
- This behaviour of broad peaks of the capacitance derivative plot for untreated Cu-rich CIS cells and narrow peaks for treated Cu-rich CIS cells was also observed after the in-situ KF PDT as discussed in Section 6.2.

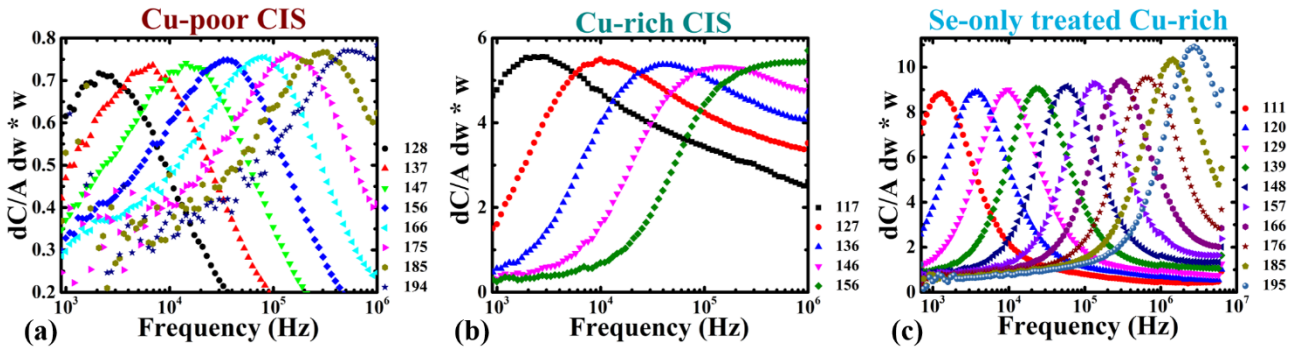

Figure 6.25: Spectra of capacitance derivative peaks from which the activation energy of the main capacitance step was extracted for a) Cu-poor CIS, b) Cu-rich CIS and c) Cu-rich CIS treated with Se-only PDT. Cu-rich CIS samples have broad peaks while Cu-poor and Cu-rich Se-treated samples have narrow peaks. Corresponding temperatures are presented on the right side of each spectra.

If my speculated explanation of the capacitance derivative plot is true, then the 130±15 meV defect should be present in Cu-rich CIS absorbers and solar cells with and without the Se-only PDT. To further support this hypothesis, I asked Finn Babbe, who is responsible for the optical characterization to check the presence of this 130±15 meV defect using PL measurements.

PL measurements are considered an effective characterization mean to identify defects. Unfortunately, the PL measurements could not identify the presence of the 200±20 meV defect in untreated Cu-rich CIS absorbers as the 200±20 meV defect lies outside our PL measurement range. However, the PL measurements should be able to detect the 130±15 meV defect if it is present. If my speculation is true, then the 130±15 meV defect should be detected on Cu-rich CIS absorbers with and without the Se-only PDT. If my speculation is not true, then the 130±15 meV defect should be detected only for the Se-treated Cu-rich CIS absorber and not for the untreated Cu-rich CIS absorber.

PL measurements performed at an intensity of 1 mW on a Cu-rich CIS absorber with and without the Se-only PDT revealed the presence of a peak at 0.9 eV as illustrated in Figure 6.26. This peak is present with and without the Se-only PDT with an activation energy in the range of 130±15 meV. We published the details explaining the extraction of this activation energy of 130±15 meV in [13]. The activation energy of 130±15 meV extracted from PL measurements for Cu-rich CIS absorbers with and without the Se-only PDT is in an excellent agreement with the activation energy of the defect extracted from admittance measurements for the Se-treated Cu-rich CIS absorber (130±15 meV).

The presence of the 0.9 eV PL peak with and without the Se-PDT indicates that this 130±15 meV defect was present even before the Se-only PDT. This 130±15 meV defect present in Cu-rich CIS absorbers before the Se-only PDT was not observed by admittance measurements as it was hidden behind the capacitance step of the 200±20 meV defect leading to the formation of a broad peak for the capacitance derivative of Cu-rich CIS absorbers and solar cells.

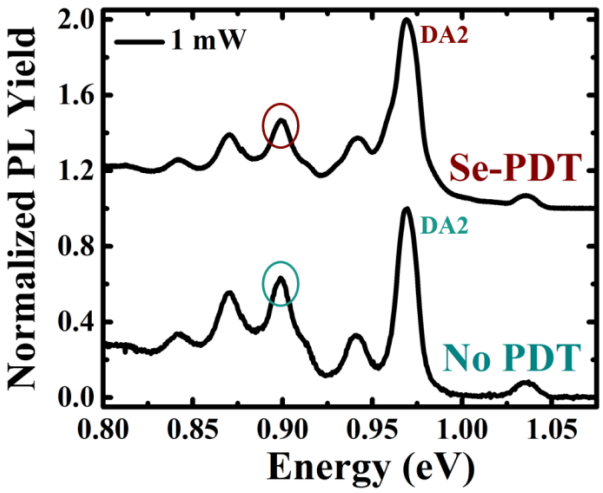

Figure 6.26: Normalized PL spectra for Cu-rich CIS with and without a Se-only PDT at an intensity of 1 mW. The PL spectra reveal the presence of a peak at 0.9 eV with and without the Se-only PDT.

The last characterization performed for the Cu-rich CIS absorbers and solar cells with and without the Se-only PDT is the CV measurements. The CV measurements are used to extract the doping from the corresponding Mott-Schottky plots as explained in Section 4.4. I believe that the extracted doping from the CV measurements below is the apparent doping and not the real absorber doping. The apparent doping is the doping at the space charge region and could be influenced by layers other than the absorber layer. More details on the apparent doping were provided in Section 4.4.

The results of the CV measurements for Cu-rich CIS absorbers and solar cells with and without the Se-only PDT are presented in Figure 6.27. Figure 6.27a illustrates the Mott-Schottky plot for Cu-rich CIS solar cells with and without the Se-only PDT, while Figure 6.27b illustrates the Mott-Schottky plot of Cu-rich CIS absorbers with and without the Se-only PDT.

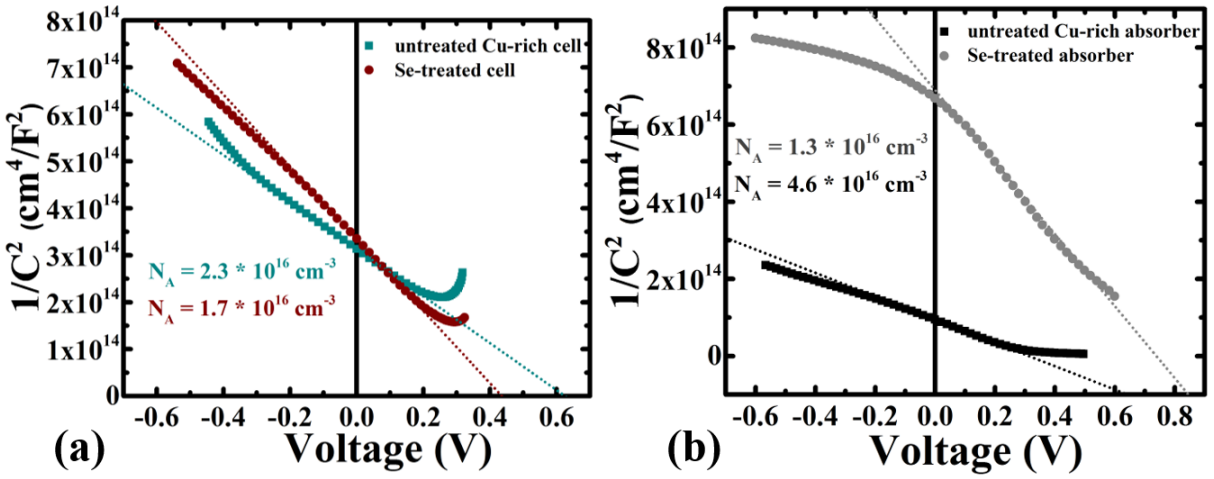

Figure 6.27: Mott-Schottky plot based on CV measurements for: a) Cu-rich CIS solar cells with and without the Se-only PDT and b) Cu-rich CIS bare-absorbers with and without the Se-only PDT. Short dotted lines represent the fitting (performed linearly at slight forward bias) from which the apparent doping was extracted. The apparent doping decreases after the Se-only PDT for both Cu-rich CIS absorbers and solar cells.

The interpretation of the CV measurements can be summarized in the following points:

- For the Cu-rich CIS solar cells, the corresponding Mott-Schottky plots presented in Figure 6.27a showed that the apparent doping decreased from 2.3 * 10^{16} cm^{-3} for the untreated Cu-rich CIS cell to 1.7 * 10^{16} cm^{-3} for the Se-treated Cu-rich CIS cell.
- For the Cu-rich CIS absorbers, the corresponding Mott-Schottky plots presented in Figure 6.27b showed a similar behaviour to the Cu-rich CIS solar cells. The apparent doping showed a more pronounced decrease after the Se-only PDT where the apparent doping decreased from 4.6 * 10^{16} cm^{-3} for the untreated Cu-rich CIS absorber to 1.3 * 10^{16} cm^{-3} for the Se-treated Cu-rich CIS absorber.
- The decrease in the apparent doping of the Cu-rich CIS absorbers and solar cells after the Se-only PDT can be attributed to the passivation of the 200±20 meV defect that is likely to be an acceptor defect as discussed in Section 7.2.

- Comparing the apparent doping of the untreated Cu-rich CIS absorber (Figure 6.27b) and the apparent doping of the untreated Cu-rich CIS cell, it can be observed that the apparent doping of the Cu-rich CIS absorber decreased after processing the Cu-rich CIS absorber to a solar cell. This decrease in apparent doping for the Cu-rich CIS cell compared to the Cu-rich CIS absorber could be explained in terms of the diffusion of Cd donors to the surface of Cu-rich CIS absorbers.
- On the other side, the apparent doping of the Se-treated Cu-rich CIS absorber (Figure 6.27b) remained nearly unchanged after further processing the Se-treated Cu-rich CIS absorber as a solar cell. This can be related to the effect of the Se-only PDT. The Se-only PDT succeeded in passivating the 200±20 meV defect by filling the Se-related defect vacancies with Se. Therefore, I speculate that:
  - ❖ Without the Se-only PDT, Cd donors from the CdS buffer layer diffuse to the surface of Cu-rich CIS absorbers filling the Se-related defect vacancies and consequently causing a decrease in the apparent doping of the Cu-rich CIS solar cells compared to the Cu-rich CIS absorbers.
  - ❖ With the Se-only PDT, the 200±20 meV acceptor defect is passivated explaining the decrease of the apparent doping of Cu-rich CIS absorbers and solar cells after the Se-only PDT.
  - ❖ Moreover, with the Se-only PDT, the Se from the Se-only PDT fills the Se-related defect vacancies in such a way that Cd donors are not able to diffuse to the Cu-rich CIS absorbers. This explains why the apparent doping remained nearly unchanged between the Se-treated Cu-rich CIS absorber and the Se-treated Cu-rich CIS solar cell. The effect of the front layers (CdS and window layers) on the apparent doping is almost negligible after passivating the surface of the Cu-rich CIS absorbers with the Se-only PDT.
  - ❖ The ability of the Se-only PDT to prevent the Cd atoms from diffusing to the Cu-rich CIS surface could be an additional explanation to the decreased EQE response at shorter wavelengths. This decreased EQE response at shorter wavelengths was attributed to an increased CdS layer thickness and was observed with any PDT that contains Se such as the ex-situ KF (Section 6.1), the in-situ KF (Section 6.2) and the Se-only PDT.

6.5 Low-bandgap Cu-poor CIS & CIGS for tandem applications

Cu-poor CIS and CIGS solar cells were optimized in terms of electrical performance. The objective of optimizing these absorbers is to provide potential high performance low-bandgap cells for tandem applications. In this section, Cu-poor CIS and CIGS solar cells were optimized in terms of absorber growth with no additional PDT. Only an ARC layer was deposited on top of the optimized cells to decrease the optical losses and improve the efficiency correspondingly. Three high performance absorbers were produced. A ternary CIS absorber with a bandgap of 0.95 eV (CIS 0.95) was developed as well as two quaternary CIGS with very low Ga content with bandgaps of 1.04 eV (CIGS 1.04) and 1.07 eV (CIGS 1.07). The bandgaps were extracted from the linear extrapolation of the EQE slope at long wavelengths [33] as explained in Section 4.2. The EQE spectra before and after adding the ARC layer for each of the three cells are presented in Figure 6.28.

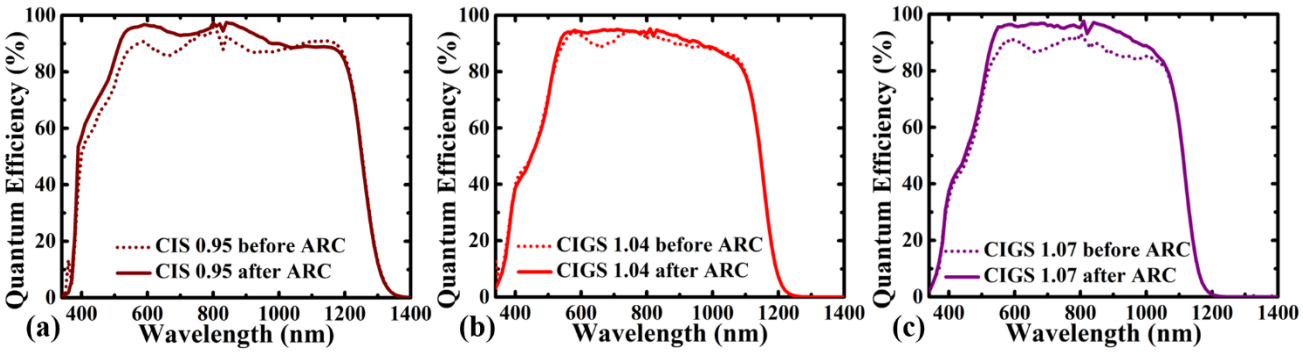

Figure 6.28: EQE spectra for a) CIS 0.95, b) CIGS 1.04 and c) CIGS 1.07 before and after adding an ARC layer

Based on the reflection measurements performed by Finn Babbe, an ARC thickness of 94 nm was targeted for CIS 0.95 and CIGS 1.07 to minimize the optical losses at a wavelength of 519 nm. For CIGS 1.04, a thickness of 99 nm was targeted to improve the optical losses at a specific high reflection maxima peak [34] with a wavelength of 548 nm. The thickness of the ARC layer was calculated using Equation 3.1 in Section 3.1.2 and shown again in Equation 6.1.

$$d = \frac{\lambda}{4\,n} \qquad [6.1]$$

The ARC thickness (d) for CIS 0.95, CIGS 1.04 and CIGS 1.07 was calculated using Equation 6.1 with n = 1.38 (Refractive index of MgF_2) for all the three cells and λ = 519, 548 and 519 nm for CIS 0.95, CIGS 1.04 and CIGS 1.07 respectively. These wavelengths of 519, 548 and 519 nm for CIS 0.95, CIGS 1.04 and CIGS 1.07 respectively correspond to the wavelengths of the reflection maxima peaks in each of the three CI(G)S cells.

The corresponding improvements at the targeted wavelengths can be observed in Figure 6.28. After performing the ARC deposition, two of the three cells were sent for certification at Fraunhofer-Institut fur Solare Energiesysteme (ISE); CIGS 1.04 and CIGS 1.07. The EQE of the certified cells were in an excellent agreement with the spectra measured at our laboratories. A comparison between the EQE spectra of the two certified cells with that of the CIS 0.95 measured in-house is presented in Figure 6.29.

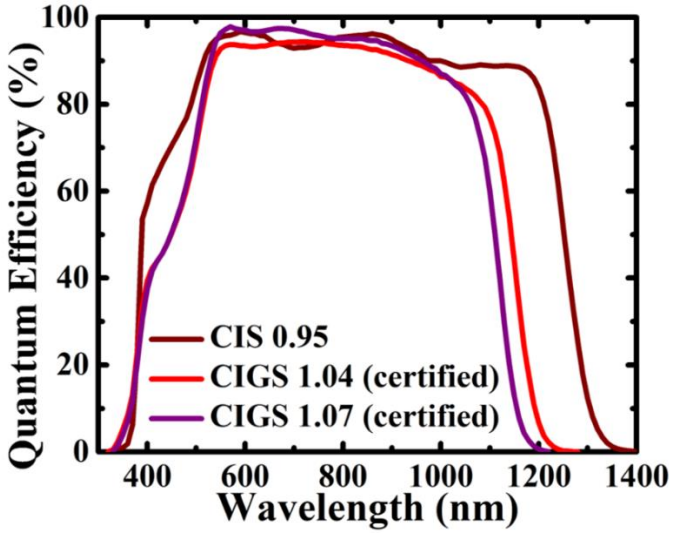

Figure 6.29: EQE spectra for CIS 0.95 measured in-house and CIGS 1.04 and CIGS 1.07 certified at Fraunhofer-ISE.

The differences in bandgaps between the three cells can be clearly observed from the EQE response in Figure 6.29 at longer wavelengths. At short wavelengths, CIS 0.95 has relatively higher EQE values. This is attributed to a thicker CdS layer (double CdS layer) for CIGS 1.04 and CIGS 1.07 compared to CIS 0.95. While processing similar CIGS absorbers from the absorber growth run just before the absorber growth run used for CIGS 1.04 and CIGS 1.07, we faced some homogeneity problems. Therefore, for the CIGS 1.04 and the CIGS 1.07 absorbers, we (me and Finn Babbe) decided to deposit a double CdS layer to avoid possible homogeneity problems. This double CdS layer on CIGS 1.04 and CIGS 1.07 absorber layers caused an increased parasitic absorption by the CdS buffer layer.

These additional absorption losses by the CdS buffer layer are reflected at the short wavelength region of the EQE spectra for CIGS 1.04 and CIGS 1.07 solar cells (Figure 6.29). The double CdS layer for CIGS 1.04 and CIGS 1.07 is responsible for the reduced EQE spectra at short wavelength regions of these two solar cells (CIGS 1.04 and CIGS 1.07) compared to CIS 0.95 with a single standard CdS layer. As a future outlook, a thinner CdS buffer layer could be deposited for similar CIGS absorbers with low bandgaps with the potential to achieve higher J_{SC} and higher efficiencies.

Moreover, Figure 6.29 illustrates the high performance of the three cells with the EQE responses showing values of more than 95 % for most of the EQE spectra (wavelengths of 600 – 1000 nm). This high performance behaviour of the three cells is reflected on the J_{SC} presented in Table 6.7 and observed in Figure 6.30 and Figure 6.31b. All the IV measurements presented below were performed after adding the ARC layer.

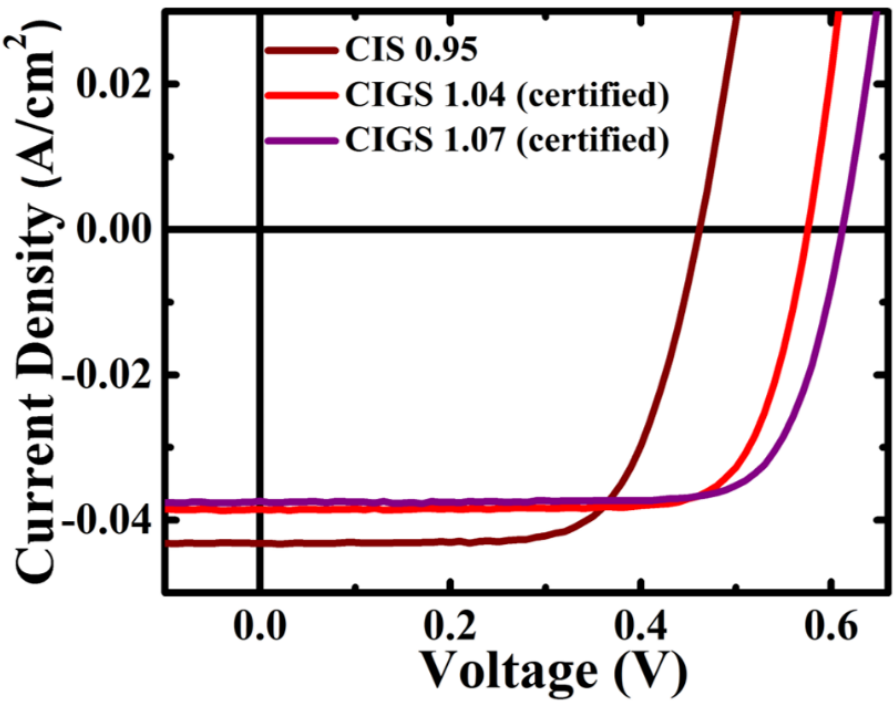

Figure 6.30: IV characteristics for CIS 0.95 solar cell measured in-house as well as CIGS 1.04 and CIGS 1.07 solar cells certified at Fraunhofer-ISE

Table 6.7: Electrical parameters for CIS 0.95, CIGS 1.04 and CIGS 1.07 solar cells. The presented values correspond to the best solar cell measured in-house while the values in brackets are the parameters for the same solar cell certified at Fraunhofer-ISE. CIS 0.95 solar cell was not sent for certification.

Sample	Efficiency (%)	*FF* (%)	V_{OC} (mV)	J_{SC} (mA/cm^2)	V_{OC} deficit (E_g) (mV)	$\eta_{elec.}$ (%)	$\eta_{op.}$ (%)	*qFLS* (meV)
CIS 0.95	14.1 (-)	70.6 (-)	462 (-)	43.2 (-)	488 (-)	53 (-)	85 (-)	494 (-)
CIGS 1.04	17.3 (15.7)	77.5 (76.6)	577 (578)	38.7 (35.4)	463 (462)	64 (64)	84 (77)	633 (-)
CIGS 1.07	18.3 (16.6)	78.9 (76.9)	621 (619)	37.3 (34.9)	449 (451)	66 (66)	83 (78)	674 (-)

Based on Table 6.7 and Figure 6.30, it can be observed that as the bandgap increases, the V_{OC} increases while the J_{SC} decreases. The values in Table 6.7 represent the IV parameters for the three cells measured in-house while the values in brackets represent the certified values measured at Fraunhofer-ISE. Comparing the values measured in-house with the certified ones, we can deduce an excellent match in terms of both V_{OC} and FF. However, an overestimated in-house J_{SC} values were measured due to a spectral mismatch of our IV setup leading to an overestimated efficiency. The high performance of the three cells can be realized from their corresponding efficiencies of 14.1 % (in-house), 15.7 % (certified) and 16.6 % (certified) for CIS 0.95, CIGS 1.04 and CIGS 1.07 respectively. It is interesting to note that at the time of publishing these results, the certified efficiency of 16.6 % for CIGS 1.07 solar cell represents the record for such CIGS solar cells with the following characteristics:

1. Bandgaps (estimated from the linear extrapolation of the EQE) less than 1.1 eV.
2. No post-deposition treatments used.

To further analyse the performance of these three cells, the V_{OC} deficit with respect to the bandgap, V_{OC} deficit (E_g), was deduced. The V_{OC} deficit (E_g) was calculated as the difference between the bandgap of each of the three cells and their corresponding V_{OC} (Equation 6.2). To differentiate between the electrical and the optical losses and understand the main cause of the high performance for these cells, the relative electrical ($\eta_{elec.}$) and optical ($\eta_{op.}$) efficiencies were calculated as in [35].

The $\eta_{elec.}$ was deduced as the ratio between the measured V_{OC} times the FF values compared to the V_{OC} and the FF values of the Shockley-Queisser (*SQ*) limit [36] at the corresponding bandgap (Equation 6.3).

On the other side, the $\eta_{op.}$ was extracted as the ratio between the measured J_{SC} value to the J_{SC} value of the SQ limit at that corresponding bandgap (Equation 6.4).

$$V_{\mathrm{OC}}\ deficit\ (E_g) = \tfrac{1}{q} E_G - V_{OC}, \tag{6.2}$$

$$\eta_{\mathrm{elec.}} = \frac{V_{\mathrm{OC}} * FF}{V_{\mathrm{OC}}^{\mathrm{SQ}} * FF^{\mathrm{SQ}}}, \tag{6.3}$$

$$\eta_{\mathrm{op.}} = \frac{J_{\mathrm{SC}}}{J_{\mathrm{SC}}^{\mathrm{SQ}}}, \tag{6.4}$$

$V_{\mathrm{OC}}{}^{\mathrm{SQ}}$ is the *SQ* limit for V_{OC} with values of 705, 789 and 817 mV, FF^{SQ} is the *SQ* limit for *FF* with values of 0.88, 0.88 and 0.89 and $J_{\mathrm{SC}}{}^{\mathrm{SQ}}$ is the *SQ* limit for J_{SC} with values of 50.9, 46.1 and 44.7 mA/cm^2 for bandgaps of 0.95, 1.04 and 1.07 eV respectively. The *SQ* limits for the V_{OC}, *FF* and J_{SC} were calculated using the *SQ* model presented in [36].

Moreover, the *SQ* V_{OC} deficit with respect to the bandgap, $V_{OC}{}^{SQ}$ deficit (E_g), was calculated as the difference between each cell bandgap and the corresponding *SQ* V_{OC} limit with values of 245, 251 and 253 mV for the bandgaps of 0.95, 1.04 and 1.07 eV respectively. The V_{OC} deficit (E_g) and $V_{OC}{}^{SQ}$ deficit (E_g) are illustrated in Figure 6.31a. The V_{OC} deficit (E_g) values plotted in Figure 6.31a indicates the improvement to the V_{OC} deficit (E_g) as a function of increasing the bandgap. The V_{OC} deficit (E_g) decreased from a value of 488 mV for CIS 0.95 to values of 462 and 451 mV for CIGS 1.04 and CIGS 1.07 respectively as presented in Table 6.7 and Figure 6.31a with the addition of Ga.

Based on the V_{OC} deficit (E_g) values, it can be concluded that the addition of Ga decreases the V_{OC} deficit (E_g) and consequently enhances the electrical efficiency as presented in Table 6.7. This means that the addition of Ga helps in improving the bulk by reducing recombination. This can be normally attributed to the Ga gradient in the 3-stage CIGS growth process increasing towards the backside that helps in preventing back contact recombination [37, 38].

Comparing the decrease of the V_{OC} deficit (E_g) (which is the difference between the bandgap and the V_{OC}) as a function of adding Ga and increasing the bandgap to the increase of the $V_{OC}{}^{SQ}$ deficit (E_g) (which is the difference between the bandgap and the *SQ* V_{OC} limit); we can understand the amount of improvements achieved.

The increase in the V_{OC}^{SQ} deficit (E_g) values as a function of the bandgap means that the gap between the bandgap energy and the V_{OC}^{SQ} is increasing as the bandgap energy increases and then it is expected that the gap between the V_{OC} and the bandgap, V_{OC} deficit (E_g), would also increase. Therefore, the decrease in the V_{OC} deficit (E_g) values as a function of the bandgap despite the increase of the V_{OC}^{SQ} deficit (E_g) values as observed in Figure 6.31a indicates a real improvement to the absorber quality as a function of increasing the bandgap. This improvement is more pronounced when observing the difference between the V_{OC} and the V_{OC}^{SQ}, or the V_{OC} deficit with respect to V_{OC}^{SQ} limit values, V_{OC} deficit (SQ), and the quasi Fermi Level splitting deficit with respect to V_{OC}^{SQ}, qFLs deficit (SQ), presented also in Figure 6.31a and explained below.

As illustrated in Figure 6.31a, the V_{OC} deficit (SQ) values decrease with the addition of Ga showing values of 243, 212 and 196 mV for CIS 0.95, CIGS 1.04 and CIGS 1.07 respectively. These values confirm the enhanced recombination as a result of adding Ga. To investigate if this enhanced recombination resulted during the absorber growth, or during the deposition of the other layers of the baseline process, the qFLs deficit with respect to the bandgap, qFLs deficit (E_g), and the qFLs deficit with respect to V_{OC}^{SQ}, qFLs deficit (SQ), were deduced and were illustrated in Figure 6.31a.

The qFLs was first measured (by Finn Babbe) at the equivalent illumination of 1-sun for the three absorbers covered with CdS only from calibrated PL measurements performed at room temperature. The qFLs showed values of 494, 633 and 674 meV for CIS 0.95, CIGS 1.04 and CIGS 1.07 respectively. The qFLs deficit (E_g) was then calculated as the difference between the bandgap and the qFLs showing a significant decrease with the addition of Ga from 456 to 407 to 396 meV.

Comparing the qFLs values with that of the V_{OC}^{SQ}, we can observe that the difference between the two values, the qFLs deficit (SQ), decreased with the addition of Ga (decreased from 211 to 156 to 143 meV) and is less than the difference between the V_{OC} and the V_{OC}^{SQ}, V_{OC} deficit (SQ), with values of 243, 212 and 196 mV. This means that the improvement observed for the absorber is more than the improvement observed for the solar cell. The other stacking layers reduced part of the improvement achieved in the electronic quality of the absorber.

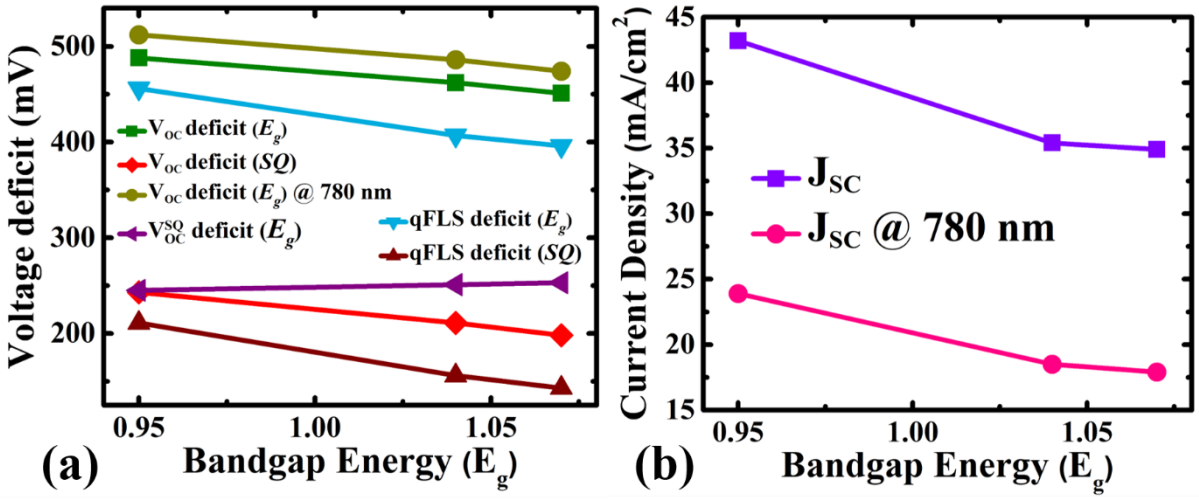

Figure 6.31: a) V_{OC} deficit (E_g), V_{OC} deficit (E_g) measured with a long-pass optical filter at a wavelength of 780 nm, V_{OC}^{SQ} deficit (E_g), V_{OC} deficit (SQ), qFLS deficit (E_g) and qFLs deficit (SQ). b) J_{SC} and J_{SC} measured with the same long-pass optical filter as function of bandgap energy (E_g) for CIS 0.95, CIGS 1.04 and CIGS 1.07

Moreover, it can be concluded from the values in Table 6.7 calculated based on the above equations (Equations 6.2, 6.3 and 6.4) that the high performance of the three cells is based mainly on the higher optical performance of the three cells compared to their electrical performance. The electrical efficiency for the three cells is showing values of 53, 64 and 66 % for CIS 0.95, CIGS 1.04 and CIGS 1.07 respectively. Although the electrical efficiency increased with the increase of the bandgap, but the electrical efficiencies for the three cells are lower than the optical efficiency that showed values in the range of 83 – 85 % for the three CI(G)S cells as depicted from Table 6.7. These higher values of the optical efficiency compared to the electrical efficiency indicate that the three cells suffer more on the electrical part in terms of recombination compared to the optical part in terms of incomplete absorption.

The main objective of these high performance solar cells is the potential of using them as low-bandgap bottom cells in tandem applications. To verify their ability to be integrated as bottom cells, a long-pass optical filter of 780 nm corresponding to a bandgap of 1.59 eV was used to measure the IV characteristics of these solar cells. This filter should simulate a top-cell with a bandgap of 1.59 eV very close to the bandgap of a perovskite top-cell used in a state-of-the-art tandem solar cell [39]. The IV characteristics of these cells under the optical long-pass filter are presented in Figure 6.32 and the corresponding parameters are extracted in Table 6.8. It is important to note that the J_{SC} of these cells measured under the optical filter was divided by a factor corresponding to the spectral mismatch between our standard J_{SC} measured in-house and the certified one measured at Fraunhofer-ISE.

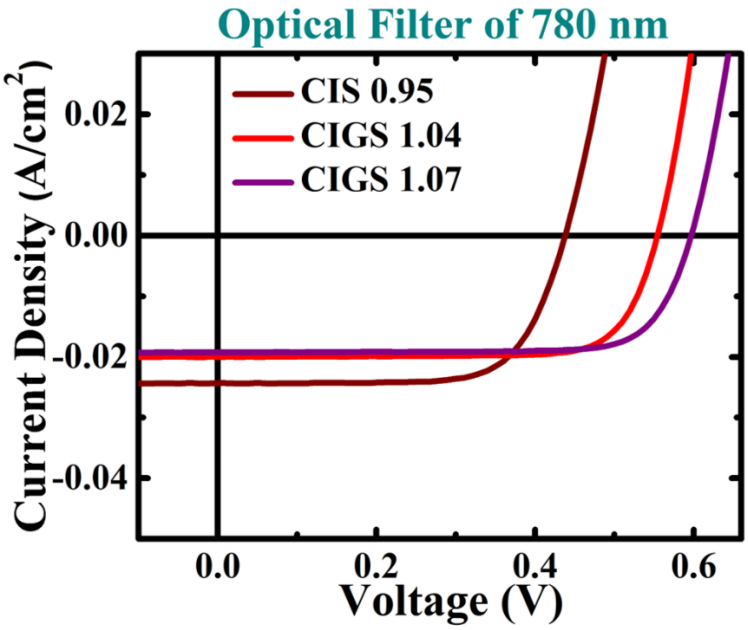

Figure 6.32: IV characteristics of CIS 0.95, CIGS 1.04 and CIGS 1.07 measured under a long-pass optical filter of 780 nm

Table 6.8: Electrical parameters for CIS 0.95, CIGS 1.04 and CIGS 1.07 measured under a long-pass optical filter of 780 nm.

Sample with an optical filter of 780 nm	Efficiency (%)	*FF* (%)	V_{OC} (mV)	J_{SC} (mA/cm^2)
CIS 0.95	7.4	71.0	438	23.9
CIGS 1.04	7.9	77.0	554	18.5
CIGS 1.07	8.3	78.0	596	17.9

From Figure 6.32 and Table 6.8, the high performance of these solar cells can be observed. The three cells showed high efficiencies of 7.4, 7.9 and 8.3 % for CIS 0.95, CIGS 1.04 and CIGS 1.07 respectively under the optical filter. These efficiency values are higher than the efficiencies reported in [39] for bottom low-bandgap cells in a state-of-the-art tandem thin film solar cell without neglecting the fact that the bottom low-bandgap cells reported in [39] were measured under a real top cell with limited transparency in the transparent region and our proposed low-bandgap cells were measured under an optical filter. Using the top-cell reported in [39], our cells have the potential of achieving efficiencies up to 24.4 %. The V_{OC} deficit (E_g) and the J_{SC} deficit of these cells were presented in Figure 6.31.

To test the high quality of the absorbers, IVT measurements were performed to identify the dominant recombination paths in these cells. IVT measurements were performed in a temperature range of 50 – 320 K and the results are depicted in Figure 6.33a.

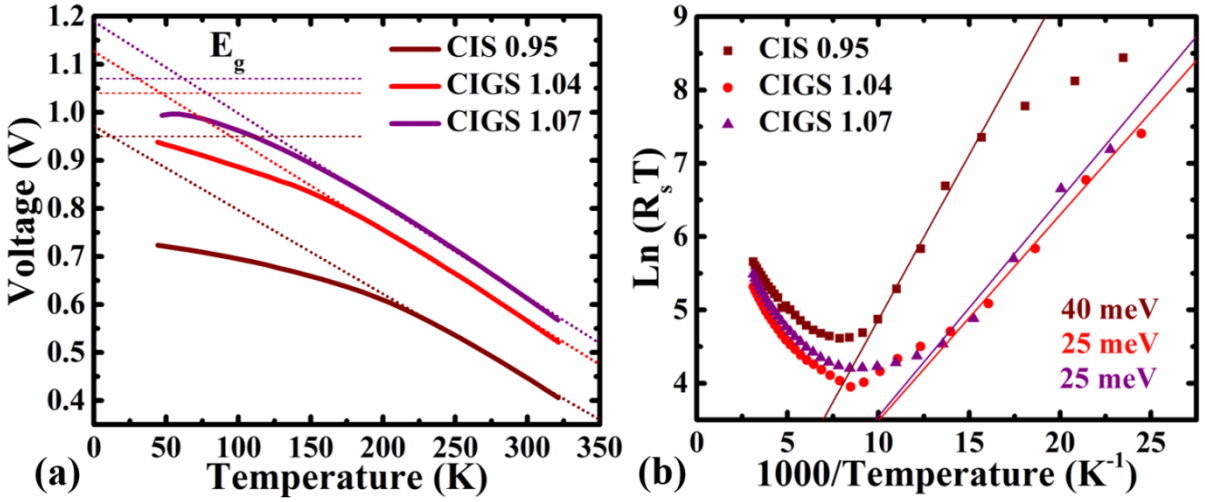

Figure 6.33: a) V_{OC} as function of temperature for CIS 0.95, CIGS 1.04 and CIGS 1.07. Short dotted lines represent the fitting at high temperature to extrapolate the activation energies at zero Kelvin. The short dashed lines represent the bandgap extracted from EQE measurements for each corresponding cell, b) Arrhenius plot of the series resistance as function of temperature for CIS 0.95, CIGS 1.04 and CIGS 1.07. Solid lines represent the fitting from which the slope was used to extract the corresponding activation energy.

Figure 6.33a represents the V_{OC} as a function of temperature for the three cells. The activation energies at zero Kelvin were extrapolated from fitting the V_{OC} (T) curves at room temperature (at which the cells operate) represented by the short dotted lines in Figure 6.23a. The extrapolation of the activation energy at zero Kelvin from the IVT measurements is explained in Section 4.3. The activation energy for the three cells showed the typical behaviour of Cu-poor CI(G)S cells extrapolating to the bandgap. The extrapolated activation energies at zero Kelvin for all three cells showed values close to their corresponding bandgap (bandgaps are represented by short dashed lines in Figure 6.33a). This means that the dominant recombination path for all the three cells is in the bulk of these absorbers as explained in Section 4.3. It is important to note that the extrapolated activation energies at zero Kelvin in Figure 6.33a show slightly higher values compared to the corresponding bandgaps. This can be attributed to the following potential reasons:

1. The expected temperature dependency of the effective density of states and the temperature dependent thermal velocity [38, 40] that can lead to an increase in the activation energies of the V_{OC} (T) of up to 75 meV.

2. The method of deducing the bandgap. In this thesis, the bandgap was deduced from the linear extrapolation of the EQE measurements as explained in Section 4.2. In [41], it has been reported that the bandgap extracted from the linear extrapolation of the EQE measurements is likely to be underestimated and the real bandgap could be a bit higher.

IVT measurements were also used to extract the activation energies of the thermally activated series resistance. The series resistance was deduced from the slope of the IV curve at far forward bias (1.2 V) as a function of temperature as explained in Section 4.3. The corresponding Arrhenius plots of the series resistance as a function of temperature for the three CI(G)S cells are presented in Figure 6.33b. The activation energies for the series resistance showed values of 40 meV for CIS 0.95 cell and values of 25 meV for both CIGS 1.04 and CIGS 1.07 solar cells.

Finally, admittance measurements were performed to deduce the main capacitance steps and identify potential defects in the three cells. The admittance spectra were measured under dark conditions for the three cells and are presented in Figure 6.34 with their corresponding Arrhenius plots.

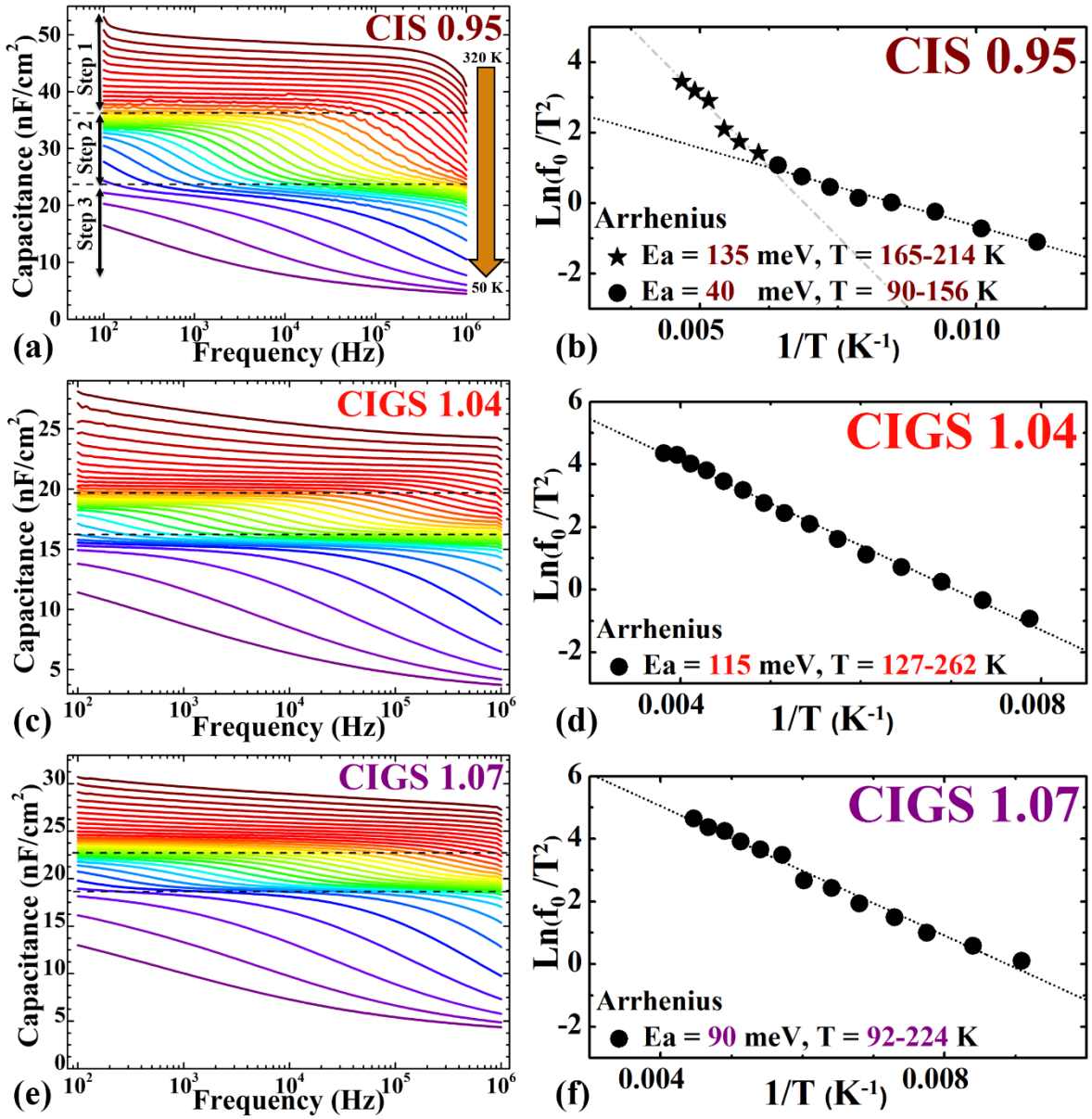

Figure 6.34: Admittance spectra for a) CIS 0.95, c) CIGS 1.04 and e) CIGS 1.07. The two dashed lines identify the three capacitance steps. Arrhenius plots for b) CIS 0.95, d) CIGS 1.04 and f) CIGS 1.07. The short dotted lines represent the fitting from which the activation energies were extracted.

The admittance spectra in Figure 6.34(a, c, e) show the presence of three capacitance steps (identified by the dashed lines) and illustrated clearly in Figure 6.34a. The three steps can be interpreted as follows:

1. The first step at high temperatures is characterized by a broad capacitance dispersion. This step could be attributed to either in-homogeneities or tail states [42] or to a broad defect-related step detectable below our frequency measurement range with only a very weak potential of recombination activities even at room temperatures.

2. The second step is the main capacitance step and our main concern.
3. The third step at low temperatures represents a carrier or mobility freeze-out as the capacitance values are close to the absorber geometrical capacitance at these temperature ranges (5 nF/cm^2). The activation energies of the third step are in the range of 50±10 meV for all three CI(G)S cells.

As mentioned earlier, the second capacitance step is the main capacitance step and recombination-active defects are expected to interact at these temperature ranges. This capacitance step is analysed by plotting the corresponding Arrhenius plot for the inflection frequencies of these capacitances divided by T^2 [43] and the activation energies for the second capacitance step were then extracted from the slope of these Arrhenius plots presented in Figure 6.34(b, d, f). The extraction of the activation energy from the Arrhenius plot of the main capacitance step is explained in more detail in Section 4.5.

For CIS 0.95 in Figure 6.34b, the second capacitance step is composed of two steps; one step with an activation energy of 130±15 meV while the other step has an activation energy of 40 meV. For CIGS 1.04 (Figure 6.34d) and CIGS 1.07 (Figure 6.34f), the activation energy of the main capacitance step showed values of 115 and 90 meV respectively. These values (115 and 90 meV) are in the range of 100±10 meV. It can be observed that the activation energies of the main capacitance step (step 2) for all the three CI(G)S cells (135, 115 and 90 meV for CIS 0.95, CIGS 1.04 and CIGS 1.07 respectively) are much higher than the activation energy extracted from the series resistance (40, 25 and 25 meV for CIS 0.95, CIGS 1.04 and CIGS 1.07 respectively). Moreover, the activation energy of the series resistance is fairly constant for the three cells, while that of the capacitance measurements decreases with the addition of Ga. In addition to that, the current densities of the forward bias were deduced for the three CI(G)S cells and indicated the behaviour of a simple diode model. This means that the activation energies deduced from admittance measurements for all the three cells represent that of shallow defects and not interface barriers as explained in Section 4.5 [44, 45].

As mentioned above, the activation energies deduced from admittance measurements for the main capacitance step (step 2) showed a reduction (135 to 115 to 90 meV) with adding more Ga. A possible interpretation for these activation energies is discussed in the following points:

- For CIS 0.95, the activation energy of 135 meV for the main capacitance step (step 2) could be attributed to the third acceptor observed by PL measurements. PL measurements performed by Finn Babbe for Cu-rich CIS absorbers indicated the presence of a defect at 0.9 eV (discussed above) and its activation energy showed values of 130±15 meV. This defect is likely to be the Indium vacancy defect. We published the results of the identification of this defect in [13]. Therefore, the activation energy of the main capacitance step in CIS 0.95 (135 meV) fits well with the third shallow acceptor defect observed by the PL measurements for CIS absorbers.
- For CIGS 1.04, the activation energy of 115 meV for the main capacitance step (step 2) could be attributed to either:
    - ❖ The same third shallow acceptor defect observed by PL measurements for CIS absorbers as the 115 meV activation energy of the main capacitance step falls in the activation energy range of the third acceptor defect with values of 130±15 meV.
    - ❖ The third shallow acceptor defect observed by PL measurements for CGS absorbers with an activation energy of around 100 meV as reported in [46, 47].

A possible contribution from both defects (third acceptor defect in CIS and CGS) with the addition of Ga could also explain the decrease of the activation energy from 135 meV for CIS 0.95 (pure CIS with no Ga) to 115 meV for CIGS 1.04 solar cell.

- For CIGS 1.07, the activation energy of 90 meV for the main capacitance step (step 2) fits well with the activation energy of the third shallow acceptor defect observed by PL measurements for CGS absorbers with an activation energy of around 100 meV [46, 47].

Therefore, we can conclude that the three cells do not show any evidence of deep defects (within our measurement limits) proving their high performance behaviour and can be considered promising potentials of bottom low-bandgap cells in tandem applications.

References Chapter 6

[1] H. Elanzeery, F. Babbe, M. Melchiorre, A. Zelenina, S. Siebentritt, "Potassium Fluoride Ex-Situ Treatment on Both Cu-Rich and Cu-Poor $CuInSe_2$ Thin Film Solar Cells", IEEE Journal of Photovoltaics 7 684–689 (2017).

[2] F. Babbe, H. Elanzeery, M. Melchiorre, A. Zelenina, S. Siebentritt, "Potassium fluoride post deposition treatment with etching step on both Cu rich and Cu poor $CuInSe_2$ thin film solar cells", Physical Review Materials, 2, 105405 (2018).

[3] L. Choubrac, T. Bertram, H. Elanzeery, S. Siebentritt, "$Cu(In,Ga)Se_2$ solar cells with improved current based on surface treated stoichiometric absorbers", Phys. Status Solidi., 214, 1600482 (2017).

[4] H. Elanzeery, M. Melchiorre, M. Sood, F. Babbe, F. Werner, G. Brammertz and S. Siebentritt, "Challenge in Cu-rich $CuInSe_2$ Thin Film Solar Cells: Defect Caused by Etching", submitted (2018).

[5] H. Elanzeery, F. Babbe, M. Melchiorre, F. Werner, S. Siebentritt, "High-performance low bandgap thin film solar cells for tandem applications", Prog. Photovolt. Res. Appl., 26, pp. 437–442 (2018).

[6] A. Chirila, P. Reinhard, F. Pianezzi, P. Bloesch, A. R. Uhl, C. Fella, L. Kranz, D. Keller, C. Gretener, H. Hagendorfer, D. Jaeger, R. Erni, S. Nishiwaki, S. Buecheler and A. N. Tiwari, "Potassium-induced surface modification of $Cu(In,Ga)Se_2$ thin films for high-efficiency solar cells," Nature Materials, 12, pp. 1107–1111 (2013).

[7] P. Pistor, D. Greiner, C. Kaufmann, S. Brunken, M. Gorgoi, A. Steigert, W. Calvet, I. Lauermann, R. Klenk, T. Unold and M. Lux-Steiner, "Experimental indication for band gap widening of chalcopyrite solar cell absorbers after potassium fluoride treatment", Applied Physics Letters, 105, 063901 (2014).

[8] R. Kamada, T. Yagioka, S. Adachi, A. Handa, K. F. Tai, T. Kato and H. Sugimoto, "New World Record $Cu(In,Ga)(Se,S)_2$ Thin Film Solar Cell Efficiency Beyond 22%", Proceedings of IEEE Photovoltaic Specialist Conference (PVSC), Portland, OR, USA, pp. 1287-1291 (2016).

[9] A. Zelenina, F. Werner, H. Elanzeery, M. Melchiorre, S. Siebentritt, "Space-charge-limited currents in CIS-based solar cells", Appl. Phys. Lett. 111, 213903 (2017).

[10] A. R. Burgers, J. A. Eikelboom, A. Schonecker, W. C. Sinke, "Improved treatment of the strongly varying slope in fitting solar cell I-V curve," in Proceedings of the 25th IEEE Photovolt. Spec. Conf., pp. 569 – 572 (1996).

[11] U. Rau, A. Jasenek, H. W. Schock, F. Engelhardt, T. H. Meyer, "Electronic loss mechanisms in chalcopyrite based heterojunction solar cells", Thin Solid Films; 361: 298–302 (2000).

[12] R. Scheer, H. W. Schock, "Chalcogenide Photovoltaics: Physics, Technologies, and Thin Film Devices", Weinheim, Germany: Wiley-VCH, 112–116 (2011).

[13] F. Babbe, H. Elanzeery, M. H. Wolter, K. Santhosh, S. Siebentritt, "The hunt for the third acceptor in $CuInSe_2$ and $Cu(In,Ga)Se_2$ absorber layers", submitted (2018).

[14] P. Reinhard, B. Bissig, F. Pianezzi, H. Hagendorfer, G. Sozzi, R. Menozzi, C. Gretener, S. Nishiwaki, S. Buecheler, A. N. Tiwari, "Alkali-templated surface nanopatterning of chalcogenide thin films: A novel approach toward solar cells with enhanced efficiency," Nano Letters, 15, pp. 3334 – 3340 (2015).

[15] E. Handick, P. Reinhard, J. H. Alsmeier, L. Köhler, F. Pianezzi, S. Krause, M. Gorgoi, E. Ikenaga, N. Koch, R. G. Wilks, S. Buecheler, A. N. Tiwari and M. Bär, "Potassium post deposition treatment-induced band gap widening at $Cu(In,Ga)Se_2$ surfaces–reason for performance leap?" ACS Appl. Mater. Interfaces, 7, 27414 (2015).

[16] M. C. Biesinger, L. W. M. Lau, A. R. Gerson, R. St. C. Smart, "Resolving surface chemical states in XPS analysis of first row transition metals, oxides and hydroxides: Sc, Ti, V, Cu and Zn", Appl. Surf. Sci., 257, pp. 887–898 (2010).

[17] D. Briggs *et al.*, "Handbook of X-Ray Photoelectron Spectroscopy", Eden Prairie, MN, USA: Perkin-Elmer Corp. (1981).

[18] I. Khatri, H. Fukai, H. Yamaguchi, M. Sugiyama, T. Nakada, "Effect of potassium fluoride post-deposition treatment on $Cu(In,Ga)Se_2$ thin films and solar cells fabricated onto soda lime glass substrates", Sol. Energy Mater. Sol. Cells, 155, 280 (2016).

[19] F. Pianezzi, P. Reinhard, A. Chirilă, B. Bissig, S. Nishiwaki, S. Buecheler, A. N. Tiwari, "Unveiling the effects of post-deposition treatment with different alkaline elements on the electronic properties of CIGS thin film solar cells", Phys. Chem. Chem. Phys., 16, 8843 (2014).

[20] A. Nakane, H. Tampo, M. Tamakoshi, S. Fujimoto, K.M. Kim, S. Kim, H. Shibata, S. Niki, H. Fujiwara, "Quantitative determination of optical and recombination losses in thin-film photovoltaic devices based on external quantum efficiency analysis", J. Appl. Phys., 120, 064505 (2016).

[21] M. Turcu, O. Pakma, U. Rau, “Interdependence of absorber composition and recombination mechanism in Cu(In,Ga)(Se,S)$_2$ heterojunction solar cells”, Appl. Phys. Lett., 80, 2598–2600 (2002).

[22] F. Werner, F. Babbe, H. Elanzeery, S. Siebentritt, “Defects, buffer layer, or artefact – what do we see in capacitance measurements of thin film solar cells?”, submitted (2018).

[23] J. Heath, P. Zabierowski, “Capacitance Spectroscopy of Thin-Film Solar Cells”, Chapter 4 in Adv. Charact. Tech. Thin Film Sol. Cells, Wiley-VCH Verlag GmbH & Co. KGaA, Weinheim, Germany, pp. 81 – 105 (2011).

[24] F. Werner, T. Bertram, J. Mengozzi, S. Siebentritt, “What is the dopant concentration in polycrystalline thin-film Cu(In,Ga)Se$_2$?”, Thin Solid Films, 633, 222 – 226 (2017).

[25] A. Laemmle, R. Wuerz, M. Powalla, “Efficiency enhancement of Cu(In,Ga)Se$_2$ thin-film solar cells by a post-deposition treatment with potassium fluoride”, Phys. Status Solidi - Rapid Res. Lett., 7, 631 – 634 (2013).

[26] S. Siebentritt, N. Rega, A. Zajogin, M. C. Lux-Steiner, “Do we really need another PL study of CuInSe$_2$?”, Phys. Status Solidi., 1, 2304 – 2310 (2004).

[27] T. Unold, L. Gütay, “Photoluminescence Analysis of Thin-Film Solar Cells”, Chapter 7 in: D. Abou-Ras, T. Kirchartz, U. Rau (Eds.), “Adv. Charact. Tech. Thin Film Sol. Cells”, Wiley-VCH Verlag GmbH & Co. KGaA, Weinheim, Germany, pp. 151 – 175 (2011).

[28] I. Dirnstorfer, M. Wagner, D. M. Hofmann, M. D. Lampert, F. Karg, B. K. Meyer, “Characterization of CuIn(Ga)Se$_2$ Thin Films”, Phys. Status Solidi., 168, 163 – 175 (1998).

[29] Mt. Wagner, I. Dirnstorfer, D. M. Hofmann, M. D. Lampert, F. Karg, B. K. Meyer, “Characterization of CuIn(Ga)Se$_2$ Thin Films”, Physica Status Solidi (a), 167, 1, pp. 131-142 (1998).

[30] T. Gödecke, T. Haalboom, F. Ernst, “Phase equilibria of Cu-In-Se I. The In$_2$Se$_3$-Se-Cu$_2$Se subsystem”, Zeitschrift Für Met., 91, 622 – 634 (1948).

[31] T. Bertram, V. Depredurand, S. Siebentritt, “Electrical Characterization of Defects in Cu-Rich Grown CuInSe$_2$ Solar Cells”, IEEE Journal of Photovoltaics, 6, 546 – 551 (2016).

[32] Y. Aida, V. Deprédurand, J. K. Larsen, H. Arai, D. Tanaka, M. Kurihara, S. Siebentritt, "Cu-rich $CuInSe_2$ solar cells with a Cu-poor surface", Prog. Photovoltaics Res. Appl., 23, 754 – 764 (2015).

[33] S. Siebentritt, G. Rey, A. Finger, D. Regesch, J. Sendler, T. P. Weiss, T. Bertram, "What is the bandgap of kesterite?", Sol. Energy Mater. Sol. Cells, 158, 2, pp. 126-129 (2016).

[34] K. B. Messaoud, G. Brammertz, M. Buffiere, S. Oueslati, H. Elanzeery, M. Meuris, M. Amlouk, J. Poortmans, "Modelling of $Cu_2ZnSnSe_4$-CdS-ZnO thin film solar cell", Materials Research Express, 4, 11 (2017).

[35] A. Polman, M. Knight, E. C. Garnett, B. Ehrler, W. C. Sinke, "Photovoltaic materials: Present efficiencies and future challenges", Science, 352, aad4424 (2016).

[36] W. Shockley, H. J. Queisser, "Detailed Balance Limit of Efficiency of p-n Junction Solar Cells", Journal of Applied Physics, 32, pp. 510-519 (1961).

[37] T. Dullweber, O. Lundberg, J. Malmstrom, M. Bodegard, L. Stolt, U. Rau, H. W. Schock, J. H. Werner, "Back surface band gap gradings in $Cu(In,Ga)Se_2$ solar cells", Thin Solid Films, 387, 11 (2001).

[38] T. Feurer, B. Bissig, T. P. Weiss, R. Carron, E. Avancini, J. Löckinger, S. Buecheler, A. N. Tiwari, "Single-graded CIGS with narrow bandgap for tandem solar cells", Science and Technology of Advanced Materials, 19:1, 263 - 270 (2018).

[39] F. Fu, T. Feurer, T. P. Weiss, S. Pisoni, E. Avancini, C. Andres, S. Buecheler, A. N. Tiwari, "High-efficiency inverted semi-transparent planar perovskite solar cells in substrate configuration", Nature Energy, 2, 16190 (2016).

[40] T. Hölscher, S. Förster, T. Schneider, M. Maiberg, W. Widdra, R. Scheer, "Light induced degradation of $Cu(In,Ga)Se_2$ thin film surfaces", Applied Physics Letters, 111, 011604 (2017).

[41] R. Carron, C. Andres, E. Avancini, T. Feurer, S. Nishiwaki, S. Pisoni, F. Fu, M. Lingg, Y. E. Romanyuk, S. Buecheler, A. N. Tiwari, "Bandgap of thin film solar cell absorbers: A comparison of various determination methods", Thin Solid Films, 669, 1, pp. 482 – 486 (2019).

[42] B. Hirschorn, M. E. Orazem, B. Tribollet, V. Vivier, I. Frateur, M. Musiani, "Determination of effective capacitance and film thickness from constant-phase-element parameters", Electrochim. Acta, 55, 6218 (2010).

[43] P. Blood, J. W. Orton, "The electrical characterization of semiconductors: Majority carriers and electron states", Academic Press, London (1992).

[44] T. P. Weiss, A. Redinger, J. Luckas, M. Mousel, Susanne Siebentritt, "Admittance spectroscopy in kesterite solar cells: defect signal or circuit response", Applied Physics Letters, 102(20):202105 (2013).

[45] F. Werner, M. H. Wolter, S. Siebentritt, G. Sozzi, S. D. Napoli, R. Menozzi, P. Jackson, W. Witte, R. Carron, E. Avancini, T. Weiss, S. Buecheler, "Alkali treatments of Cu(In,Ga)Se_2 thin-film absorbers and their impact on transport barriers", Prog. in Photovoltaics, 26, 11, pp. 911 - 923 (2018).

[46] A. Bauknecht, S. Siebentritt, J. Albert, M. Ch. Lux-Steiner, "Radiative recombination via intrinsic defects in $Cu_xGa_ySe_2$", J. Appl. Phys., 89, 8, 4391 - 4400 (2001).

[47] S. Siebentritt, U. Rau, "Wide-Gap Chalcopyrites", Springer, Berlin, Heidelberg, 113 - 156 (2006).

Chapter 7. Root cause for the interface recombination in Cu-rich CI(G)S cells

Chapter 5 has introduced the electrical characteristics of Cu-rich CIS and Cu-rich CIGS solar cells. It has been observed in Chapter 5 (in agreement with literature) that Cu-rich CI(G)S solar cells suffer from strong deficiency in the V_{OC} values. This strong V_{OC} deficiency has been attributed to recombination losses at the absorber/buffer interface as explained in Chapter 5. The root cause for these interface recombination losses is not fully understood.

Moreover, the admittance signals for Cu-rich CIS and CIGS solar cells were shown to be related to defects and not interface barriers. The activation energies of these defects are in the range of 200±20 meV for Cu-rich CIS and 130±15 meV for Cu-rich CIGS with bandgaps less than 1.2 eV as presented in Section 5.4. The identification of the 200±20 meV defect in Cu-rich CIS solar cells is also not yet clear. This chapter unveils the nature of the 200±20 meV defect in Section 7.1.

Section 7.1 will characterize the 200±20 meV defect as an absorber-related defect. The results of this section are under review [1]. This 200±20 meV defect has been passivated by the different post-deposition treatments performed on Cu-rich CIS absorbers introduced in Chapter 6. These post-deposition treatments are the ex-situ KF PDT (Section 6.1), the in-situ KF PDT (Section 6.2) and the Se-only PDT (Section 6.4). The results of these post-deposition treatments were published in [1 – 3]. These three post-deposition treatments succeeded also in improving the absorber/buffer interface and thus the V_{OC} for Cu-rich CIS solar cells. For Cu-rich CIGS solar cells, a Ga-Se post-deposition treatment was introduced in Section 6.3. This Ga-Se post-deposition treatment succeeded in improving the V_{OC} and the absorber/buffer interface for Cu-rich CIGS solar cells. The results of this Ga-Se post-deposition treatment were published in [4]. A summary of the changes observed with and without these four post-deposition treatments (ex-situ KF, in-situ KF, Se-only and Ga-Se PDTs) will be described in Section 7.2.

According to the observations of the changes taking place after performing the post-deposition treatments, the root cause for the interface recombination losses in Cu-rich CI(G)S solar cells can be identified. The root cause for the interface recombination losses in Cu-rich CIS solar cells will be attributed to the 200±20 meV defect that will be identified as a Se-related acceptor defect.

Furthermore, in Section 7.2, I will speculate that the root cause of the interface recombination losses in Cu-rich CIGS solar cells is a Se-related defect, similar to the 200±20 meV defect observed for Cu-rich CIS solar cells, but is not detectable within our admittance measurement range.

Section 7.3 provides an explanation for the mechanism and the origin behind the formation of this 200±20 meV defect. This 200±20 meV defect is formed as a consequence of the mandatory etching step required to remove conductive copper selenide secondary phases from Cu-rich chalcopyrite absorbers. Section 7.3 will also explain why the etching process leads to the formation of the 200±20 meV defect. The chemical instability of the Cu-rich CI(G)S absorber surface plays a role in the formation of this 200±20 meV defect as will be explained in Section 7.3. The results of this section are in preparation [5].

After identifying the root cause of the interface recombination losses in Cu-rich CIS solar cells in terms of the 200±20 meV defect and the origin behind the formation of this 200±20 meV defect, Section 7.4 will introduce alternative means of passivating this 200±20 meV defect and improving the absorber/buffer interface using modified buffer layers. Finally, Section 7.5 summarizes this chapter.

7.1 Characterization of the 200±20 meV defect in Cu-rich CI(G)S cells

Chapter 5 has discussed the admittance characteristics of Cu-rich CI(G)S solar cells in Section 5.4. The main capacitance step revealed an activation energy of 200±20 meV for Cu-rich CIS cells as presented in Figure 5.8 and an activation energy of 130±15 meV for Cu-rich CIGS cells with bandgaps up to 1.2 eV. The activation energy of the main capacitance step starts to decrease for Cu-rich CIGS cells with bandgaps higher than 1.2 eV as presented in Figure 5.9. Section 5.4 also discussed the identification of those capacitance steps as defects and not barriers by comparing the activation energy extracted from series resistance with that extracted from admittance measurements. The activation energies extracted from series resistance showed values much less than that of admittance measurements. This implied that the main capacitance step should be related to defects and not barriers as explained in Sections 4.5 and 5.4. The 130±15 meV defect observed for Cu-rich CIGS solar cells was likely attributed to the third shallow acceptor defect observed by PL measurements performed by Finn Babbe as discussed in Section 6.4 and Section 6.5. The results of these PL measurements and the characterization of the third shallow acceptor with an activation energy of 130±15 meV were published in [6].

On the other side, the characteristics of the 200±20 meV defect observed for Cu-rich CIS solar cells are not yet clear. It is still not clear whether this defect is a bulk or an interface defect as well as the origin of this defect. This section focuses on the characterization of the 200±20 meV defect observed in Cu-rich CIS solar cells and Section 7.3 will explain the origin of this 200±20 meV defect.

To investigate the characteristics of the 200±20 meV defect, a series of three Cu-rich CIS absorber-growing processes were performed with three different Se-fluxes; Low, medium and high fluxes referred to as “Low-Se”, “Med-Se” and High-Se” respectively. The pressure of the Low-Se flux is in the range of 3.0 – 4.0 * 10^{-6} mbar. The pressure for the Med-Se flux is in the range of 1.0 – 1.5 * 10^{-5} mbar and for the High-Se flux is in the range of 1.5 – 4.0 * 10^{-5} mbar. The Se cracker temperature used for all the experiments in this chapter is 1000 ^{0}C. The objective of the different Se-fluxes is to observe the effect of changing the Se-flux on the main capacitance step of the admittance measurements for Cu-rich CIS absorbers and solar cells.

Each of the three absorber-growth runs with different Se-fluxes (Low-Se, Med-Se and High-Se) produces four absorbers. One absorber was used as a reference. The other three remaining absorbers were etched using a KCN strong etching (10 % aqueous potassium cyanide (KCN) solution for 5 minutes to remove additional copper selenide (Cu_2Se) secondary phases as explained in sub-section 3.2.1).

After the etching step, these three absorbers were processed in three different structures as illustrated in Figure 7.1. The different structures of the three Cu-rich CIS absorbers illustrated in Figure 7.1 can be described as follows:

1. The first absorber was used as a bare-absorber with no further processing. Aluminium (Al) is deposited on top of this Cu-rich CIS etched film to form a Schottky contact and allow performing different electrical characterizations [7, 8]. This absorber structure will be referred to as "absorber-Schottky" (Figure 7.1a).
2. For the second absorber, a standard CdS buffer layer was deposited on top of the Cu-rich CIS etched film followed by an Aluminium (Al) Schottky contact. This absorber structure will be referred to as "absorber-buffer" (Figure 7.1b).
3. For the third absorber, a standard CdS buffer layer (the same CdS buffer layer used for the "absorber-buffer" Cu-rich CIS in Figure 7.1b) was deposited on top of this third Cu-rich CIS etched film followed by our standard baseline process of window layers and grids forming a complete solar cell. This absorber structure will be referred to as "absorber-cell" (Figure 7.1c).

The above three structures were developed for each of the three Cu-rich CIS absorber-growing processes with different Se-fluxes: Low-Se, Med-Se and High-Se.

Electrical measurements were then performed to characterize these nine different types of samples ("absorber-Schottky", "absorber-buffer" and "absorber-cell" for Low-Se, Med-Se and High-Se fluxes). It is important to note that the unetched and the weakly etched (using "KCN weak" with 5 % aqueous KCN solution for 30 seconds as explained in sub-section 3.2.1) Cu-rich CIS absorbers could not be electrically measured due to the highly conductive copper selenide secondary phases present in all Cu-rich CIS samples.

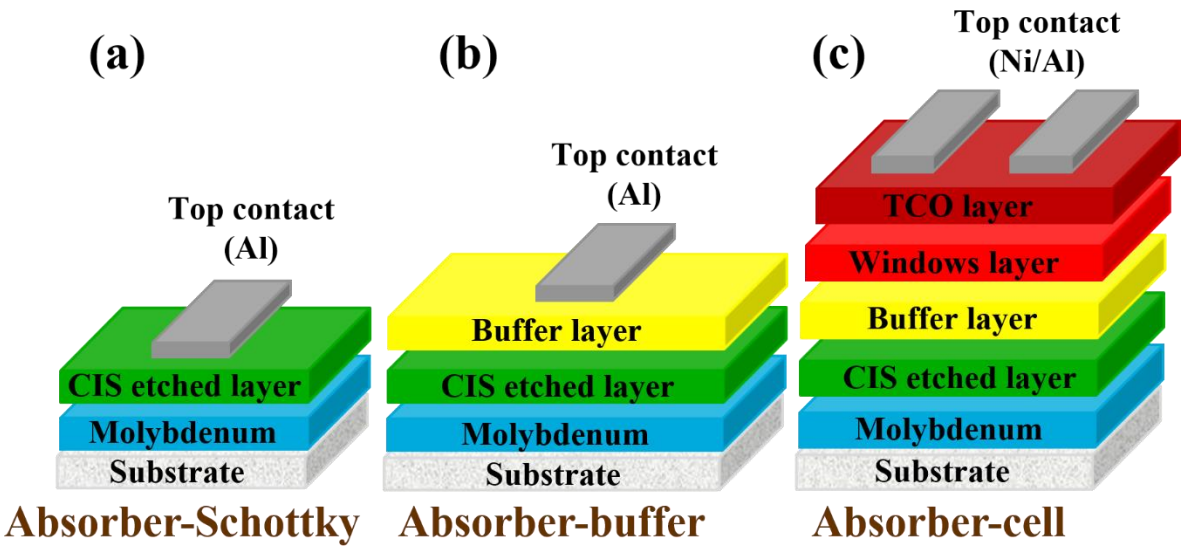

Figure 7.1: Schematics for Cu-rich CIS etched absorbers processed in three different structures: a) absorber with only Schottky contacts referred to as "Absorber-Schottky", b) absorber processed with CdS buffer layer and Schottky contacts on top referred to as "absorber-buffer" and c) absorber processed with CdS buffer layer (same CdS buffer layer in b), ZnO window layers and contacting grids referred to as "absorber-cell".

Admittance measurements were performed for the nine samples. The admittance spectra and corresponding Arrhenius plots for the "absorber-Schottky", "absorber-buffer" and "absorber-cell" samples of the three Cu-rich CIS absorber runs with Low-Se, Med-Se and High-Se fluxes are presented in Figures 7.2, 7.3 and 7.4 respectively.

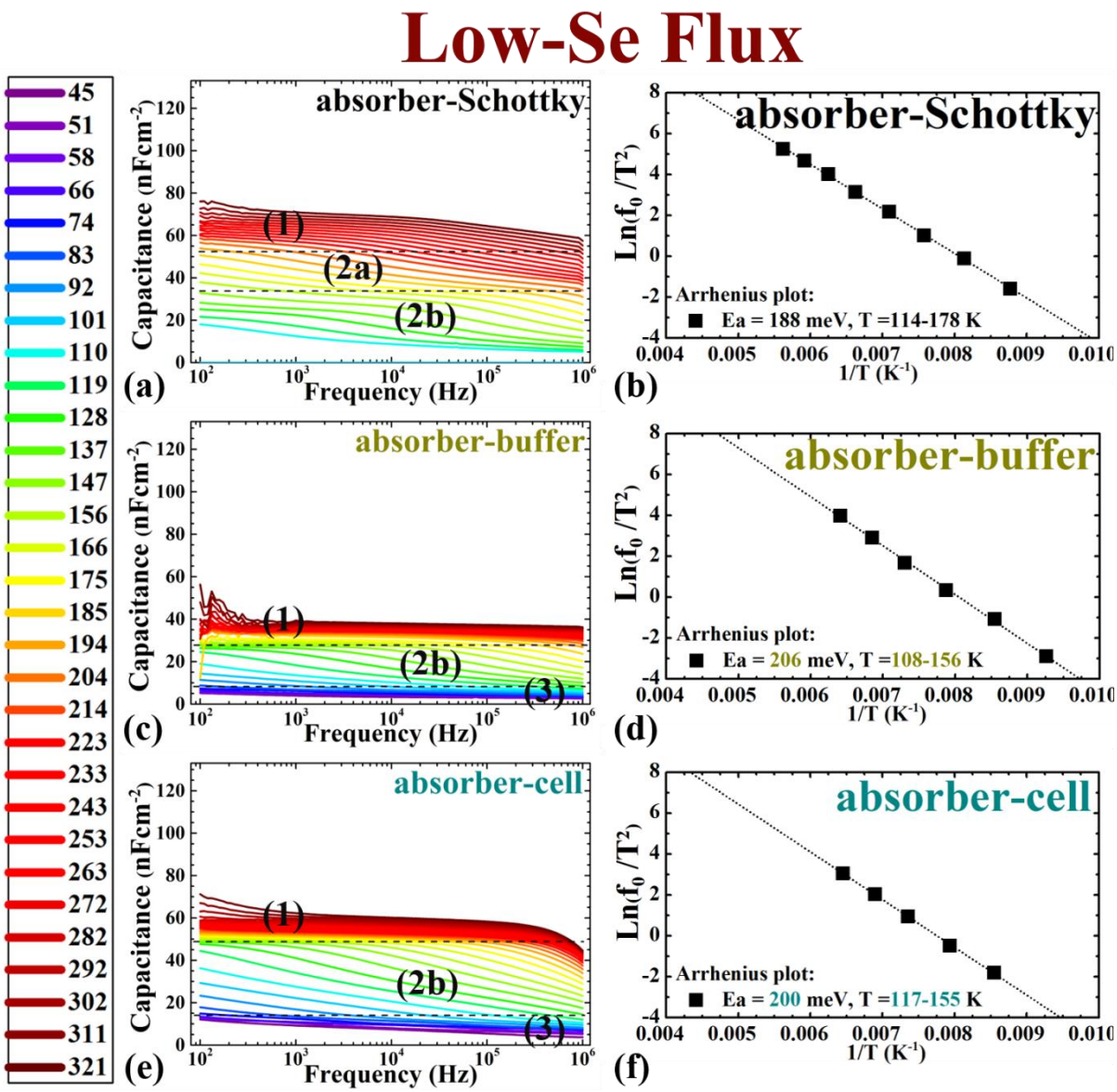

Figure 7.2: Admittance capacitance spectra for Cu-rich CIS absorbers grown under Low-Se flux with: a) absorber-Schottky, c) absorber-buffer and e) absorber cell. The dashed lines identify three regions of capacitance steps. The measurement temperature range is indicated by the scale on the left. The corresponding Arrhenius plots with the activation energies of the main capacitance step (Region 2b) extracted from the slope of the Arrhenius plots for: b) absorber-Schottky, d) absorber-buffer and f) absorber-cell.

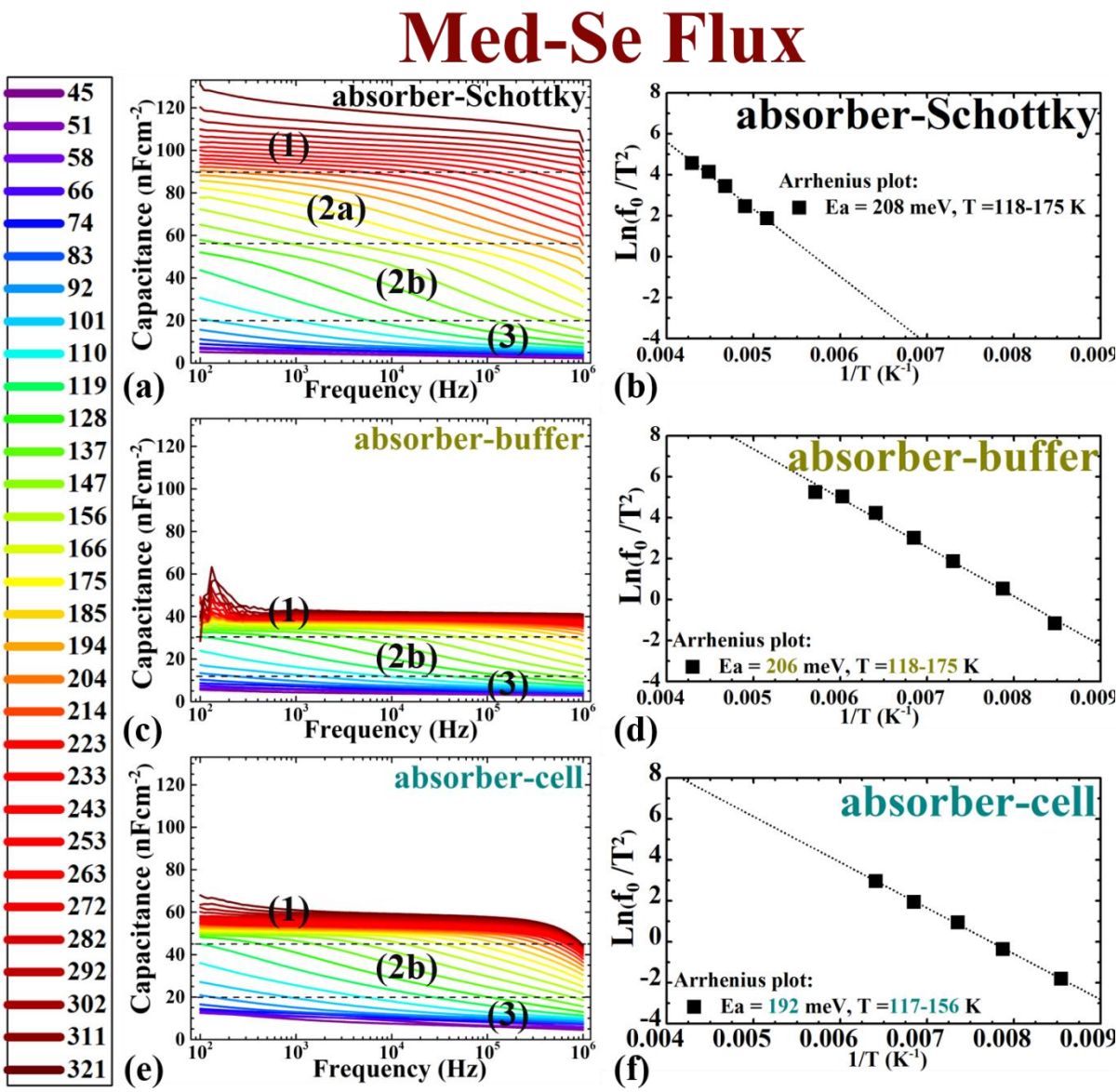

Figure 7.3: Admittance capacitance spectra for Cu-rich CIS absorbers grown under Med-Se flux with: a) absorber-Schottky, c) absorber-buffer and e) absorber cell. The dashed lines identify three regions of capacitance steps. The measurement temperature range is indicated by the scale on the left. The corresponding Arrhenius plots with the activation energies of the main capacitance step (Region 2b) extracted from the slope of the Arrhenius plots for: b) absorber-Schottky, d) absorber-buffer and f) absorber-cell.

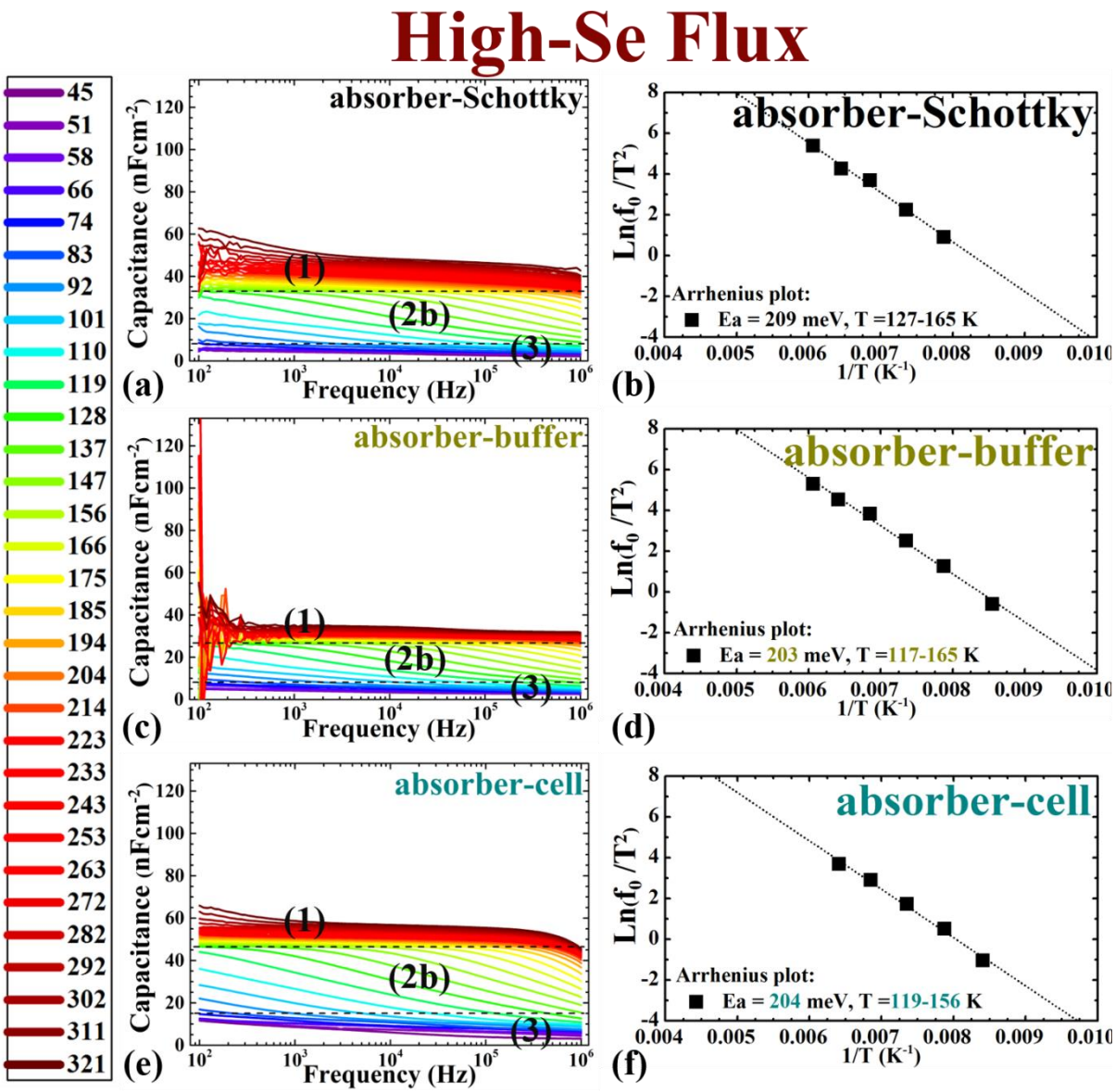

Figure 7.4: Admittance capacitance spectra for Cu-rich CIS absorbers grown under High-Se flux with: a) absorber-Schottky, c) absorber-buffer and e) absorber cell. The dashed lines identify three regions of capacitance steps. The measurement temperature range is indicated by the scale on the left. The corresponding Arrhenius plots with the activation energies of the main capacitance step (Region 2b) extracted from the slope of the Arrhenius plots for: b) absorber-Schottky, d) absorber-buffer and f) absorber-cell.

Based on the admittance spectra in Figure 7.2 (a, c, e), Figure 7.3 (a, c, e) and Figure 7.4 (a, c, e), three different capacitance steps could be identified (explained in detail in Section 4.5) as follows:

1. A high temperature step, named here as "Step 1" observed in a temperature range of 240 – 320 K. This high temperature capacitance step (Step 1) was observed for all nine samples in Figures 7.2 (a, c, e), Figures 7.3 (a, c, e) and Figures 7.4 (a, c, e). This high temperature step (Step 1) could not be resolved within our measurement range.
2. An intermediate temperature step, named here as "Step 2", can be identified as follows:
    a. A higher intermediate temperature step, named here as "Step 2a". This capacitance step (Step 2a) was observed in a temperature range of 180 – 240 K. This capacitance step (Step 2a) was observed only for the absorber-Schottky samples of the Low-Se (Figure 7.2a) and Med-Se fluxes (Figure 7.3a). The activation energy of this capacitance step (Step 2a) was extracted from the corresponding Arrhenius plot as explained in Section 4.5 showing values of 285 ± 10 meV. It is interesting to note that this higher intermediate temperature step (Step 2a) disappears after adding our standard CdS buffer layer as observed with the "absorber-buffer" (Figure 7.2c and Figure 7.3c) and the "absorber-cell" (Figure 7.2e and Figure 7.3e) of the Low-Se and Med-Se flux samples. This capacitance step (Step 2a) could therefore be related to a defect or a barrier that was caused by the Al contact or passivated by adding our standard CdS buffer layer.
    b. A lower intermediate temperature step, named here as "Step 2b". This capacitance step (Step 2b) was observed in a temperature range of 100 – 180 K. Moreover, this capacitance step (Step 2b) was observed for all nine samples in Figures 7.2 (a, c, e), Figures 7.3 (a, c, e) and Figures 7.4 (a, c, e). This capacitance step (Step 2b) is considered the main capacitance step for all the nine samples. The activation energy of this main capacitance step (Step 2b) showed values of 200 ± 20 meV for all the nine sample as will be discussed below.

3. A low temperature step, named here as “Step 3” observed in a temperature range of 50 – 100 K. This low temperature step (Step 3) was observed for all the nine samples in Figures 7.2 (a, c, e), Figures 7.3 (a, c, e) and Figures 7.4 (a, c, e) except for the absorber-Schottky sample of the Low-Se flux (Figure 7.2a) due to a measurement error. The admittance measurements of this absorber-Schottky sample of the Low-Se flux run were lost at low temperatures and no valid data could be extracted for this sample at low temperatures as can be observed in Figure 7.2a. The activation energy of this low temperature capacitance step (Step 3) showed values in the range of 50 ± 10 meV. This capacitance step (Step 3) could be related to freeze out as it showed values close to the geometric capacitance of the Cu-rich CIS absorber (around 5 nF/cm^2) as explained in Section 5.4.

From the above interpretation of the admittance measurements, it can be concluded that the main capacitance step is then the intermediate temperature capacitance step (Step 2b) observed in a temperature range of 100 – 180 K for all the nine samples in Figures 7.2 (a, c, e), Figures 7.3 (a, c, e) and Figures 7.4 (a, c, e). The activation energy of this main capacitance step (Step 2b) was extracted from the corresponding Arrhenius plots as explained in Section 5.4. The corresponding Arrhenius plots for this main capacitance step (Step 2b) are presented in Figures 7.2 (b, d, f), Figures 7.3 (b, d, f) and Figures 7.4 (b, d, f) for the three absorber structures of the Low-Se, Med-Se and High-Se fluxes respectively. The activation energies of the main capacitance step (Step 2b) extracted from the corresponding Arrhenius plots for all the nine samples (“absorber-Schottky”, “absorber-buffer” and “absorber-cell” for Low-Se, Med-Se and High-Se fluxes) are presented in the bar chart of Figure 7.5.

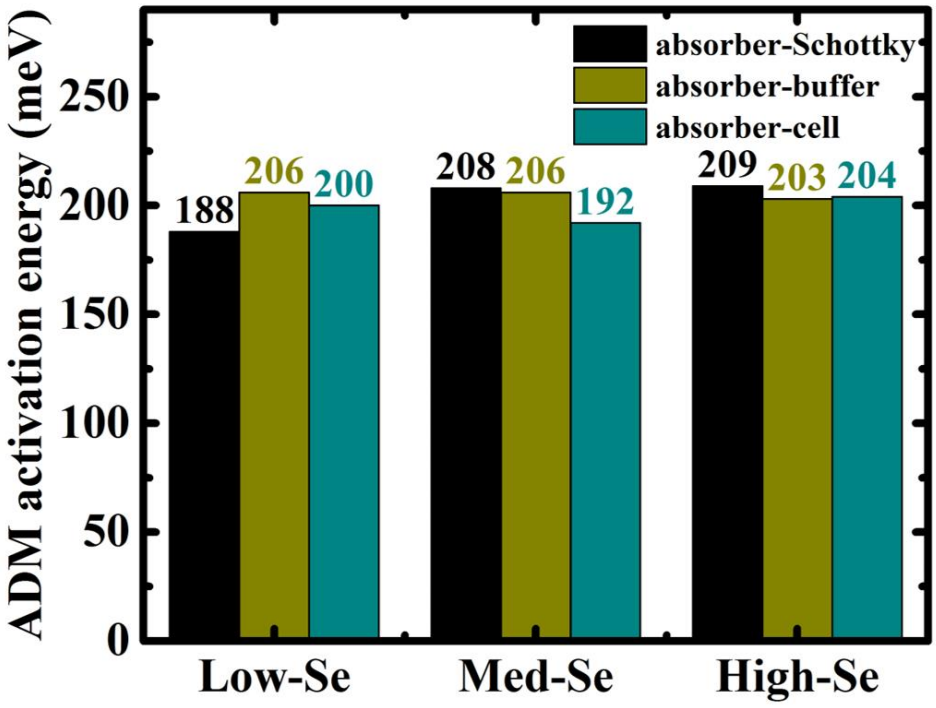

Figure 7.5: Activation energies extracted from the admittance measurements for each of the "absorber-Schottky", "absorber-buffer" and "absorber-cell" of the three Cu-rich growth processes with "Low-Se", "Med-Se" and "High-Se" fluxes.

From Figure 7.5, it is interesting to observe that the activation energy of the main capacitance step (Step 2b) for all the nine samples showed similar values of 200±20 meV and in the same temperature range (100 – 180 K). On the other side, the series resistance activation energies deduced from the IVT measurements (as explained in Section 4.3) indicated values in the range of 90 – 160 meV in the same temperature range as presented in Figure 7.6. These activation energies deduced from series resistance as a function of temperature (90 – 160 meV) are lower than those deduced from admittance measurements (200±20 meV). This confirms that the capacitance steps observed from admittance measurements are related to defects and not barriers. If these capacitance steps are related to barriers, the activation energy extracted from the series resistance should show values similar to those activation energies extracted from the admittance measurements (200±20 meV) as explained in Sections 4.5 and 5.4. It is important to note that the IVT measurements for the "absorber-Schottky" sample of the "Low-Se" flux growth process could not be measured due to contacting problems and the corresponding series resistance activation energy could not be deduced as reflected in Figure 7.6.

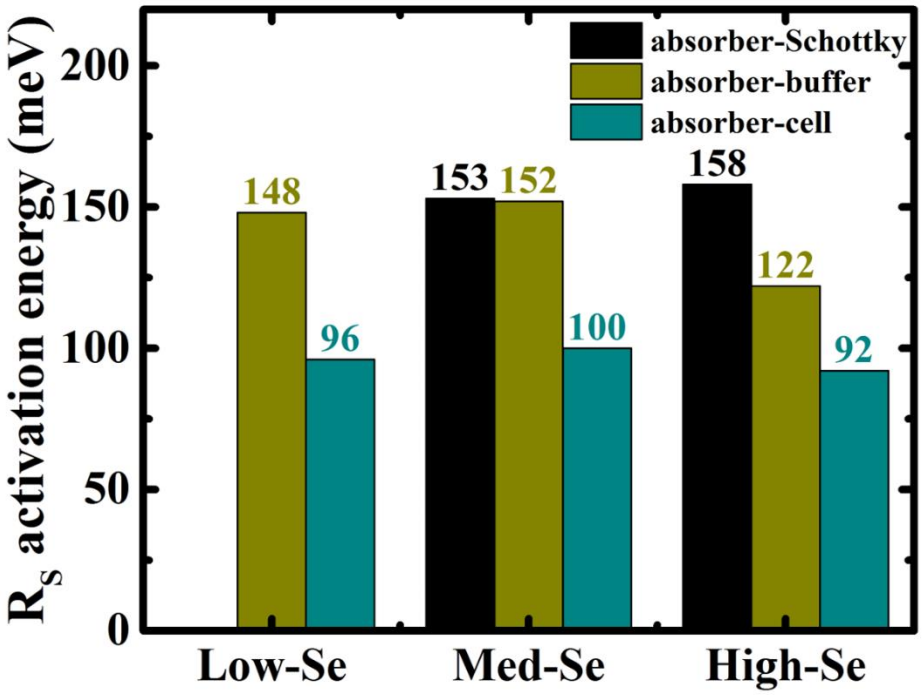

Figure 7.6: Activation energies for series resistance deduced from IVT measurements for each of the "absorber-Schottky", "absorber-buffer" and "absorber-cell" of the "Med-Se" and "High-Se" Cu-rich CIS growth processes. For the "Low-Se" process, only the "absorber-buffer" and the "absorber-cell" were successfully measured.

Therefore, based on the explanation above, it was concluded that the main capacitance step (Step 2b) for all Cu-rich CIS samples (bare-absorbers, absorbers with buffer layers or complete solar cells) corresponds to a defect, not a barrier with an activation energy of 200±20 meV. This defect is an absorber-related defect as it is present in Cu-rich CIS absorbers with Schottky contacts only and no additional interface layers. Moreover, this 200±20 meV defect is not affected by changing the Cu, In or Se fluxes ratios during absorber-growth supported by the following points:

- This 200±20 meV defect appeared in all Cu-rich CIS absorbers and solar cells with different Cu/In ratios as discussed in Section 5.4 and reported in [9].
- This 200±20 meV defect appeared in all Cu-rich CIS absorbers and solar cells with Low-Se, Med-Se and High-Se fluxes as presented in Figure 7.5

To conclude, the 200±20 meV defect can be characterized as an absorber-related defect that is not affected by changing the Cu, In or Se fluxes during the CIS absorber fabrication process as long as the absorbers are grown under Cu-rich conditions. I will discuss this defect for Cu-poor and stoichiometric CIS absorbers in sub-section 7.3.2.

7.2 Summary of the effects of PDTs on Cu-rich CI(G)S solar cells

This section is a summary of the observations deduced from the different characterizations performed in Chapter 5 and Chapter 6. This section will be divided into three parts:

1. The first part (sub-section 7.2.1) will be discussing the observations related to Cu-rich CI(G)S solar cells based on the characterizations performed in Chapter 5.
2. The second part (sub-section 7.2.2) will focus on the observations related to the effect of the post-deposition treatments on Cu-rich CI(G) solar cells from the characterizations presented in Chapter 6.
3. The third part (sub-section 7.2.3) will be a conclusion to the above two parts.

7.2.1 Observations related to Cu-rich CI(G)S solar cells

In Chapter 5, Cu-rich CI(G)S solar cells were compared to Cu-poor CI(G)S solar cells and the following observations could be deduced:

- Cu-rich CI(G)S solar cells suffer from significant V_{OC} and FF losses compared to Cu-poor CI(G) solar cells as observed by the IV measurements (Section 5.2).
- Cu-rich CI(G)S solar cells suffer from recombination losses in the absorber/buffer interface as observed by the extrapolated activation energy of the V_{OC} (T) curve at zero Kelvin showing values much lower than the Cu-rich CI(G)S bandgap (Section 5.3). These interface recombination losses play a significant role in the losses observed for the V_{OC}.
- The V_{OC} (T) curve shows two negative slopes for Cu-rich CI(G)S solar cells before the V_{OC} values saturate (or decrease) at lower temperatures compared to one negative slope for the V_{OC} (T) curve of Cu-poor CI(G)S solar cells as observed by the IVT measurements (Section 5.3).
- The apparent doping for Cu-rich CI(G)S solar cells is higher than the apparent doping of Cu-poor CI(G)S solar cells as observed by the CV measurements (Section 5.4).
- A 200 ± 20 meV defect was observed for the admittance signals of Cu-rich CIS absorbers and solar cells (Section 5.4 and Section 7.1). This 200 ± 20 meV defect was not observed for Cu-rich CIGS solar cells within our admittance measurement range.
- The derivative capacitance plots for Cu-rich CIS solar cells showed broad peaks with the presence of the 200 ± 20 meV capacitance step (defect) compared to narrow peaks in the absence of the 200 ± 20 meV defect with Cu-rich CIGS and Cu-poor CI(G)S solar cells as observed by the admittance measurements (Section 5.4).

7.2.2 Observations related to the effect of PDTs

Four post-deposition treatments were introduced in Chapter 6. Three post-deposition treatments (PDTs) were applied on Cu-rich CIS absorbers: the ex-situ KF PDT in Section 6.1, the in-situ KF PDT in Section 6.2 and the Se-only PDT in Section 6.4. The fourth post-deposition treatment was a Ga-Se PDT applied on Cu-rich CIGS absorbers and presented in Section 6.3. The following observations could be deduced as effects of these post-deposition treatments on Cu-rich CI(G)S solar cells:

- The V_{OC} values increased after all those post-deposition treatments. The ex-situ KF and the Se-only PDTs increased the V_{OC} values of Cu-rich CIS solar cells by around 30 mV, while the in-situ KF PDT increased the V_{OC} values of Cu-rich CIS solar cells by around 50 – 60 mV. The Ga-Se PDT improved the V_{OC} of Cu-rich CIGS solar cells by around 150 mV.
- The FF improved after all those post-deposition treatments except for the ex-situ KF PDT. The ex-situ KF PDT introduced a transport barrier that hindered the improvement of the FF. For all other post-deposition treatments, the FF improved by more than 10 %-absolute.
- The shunt resistance values improved significantly for the Cu-rich CI(G)S solar cells after the post-deposition treatments.
- The breakdown behaviour of the IV curves at reverse-bias voltages was not observed within our IV measurement range for Cu-rich CI(G)S solar cells after the post-deposition treatments.
- The extrapolated activation energy of the V_{OC} (T) curve at zero Kelvin of the Cu-rich CI(G)S solar cells improved significantly (to values closer to the bandgap compared to untreated Cu-rich CI(G)S solar cells) after the post-deposition treatments. This improvement in the extrapolated activation energy at zero Kelvin implies reduced interface recombination losses and a better absorber/buffer interface of Cu-rich CI(G)S solar cells after the post-deposition treatments.
- The V_{OC} (T) curve shows only one negative slope for Cu-rich CI(G)S solar cells after the post-deposition treatments before the V_{OC} values saturate (or decrease) at low temperatures. The post-deposition treatments succeeded in removing one of the two negative slopes used to be observed for Cu-rich CI(G)S solar cells.

- The apparent doping decreased for Cu-rich CI(G)S solar cells after the post-deposition treatments on the cell level as well as the absorber level.
- For Cu-rich CIS solar cells, the 200±20 meV defect (observed for untreated Cu-rich CIS solar cells) disappeared after the in-situ KF and the Se-only post-deposition treatments. For the ex-situ KF PDT, a capacitance step of 260±20 meV was observed for Cu-rich CIS solar cells after the ex-situ KF PDT. This 260±20 meV was attributed to a transport barrier as discussed in Section 6.1. Thus, from admittance measurements only, I am not able to confirm the passivation of the 200±20 meV defect from Cu-rich CIS solar cells after the ex-situ KF PDT. However, I speculate that the 200±20 meV defect was also passivated by the ex-situ KF PDT as the ex-situ KF PDT showed similar improvements to the in-situ KF and the Se-only PDTs as deduced from the above observations. I speculate that the above observations are related to the passivation of the 200±20 meV defect as will be discussed in sub-section 7.2.3.
- The capacitance derivative plots of Cu-rich CIS solar cells showed narrow peaks after the post-deposition treatments compared to broad peaks before the post-deposition treatments.
- For Cu-rich CIGS solar cells, the admittance signals did not show any observable changes within our admittance measurement range.

7.2.3 The root cause of interface recombination: Se-related defect

As the improvements observed on Cu-rich CIS cells after the Se-only PDT are similar to the improvements observed for Cu-rich CIS cells after the ex-situ KF, the in-situ KF PDTs and the In-Se PDT [9] and similar to the improvements observed for Cu-rich CIGS cells after the Ga-Se PDT (sub-section 7.2.2), I can speculate that Se plays a main role in those improvements. Se is then able to passivate the surface of Cu-rich CI(G)S absorbers leading to the improvements observed in sub-section 7.2.2 after the post-deposition treatments. I speculate that the main role of Se in the improvements observed on Cu-rich CI(G)S cells after the PDTs (sub-section 7.2.2) is that the Se passivates:

- The 200±20 meV defect in Cu-rich CIS solar cells
- Another defect in Cu-rich CIGS solar cells that is similar to the 200±20 meV defect (observed for untreated Cu-rich CIS solar cells) but is not detectable within our admittance measurement range.

These two speculations are based on the following reasons:

1. For Cu-rich CIS solar cells:
   - The 200±20 meV defect has been passivated from Cu-rich CIS solar cells using the Se-only PDT.
   - The Se-only PDT succeeded also in passivating the 200±20 meV defect from the Cu-rich CIS absorbers with Schottky contacts only and with no additional interface layers as discussed in Section 6.4. The 200±20 meV defect can then be characterized as a Se-related defect.
   - The 200±20 meV defect did not disappear by changing the Cu, In or Se-fluxes during absorber-growth as presented in Section 7.1. However, the 200±20 meV defect disappeared after any post-deposition treatments that contains Se including a Se-only PDT.
   - The improvements observed on Cu-rich CIS solar cells in sub-section 7.2.2 were only observed after any post-deposition treatments containing Se and were not observed without additional surface treatments despite changing the Cu, In and Se-fluxes during the absorber-growth process.
   - This passivation of the 200±20 meV defect after any post-deposition treatment including Se and not with the Se from the absorber-growth implies that:

a. The 200±20 meV defect has been formed after the absorber-growth process (will be confirmed in Section 7.3 that the 200±20 meV defect has been formed after the etching step).
b. The 200±20 meV defect can only be passivated after the absorber-growth (after the etching step as will be understood from Section 7.3) using high enough chalcogen either from the high Se of the surface post-deposition treatments (Chapter 6) or from the high S of the modified buffer layers (Section 7.4).

2. For Cu-rich CIGS solar cells:
   - The Ga-Se PDT showed improvements on Cu-rich CIGS solar cells that are similar to the improvements observed on Cu-rich CIS solar cells after the Se-only PDT (similar also to the improvements observed on Cu-rich CIS solar cells after the ex-situ KF and the in-situ KF PDTs) as discussed in sub-section 7.2.2.
   - During the development of the Ga-Se PDT, the high Se step was described as an essential step to improve the performance of Cu-rich CIGS solar cells (mainly improves the V_{OC}) as discussed in Section 6.3.
   - This effect of the high Se step in Ga-Se PDT on improving the Cu-rich CIGS solar cells showed similar observations to the improvements observed on Cu-rich CIS solar cells with the high Se in the Se-only PDT.
   - The admittance signals of the Cu-rich CIGS solar cells did not show any changes with and without the Ga-Se PDT. The activation energy of the main capacitance step in Cu-rich CIGS solar cells showed an activation energy of 130±15 meV with and without the Ga-Se PDT as discussed in Section 6.3. This 130±15 meV capacitance step does not play any role in the improvements observed for Cu-rich CIGS solar cells after the Ga-Se PDT as the 130±15 meV capacitance step is present with and without the Ga-Se PDT.
   - Therefore, I speculate that a defect similar to the 200±20 meV Se-related defect of Cu-rich CIS solar cells should be present in Cu-rich CIGS solar cells but not detectable within our admittance measurement range. I speculate that the concentration of this Se-related defect is too low to be detected by admittance measurements of Cu-rich CIGS cells (compared to Cu-rich CIS cells) but still high enough to reduce the V_{OC} of Cu-rich CIGS solar cells. This hidden defect in Cu-rich CIGS solar cells is passivated using the high Se step and plays a key role in the improvements observed on Cu-rich CIGS solar cells after the Ga-Se PDT (sub-section 7.2.2).

I also investigated if I can detect a capacitance step on Cu-rich CIGS Schottky contacts, that is different than the 130±15 meV capacitance step observed for Cu-rich CIGS solar cells, but I could not. The same 130±15 meV defect was detected on Cu-rich CIGS Schottky contacts and solar cells as explained below and as presented in Figure 7.7.

Two Cu-rich CIGS absorbers of the same absorber-grown deposition run with a bandgap of 1.17 eV were etched using KCN strong etching (10 % aqueous KCN solution for 5 minutes) and then processed differently. Al contacts were deposited on top of one of the two Cu-rich CIGS etched absorbers to form a Schottky contact as explained in Section 7.1, referred to here in the text as "CIGS Schottky". The other Cu-rich CIGS absorber was fully processed with our standard baseline process, referred to here in the text as "CIGS cell".

Admittance measurements were performed for both samples as presented in Figure 7.7 (a, b) and the activation energies were extracted from their corresponding Arrhenius plots as explained in Section 4.5 and presented in Figure 7.7 (c, d).

Admittance measurements in Figure 7.7 (a, b) revealed again three capacitance step regions, similar to what has been explained in Section 5.4. The inflection points of the high temperature capacitance step (Step 1) for both samples could not be observed within our measurement range. The low temperature capacitance step (Step 3) has been attributed to freeze out as the capacitance values approach the values of the geometric capacitance (around 5 nF/cm^2) with activation energies in the range of 50±10 meV. The medium temperature capacitance step (Step 2) is then the main capacitance step similar to the interpretation provided in Section 5.4 and Section 7.1.

The activation energy of the main capacitance step (Step 2) was extracted from the slope of the Arrhenius plots in Figure 7.7 (c, d) (as explained in Section 4.5) showing similar values of 125±2 meV for both Cu-rich CIGS Schottky and solar cell.

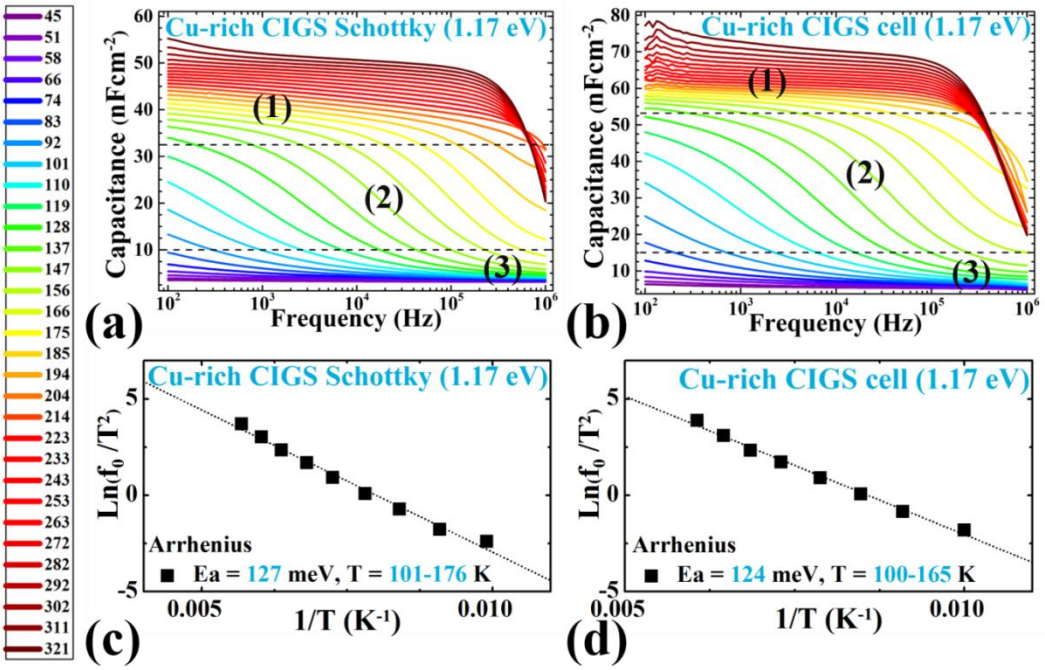

Figure 7.7: Admittance spectra for a) Cu-rich CIGS Schottky absorber and b) Cu-rich CIGS solar cell based on the same Cu-rich CIGS absorber with a bandgap of 1.17 eV. The dashed lines separate three different capacitance step regions. The temperature scale of the admittance spectra is represented on the left side of the Figure. The activation energy of the main capacitance step (Step 2) was extracted from the slope of the Arrhenius plot for c) Cu-rich CIGS Schottky absorber and d) Cu-rich CIGS solar cell of the same samples presented in (a, b). The activation energies of the main capacitance step (Step 2) showed similar values of 125±2 meV for both samples.

Based on the above discussion, I can propose the following model for the improved performance of Cu-rich CI(G)S solar cells after the high Se post-deposition treatments (sub-section 7.2.2):

- The high Se in the post-deposition treatments (introduced in Chapter 6) passivated a Se-related defect (the 200±20 meV defect in Cu-rich CIS absorbers and a similar defect in Cu-rich CIGS absorbers) from the surface of Cu-rich CI(G)S absorbers.
- The passivation of this Se-related defect helped in passivating the Cu-rich CI(G)S absorber surface by filling the defect vacancies and preventing shunt paths.
- The improvement of the shunt paths on the surface of Cu-rich CI(G)S absorbers leads to the improvement (increase) of the shunt resistances and consequently the improvement of the FF values for Cu-rich CI(G)S solar cells.
- The passivated Cu-rich CI(G)S absorber surface and the improvement of the shunt paths also helped in the disappearance of the breakdown behaviour (typically observed for the IV curves at reverse-bias voltages) within our IV measurement range from the IV curves of the Cu-rich CI(G)S solar cells.

- The passivation of this Se-related defect from the surface of Cu-rich CI(G)S absorbers helped in improving the absorber/buffer interface through the reduction of the interface recombination losses as indicated by the improvement of the extrapolated activation energy at zero Kelvin showing values close to the bandgap of Cu-rich CI(G)S solar cells.
- The reduction of the interface recombination losses with the passivation of the Se-related defect from the surface of the Cu-rich CI(G)S absorbers played a role in the disappearance of one of the two negative slopes typically observed for the V_{OC} (T) curve of the untreated Cu-rich CI(G)S solar cells.
- The Se-related defect (200±20 meV defect in the case of Cu-rich CIS and speculated for Cu-rich CIGS solar cells) is likely to be an acceptor defect as the apparent doping decreased for Cu-rich CI(G)S solar cells after all the different post-deposition treatments introduced in Chapter 6. This decrease in the apparent doping is also observed on Cu-rich CIS absorbers only with no front interface layers after the Se-only PDT. This decrease in the apparent doping from the Cu-rich CIS absorbers and solar cells after the different post-deposition treatments with the passivation of the Se-related defect supports that the Se-related defect is an acceptor defect.
- The passivation of the 200±20 meV Se-related defect from the admittance spectra of Cu-rich CIS solar cells helped in the appearance of the other defect (130±15 meV defect), hidden under the Se-related defect, and turned the peaks of the capacitance derivative plot from broad to narrow peaks.
- The passivation of the Se-related defect, the improvement of the absorber/buffer interface as a result of reducing the interface recombination losses and the decrease in the apparent doping can be considered the main factors leading to the improvement of the V_{OC} values observed on Cu-rich CI(G)S solar cells after the different post-deposition treatments.

To conclude, the root cause of the interface recombination losses in Cu-rich CI(G)S solar cells can be attributed to the 200±20 meV Se-related acceptor defect in Cu-rich CIS cells and a similar Se-related defect in Cu-rich CIGS solar cells (speculated but not detected). The passivation of this Se-related defect can be performed using high enough chalcogen (Se in the post-deposition treatments) leading to the improvement of the absorber/buffer interface and a corresponding increase in the V_{OC} values of Cu-rich CI(G)S solar cells. The origin of the formation of the 200±20 meV defect in Cu-rich CIS cells will be discussed in Section 7.3.

7.3 The origin of the formation of the 200±20 meV defect

The root cause of the interface recombination losses in Cu-rich CIS solar cells has been attributed to the 200±20 meV defect typically observed for Cu-rich CIS solar cells as discussed in sub-section 7.2.3. However, the origin of the formation of this 200±20 meV defect is not yet clear. Before I investigate the origin of the formation of the 200±20 meV defect, there are some facts related to the 200±20 meV defect that need to be put in consideration. These facts will help in discovering the origin behind the formation of this 200±20 meV defect and can be listed in the following points:

- The 200±20 meV defect is observed for Cu-rich CIS cells but not for Cu-poor CIS cells.
- The 200±20 meV defect is observed for Cu-rich CIS absorbers with Schottky contacts and without front interface layers.
- The 200±20 meV defect is not affected by changing the Cu, In or Se fluxes during the absorber-growth process of Cu-rich CIS absorbers as long as the Cu-rich CIS absorbers are grown under Cu-excess conditions.
- The 200±20 meV defect is passivated from Cu-rich CIS solar cells by any surface post-deposition treatment including Se.
- The passivation of the 200±20 meV defect after a post-deposition treatment including Se can be observed on Cu-rich CIS absorbers with only Schottky contacts and without any front interface layers.
- According to the phase diagram [10], there is no chalcopyrite Cu-rich phase, but chalcopyrite absorbers grown under Cu-excess form a stoichiometric chalcopyrite phase in addition to copper selenide secondary phases.
- CIS absorbers grown under Cu-excess are etched using strong KCN etching (10 % aqueous KCN solution for 5 minutes), while Cu-poor CIS absorbers are etched using KCN weak etching (5 % aqueous KCN solution for 30 seconds).

Based on the above facts, it can be concluded that the 200±20 meV defect is formed after the absorber-growth process and before adding the buffer layer. Moreover, this 200±20 meV defect is formed as a result of a difference between Cu-rich and Cu-poor CIS absorbers. Therefore, two possible origins behind the formation of the 200±20 meV defect could be deduced:

1. The stoichiometric CIS phase: will be discussed in sub-section 7.3.1.
2. The strong KCN etching step: will be discussed in sub-section 7.3.2.

7.3.1 The Stoichiometric CIS phase

A stoichiometric CIS absorber was fabricated with EDX value of 1.0±0.1% before and after the strong KCN etching indicating that the etching process did not remove any additional copper selenide phases (to the extent of the EDX tool's measurement limit) and that the grown absorber is indeed stoichiometric.

A similar stoichiometric CIS absorber from the same absorber-growth run of the etched stoichiometric sample was used for different characterization measurements. This stoichiometric CIS absorber was not etched to eliminate the effect of etching and investigate the presence of the 200±20 meV defect in the stoichiometric CIS phase itself. This stoichiometric CIS unetched absorber was divided into three parts as follows:

1. The first part was used for SEM, XRD and PL measurements.
2. Al Schottky contacts were deposited on top of the second part of this stoichiometric CIS unetched absorber to perform admittance measurements.
3. The third part of this stoichiometric CIS unetched absorber was further processed with our standard baseline process similar to the one used for Cu-rich CIS cells (without the etching step) before being characterized by IV, EQE and IVT measurements.

For comparison, a Cu-rich and a Cu-poor CIS absorber runs were grown on the same day of growing the stoichiometric CIS absorbers with the same parameters (only changing Cu content). Cu-rich and Cu-poor CIS absorbers were characterized with the stoichiometric CIS absorbers. Cu-rich and Cu-poor CIS solar cells were processed in the same baseline process of the stoichiometric CIS solar cell.

SEM measurements were performed for the three absorbers (Cu-rich, stoichiometric and Cu-poor CIS). All the three absorbers were unetched. The top and cross-section micrographs of the three CIS absorbers are presented in Figure 7.8. Figure 7.8 illustrates a trend in the grain size where the grain size decreases with the decrease of the Cu-content. Cu-rich CIS absorbers in Figure 7.8 (a, b) showed the largest grain size. Stoichiometric CIS absorbers in Figure 7.8 (c, d) have relatively smaller grains compared to Cu-rich CIS absorbers, but still larger than Cu-poor CIS absorbers in Figure 7.8 (e, f).

The objective of these SEM measurements is to show that the three CIS unetched absorbers (Cu-rich, stoichiometric and Cu-poor CIS) do not show any signature for hole or defect formation without the etching process.

However, after performing the strong KCN etching process for Cu-rich CIS absorbers and removing the copper selenide secondary phases, holes start to appear on the surface of Cu-rich CIS absorbers as reported in [11]. The effect of the etching process on the formation of defects in Cu-rich, stoichiometric and Cu-poor CIS absorbers will be discussed in the following sub-section (sub-section 7.3.2).

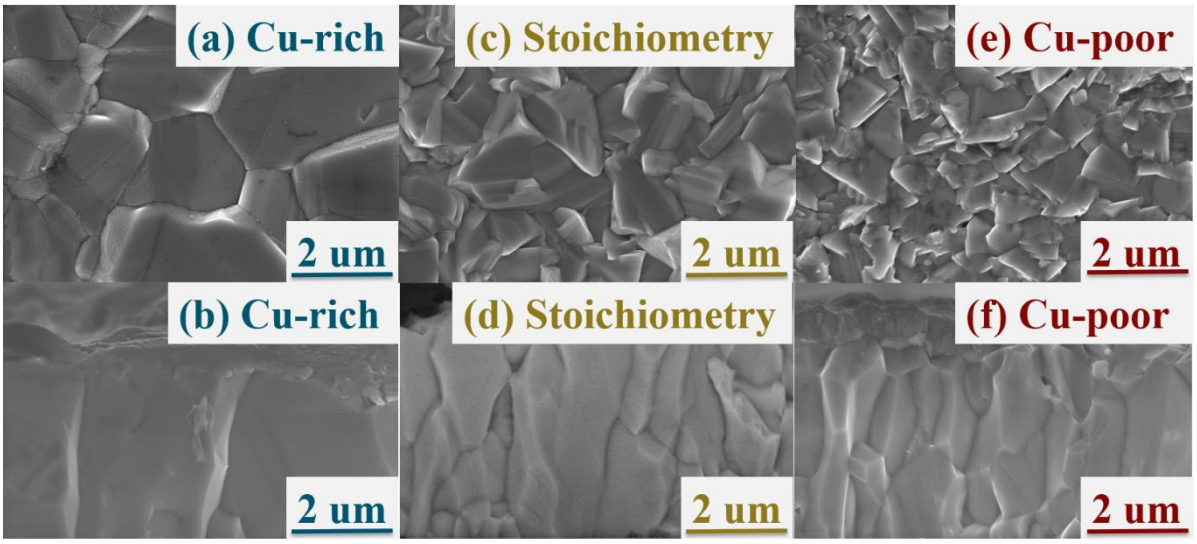

Figure 7.8: Top view micrographs for: a) Cu-rich, c) Stoichiometric and e) Cu-poor CIS unetched absorbers. Cross-section micrographs for b) Cu-rich, d) Stoichiometric and f) Cu-poor CIS unetched absorbers.

Further characterizations were performed for the three unetched CIS absorbers (Cu-rich, stoichiometric and Cu-poor) deposited on Mo-coated SLG substrate using X-Ray Diffraction (XRD) as presented in Figure 7.9. The main objective of the XRD measurements is to check if there are any observable changes for the stoichiometric CIS absorber compared to the Cu-rich or the Cu-poor CIS absorbers or not.

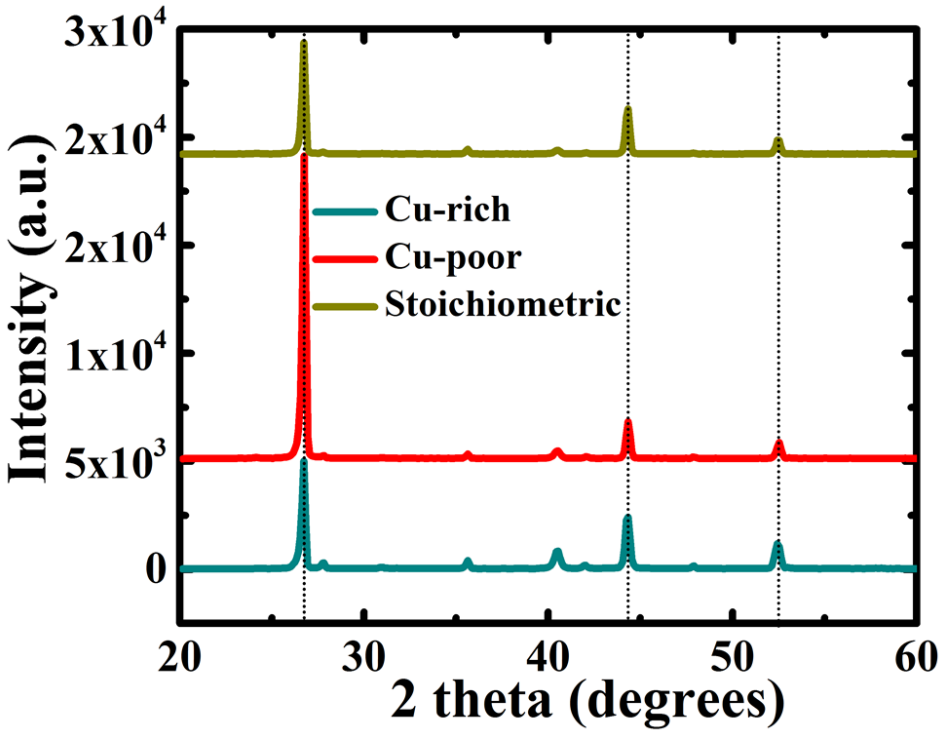

Figure 7.9: X-Ray Diffraction measurements for Cu-rich, stoichiometric and Cu-poor CIS absorbers without etching.

Figure 7.9 reveals the presence of the main CIS peaks for the three CIS absorbers: the (112) plane at 26.8 degrees, the (220) plane at 44.3 degrees and the (116) plane at 52.5 degrees as indicated by the short dotted lines in Figure 7.9. The XRD peaks for CIS were extracted from the PDF card of the CIS phase (JCPDS card No 40-1487) [12]. The XRD diffractograms of Cu-rich, stoichiometric and Cu-poor CIS unetched absorbers were shifted in angle to match the Mo peak at 40.5 degrees. From Figure 7.9, it can be observed that the intensity of the (112) CIS plane peak at 26.8 degrees showed higher intensity values for Cu-poor CIS absorber compared to Cu-rich and stoichiometric CIS absorbers. However, the XRD diffractograms in Figure 7.9 did not show significant differences between Cu-rich, stoichiometric and Cu-poor unetched CIS absorbers.

Admittance measurements were performed on the stoichiometric CIS unetched absorber with Schottky contacts. These admittance measurements revealed a double step for the main capacitance step of the stoichiometric CIS unetched Schottky absorber. The activation energies of this double step showed values in the range of 100 ± 10 and 40 ± 10 meV as illustrated in the Arrhenius plot in Figure 7.10. The activation energies were extracted from the Arrhenius plot as explained in Section 4.5.

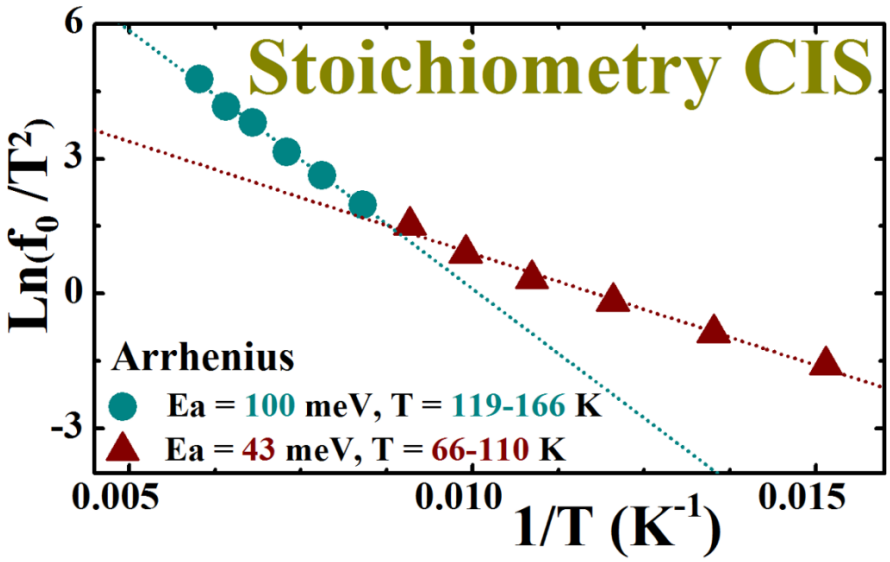

Figure 7.10: Arrhenius plot indicating the activation energies of the main capacitance step for stoichiometric CIS unetched absorber. The main capacitance step is a double step observed in the temperature range of 66 – 166 K.

The activation energies of the main capacitance step (double step) in the stoichiometric CIS unetched Schottky absorber calculated based on the Arrhenius plot in Figure 7.10 showed values of 100±10 and 40±10 meV. We published a potential identification of these CIS shallow acceptor defects from PL measurements in [6]. It is important to note that the PL measurements performed for this stoichiometric CIS unetched absorber (PL measurements were performed by Finn Babbe) showed one broad PL peak that is similar to the PL response of Cu-poor CIS absorbers.

Therefore, based on the admittance measurements in Figure 7.10, it can be revealed that the stoichiometric CIS unetched absorber did not show any signature for the presence of the 200±20 meV defect typically observed for Cu-rich CIS etched Schottky absorbers and solar cells.

IV, EQE and IVT measurements were performed for the stoichiometric CIS solar cell and were compared to the Cu-rich and the Cu-poor CIS solar cells. The three CIS solar cells (Cu-rich, Cu-poor and stoichiometric) are based on Cu-rich, Cu-poor and stoichiometric CIS absorbers deposited on the same day with the same parameters (only changing Cu content) and processed with the same baseline process (except for the etching step).

In terms of the solar cell performance, the results of the IV measurements performed for the three solar cells (Cu-rich, stoichiometric and Cu-poor) are presented in Figure 7.11. While Cu-rich CIS solar cell (green) showed the standard behaviour of strong V_{OC} and FF deficiency compared to Cu-poor CIS solar cell (red), the stoichiometric CIS solar cell (yellow) showed similar electrical performance behaviour to the Cu-poor CIS solar cell (red) as presented in Figure 7.11. The electrical parameters extracted from the IV characteristics in Figure 7.11 and presented in the table in the inset of Figure 7.11, indicated V_{OC} values of 436.8 mV and FF values of 67.9 % for the stoichiometric CIS solar cell similar to the values of the Cu-poor CIS solar cell. The Cu-poor CIS solar cell showed V_{OC} values of 441.9 mV and FF values of 69.2 %. On the other side, Cu-rich CIS solar cell showed the typical V_{OC} and FF deficiency with a V_{OC} value of 339.8 mV and a FF value of 50.8 %.

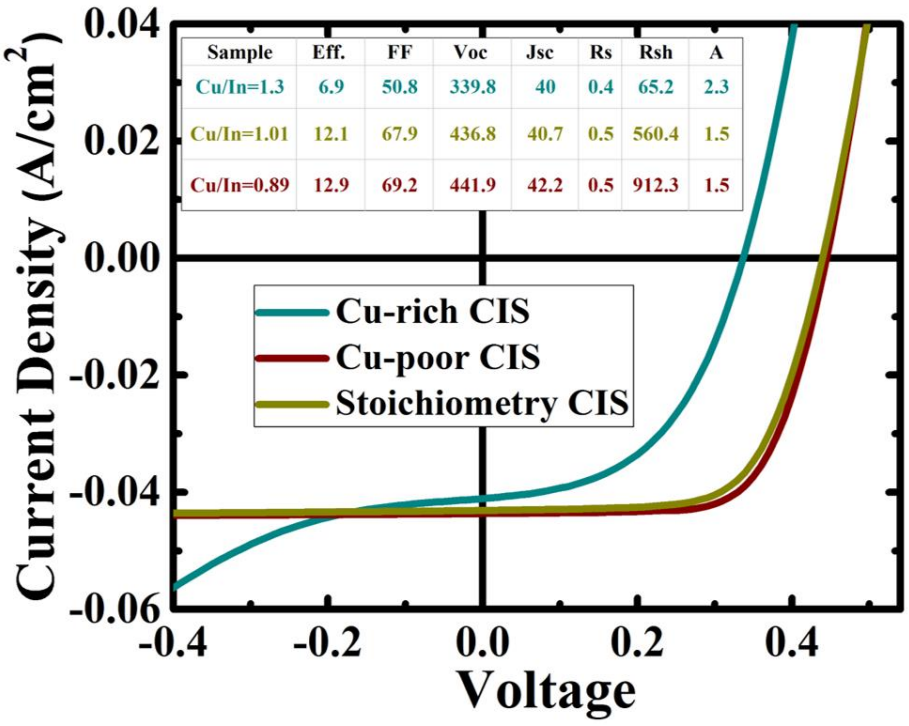

Figure 7.11: IV characteristics for Cu-rich, Cu-poor and stoichiometric CIS solar cells.

Based on Figure 7.11, there is no signature for V_{OC} or FF deficiency in the stoichiometric CIS solar cell. The high electrical performance for the stoichiometric CIS solar cell is reflected on the efficiency showing values of 12.1 % for the stoichiometric CIS solar cell that is in close proximity to the efficiency value of the Cu-poor CIS solar cell (12.9 %) and much higher than the efficiency value of the Cu-rich CIS solar cell with 6.9 %.

EQE measurements were also performed for the stoichiometric CIS solar cell and were compared to Cu-rich and Cu-poor CIS solar cells. The results of these EQE measurements are presented in Figure 7.12. The behaviour of the stoichiometric CIS solar cell shared similar characteristics with the Cu-rich CIS solar cell in terms of steep longer wavelength (1150 – 1250 nm) EQE response as indicated in Figure 7.12.

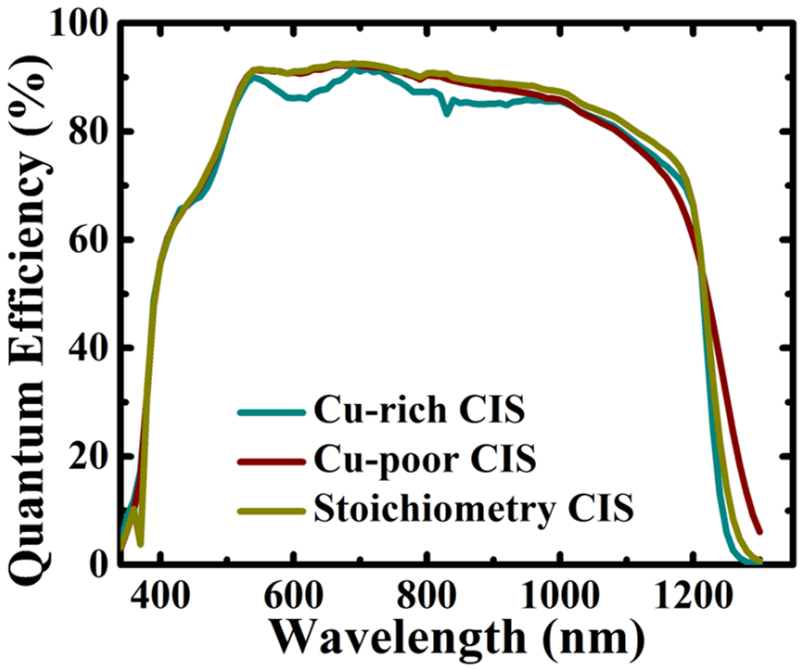

Figure 7.12: EQE spectra for Cu-rich, Cu-poor and stoichiometric CIS solar cells.

Figure 7.12 illustrates a comparison between Cu-rich, stoichiometric and Cu-poor CIS solar cells in terms of the EQE response. The EQE spectra in Figure 7.12 show similar response for all the three cells in the short wavelength region (400 – 550 nm) as a result of the same baseline process performed similarly for all the three CIS absorbers. At longer wavelengths, the EQE response differs showing the steepest response for the Cu-rich CIS solar cell, a somewhat less steep response for the stoichiometric CIS solar cell and the least steep response for the Cu-poor CIS solar cell.

The bandgap linear extrapolation based on these EQE measurements reflected a difference between the three CIS solar cells in terms of bandgap. The linear extrapolation of the bandgap showed values of 0.996 eV for Cu-rich CIS, 0.985 eV for the stoichiometric CIS and 0.954 for the Cu-poor CIS solar cells.

Finally, IVT measurements were performed for the stoichiometric CIS solar cell as well as the Cu-rich and Cu-poor CIS solar cells. The V_{OC} (T) curves of the three CIS solar cells (Cu-rich, Cu-poor and stoichiometric CIS solar cells) are plotted in Figure 7.13.

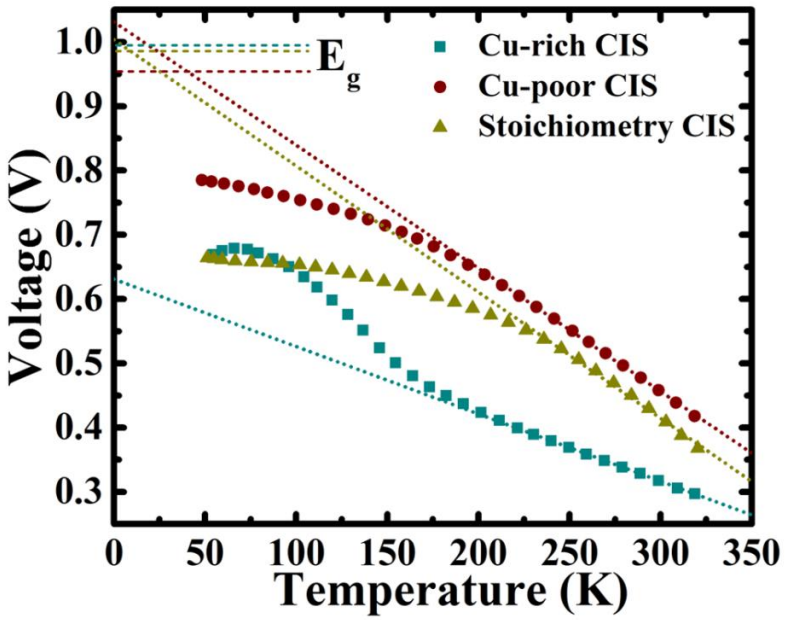

Figure 7.13: V_{OC} (T) curve for Cu-rich CIS (green), Cu-poor CIS (red) and stoichiometric CIS (yellow) solar cells. Stoichiometric CIS solar cell has an extrapolated activation energy at zero Kelvin close to the bandgap. The bandgap (E_g) is indicated by the short dashed lines for Cu-rich CIS (green), Cu-poor CIS (red) and stoichiometric CIS (yellow) solar cells

Figure 7.13 showed clearly the difference between Cu-rich (green), stoichiometric (yellow) and Cu-poor (red) CIS solar cells as follows:

- For Cu-rich CIS solar cell: the extrapolated activation energy at zero Kelvin of the V_{OC} (T) curve (green curve) showed values around 0.6 eV that is much lower than the bandgap (0.995 eV) indicated by the short dashed line in Figure 7.13. Moreover, the V_{OC} (T) curve of the Cu-rich CIS solar cell showed the typical two negative slopes before the V_{OC} values saturate (or decrease) at lower temperatures. This behaviour of the V_{OC} (T) curve of the Cu-rich CIS solar cell is the typical behaviour observed for all Cu-rich CIS solar cells as explained in Section 5.4.
- For Cu-poor CIS solar cell: the extrapolated activation energy at zero Kelvin of the V_{OC} (T) curve (red curve) showed values close to the bandgap (0.954 eV). The V_{OC} (T) curve of the Cu-poor CIS solar cell showed one negative slope before the V_{OC} values saturate at lower temperatures. This behaviour of the V_{OC} (T) curve for Cu-poor CIS cell is also the typical behaviour observed for Cu-poor CIS solar cells as discussed in Section 5.4.

- For the stoichiometric CIS solar cell: The V_{OC} (T) curve (yellow curve) showed a behaviour that is similar to the behaviour of the V_{OC} (T) curve of the Cu-poor CIS solar cells. The extrapolated activation energy at zero Kelvin of the V_{OC} (T) curve of the stoichiometric CIS solar cell showed values close to the bandgap (0.985 eV). The V_{OC} (T) curve of the stoichiometric CIS solar cell showed one negative slope (similar to Cu-poor CIS solar cells) before the V_{OC} values saturate at low temperatures.

Based on the IVT measurements, it can be deduced that the dominant recombination path of the stoichiometric CIS solar cell is in the bulk of the stoichiometric CIS absorber and the stoichiometric CIS solar cell does not suffer from interface recombination losses. This interpretation is based on the extrapolated activation energy of the V_{OC} (T) curve of the stoichiometric CIS solar cell that showed values close to the bandgap (0.985 eV). More details on the interpretation of the IVT measurements are provided in Section 4.3.

A summary of the main characterization results presented in this sub-section is provided in the following points:

- A stoichiometric CIS absorber was grown with a Cu/In ratio of 1.0 ± 0.1 % as indicated by the EDX measurements.
- The admittance measurements of the stoichiometric CIS Schottky absorber did not show any signature for the presence of the 200 ± 20 meV defect typically observed for Cu-rich CIS Schottky absorbers.
- The stoichiometric CIS cell showed V_{OC} and FF values close to the values of the Cu-poor CIS solar cells as revealed by the IV measurements. The stoichiometric CIS solar cell did not suffer from the V_{OC} and the FF deficiency observed for Cu-rich CIS cells.
- The stoichiometric CIS solar cell did not suffer from interface recombination losses unlike Cu-rich CIS solar cells that are characterized by significant recombination losses at the absorber/buffer interface as interpreted from the IVT measurements.
- The stoichiometric CIS solar cell showed only one negative slope of the V_{OC} (T) curve unlike Cu-rich CIS solar cell that showed two slopes for the V_{OC} (T) curve.

To conclude, the stoichiometric CIS absorber and cell did not show any signature for the presence of the 200 ± 20 meV defect or the presence of recombination losses at the absorber/buffer interface. Therefore, the stoichiometric CIS phase can be excluded from being the origin behind the formation of this defect leaving the etching process as the other potential possibility for the origin behind the formation of the 200 ± 20 meV defect.

7.3.2 The KCN etching process

Cu-rich CIS absorbers are subjected a strong KCN etching, while Cu-poor CIS are subjected to a relatively weak KCN etching as explained in sub-section 3.2.1. To perform a detailed investigation analysis on the effect of etching on the three CIS absorbers (Cu-rich, stoichiometric and Cu-poor), three types of etching conditions were used on each of the three CIS absorbers. The three types of etching conditions are:

1. No etching
2. Weak KCN etching (5 % KCN aqueous solution for 30 seconds)
3. Strong KCN etching (10 % aqueous solution for 5 minutes)

Admittance measurements were then performed for the nine samples (three etching conditions for the three CIS absorbers) using Al Schottky contacts as explained in Section 7.1.

For Cu-rich CIS absorbers, conductive secondary phases hindered the possibility of measuring Cu-rich CIS absorbers under no etching and weak KCN etching conditions. Only the strong KCN etching condition allowed such admittance measurements revealing the presence of the 200 ± 20 meV defect.

For the stoichiometric and the Cu-poor CIS absorbers under no etching and weak KCN etching conditions, admittance measurements were successfully performed due to the absence of the copper selenide secondary phases. The admittance measurements for such absorbers revealed values of 130 ± 15 meV for Cu-poor CIS Schottky absorbers similar to what had been presented in Section 5.4 and 100 ± 10 meV for the stoichiometric CIS Schottky absorber similar to the results of the stoichiometric CIS unetched Schottky absorber presented in sub-section 7.3.1.

Interestingly, the admittance measurements performed for both the stoichiometric and the Cu-poor CIS Schottky absorbers under strong KCN etching conditions showed an activation energy of 200 ± 20 meV for their main capacitance step as presented in Figure 7.14.

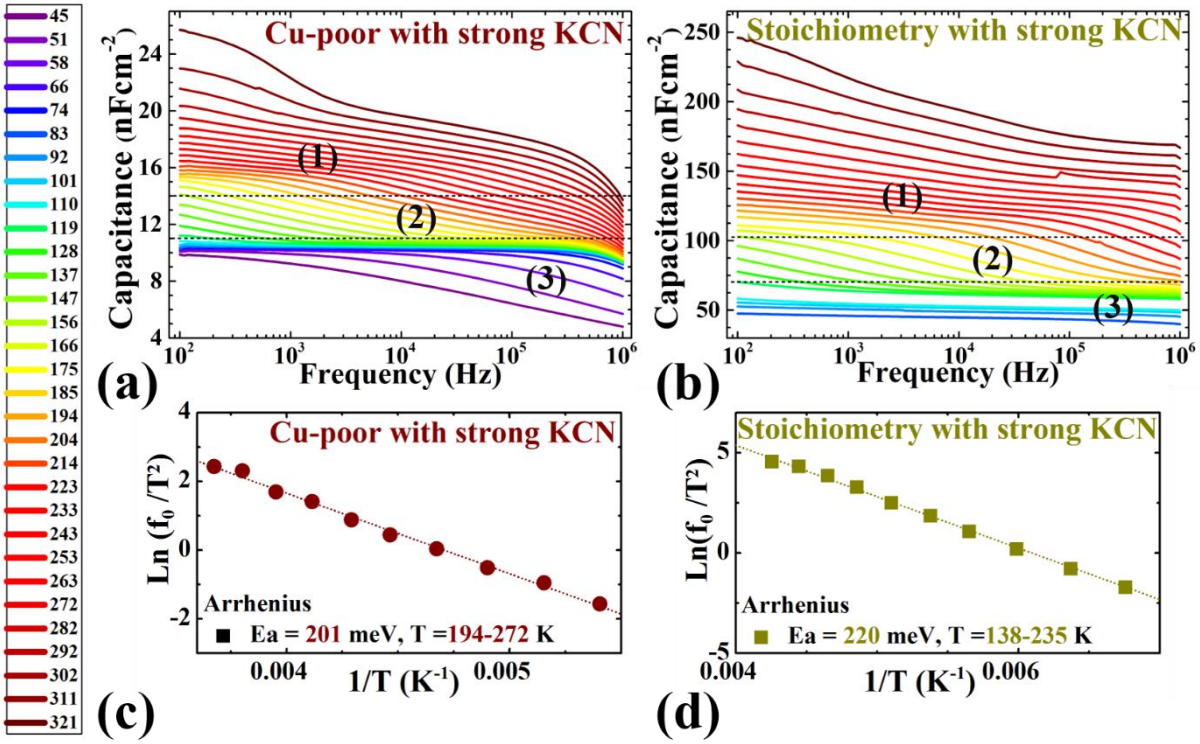

Figure 7.14: Admittance spectra for: a) Cu-poor and b) stoichiometric CIS Schottky absorbers etched under strong KCN conditions. The admittance measurements were performed at temperatures between 50 – 320 K as indicated by the temperature scale on the left side of the figure. The short dashed lines identify three capacitance regions. The main capacitance step is the intermediate temperature step (Step 2). The activation energy of this main capacitance step (Step 2) is extracted from the slope of the Arrhenius plot for: c) Cu-poor and d) stoichiometric CIS Schottky absorbers etched under strong KCN conditions. The activation energy of the main capacitance step showed values of 200±20 meV for both stoichiometric and Cu-poor Schottky absorbers etched under strong KCN conditions.

Figure 7.14 presents the admittance spectra for both Cu-poor CIS (Figure 7.14a) and stoichiometric CIS (Figure 7.14b) absorbers etched under strong KCN conditions. The dashed lines in Figure 7.14 (a, b) represent the three different capacitance regions as explained earlier. The high temperature capacitance step (Step 1) step could not be resolved within our measurements range and the low temperature capacitance step (Step 3) step was attributed to freeze out. The main capacitance step is the intermediate temperature step (Step 2). The corresponding Arrhenius plots of this capacitance step (Step 2) are illustrated in Figure 7.14c for Cu-poor and in Figure 7.14d for stoichiometric CIS Schottky absorbers etched under strong KCN conditions. The activation energy of the main capacitance step (Step 2) extracted from the slope of the Arrhenius plots showed values of 200±20 meV for both the Cu-poor (Figure 7.14c) and the stoichiometric (Figure 7.14d) CIS Schottky absorbers with strong KCN etching conditions.

Based on the above admittance characterizations, it can be concluded that the strong KCN etching condition is the origin behind the formation of the 200±20 meV defect and this defect appears in all Cu-rich, stoichiometric and Cu-poor CIS absorbers exposed to such strong KCN etching conditions.

It is important to note that this 200±20 meV defect appears for Cu-poor and stoichiometric CIS only on bare-absorbers etched with strong KCN conditions and not on fully processed cells even if the absorber is etched using strong KCN. Our standard CdS buffer layer is then able to passivate the 200±20 meV defect from such strongly etched Cu-poor and stoichiometric CIS absorbers. Motivated by the fact that our standard CdS buffer layer can already passivate such 200±20 meV defect from Cu-poor and stoichiometric CIS absorbers, modified buffer layers will be implemented to passivate the 200±20 meV defect from Cu-rich CIS absorbers as will be described in Section 7.4.

To further analyse the effect of the KCN strong etching, PL measurements were performed. PL measurements were performed on three Cu-rich and three Cu-poor CIS absorbers with the three different etching conditions (unetched, etched under weak KCN and etched under strong KCN conditions). The results of these PL measurements on the six CIS absorbers are presented in Figure 7.15.

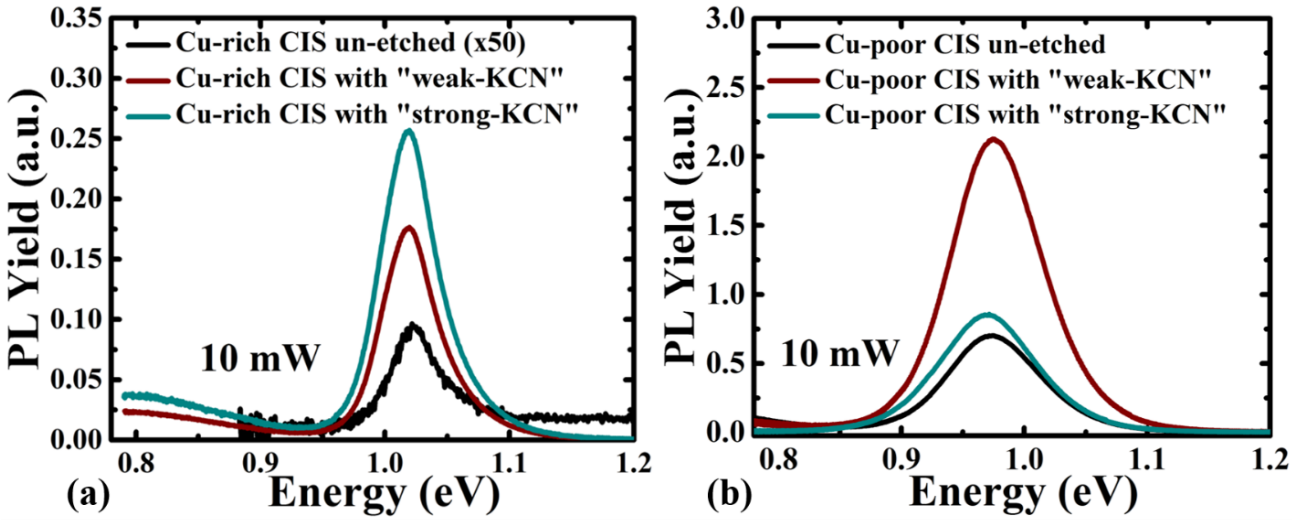

Figure 7.15: PL yield intensities at 10 mW for: a) Cu-rich CIS unetched, Cu-rich CIS with weak KCN and Cu-rich CIS with strong KCN etching conditions and b) Cu-poor CIS unetched, Cu-poor CIS with weak KCN and Cu-poor CIS with strong KCN etching conditions.

Figure 7.15a reveals the effect of KCN etching on Cu-rich CIS absorbers. More etching increases the PL yield intensity from Cu-rich unetched to Cu-rich etched with weak KCN to Cu-rich etched with strong KCN. This increase in the PL intensity of Cu-rich CIS absorbers as a function of increasing the etching conditions could be attributed to an optical effect as a result of scattering and absorption in the copper selenide layer that is removed more with stronger etching conditions.

On the other side, Figure 7.15b reveals that the PL yield intensity indeed increased for Cu-poor CIS as we move from unetched Cu-poor CIS to Cu-poor CIS etched under weak-KCN conditions. This can be attributed to the removal of excess secondary phases like copper selenide or indium oxides. Unlike expected, strong etching of the Cu-poor CIS absorber was not beneficial where the PL yield intensity decreased significantly when etching the Cu-poor CIS absorber under strong KCN etching conditions. This can be attributed to the formation of a deep defect after etching the Cu-poor CIS with strong KCN. Relating this information to the admittance measurements, we can conclude that the strong KCN etching condition causes increased non-radiative recombination losses and is responsible for the formation of the 200 ± 20 meV defect in CIS absorbers.

Understanding that the root cause behind the formation of the 200 ± 20 meV defect is related to the strong KCN etching, it was interesting to investigate if this effect is coming from the potassium "K^+" part or the cyanide "CN^-" part. To discover that, two Cu-rich CIS absorbers were used as follows:

- One Cu-rich CIS absorber was etched with the standard strong KCN etching
- The other Cu-rich CIS absorber was etched using a strong NaCN etching with similar procedures to the strong KCN (10 %-weight aqueous solution for 5 minutes).

Admittance measurements were performed for both Cu-rich CIS Schottky absorbers and the activation energy of their main capacitance step was extracted from their corresponding Arrhenius plots presented in Figure 7.16. Figure 7.16 shows clearly that etching the Cu-rich CIS absorbers with either strong KCN (Figure 7.16a) or strong NaCN (Figure 7.16b) reveals the formation of the same 200 ± 20 meV defect. This means that the alkali part is not the one responsible for the formation of the defect, but the removal of the copper selenide secondary phases through the cyanide part is the main root cause behind the formation of this defect.

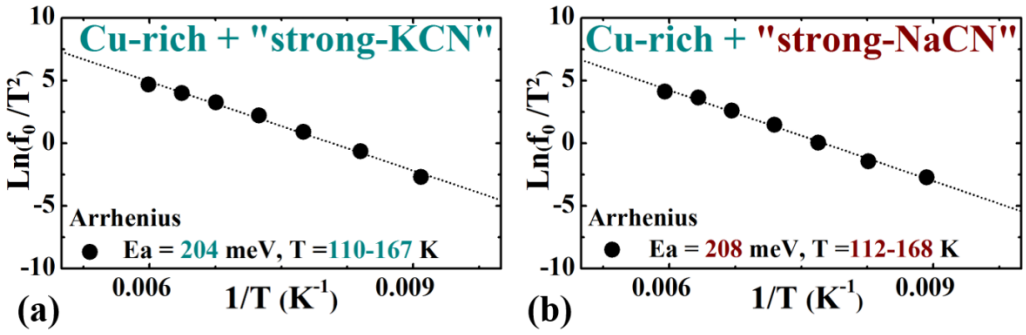

Figure 7.16: Arrhenius plots indicating the activation energy of the main capacitance step based on the admittance measurements for: a) Cu-rich CIS Schottky absorber etched with strong KCN and b) Cu-rich CIS Schottky absorber etched with strong NaCN. The activation energy of the main capacitance step is the same (200±20 meV) in both cases.

In this sub-section, the KCN strong etching step has been identified as the origin behind the formation of the 200±20 meV defect in CIS absorbers. Diego Colombara succeeded in explaining the mechanism behind the formation of the 200±20 meV defect with the KCN strong etching in terms of the surface chemical instability of CIS absorbers. The detailed explanation of this mechanism is under preparation [5]. I will summarize the proposed mechanism in the following points:

- The surface of CIS absorbers is not chemically stable even at room temperature
- When the surface of the CIS absorbers is exposed to air, it becomes oxidized
- The oxidation process for CIS absorbers can be expressed by the following equation (Equation [7.1]):

$$CuInSe_2 + \frac{3}{2}\,O_2 \rightleftharpoons In_2O_3 + Cu_2Se + \frac{3}{n}\,Se_n \qquad [7.1]$$

- The oxidation process of the surface of the CIS absorbers involves two reactions:
    1. The first reaction is the reaction where the oxygen reacts with indium from the CIS lattice forming indium oxide (In_2O_3). This reaction leads to the formation of indium vacancies as well as a Cu-richer CIS phase.
    2. The second reaction is the reaction where copper and selenium from the CIS lattice react together forming copper selenide (Cu_2Se). This reaction leads to the formation of copper and selenium vacancies as well as a Cu-poorer CIS phase.
- According to the calculations performed by Diego Colombara, in the presence of copper interstitials (potentially available more in Cu-rich than in Cu-poor CIS absorbers), the oxidation process is different on Cu-rich CIS absorbers than on Cu-poor CIS absorbers as follows:

a. In Cu-rich CIS absorbers, the formation of copper selenide is more favourable than the formation of indium oxide.
b. In Cu-poor CIS absorbers, the formation of indium oxide is more favourable than the formation of copper selenide.

- Therefore:

1) For Cu-rich CIS absorbers:
    a. Copper selenide secondary phases are formed as a result of the absorber-growth process as well as the surface oxidation process.
    b. Copper selenide phases from the surface oxidation process are formed as a result of the reaction between the copper interstitials with the selenium removed from the CIS lattice.
    c. The removal of selenium from the CIS lattice forms selenium vacancies.
    d. This double source of formation of the copper selenide secondary phases (from absorber growth process and from oxidation process) explains why the KCN weak etching conditions are not enough to remove the copper selenide secondary phases from the surface of Cu-rich CIS absorbers.
    e. A strong KCN etching is then required to remove the excessive amount of copper selenide secondary phases formed.
    f. The strong KCN etching with the copper selenide secondary phases formed as a result of the oxidation process are responsible for the formation of selenium vacancies in the CIS lattice.
    g. I speculate that these selenium vacancies play a fundamental role in the formation of the 200 ± 20 meV defect.
    h. From the oxidation process equation (Equation 7.1), indium oxides are also formed.
    i. The formation of the indium oxides by removing indium from the CIS lattice leads to the formation of indium vacancies.
    j. I speculate that these indium vacancies are related to the 130 ± 15 meV defect [6] observed by admittance measurements in Cu-rich CIS solar cells after passivating the 200 ± 20 meV defect by the 4- and 8-minute in-situ KF PDT (Section 6.2) and the Se-only PDT (Section 6.4).

2) For Cu-poor CIS absorbers:
    a. Indium oxides are formed as a result of the oxidation process at the surface of Cu-poor CIS absorbers.
    b. The formation of indium oxides takes place by the reaction of indium from the CIS lattice with oxygen. This removal of indium from the CIS lattice forms indium vacancies.
    c. I speculate that these indium vacancies are related to the 130±15 meV defect [6] observed by admittance measurements for all Cu-poor CIS solar cells as presented in Section 5.4. Finn Babbe has identified this 130±15 meV defect as a third shallow acceptor (potentially indium vacancy) as discussed in Section 6.4.
    d. Copper selenides are still formed on the surface of Cu-poor CIS absorbers as a result of the oxidation process according to Equation 7.1 but not in massive amounts compared to Cu-rich CIS absorbers.
    e. Weak KCN etching is then sufficient to remove excess indium oxide and copper selenide secondary phases. With no etching, high efficiencies (close to the efficiencies of Cu-poor CIS solar cells with weak KCN etching) could still be achieved.
    f. The KCN strong etching on Cu-poor CIS absorbers leaches selenium from the CIS lattice forming selenium vacancies.
    g. I speculate again that these selenium vacancies are related to the formation of the 200±20 meV defect on Cu-poor CIS absorbers etched under strong KCN etching conditions.

To conclude, the origin behind the formation of the 200±20 meV defect is the strong KCN etching. The mechanism behind the formation of the 200±20 meV defect by the KCN strong etching can be explained in terms of the chemical instability of the surface of CIS absorbers.

7.4 Passivation of the 200±20 meV defect using modified buffer layers

The nature of the 200±20 meV defect has been unveiled in Section 6.4 and Section 7.1 as a Se-related absorber defect. Understanding the nature and the root causes behind the formation of the 200±20 meV defect enabled us to find different means of passivating this defect. This 200±20 meV defect has been passivated using different post-deposition treatments such as:

1. A Se-only PDT presented in Section 6.4 and published in [1]
2. An ex-situ KF PDT presented in Section 6.1 and published in [2]
3. An in-situ KF PDT presented in Section 6.2 and published in [3]
4. In-Se PDT [9].

It was interesting to investigate if this 200±20 meV defect can be also passivated by modifying the buffer layers without any post-deposition treatments or not. As the 200±20 meV defect has been speculated as a Se-related defect and the buffer layer is a source of chalcogen, I speculated that modifying the buffer layer and adding more chalcogen (sulphur) would enable the passivation of the 200±20 meV defect from Cu-rich CIS solar cells.

Moreover, sub-section 7.3.2 introduced the formation of the 200±20 meV defect on Cu-poor and stoichiometric CIS absorbers under strong KCN etching conditions in the Schottky devices, whereas this 200±20 meV defect gets passivated using our standard CdS buffer layer. Motivated by this ability of our standard CdS buffer layer to passivate the 200±20 meV defect from Cu-poor and stoichiometric CIS absorbers, it was encouraging to develop an alternative similar method to passivate the same 200±20 meV defect from Cu-rich CIS absorbers.

Based on the above discussion, it can be observed that high enough chalcogen (Se or S) should in principle be able to passivate this 200±20 meV defect depending on the concentration of the defect present in the absorber. Therefore, I speculated that more chalcogen is needed to passivate this 200±20 meV defect from Cu-rich CIS absorbers.

To verify that enough chalcogen can passivate the 200±20 meV defect from Cu-rich CIS absorbers, an experiment using CdS buffer layer from EMPA laboratories as well as Zn(O,S) from our laboratories was performed on a set of Cu-rich CIS absorbers from the same deposition process.

The CdS buffer layer deposited at EMPA laboratories is characterized with its high thiourea (source of S) concentrations (374 mM thiourea) as well as longer deposition durations [13] and the Zn(O,S) buffer layer deposited in our laboratories has slightly higher thiourea (source of S) concentrations (75 mM thiourea) compared to our standard CdS buffer layer (50 mM thiourea).

Three Cu-rich CIS absorbers from the same absorber growth deposition run were used for this experiment. The three Cu-rich CIS absorbers were etched using a strong KCN etching and processed as follows:

1. The first Cu-rich CIS etched absorber was covered with our standard CdS buffer layer and was further processed with our standard baseline process.
2. The second Cu-rich CIS etched absorber was sent to EMPA to deposit the CdS buffer layer only and then returned back to our laboratories to be further processed in the same baseline process used for the first Cu-rich CIS absorber.
3. The third Cu-rich CIS etched absorber was covered with our standard Zn(O,S) buffer layer and then completed with Al Schottky contacts.

In total, we have three Cu-rich CIS solar cells, one Cu-rich CIS solar cell based on our standard CdS buffer layer (CdS LPV) and two other Cu-rich CIS solar cells based on buffer layers with slightly higher chalcogen concentrations (CdS from EMPA and Zn(O,S) from LPV).

Admittance measurements were performed for the three devices and the results of these admittance measurements are presented in Figure 7.17. Figure 7.17 (a, c, e) represents the admittance spectra for the Cu-rich CIS devices with standard CdS buffer layer deposited at our LPV laboratories (Figure 7.17a), CdS buffer layer deposited at EMPA laboratories (Figure 7.17c) and standard Zn(O,S) buffer layer deposited at our LPV laboratories (Figure 7.17e). The dashed lines in Figure 7.17 (a, c, e) define three different capacitance step regions as explained previously in Section 4.5. The high temperature capacitance step (Step 1) could not be resolved within our measurement range. The low temperature capacitance step (Step 3) has been attributed to freeze out. The intermediate temperature step (Step 2) is the main capacitance step for all the three samples.

The activation energy of the main capacitance step (Step 2) in the three samples was calculated from the slope of the corresponding Arrhenius plots in Figure 7.17 (b, d, f) as explained in Section 4.5. The activation energy of the main capacitance step (Step 2) for the Cu-rich CIS solar cell with our standard CdS buffer layer (CdS LPV) showed the presence of the 200±20 meV defect (Figure 7.17b). However, the activation energies for the Cu-rich CIS samples with higher chalcogen concentrations, the one with the CdS buffer deposited at EMPA (Figure 7.17d) and the one with the Zn(O,S) buffer deposited at our laboratories (Figure 7.17f), showed values of 175±5 meV in the same temperature range observed for the 200±20 meV defect (100 – 160 K). I can identify this 175±5 meV capacitance step as a defect because the activation energies extracted from the series resistance as a function of temperature for these two solar cells (Cu-rich CIS solar cells with EMPA CdS and with our standard Zn(O,S) buffer layers) showed values lower than the activation energies extracted from admittance measurements. However, I do not have a clear picture on the identification of this defect. The only observation that I can highlight, is that this 175±5 meV defect appears in the presence of Sulphur, so I will speculate this 175±5 meV defect for the time being as a Sulphur related (S-related) defect. These activation energies of 175±5 meV indicates the passivation of the 200±20 meV defect from Cu-rich CIS absorbers when using a buffer layer with relatively higher chalcogen concentrations.

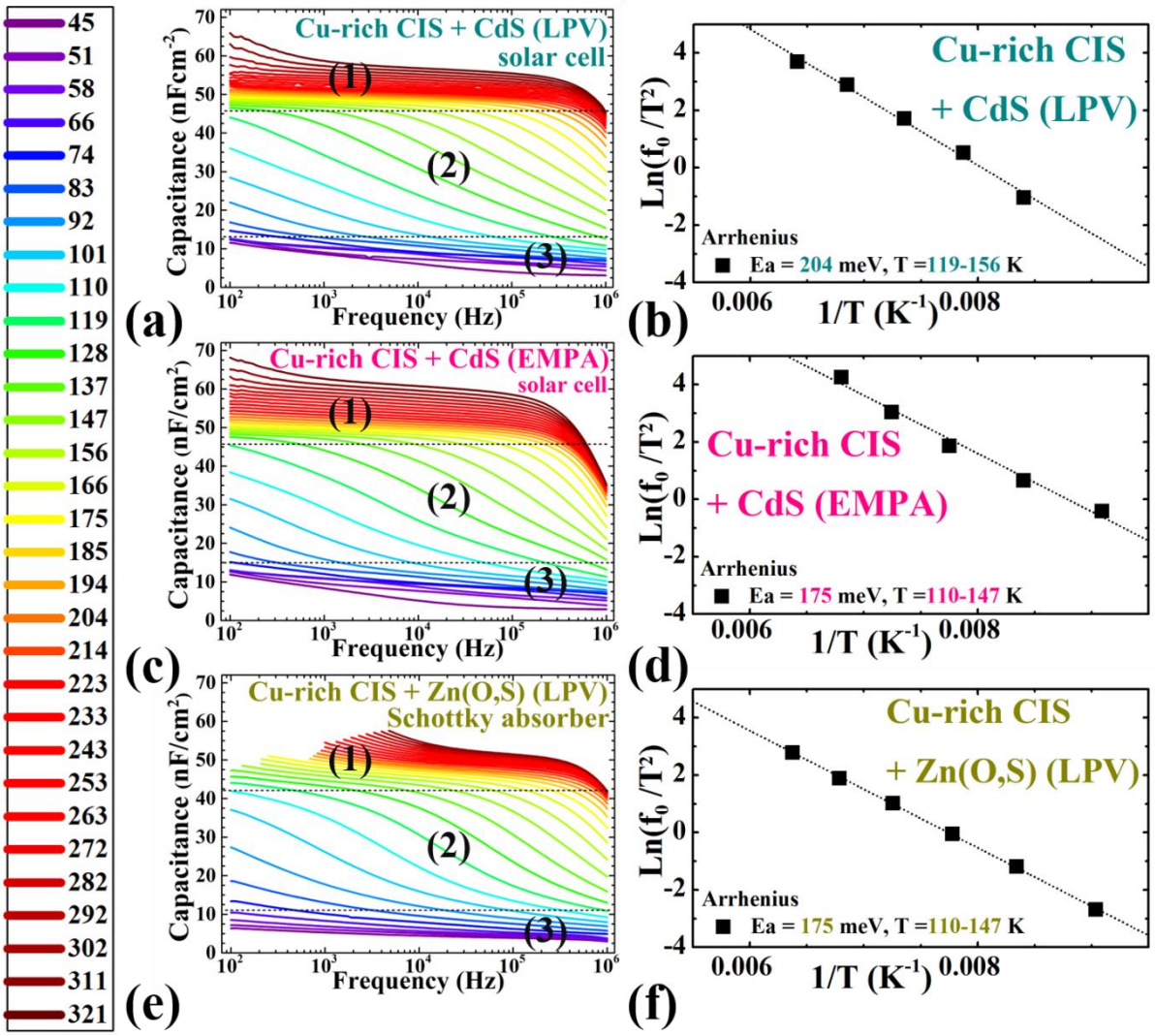

Figure 7.17: Admittance spectra measured between 50 – 320 K as indicated by the temperature scale on the left side of the figure for Cu-rich CIS devices with: a) standard CdS buffer layer deposited in-house (CdS LPV), c) CdS buffer layer deposited at EMPA and e) Zn(O,S) buffer layer deposited in-house, Zn(O,S) LPV. The short dashed lines define three capacitance regions. The activation energy of the main capacitance step (Step 2) was extracted from the corresponding Arrhenius plots for: b) standard CdS buffer layer deposited in-house (CdS LPV), d) CdS buffer layer deposited at EMPA and f) Zn(O,S) buffer layer deposited in-house, Zn(O,S) LPV.

Motivated by the previous experiment, three Zn(O,S) buffer layers with three different higher thiourea (TU) concentrations compared to the TU concentration in our standard CdS buffer layer (50 mM TU) were developed in our laboratories. The objective of this experiment is to observe the effect of adding more chalcogen (adding more TU as the source of Sulphur) on the passivation of the 200±20 meV defect from Cu-rich CIS absorbers etched under strong KCN etching conditions. The three Zn(O,S) buffer layers are developed as follows:

1. Zn(O,S) buffer layer with 6 times higher TU concentrations (300 mM TU) compared to our standard CdS buffer layer (50 mM TU). This Zn(O,S) buffer layer is referred to as TU X 6.
2. Zn(O,S) buffer layer with 8 times higher TU concentrations (400 mM TU) compared to our standard CdS buffer layer (50 mM TU). This Zn(O,S) buffer layer is referred to as TU X 8.
3. Zn(O,S) buffer layer with 16 times higher TU concentrations (800 mM TU) compared to our standard CdS buffer layer (50 mM TU). This Zn(O,S) buffer layer is referred to as TU X 16.

The three different Zn(O,S) buffer layers were deposited on three similar Cu-rich CIS absorbers from the same absorber growth run etched under strong KCN etching conditions. After that, the three Cu-rich CIS etched absorbers with the three different Zn(O,S) buffer layers were further processed with the same baseline process. The three Cu-rich CIS solar cells based on the three different Zn(O,S) buffer layers were compared to a fourth Cu-rich CIS solar cell based on our standard CdS buffer layer as a reference cell. It is important to note that the Cu-rich CIS absorbers used for this experiment are similar to the Cu-rich CIS absorbers used for the previous experiment.

Admittance measurements were performed for all the four Cu-rich CIS solar cells. The activation energy of the main capacitance step for the reference Cu-rich CIS solar cell with our standard CdS buffer layer showed the typical 200±20 meV defect. The results of the admittance measurements for the other three solar cells with Zn(O,S) buffer layers (6 X TU, 8 X TU and 16 X TU) are presented in Figure 7.18.

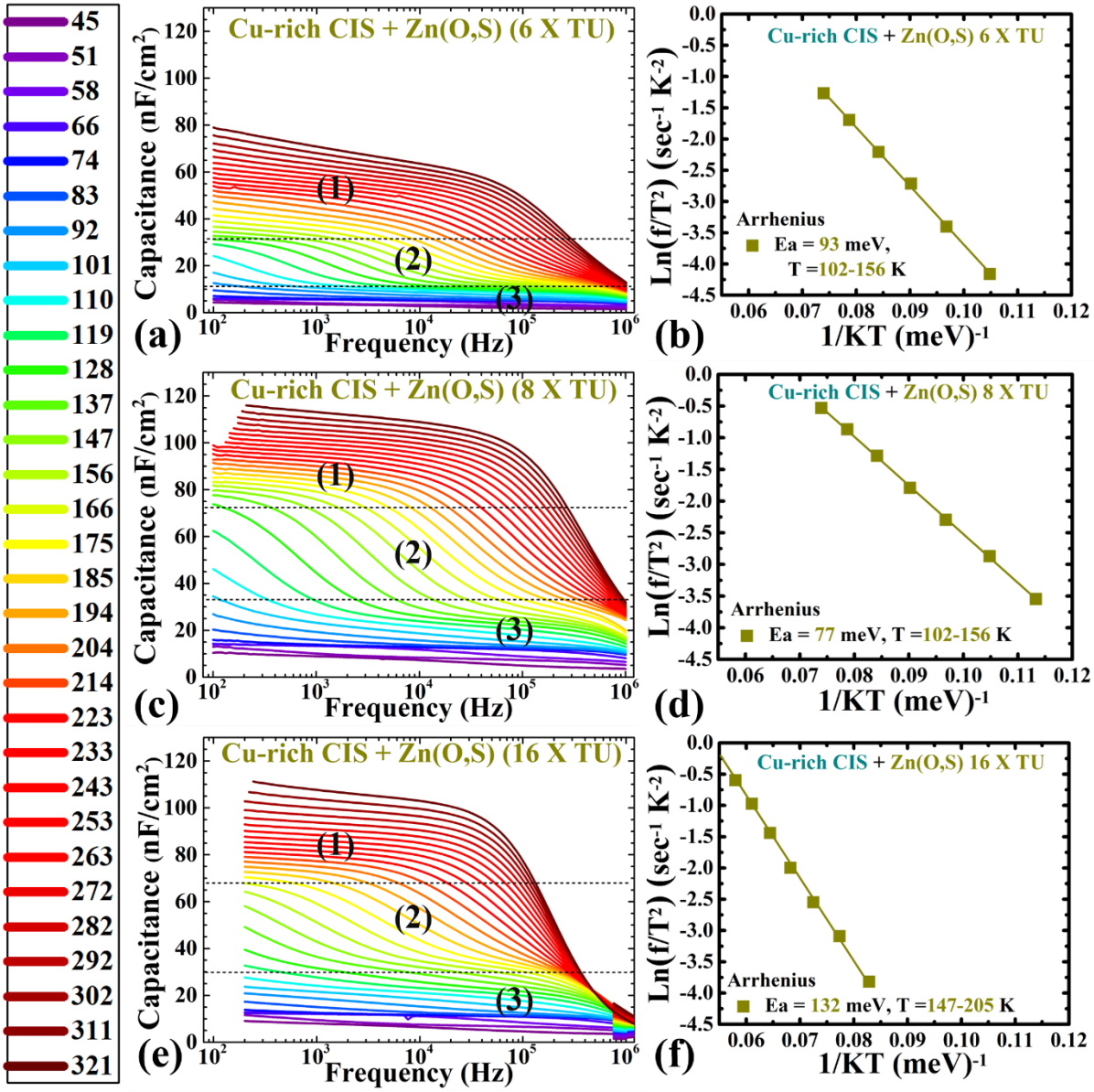

Figure 7.18: Admittance spectra measured between 50 – 320 K as indicated by the temperature scale on the left side of the figure for Cu-rich CIS solar cells with Zn(O,S) buffer layers deposited in-house with: a) 6 X TU concentrations, c) 8 X TU concentrations and e) 16 X TU concentrations. The short dashed lines define three capacitance regions. The activation energies of the main capacitance step (Step 2) were calculated from the slope of the corresponding Arrhenius plots of the Cu-rich CIS solar cells with Zn(O,S) buffer layers deposited in-house with: b) 6 X TU concentrations, d) 8 X TU concentrations and f) 16 X TU concentrations. The activation energies of this main capacitance step (Step 2) showed values of 93, 77 and 132 meV for the Cu-rich CIS solar cells based on Zn(O,S) buffer layers with 6 X TU, 8 X TU and 16 X TU concentrations respectively.

Figure 7.18 (a, c, e) presents the admittance spectra for the Cu-rich CIS solar cells with the Zn(O,S) buffer layer developed with 6 X TU (Figure 7.18a), 8 X TU (Figure 7.18c) and 16 X TU (Figure 7.18e). The dashed lines in Figure 7.18 (a, c, e) identify three capacitance regions as explained in Section 4.5. The high temperature capacitance step (Step 1) could not be identified within our admittance measurement range and the low temperature capacitance step (Step 3) was attributed to freeze-out.

The intermediate temperature capacitance step (Step 2) is then the main capacitance step for these three solar cells. The activation energies of this main capacitance step (Step 2) for the three cells were calculated from the slope of the corresponding Arrhenius plots in Figure 7.18 (b, d, f) for Cu-rich CIS solar cells with Zn(O,S) buffer layer of 6 X TU (Figure 7.18b), 8 X TU (Figure 7.18d) and 16 X TU (Figure 7.18f) respectively.

The activation energy of the main capacitance step (Step 2) for the Cu-rich CIS solar cells with Zn(O,S) buffer layers of high TU concentrations in Figure 7.18 showed values of 93, 77 and 132 meV for the solar cells with 6 X TU (Figure 7.18b), 8 X TU (Figure 7.18d) and 16 X TU (Figure 7.18f) concentrations respectively.

These activation energies (93, 77 and 132 meV) are much lower than the activation energy of the 200±20 meV capacitance step (defect) in Cu-rich CIS absorbers and also lower than the 175±5 meV capacitance step observed in Cu-rich CIS sample with our standard Zn(O,S) buffer layer presented in Figure 7.17f. I did not further investigate the identity of these activation energies (93, 77 and 132 meV) for the Cu-rich CIS solar cells with the three different Zn(O,S) buffer layers but I speculate that these activation energies (93, 77 and 132 meV) correspond to shallow defects.

The main objective of this experiment with the three different Zn(O,S) buffer layers is to investigate the effect of adding more chalcogen on the activation energy of the main capacitance step from admittance measurements. Therefore, the results in Figure 7.18 implies that high enough Sulphur in TU solutions of the Zn(O,S) buffer layer leads to the passivation of the 200±20 meV defect typically observed for Cu-rich CIS solar cells.

Based on the above results, it can be concluded that high enough chalcogen (high enough Sulphur in TU solutions of CdS and Zn(O,S) buffer layers or high enough Se in the PDTs) are able to passivate the 200±20 meV defect typically observed for Cu-rich CIS absorbers and solar cells.

To further analyse the effect of adding more chalcogen on the absorber/buffer interface recombination losses typically observed for Cu-rich CIS solar cells with our standard CdS buffer layer, the following characterizations using IVT measurements were performed. The V_{OC} (T) curves presented in Figure 7.19 were extracted from the IVT measurements performed for three Cu-rich CIS solar cells with the following characteristics:

1. Cu-rich CIS solar cell based on our standard in-house CdS buffer layer (CdS LPV) with a TU concentration of 50 mM.
2. Cu-rich CIS solar cell based on the CdS buffer layer deposited in EMPA laboratories with higher TU concentrations (374 mM) compared to our standard CdS buffer layer (50 mM TU) as explained earlier.
3. Cu-rich CIS solar cell based on our in-house Zn(O,S) buffer layer developed with higher TU (400 mM) concentrations compared to our standard CdS buffer layer (50 mM TU), referred to as Zn(O,S) 8 X TU.

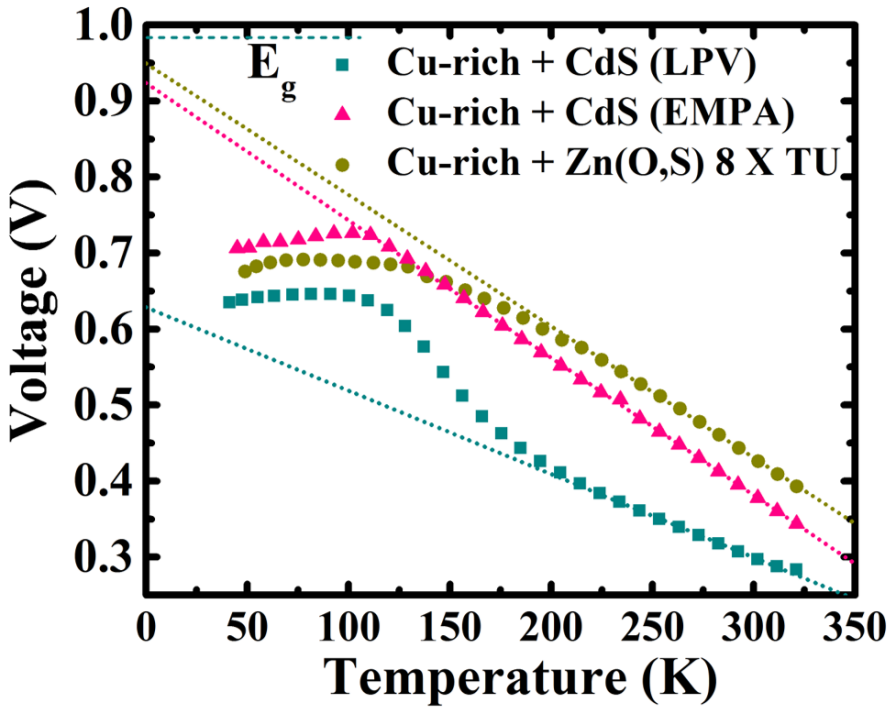

Figure 7.19: Open Circuit Voltage (V_{OC}) dependence curves as function of temperature for Cu-rich CIS solar cells with our in-house standard CdS buffer layer (green curve), CdS buffer layer deposited at EMPA laboratories (pink curve) and Zn(O,S) buffer layer with 8 times higher thiourea (TU) concentrations (yellow curve) compared to our standard CdS buffer layer. The short dotted lines represent the fitting of the V_{OC} (T) curves fitted at room temperatures. The extrapolated activation energies at zero Kelvin from those fitted curves show values around 0.6 V for Cu-rich CIS cells with our standard CdS buffer layer (green curve) and values above 0.9 V for Cu-rich CIS solar cells with both CdS buffer layer deposited at EMPA laboratories (pink curve) and Zn(O,S) buffer layer with higher TU concentrations (yellow curve).

Figure 7.19 reveals two observations:

1. The first observation is related to the extrapolated activation energy at zero Kelvin of the V_{OC} (T) curve. The interpretation of the V_{OC} (T) curve was explained in Section 4.3. The extrapolated activation energy of the V_{OC} (T) curves in Figure 7.19 at zero Kelvin showed values around 0.6 V for the Cu-rich CIS solar cell with our standard CdS buffer layer (green curve). However, the extrapolated activation energy at zero Kelvin in Figure 7.19 showed values closer to the bandgap (above 0.9 V) for Cu-rich CIS solar cells with higher chalcogen concentrations achieved by both the CdS buffer layer deposited at EMPA (pink curve) and the Zn(O,S) buffer layer with 8 X higher TU concentrations (yellow curve). The significant increase in the extrapolated activation energy at zero Kelvin of the Cu-rich CIS solar cells after using buffer layers with high enough thiourea concentrations (activation energy increased from 0.6 V to above 0.9 V) implies a significant improvement in the Cu-rich CIS absorber/buffer interface. The interface recombination losses were significantly reduced in Cu-rich CIS solar cells after using buffer layers with high enough chalcogen.
2. The second observation is related to the number of negative slopes in the V_{OC} (T) curves of the Cu-rich CIS solar cells before the V_{OC} values saturate (or decrease) at low temperatures (lower than 100 K). In Figure 7.19, it can be observed that the Cu-rich CIS solar cell based on our standard CdS buffer layer (green curve) showed two negative slopes: one slope can be observed at temperatures between 200 – 300 K and the other slope at temperatures between 100 – 200 K. However, the V_{OC} (T) curves indicated only one negative slope in the temperature range between 100 – 300 K for Cu-rich CIS solar cells with both the CdS buffer layer deposited at EMPA (pink curve) and the Zn(O,S) buffer layer with 8 X higher TU concentrations (yellow curve) compared to our standard CdS buffer layer.

The above two observations in Figure 7.19 indicate that using buffer layers with high enough chalcogen (high enough TU concentrations as TU is the source of Sulphur) improves the Cu-rich CIS absorber/buffer interface by reducing the recombination losses at the absorber/buffer interface. The above two observations fit well with the improvements observed in sub-section 7.2.2 after using post-deposition treatments with high enough chalcogen (high enough Se).

The final characterization that was performed for the Cu-rich CIS solar cells with modified buffer layers (buffer layers with high TU concentrations) was the IV characterization. The IV measurements were performed for the following solar cells:

- A Cu-rich CIS solar cell based on our standard CdS buffer layer with a TU concentration of 50 mM as a reference cell.
- A Cu-rich CIS solar cell based on the CdS buffer layer deposited at EMPA with a TU concentration of 374 mM.
- Three Cu-rich CIS solar cells based on Zn(O,S) buffer layer developed in-house with TU concentrations of 300, 400 and 800 mM referred to as TU X 6, TU X 8 and TU X 16.

The IV parameters were extracted from these IV measurements and are presented in Table 7.1.

Table 7.1 IV parameters for the average of six solar cells comparing a reference Cu-rich CIS solar cell with standard CdS deposited in-house with Cu-rich CIS solar cells with higher thiourea (chalcogen) concentrations developed with CdS deposited in EMPA and Zn(O,S) buffer layers deposited in-house with 6 X TU, 8 X TU and 16 X TU concentrations compared to the TU concentrations of our standard CdS buffer layer. Values in brackets represent the best solar cells.

Sample	Efficiency (%)	*FF* (%)	V_{OC} (mV)	J_{SC} (mA/cm^2)
Cu-rich CIS with our standard CdS buffer layer (reference)	7.7 (8.1)	51.0 (52.3)	357 (358)	42.4 (44.0)
Cu-rich CIS with EMPA CdS buffer layer	7.4 (8.3)	48.9 (53.0)	390 (393)	38.5 (40.6)
Cu-rich CIS with Zn(O,S) buffer layer of 6 times higher thiourea concentrations	6.7 (7.0)	40.9 (41.9)	399 (399)	41.0 (41.9)
Cu-rich CIS with Zn(O,S) buffer layer of 8 times higher thiourea concentrations	5.6 (7.2)	38.7 (43.1)	423 (424)	33.9 (39.5)
Cu-rich CIS with Zn(O,S) buffer layer of 16 times higher thiourea concentrations	5.9 (6.0)	34.9 (35.9)	410 (412)	40.9 (41.3)

The V_{OC} values in Table 7.1 show an increase of more than 30 mV for Cu-rich CIS solar cells with the CdS buffer layer deposited at EMPA laboratories compared to the Cu-rich CIS solar cells with our in-house standard CdS buffer layer. A more pronounced increase in the V_{OC} values was observed when using higher chalcogen concentrations through using Zn(O,S) buffer layers of much higher thiourea concentrations compared to Cu-rich CIS solar cells with our standard CdS buffer layer. Table 7.1 shows an increase of more than 40, 60 and 50 mV for Cu-rich CIS solar cells with Zn(O,S) buffer layers of 6 X TU, 8 X TU and 16 X TU concentrations respectively compared to the reference Cu-rich CIS solar cell. The V_{OC} values increased from 357 mV for the reference Cu-rich CIS solar cell to values of 399, 423 and 410 mV for the Cu-rich CIS solar cells with 6 X TU, 8 X TU and 16 X TU concentrations respectively. This increase in the V_{OC} values after using buffer layers with high enough chalcogen is another characteristic observed with the passivation of the 200 ± 20 meV defect from Cu-rich CIS solar cells as discussed in sub-section 7.2.2 and sub-section 7.2.3.

For the Cu-rich CIS solar cells with Zn(O,S) buffer layers, there is an inverse relationship between the FF values and adding more thiourea where the FF values decreased from 51 % for the reference Cu-rich CIS solar cell to values of 40.9, 38.7 and 34.9 % after using 6 X TU, 8 X TU and 16 X TU concentrations respectively. This decrease in the FF is attributed to a stronger increase in the series resistances observed when adding more thiourea. For the J_{SC} of the Cu-rich CIS solar cells with Zn(O,S) buffer layers, there is no clear trend when adding higher thiourea concentrations, but adding any amount of higher thiourea concentrations decreased the J_{SC} values compared to our reference cell. This decrease in the FF and the J_{SC} values when adding higher thiourea concentrations did not help improving the efficiency of Cu-rich CIS solar cells compared to our reference cell regardless the significant increase in the V_{OC} values. Further development to the Zn(O,S) buffer layer deposition procedures is needed to minimize the detrimental effect of adding more thiourea on the FF and the J_{SC} values and benefit from the improvement in the V_{OC} values with adding more thiourea.

For the Cu-rich CIS solar cell with the CdS buffer layer deposited at EMPA laboratories, an increase of more than 30 mV in the V_{OC} values was observed compared to the reference cell as discussed above. However, a corresponding decrease in the FF and the J_{SC} values were observed on the Cu-rich CIS solar cells with the CdS buffer layer deposited at EMPA compared to our reference cell. This decrease in the FF and the J_{SC} values compensated the increase in the V_{OC} values leading to efficiencies similar to our Cu-rich CIS reference cell. The decrease in the FF and J_{SC} could be attributed to a higher resistances in terms of FF and a thicker CdS buffer layer in terms of J_{SC} as a result of the much longer durations of the CdS deposition process performed at EMPA laboratories compared to our standard CdS process. This hypothesis can be confirmed for the J_{SC} by observing the EQE spectra illustrated in Figure 7.20.

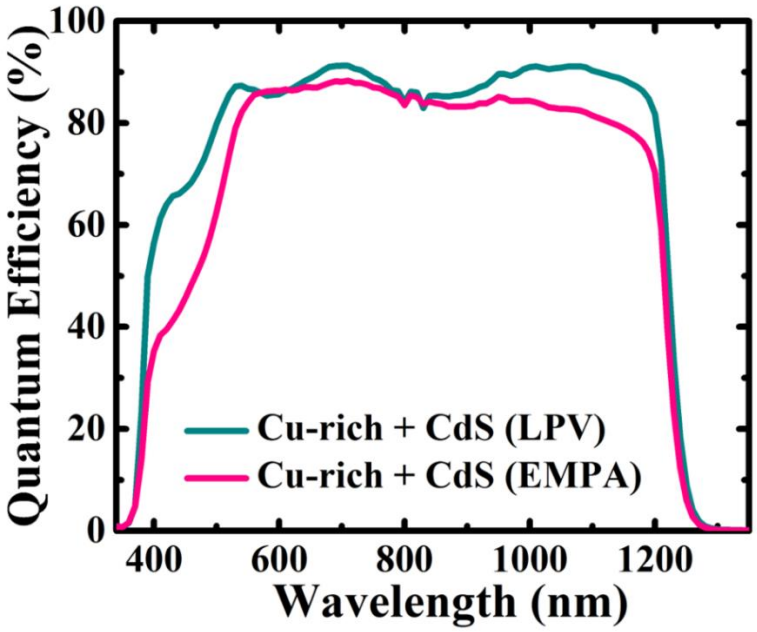

Figure 7.20: EQE spectra for Cu-rich CIS solar cells with a CdS buffer layer deposited in-house (green curve) and with a CdS buffer layer deposited at EMPA laboratories (pink curve).

Figure 7.20 illustrates the EQE spectra of Cu-rich CIS solar cells with a reference CdS buffer layer (green curve) and with the CdS buffer layer deposited at EMPA laboratories (pink curve). The EQE spectra showed a decreased response in the short wavelength region (400 – 550 nm) for the Cu-rich CIS solar cell with the EMPA CdS buffer layer compared to our reference Cu-rich CIS solar cell. This is due to the longer durations of the CdS chemical path deposition procedures at EMPA compared to our in-house procedures resulting in a thicker CdS buffer layer and consequently increased absorption from the CdS buffer layer deposited at EMPA compared to our in-house CdS buffer layer.

Moreover, the Cu-rich CIS solar cells with the EMPA CdS buffer layer suffered from additional losses at longer wavelengths (1000 – 1200 nm) compared to our reference cell but the reason behind these losses could not be completely resolved. This decrease in the EQE response at shorter and longer wavelengths is the main responsible for the corresponding decrease in the J_{SC} values of the Cu-rich CIS solar cells with the EMPA CdS buffer layer compared to the reference Cu-rich CIS solar cell with our standard CdS buffer layer as observed in Table 7.1.

To conclude, Table 7.1 presents an additional positive effect of using high enough chalcogen (adding more TU as TU is the source of Sulphur) in the buffer layers of the Cu-rich CIS solar cells to the electrical performance of Cu-rich CIS solar cells. Adding high enough chalcogen leads to the passivation of the 200 ± 20 meV defect, the improvement of the absorber/buffer interface and the improvement of the V_{OC} values of the Cu-rich CIS solar cells.

7.5 Summary on interface recombination challenge in Cu-rich CIS cells

Chapter 7 focused on the challenge of interface recombination losses observed for all Cu-rich CIS solar cells.

Section 7.1 identified the 200±20 meV defect typically observed for Cu-rich CIS solar cells as a Se-related absorber defect. This 200±20 meV defect is not affected by changing the Cu, In or Se fluxes during the CIS absorber growth process.

Section 7.2 first highlights some observations related to Cu-rich CIS solar cells. These observations can be summarized mainly in the V_{OC} deficiency, the recombination losses at the absorber/buffer interface and the 200±20 meV defect present in Cu-rich CIS solar cells. Then, Section 7.2 highlights the improvements observed after using post-deposition treatments with high enough chalcogen (high enough Se). These improvements are mainly related to the improvement in the V_{OC} values, the improved absorber/buffer interface with the reduction in the interface recombination losses and the passivation of the 200±20 meV defect in Cu-rich CIS solar cells treated with post-deposition treatments of high enough chalcogen. The results in Section 7.2 implied that the root cause of the interface recombination losses in Cu-rich CIS solar cells is attributed to the 200±20 meV defect. The passivation of this 200±20 meV defect improves the absorber/buffer interface and increase the V_{OC} values of the Cu-rich CIS solar cells.

Section 7.3 discussed the origin behind the formation of the 200±20 meV defect. Two potential origins were proposed: the stoichiometric CIS phase and the KCN strong etching conditions. The first part of Section 7.3 showed that the stoichiometric CIS phase is not responsible for the formation of the 200±20 meV defect. The stoichiometric CIS solar cells did not show any signature for the presence of the 200±20 meV defect or the recombination losses at the absorber/buffer interface. The other part of Section 7.3 showed that the origin behind the formation of the 200±20 meV defect in Cu-rich CIS solar cells is the KCN strong etching condition that is mandatory for Cu-rich CIS absorbers to remove conductive copper selenide secondary phases. Applying this strong KCN etching conditions to Cu-poor and stoichiometric CIS absorbers leads to the formation of the 200±20 meV defect. The mechanism behind the formation of the 200±20 meV defect by the KCN strong etching was explained in terms of the chemical instability of the surface of CIS absorbers.

Finally, Section 7.4 provided an alternative mean of passivating the 200±20 meV defect from Cu-rich CIS solar cells using modified buffer layers with high enough chalcogen (high enough thiourea concentrations, as thiourea is the source of Sulphur).

In summary, the 200±20 meV defect in Cu-rich CIS solar cells has been identified as a Se-related absorber defect. This defect is passivated by high enough chalcogen through either high enough Selenium in the post-deposition treatments or high enough Sulphur in the buffer layer. A summary of these different means of passivating the 200±20 mev defect from Cu-rich CIS solar cells is provided in Figure 7.21.

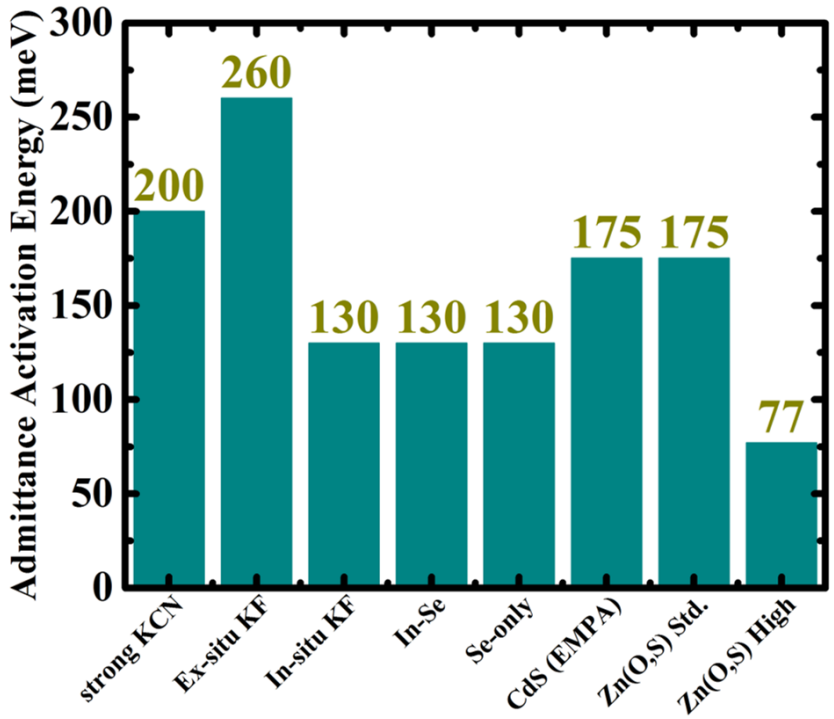

Figure 7.21: An overview of the capacitance steps observed by admittance measurements in this thesis. The activation energy deduced from admittance measurements is presented on the y-axis for different treatments (including etching, PDTs and buffer layers) presented on the x-axis.

Figure 7.21 provides a collected overview on most of the capacitance steps observed by admittance measurements and discussed all along this thesis. A 200±20 meV capacitance step (shown to be a defect) is formed for Cu-rich, stoichiometric and Cu-poor CIS absorbers when introduced to strong KCN etching conditions. This 200±20 meV defect can be passivated with high enough chalcogen treatments. For Cu-poor and stoichiometric CIS absorbers, our standard CdS buffer layer has high enough chalcogen to passivate such 200±20 meV defect. For Cu-rich CIS absorbers, our standard CdS buffer layer has no enough chalcogen concentrations to passivate the 200±20 meV defect.

Therefore, to passivate the 200±20 meV defect from the surface of Cu-rich CIS absorbers, different means of treatments were introduced:

1. An ex-situ KF PDT passivates the 200±20 meV defect as discussed in Section 6.1 but introduces a transport barrier with an activation energy of 260±20 meV as presented in Figure 7.21.
2. An in-situ KF PDT passivates the 200±20 meV defect as presented in Section 6.2 and unveils the presence of another defect with an activation energy of 130±15 meV that was hidden under the 200±20 meV defect as presented in Figure 7.21.
3. An In-Se PDT passivates the 200±20 meV defect [9] leaving the other defect with an activation energy of 130±15 meV as presented in Figure 7.21.
4. A Se-only PDT passivates the 200±20 meV defect as described in Section 6.4 and shows the presence of the other defect with an activation energy of 130±15 meV as presented in Figure 7.21. This 130±15 meV defect can be attributed to the A3 acceptor defect as observed in Cu-poor CIS solar cells.
5. CdS buffer layer deposited at EMPA laboratories with higher thiourea concentrations (compared to our standard CdS buffer layer) and no post-deposition treatments passivates the 200±20 meV defect as discussed in Section 7.4 and shows an activation energy of 175±5 meV for the main capacitance step as presented in Figure 7.21. I speculated that this 175±5 meV capacitance step is a S-related defect as discussed in Section 7.4.
6. Standard Zn(O,S) buffer layer with relatively higher thiourea concentrations compared to our standard CdS buffer layer passivates the 200±20 meV defect as indicated in Section 7.4 and shows an activation energy of 175±5 meV for the main capacitance step as presented in Figure 7.21. I speculated that this 175±5 meV capacitance step is the same S-related defect observed for Cu-rich CIS solar cells with the CdS buffer layer deposited at EMPA laboratories.
7. Zn(O,S) buffer layer with higher thiourea concentrations (compared to our standard CdS buffer layer) passivates the 200±20 meV defect as explained in Section 7.4. The activation energy extracted from the main capacitance step showed values of 77 meV for Cu-rich CIS solar cells with Zn(O,S) buffer layer of 8 times higher thiourea concentrations compared to our standard CdS buffer layer as presented in Figure 7.21.

References Chapter 7

[1] H. Elanzeery, M. Melchiorre, M. Sood, F. Babbe, F. Werner, G. Brammertz and S. Siebentritt, "Challenge in Cu-rich $CuInSe_2$ Thin Film Solar Cells: Defect Caused by Etching", submitted (2018).

[2] H. Elanzeery, F. Babbe, M. Melchiorre, A. Zelenina, S. Siebentritt, "Potassium Fluoride Ex-Situ Treatment on Both Cu-Rich and Cu-Poor $CuInSe_2$ Thin Film Solar Cells", IEEE J. Photovoltaics, 7: 684–689 (2017).

[3] F. Babbe, H. Elanzeery, M. Melchiorre, A. Zelenina, S. Siebentritt, "Potassium fluoride post deposition treatment with etching step on both Cu rich and Cu poor $CuInSe_2$ thin film solar cells", Physical Review Materials, 2: 105405 (2018).

[4] L. Choubrac, T. Bertram, H. Elanzeery, S. Siebentritt, "$Cu(In,Ga)Se_2$ solar cells with improved current based on surface treated stoichiometric absorbers", Phys. Status Solidi. 214, 1600482 (2017).

[5] D. Colombara, H. Elanzeery, N. Nicoara, A. Koprek, M. Wolter, N. Valle, O. Bondarchuk, M. Melchiorre, F. Babbe, C. Spindler, O. Cojocaru-Miredin, D. Raabe, P. J. Dale, S. Sadewasser, S. Siebentritt, "Chemical instability of chalcogenide surfaces near phase boundaries", in preparation (2018).

[6] F. Babbe, H. Elanzeery, M. H. Wolter, K. Santhosh, S. Siebentritt, "The hunt for the third acceptor in $CuInSe_2$ and $Cu(In,Ga)Se_2$ absorber layers", submitted (2018).

[7] B. Theys, T. Klinkert, F. Mollica, E. Leite, F. Donsanti, M. Jubault, D. Lincot, "Revisiting Schottky barriers for CIGS solar cells: Electrical characterization of the $Al/Cu(InGa)Se_2$ contact", Physica status solidi (a): applications and material science, 213, 9: 2425-2430 (2016).

[8] E. Schlenker, V. Mertens, J. Parisi, R. Reineke-Koch, M. Köntges, "Schottky contact analysis of photovoltaic chalcopyrite thin film absorbers", Physics Letters A, 362, 2–3, 26: 229-233 (2007).

[9] T. Bertram, "Doping, Defects and Solar Cell Performance of Cu-rich Grown $CuInSe_2$", PhD Thesis (2016). Available at http://orbilu.uni.lu/handle/10993/28325

[10] T. Gödecke, T. Haalboom, F. Ernst, "Phase Equilibria of Cu-In-Se I. Stable States and Nonequilibrium States of the In_2Se_3-Cu_2Se Subsystem", Z. Metallkd., 91: 622-634 (2000).

[11] V. Depredurand, D. Tanaka, Y. Aida, M. Carlberg, N. Fevre and S. Siebentritt, "Current loss due to recombination in Cu-rich $CuInSe_2$ solar cells", Journal of Applied Physics 115, 044503 (2014).

[12] A. E. Zaghi, M. Buffiere, J. Koo, G. Brammertz, M. Batuk, C. Verbist, J. Hadermann, W. K. Kim, M. Meuris, J. Poortmans, J. Vleugels, "Effect of selenium content of $CuInSe_x$ alloy nanopowder precursors on recrystallization of printed $CuInSe_2$ absorber layers during selenization heat treatment", Thin Solid Films, 582, pp. 11-17 (2015).

[13] A. Chirila, P. Reinhard, F. Pianezzi, P. Bloesch, A. Uhl, C. Fella, L. Kranz, D. Keller, C. Gretener, H. Hagendorfer, D. Jaeger, R. Erni, S. Nishiwaki, S. Buecheler, A. Tiwari, "Potassium-induced surface modification of $Cu(In,Ga)Se_2$ thin films for high-efficiency solar cells", Nature Materials, 12: 1107-1111 (2013).

Chapter 8: Conclusion and Outlook

The goal of this thesis was to answer three main scientific challenges that were introduced in Chapter 1. These three challenges are:

1. What is the root cause of the interface recombination losses in Cu-rich CI(G)S solar cells?
2. Will the post-deposition treatments succeed in improving the absorber/buffer interface, increase the V_{OC} and improve the efficiency of Cu-rich CI(G)S solar cells?
3. Can we develop in our laboratories high performance CI(G)S solar cells with low bandgap without any post-deposition treatments?

Cu-rich CI(G)S solar cells were characterized and compared to Cu-poor CI(G)S solar cells. Cu-rich CI(G)S solar cells showed lower efficiencies compared to Cu-poor CI(G)S solar cells. The main reason behind this lower efficiency in Cu-rich CI(G)S solar cells is the V_{OC} and the FF deficiencies. It has been observed that the FF decreases in Cu-rich CI(G)S solar cells due to a strong decrease in the shunt resistances of Cu-rich CI(G)S solar cells compared to Cu-poor CI(G)S solar cells.

On the other side, Cu-rich CI(G)S solar cells suffer from recombination losses at the absorber/buffer interface and show higher doping compared to Cu-poor CI(G)S solar cells. The root cause behind the interface recombination losses and the higher doping in Cu-rich CI(G)S solar cells was explained in terms of a Se-related acceptor defect (identified for Cu-rich CIS solar cells as the 200 ± 20 meV defect observed by admittance measurements and speculated for Cu-rich CIGS solar cells). This Se-related defect appears after the strong etching step that is an essential step for Cu-rich CI(G)S absorbers to remove the conductive copper selenide secondary phases. This Se-related acceptor defect causes recombination losses at the Cu-rich CI(G)S absorber/buffer interface, increases the doping and is then responsible for the lower values of the V_{OC} in Cu-rich CI(G)S solar cells compared to Cu-poor CI(G)S solar cells.

Different post-deposition treatments were introduced with the purpose of improving the electrical performance of Cu-rich CI(G)S solar cells and observing the changes taking place on Cu-rich CI(G)S absorbers and solar cells with and without the post-deposition treatments.

The first post-deposition treatment introduced was an ex-situ KF PDT where the deposition and the annealing steps of the KF were performed in two different steps. This ex-situ KF PDT was optimized for Cu-rich CIS solar cells. The ex-situ KF PDT succeeded in passivating the 200±20 meV defect, improving the Cu-rich CIS absorber/buffer interface, decreasing the doping and consequently increasing the V_{OC} of Cu-rich CIS solar cells. However, this ex-situ KF PDT introduced a transport barrier with an activation energy of 260±20 meV. This transport barrier appeared due to the hygroscopic nature of KF absorbing water from air and caused a decrease in the FF values of Cu-rich CIS solar cells. Moreover, the ex-situ KF PDT facilitated the growth of the CdS buffer layer leading to a thicker CdS buffer layer (compared to our standard CdS buffer layer) grown on top of the Cu-rich CIS absorbers. This thicker CdS buffer layer was responsible for decreasing the J_{SC} values of Cu-rich CIS solar cells after the ex-situ KF PDT. The increase in the V_{OC} observed for Cu-rich CIS solar cells after the ex-situ KF PDT was not enough to compensate the corresponding decrease in FF and J_{SC} values leading to a lower efficiency of Cu-rich CIS solar cells after the ex-situ KF PDT compared to untreated Cu-rich CIS solar cells.

The second post-deposition treatment introduced was an in-situ KF PDT with the deposition and the annealing steps of KF performed in the same step. The in-situ KF PDT was also optimized for Cu-rich CIS solar cells. This in-situ KF PDT succeeded in passivating the 200±20 meV defect, improving the absorber/buffer interface and decreasing the doping leading to an increase in the V_{OC} values of Cu-rich CIS solar cells after the in-situ KF PDT. Performing the deposition and the annealing of KF in one step helped in avoiding a water layer due to the hygroscopic nature of KF and consequently avoiding the formation of the transport barrier observed for Cu-rich CIS solar cells after the ex-situ KF PDT leading to an increase in the FF of the Cu-rich CIS solar cells after the in-situ KF PDT. Similar to the ex-situ KF PDT, the in-situ KF PDT facilitated the growth of a thicker CdS buffer layer leading to a decrease in the J_{SC} values of Cu-rich CIS solar cells after the in-situ KF PDT. The main difference between the ex-situ and the in-situ KF PDTs is that the ex-situ KF PDT improved the V_{OC} but decreased the FF, the J_{SC} and the efficiency of Cu-rich CIS solar cells, while the in-situ KF PDT decreased only the J_{SC} values and succeeded in improving both the V_{OC} and the FF of Cu-rich CIS solar cells. This improvement in the V_{OC} and the FF was higher than the decrease of the J_{SC} values leading to an increase in the efficiency of Cu-rich CIS solar cells after the in-situ KF PDT.

The third post-deposition treatment introduced for Cu-rich CIS absorbers was a Se-only PDT. The parameters used for performing the Se-only PDT were exactly the same as the parameters used for the in-situ KF PDT without the deposition of KF. The Se-only PDT succeeded in passivating the 200±20 meV defect, improving the absorber/buffer interface, decreasing the doping and consequently improving the V_{OC} values for Cu-rich CIS solar cells. With the Se-only PDT, the FF improved but the J_{SC} decreased for Cu-rich CIS solar cells. The improvements of the V_{OC} and the FF were higher than the decrease of the J_{SC} leading to an increase in the efficiency of Cu-rich CIS solar cells after the Se-only PDT.

Based on the above three post-deposition treatments, the mechanism behind the improvements achieved by the alkali (ex-situ and the in-situ KF) post-deposition treatments was speculated. The alkali post-deposition treatments caused two separate effects: one effect is related to the Se-part and the other effect is related to the alkali part. These two effects can be explained as follows:

- The Se-part of the ex-situ and the in-situ KF PDT succeeded in passivating the Cu-rich CIS absorber surface by passivating the Se-related acceptor defect formed after the strong etching step of Cu-rich CIS absorbers. The passivation of the Se-related defect helped to improve the Cu-rich CIS absorber/buffer interface by reducing recombination losses at the interface. Moreover, as the Se-related defect is an acceptor, the passivation of this defect resulted in a decrease in the doping of Cu-rich CIS solar cells. These improvements in the Cu-rich CIS absorber/buffer interface with the decrease in doping were the main drive factors behind the increase in the V_{OC}, FF and consequently the efficiency for Cu-rich CIS solar cells after the in-situ KF and the Se-only PDTs. The same interface improvements were achieved for the Cu-rich CIS solar cells after passivating the Se-related defect with the ex-situ KF PDT leading to an increase in the V_{OC} of Cu-rich CIS solar cells. However, the ex-situ KF PDT introduced a transport barrier that was responsible for decreasing the FF and eventually decreasing the efficiency of Cu-rich CIS solar cells after the ex-situ KF PDT.
- The alkali part in the ex-situ and the in-situ KF PDTs played a different role than the Se-part. The KF part of the ex-situ and the in-situ KF PDTs formed a Cu-poor layer on the surface of the Cu-rich CIS absorbers after the alkali PDTs. This new formed layer after the alkali PDTs is considered the main difference between the alkali PDTs (ex-situ and in-situ KF) and the Se-only PDTs. While both the ex-situ and the in-situ KF PDTs turned the surface of Cu-rich CIS absorbers to a Cu-poor surface, the Se-only PDT maintained the

surface of Cu-rich CIS absorbers as a Cu-rich surface. The effect of this new additional Cu-poor layer (formed at the surface of the Cu-rich CIS absorbers after the alkali PDTs) on the electrical performance of the alkali treated Cu-rich CIS solar cells is not clear. I am not sure if this new formed layer adds an additional improvement to the electrical performance of the alkali treated Cu-rich CIS solar cells or not but I can confirm that this new formed layer does not affect the electrical performance of the alkali treated Cu-rich CIS solar cells negatively.

Motivated by this understanding of the Se-related defect, buffer layers were modified to passivate this defect. CdS and Zn(O,S) buffer layers were modified by adding more thiourea as a source of Sulphur to the CdS and the Zn(O,S) buffer layers. Cu-rich CIS solar cells processed with the modified buffer layers (CdS and Zn(O,S) buffer layers with high thiourea concentrations) showed the passivation of the Se-related defect, the improvement of the absorber/buffer interface, the decrease of the doping and the increase of the V_{OC} of Cu-rich CIS solar cells with such modified buffer layers.

For Cu-rich CIGS solar cells, a Ga-Se post-deposition treatment was developed by Leo Choubrac and I characterized some of the treated Cu-rich CIGS solar cells. The Ga-Se PDT improved the electrical performance of Cu-rich CIGS solar cells through two separate effects: the first effect is the effect of Se and the second effect is the Ga effect. These two effects are also explained as follows:

- The Se effect of the Ga-Se PDT on Cu-rich CIGS solar cells is similar to the Se effect observed for Cu-rich CIS solar cells after the ex-situ, the in-situ and the Se-only PDTs. The Se part of the Ga-Se PDT passivates a Se-related defect (I speculated the presence of this defect but I do not have a physical proof for its presence yet). The passivation of this Se-related defect improves the Cu-rich CIGS absorber/buffer interface by reducing the recombination losses at the interface, decreases the doping and consequently improves the V_{OC} and the FF values of Cu-rich CIGS solar cells after the Ga-Se PDT.
- The Ga part of the Ga-Se PDT turns the surface of Cu-rich CIGS absorbers into a Cu-poor surface similar to the effect of the alkali part in the ex-situ and the in-situ KF PDTs performed on Cu-rich CIS absorbers. This effect of Ga turning the surface of Cu-rich CIGS absorbers to a Cu-poor surface adds an additional improvement to the V_{OC} and the FF values leading to a significant increase in the efficiency of Cu-rich CIGS solar cells after the Ga-Se PDT.

For Cu-poor CI(G)S solar cells, one CIS and two CIGS solar cells were developed with low bandgaps (bandgaps of less than 1.1 eV) and without any post-deposition treatments. The three CI(G)S solar cells showed high performance in terms of efficiency. The efficiency of the two CIGS solar cells were certified while the efficiency of the CIS solar cell was measured in-house. The three Cu-poor CI(G)S solar cells did not show any signature for deep defects within our measurement limits. Moreover, the three Cu-poor low bandgap CI(G)S solar cells were measured under an optical filter of 780 nm and the three solar cells achieved high efficiencies compared to state-of-the-art bottom solar cells in tandem applications. Based on the characterizations performed for the three solar cells, the three low bandgap CI(G)S solar cells showed high performance and high potential to be integrated in tandem applications.

In conclusion, this thesis succeeded in answering the above three challenges as follows:

1. For the first challenge: the reason behind the low efficiency of Cu-rich CI(G)S solar cells compared to Cu-poor CI(G)S solar cells is the deficiency in V_{OC} and FF values. This deficiency in V_{OC} and FF is attributed to recombination losses at the absorber/buffer interface. The root cause of these interface recombination losses in Cu-rich CI(G)S solar cells is a Se-related acceptor defect. The passivation of this Se-related acceptor defect can be achieved by using high enough chalcogen: high enough Selenium in the post-deposition treatments or high enough Sulphur in the buffer layers.
2. For the second challenge: yes, the post-deposition treatments succeeded in improving the absorber/buffer interface of Cu-rich CI(G)S solar cells by passivating the Se-related defect, reducing the interface recombination losses and decreasing the doping. These interface improvements succeeded in improving the V_{OC} and the efficiency of Cu-rich CI(G)S solar cells.
3. For the third challenge: three CI(G)S solar cells with low bandgaps and without any post-deposition treatments were developed and characterized showing their high electrical performance and their high potential to be integrated for tandem applications.

Future Outlook:

The work of this thesis helped in understanding several scientific challenges, but also introduced other challenges that still need to be understood. These challenges can be classified as follows:

1. For the defects in Cu-rich CI(G)S solar cells:
    - The identification of the 200±20 meV Se-related defect observed in Cu-rich CIS solar cells. What is this defect exactly and is the 200±20 meV its real activation energy or not?
    - The detection of the 200±20 meV defect by PL measurements. Could we detect this 200±20 meV defect using PL measurements?
    - The detection of the speculated Se-related defect in Cu-rich CIGS solar cells.
    - The identification of the 175±5 meV speculated to be a S-related defect.
    - The understanding of the change in the activation energy of defects as a function of adding more KF during the in-situ KF PDT or as a function of adding more thiourea in the Zn(O,S) buffer layers.
    - The relationship between the passivation of the Se-related defect and the disappearance of the second slope from the V_{OC} (T) curve of the Cu-rich CI(G)S solar cells.
2. For the post-deposition treatments:
    - The improvement of the J_{SC} by depositing a thinner CdS buffer layer.
    - The role of the new formed Cu-poor layer at the surface of Cu-rich CIS absorbers after the alkali post-deposition treatments on the electrical performance of Cu-rich CIS solar cells
    - The optimization of the alkali post-deposition treatments on Cu-rich CIGS solar cells.
    - The effect of the Se-only PDT on Cu-rich CIGS and Cu-poor CI(G)S solar cells.

Acknowledgement

The journey is coming to an end. My PhD journey was full of special feelings and unforgettable moments. This PhD journey represents one of the most amazing journeys in my life. I can say that now I am achieving one of the most exciting dreams in my life. This dream would not have come true without the presence of some people who helped me a lot throughout this journey. These people mean a lot to me and for me they are the real treasure of this journey.

On top of these people is my supervisor, Susanne Siebentritt. Susanne is not just a supervisor; she is a friend, a mentor and a real supporter. I went with Susanne through many different challenges. I was enthusiastic to discover different research areas and scientific challenges that some of them were already outside the scope of my work. Susanne was patient enough and at the same time supportive enough to make me focus on the real scientific challenges related to my topic. I would like to deeply thank Susanne for being always there for us no matter how busy she is and for issues that are even not related to our research work.

I would also like to thank my CET committee: Guy Brammertz, Thomas Schmidt and again Susanne Siebentritt. They were very helpful and supportive throughout my PhD journey. Moreover, I would like to thank my dissertation committee (my CET committee members, Marika Edoff and Alex Redigner) who are an important part of this PhD journey. I would like to thank them for their fruitful feedback and support.

Luxembourg National Research Fund (FNR) is gratefully acknowledged throughout my PhD journey. FNR supported me through funding the CURI-K project that I am part of. Not only that, but FNR supported me in attending different conferences, workshops and activities that enriched my personal and scientific skills. On top of these activities that FNR supported me was the Lindau Nobel Laureates Meeting. In this meeting, I managed to meet about 30 Nobel Laureates and benefit from the priceless experiences they shared.

A big thank you goes to my team member, Finn Babbe. I consider Finn an exceptional team player. Finn helped me a lot with the PVD, growing the CIS and CIGS samples and the optical characterization of all the samples in terms of Photoluminescence, Reflection and Transmission measurements. With Finn, we developed the ex-situ KF, the in-situ KF and the Se-only post-deposition treatments. Finn is also the one who grew the high quality CIGS absorbers that turned to be high performance solar cells whose efficiencies were eventually

certified. Moreover, Finn helped me in discovering the third acceptor defect and for the observation of this defect for both CIS and CIGS absorbers.

A special thank you should go to Michele Melchiorre. I consider Michele the hidden real player behind the results I achieved in this thesis. Michele was responsible for the baseline process starting from the etching, the deposition of the buffer layers, the sputtering of the window layers and the evaporation of the contacting grids. Michele helped me a lot in the identification of the Se-related defect. Michele was the one responsible for depositing the Aluminium Schottky contacts that enabled me in the identification of this Se-related defect. Michele also developed the Zn(O,S) buffer layer that was later on modified and succeeded in passivating the Se-related defect.

Another special thank you I will dedicate it to Diego Colombara. Diego was always supportive to me in every single moment of my PhD journey. The strong chemical background of Diego, his enthusiasm, his endless experiments, his deep research analysis, his hardworking skills and his eagerness to understand real scientific challenges motivated and supported me a lot throughout my PhD journey. Eventually, we managed to understand the behaviour of the CIS absorber surface with the oxidation process and the differences of this behaviour when crossing the edge of the existence region moving from Cu-poor to stoichiometric to Cu-rich CIS surface. I consider this integration as one of the most important achievements I am proud of during my PhD thesis.

Although I worked with Leo Choubrac for less than six months, but I learnt from Leo a lot. Leo is the one who developed the Ga-Se post-deposition treatment for Cu-rich CIGS solar cells. Leo helped me understanding how the tools work, explaining the procedures of the PVD, the development of the 3-stage CIGS absorbers using the PVD and the interpretation of the different electrical characterizations that I used in this thesis.

If I mentioned the PVD, then I should mention Tobias Bertram. I would like to thank Tobias for all the support he showed to me. Tobias explained for me how the PVD works and its different parts, gave me a training on the PVD, showed me how to develop the 1-stage CIS absorbers, how to produce high quality absorbers and assisted me in interpreting different electrical characterization techniques. Moreover, Tobias is the one who first observed the 200 ± 20 meV capacitance step and he speculated this step as a defect before I finally managed to give more evidences that this capacitance step is a Se-related defect. The electrical characterizations performed by Tobias for Cu-rich CIS solar cells were always guiding me in

understanding the behaviour of Cu-rich CIS solar cells. For the interpretation of some of the electrical characterization measurements I performed, I used scripts developed by Tobias.

Moving to the interpretation of the electrical characterizations measurements I performed during my PhD thesis, I have to send a special thank you to Thomas Paul Weiss. Thomas developed most of the scripts I used to analyse the electrical measurements performed. The scripts developed by Thomas indeed saved a lot of my time and helped me a lot in understanding the behaviour of all the measured absorbers and solar cells. In addition to that, the electrical characterizations performed by Thomas on Kesterite solar cells motivated me to apply a similar characterization to my chalcopyrite solar cells. Moreover, the PhD thesis of Thomas was also inspiring for me while writing my own PhD thesis.

I would like to thank Anastasiya Zelenina who has been my post-doc for part of my PhD research project. Anastasiya helped me in different absorber depositions and electrical characterizations.

I would like to specially thank Mohit Sood for helping me with depositing different buffer layers, modifying these buffer layers and performing different electrical characterizations. These modified buffer layers succeeded in passivating the Se-related defect, which is an important part of my research work. Moreover, Mohit helped me a lot in performing different metastable analysis and characterizations that were an essential part in understanding the nature of the Se-related defect.

I would like to express my sincere gratitude to Thomas Schuler and Patricia Ramoa. Thomas was always there helping me in fixing the tools and solving any issues rising up with the tools. All the problems related to the tools, changing parts of the tools, maintenance of the tools setup and the internal programming of the tools were all performed by Thomas. On the other side, Patricia was always there for all the administrative and paper work. Moreover, Patricia helped me a lot with the bookings of hotels, flight tickets, the registrations for the conferences and the preparations of many other events and activities. Without the help of Thomas and Patricia, I would not have been able to complete my PhD journey.

I would like to send a special thank you to Florian Werner who helped me a lot with the electrical characterizations, the explanation of how the tools work, the interpretation of the data and the results and the fruitful modifications and discussions we had together. I would also like to thank Max Wolter, Conrad Spindler and Germain Rey for all the deep fruitful discussions that helped me a lot in understanding the defects in CIS and CIGS solar cells.

I would like to thank all the team of LPV, LEM and SPM for the fruitful discussions and the time we spent together outside work.

Moreover, I would like to acknowledge Jerome Guillot and Yves Fleming from Luxembourg Institute of Science and Technology for performing the XPS measurements presented in this thesis. I would like to thank Erika Robert for assisting me to perform the XRD measurements.

I would like to send a special lovely thank you for my special lovely wife, Mariam. This PhD journey is very special for her and me. This PhD journey witnessed the moment when we got married and we started a new chapter in our lives. Mariam was always there for me in every single moment beside me supporting me and motivating me through all the different challenges I passed by. No words can describe how much I love her and how much I am grateful to everything she did for me.

I would not have been able to complete this PhD journey without the support of my father, my mother and my sisters: Hagar, Nouran and Amna who were always behind me. I would like to deeply thank you, you are the best family ever.

I would like to thank all my friends in Luxembourg specially Abdallah Ali and Mohamed Ceman for all the help, support, activities and trips that we enjoyed together.

Finally, I would like to say: Thank you all, You are all my family and without you, my PhD journey would not have been that successful.

Annex A.1: *Sample list for Chapter 5*

Figures/Tables	Samples	References
Figure 5.1	a) CIS315d (Cu-rich) b) CIS312d (Cu-poor) c) CIS314d (Cu-rich) d) CIS312d (Cu-poor)	
Table 5.1	CIS252 (Cu-rich) CIS253 (Cu-poor)	
Figure 5.2a	CIS252a (Cu-rich CIS) CIS253a (Cu-poor CIS)	
Figure 5.2b	CIGS120 (Cu-rich CIGS 1.03 eV) CIGS128 (Cu-poor CIGS 1.04 eV) CIGS110 (Cu-rich CIGS 1.09 eV) CIGS107 (Cu-poor CIGS 1.09 eV) CIGS142 (Cu-rich CIGS 1.17 eV) CIGS139 (Cu-rich CIGS 1.18 eV)	
Table 5.2	Cu-rich & Cu-poor CIS (Average of all samples) CIGS120 (Cu-rich CIGS 1.03 eV) CIGS128 (Cu-poor CIGS 1.04 eV) CIGS110 (Cu-rich CIGS 1.09 eV) CIGS107 (Cu-poor CIGS 1.09 eV) CIGS142 (Cu-rich CIGS 1.17 eV) CIGS139 (Cu-rich CIGS 1.18 eV)	
Figure 5.3a	CIS252 (Cu-rich) CIS253 (Cu-poor)	
Figure 5.3b	CIGS120 (Cu-rich CIGS 1.03 eV) CIGS128 (Cu-poor CIGS 1.04 eV) CIGS110 (Cu-rich CIGS 1.09 eV) CIGS107 (Cu-poor CIGS 1.09 eV) CIGS142 (Cu-rich CIGS 1.17 eV) CIGS139 (Cu-rich CIGS 1.18 eV)	
Figure 5.3c	CIS252 (Cu-rich CIS 0.995 eV) CIGS120 (Cu-rich CIGS 1.03 eV) CIGS110 (Cu-rich CIGS 1.09 eV) CIGS142 (Cu-rich CIGS 1.17 eV) CIGS140 (Cu-rich CIGS 1.22 eV)	
Figure 5.3d	CIS253 (Cu-poor CIS 0.95 eV) CIGS128 (Cu-poor CIGS 1.04 eV) CIGS127 (Cu-poor CIGS 1.07 eV) CIGS107 (Cu-poor CIGS 1.09 eV) CIGS139 (Cu-poor CIGS 1.18 eV)	
Table 5.3	CIS252 (Cu-rich) CIS253 (Cu-poor) CIGS110 (Cu-rich CIGS 1.09 eV) CIGS107 (Cu-poor CIGS 1.09 eV) CIGS142 (Cu-rich CIGS 1.17 eV) CIGS139 (Cu-rich CIGS 1.18 eV)	
Figure 5.4	CIS252 (Cu-rich)	

	CIS253 (Cu-poor)	
Figure 5.5a	CIS308 (Cu-rich CIS) CIS313 (Cu-poor CIS) CIGS140 (Cu-rich CIGS) CIGS127 (Cu-poor CIGS)	
Figure 5.5b	CIS295 (Cu-rich CIS) CIS253 (Cu-poor CIS)	
Table 5.4	CIS334 (Cu-rich CIS) CIS263 (Cu-poor CIS) CIGS140 (Cu-rich CIGS) CIGS 127 (Cu-poor CIGS)	
Figure 5.6	CIS334 (Cu-rich CIS) CIS263 (Cu-poor CIS) CIGS140 (Cu-rich CIGS) CIGS 127 (Cu-poor CIGS)	
Figure 5.7	CIS308d (Cu-rich CIS) CIS327 (Cu-poor CIS) CIGS140d (Cu-rich CIGS) CIGS128 (Cu-poor CIGS)	
Figure 5.8	CIS333 (Cu-rich CIS) CIS327 (Cu-poor CIS)	
Figure 5.9	CIGS120 (Cu-rich CIGS 1.03 eV) CIGS134 (Cu-rich CIGS 1.11 eV) CIGS142 (Cu-rich CIGS 1.17 eV) CIGS140 (Cu-rich CIGS 1.22 eV)	
Figure 5.10	CIGS128 (Cu-poor CIGS 1.04 eV) CIGS127 (Cu-poor CIGS 1.07 eV) CIGS097 (Cu-poor CIGS 1.11 eV) CIGS092 (Cu-poor CIGS 1.17 eV)	
Table 5.5	CIS334 (Cu-rich CIS) CIS263 (Cu-poor CIS) CIGS140 (Cu-rich CIGS) CIGS 127 (Cu-poor CIGS)	
Figure 5.11	CIS333b (Cu-rich CIS Se-treated) CIGS120 (Cu-rich CIGS 1.03 eV) CIGS134 (Cu-rich CIGS 1.11 eV) CIGS142 (Cu-rich CIGS 1.17 eV) CIGS140 (Cu-rich CIGS 1.22 eV) CIS327 (Cu-poor CIS) CIGS128 (Cu-poor CIGS 1.04 eV) CIGS127 (Cu-poor CIGS 1.07 eV) CIGS097 (Cu-poor CIGS 1.11 eV) CIGS092 (Cu-poor CIGS 1.17 eV)	

Annex A.2: ***Sample list for Chapter 6***

Figures/Tables	Samples
Table 6.1	CIS249a (Cu-rich reference) CIS249c (Cu-rich annealed 300 ^{0}C) CIS248b (Cu-rich KCN, annealed 350 ^{0}C) CIS248c (Cu-rich de-ionized, annealed 350 ^{0}C) CIS249b (Cu-rich de-ionized, annealed 400 ^{0}C)
Figure 6.1, Table 6.2, Figure 6.2, Table 6.3, Figure 6.3, Figure 6.4, Figure 6.6	CIS252a (Cu-rich untreated) CIS252b (Cu-rich + ex-situ KF) CIS253a (Cu-poor untreated) CIS253b (Cu-poor + ex-situ KF)
Figure 6.5, Figure 6.7	CIS252b (Cu-rich + ex-situ KF) CIS253b (Cu-poor + ex-situ KF)
Figure 6.8, Figure 6.14	CIS308d (Cu-rich untreated) CIS308b (Cu-rich + in-situ KF 8 min)
Figure 6.9, Table 6.4, Figure 6.12	CIS308d (Cu-rich untreated) CIS308a (Cu-rich + in-situ KF 12 min) CIS308b (Cu-rich + in-situ KF 8 min) CIS308c (Cu-rich + in-situ KF 4 min) CIS313d (Cu-poor untreated) CIS313a (Cu-poor + in-situ KF 6 min)
Figure 6.10a, Figure 6.11, Figure 6.13a, Figure 6.15, Figure 6.16	CIS308d (Cu-rich untreated) CIS308a (Cu-rich + in-situ KF 12 min) CIS308b (Cu-rich + in-situ KF 8 min) CIS308c (Cu-rich + in-situ KF 4 min)
Figure 6.10b, Figure 6.13b	CIS313d (Cu-poor untreated) CIS313a (Cu-poor + in-situ KF 6 min)
Figure 6.17	CIGS77 (Cu-rich untreated) CIGS77Ga (Cu-rich + Ga-Se PDT) CIGS107 (Cu-poor untreated)
Table 6.5, Figure 6.18, Figure 6.19	CIGS77 (Cu-rich untreated) CIGS77Ga (Cu-rich + Ga-Se PDT)
Figure 6.21, Table 6.6, Figure 6.22, Figure 6.23, Figure 6.26	CIS333d (Cu-rich) CIS333b (Cu-rich + Se PDT)
Figure 6.24a, Figure 6.24b, Figure 6.27b	CIS333b_Se (Cu-rich Schottky + Se PDT)
Figure 6.24c, Figure 6.24d, Figure 6.27a	CIS333b (Cu-rich cell + Se PDT)

Figure 6.25	CIS333d (Cu-rich) CIS333b (Cu-rich + Se PDT) CIS327d (Cu-poor)
Figure 6.28	a) CIS327 (Cu-poor CIS 0.95 eV) b) CIGS128 (Cu-poor CIGS 1.04 eV) c) CIGS127 (Cu-poor CIGS 1.07 eV)
Figure 6.29, Figure 6.30, Table 6.7, Figure 6.31, Figure 6.32, Table 6.8, Figure 6.33, Figure 6.34	CIS327 (Cu-poor CIS 0.95 eV) CIGS128 (Cu-poor CIGS 1.04 eV) CIGS127 (Cu-poor CIGS 1.07 eV)

Annex A.3: ***Sample list for Chapter 7***

Figures/Tables	Samples
Figure 7.2	a), b) CIS332c (Cu-rich Low-Se Schottky) c), d) CIS332c_CdS (Cu-rich Low-Se Schottky + CdS) e), f) CIS332d (Cu-rich Low-Se solar cell)
Figure 7.3	a), b) CIS333c (Cu-rich Med-Se Schottky) c), d) CIS333c_CdS (Cu-rich Med-Se Schottky + CdS) e), f) CIS333d (Cu-rich Med-Se solar cell)
Figure 7.4	a), b) CIS334c (Cu-rich High-Se Schottky) c), d) CIS334c_CdS (Cu-rich High-Se Schottky + CdS) e), f) CIS334d (Cu-rich High-Se solar cell)
Figure 7.5	CIS332c (Cu-rich Low-Se Schottky) CIS332c_CdS (Cu-rich Low-Se Schottky + CdS) CIS332d (Cu-rich Low-Se solar cell) CIS333c (Cu-rich Med-Se Schottky) CIS333c_CdS (Cu-rich Med-Se Schottky + CdS) CIS333d (Cu-rich Med-Se solar cell) CIS334c (Cu-rich High-Se Schottky) CIS334c_CdS (Cu-rich High-Se Schottky + CdS) CIS334d (Cu-rich High-Se solar cell)
Figure 7.6	CIS332c_CdS (Cu-rich Low-Se Schottky + CdS) CIS332d (Cu-rich Low-Se solar cell) CIS333c (Cu-rich Med-Se Schottky) CIS333c_CdS (Cu-rich Med-Se Schottky + CdS) CIS333d (Cu-rich Med-Se solar cell) CIS334c (Cu-rich High-Se Schottky) CIS334c_CdS (Cu-rich High-Se Schottky + CdS) CIS334d (Cu-rich High-Se solar cell)
Figure 7.7	a), c) CIGS142c (Cu-rich CIGS Schottky) b), d) CIGS142d (Cu-rich CIGS solar cell)
Figure 7.8	a), b) CIS252 (Cu-rich CIS) c), d) CIS254 (Stoichiometric CIS) e), f) CIS253 (Cu-poor CIS)
Figure 7.9, Figure 7.11, Figure 7.12, Figure 7.13	CIS252 (Cu-rich CIS) CIS254 (Stoichiometric CIS) CIS253 (Cu-poor CIS)
Figure 7.10	CIS254_noKCN (unetched Stoichiometric CIS)
Figure 7.14	a), c) CIS253_rich (strong KCN Cu-poor CIS) b), d) CIS254_strong KCN (strong KCN Stoichiometric CIS)
Figure 7.16	a) CIS332b_KCN b) CIS332b_NaCN
Figure 7.17	a), b) CIS334d (Cu-rich CIS) c), d) CIS334c_EMPA (Cu-rich CIS + EMPA CdS) e), f) CIS334a_Low TU (Cu-rich CIS + Zn(O,S))
Figure 7.18	a), b) CIS334a_6x TU (Cu-rich CIS + Zn(O,S) 6 X TU) c), d) CIS334a_8x TU (Cu-rich CIS + Zn(O,S) 8 X TU) e), f) CIS334a_16x TU (Cu-rich CIS + Zn(O,S) 16 X TU)
Figure 7.19	CIS334d (Cu-rich CIS)

	CIS334c_EMPA (Cu-rich CIS + EMPA CdS) CIS334a_8x TU (Cu-rich CIS + Zn(O,S) 8 X TU)
Table 7.1	CIS334d (Cu-rich CIS) CIS334c_EMPA (Cu-rich CIS + EMPA CdS) CIS334a_6x TU (Cu-rich CIS + Zn(O,S) 6 X TU) CIS334a_8x TU (Cu-rich CIS + Zn(O,S) 8 X TU) CIS334a_16x TU (Cu-rich CIS + Zn(O,S) 16 X TU)
Figure 7.20	CIS334d (Cu-rich CIS) CIS334c_EMPA (Cu-rich CIS + EMPA CdS)
Figure 7.21	Cu-rich CIS CIS252b (Cu-rich CIS + ex-situ KF) CIS308a,b,c (Cu-rich CIS + in-situ KF) CIS333b (Cu-rich CIS + Se-PDT) CIS334c_EMPA (Cu-rich CIS + EMPA CdS) CIS334a_Low TU (Cu-rich CIS + standard Zn(O,S)) CIS334a_8x TU (Cu-rich CIS + Zn(O,S) 8 X TU)

Annex B: List of Publications

2019:

- *H. Elanzeery*, M. Melchiorre, F. Babbe, M. Sood, F. Werner, S. Siebentritt, "Challenge in Cu-rich Thin Film Solar Cells: Defect Caused by Etching", submitted.
- *H. Elanzeery*, D. Colombara, M. Melchiorre, F. Babbe, S. Siebentritt, "Chemical potentials as the drivers of chalcopyrite photovoltaic performance", in review.
- F. Babbe, *H. Elanzeery*, M. H. Wolter, K. Santhosh, S. Siebentritt, "The hunt for the third acceptor in $CuInSe_2$ and $Cu(In,Ga)Se_2$ absorber layers", submitted.
- M. Sood, *H. Elanzeery*, A. Lomuscio, M. Melchiorre, S. Siebentritt, "Annealing effects on Cu rich and Cu poor chalcopyrite solar cells", in review.
- F. Werner, F. Babbe, *H. Elanzeery*, S. Siebentritt, "Defects, buffer layer, or artefact – what do we see in capacitance measurements of thin-film solar cells?", submitted.

2018:

- *H. Elanzeery*, F. Babbe, M. Melchiorre, F. Werner, S. Siebentritt "High performance low bandgap thin film solar cells for tandem applications", Progress in Photovoltaics: Research and Applications, 26, 7, 437 - 442.
- F. Babbe , *H. Elanzeery*, M. Melchiorre, A. Zelenina, S. Siebentritt, "In-situ potassium fluoride treatment on both Cu-rich and Cu-poor $CuInSe_2$ thin film solar cells", Physical Review Materials, 2, 105405.
- F. Werner, F. Babbe, J. Burkhart, C. Spindler, *H. Elanzeery*, S. Siebentritt, "Interdiffusion and doping gradients at the buffer/absorber interface in thin-film solar cells", ACS Applied Materials & Interfaces, 10, 34, 28553 - 28565.
- E. Robert, R. Gunder, J. de Wild, C. Spindler, F. Babbe, *H. Elanzeery*, B. El Adib, R. Treharne, H. Miranda, L. Wirtz, S. Schorr, P. Dale, "Synthesis, theoretical and experimental characterisation of thin film $Cu_2Sn_{1-x}Ge_xS_3$ ternary alloys (x = 0 to 1): homogeneous intermixing of Sn and Ge", Acta Materialia, 151, 125-136.

2017:

- *H. Elanzeery*, F. Babbe, M. Melchiorre, A. Zelenina, S. Siebentritt, "Potassium fluoride ex-situ treatment on both Cu-rich and Cu-poor $CuInSe_2$ thin film solar cells", IEEE Journal of Photovoltaics, 7, 2, 684 - 689.
- *H. Elanzeery*, F. Babbe, A. Zelenina, M. Melchiorre, S. Siebentritt, "Interface effects of alkali treatment on Cu-rich thin film solar cells", Proceedings of IEEE Photovoltaics specialist conference (PVSC) proceedings.
- A. Zelenina, F. Werner, *H. Elanzeery*, M. Melchiorre, S. Siebentritt, "Space-charge-limited currents in CIS-based solar cells", Applied Physics Letters, 111, 213903.
- G. Rey, F. Babbe, T. P. Weiss, *H. Elanzeery*, M. Melchiorre, N. Valle, B. El Adib, S. Siebentritt, "Post-deposition treatment of $Cu_2ZnSnSe_4$ with alkalis", Thin Solid Film, 633, 162-165.
- F. Babbe, *H. Elanzeery*, M. Melchiorre, S. Siebentritt, "$CuInSe_2$ absorber layer grown under copper excess with a copper poor surface formed by an KF post deposition treatment", Proceedings of IEEE PVSC proceedings.

2016:

- L. Choubrac, T. Bertram, *H. Elanzeery*, S. Siebentritt, "Cu(In,Ga)Se_2 solar cells with improved current based on surface treated stoichiometric absorbers" Physica Status Solidi (a), 214, 1, 1600482.

Annex C: List of Conferences and workshops

Oral presentations:

- European Photovoltaic Solar Energy Conference (EUPVSEC), Brussels, (Sep. 2018).
  Title: Characterization of high performance Cu(In,Ga)Se_2 bottom cells in thin film solar tandem applications
- Nanotechnology & next generation high efficiency photovoltaics (NEXTGEN), Spain, (Sep. 2017).
  Title: Decreasing doping and improving interface recombination in Cu-rich CIS by means of alkali-treatment
- IEEE Photovoltaic Specialists Conference (PVSC), Washington, USA, (June 2017).
  Title: Interface effects of alkali treatment on Cu-rich thin film solar cells
- European Photovoltaic Solar Energy Conference (EUPVSEC), Munich, (June 2016).
  Title: Potassium Fluoride Ex-Situ Treatment for Cu-rich $CuInSe_2$ Thin Film Solar Cells

Poster presentations:

- European Material Research Society (E-MRS), Strasbourg, (June 2018).
  Title: Defect characterization for Cu-rich CIS thin film solar cells with Se post-deposition treatment

Conferences and workshops participation:

- New Space Europe Conference, Luxembourg, (November 2017).
- World Youth Forum Conference (WYF), Sharm Elsheikh, Egypt, (November 2017).
- Climate Innovation Workshop, Luxembourg, (2018).
- Lecturing & Teaching at the university workshop, Belval, Luxembourg, (2017).
- FNR Leadership & Communication workshop, Belval, Luxembourg, (2016).
- FNR Media workshop, Belval, Luxembourg, (2016).
- Lindau Nobel Laureates Meeting, Lindau, Germany, (2016).
- Quantsol Photovoltaics Summer School, Hirschegg, Austria, (2016).
- New Energies workshop: The Future of Energy at the Interface of Technology, Saarbrücken, Germany (2015).

Teaching activities

- Solid State Physics, tutorial class (2016).
- Physics II, laboratory class (2016).
- Physics I, laboratory class (2015).